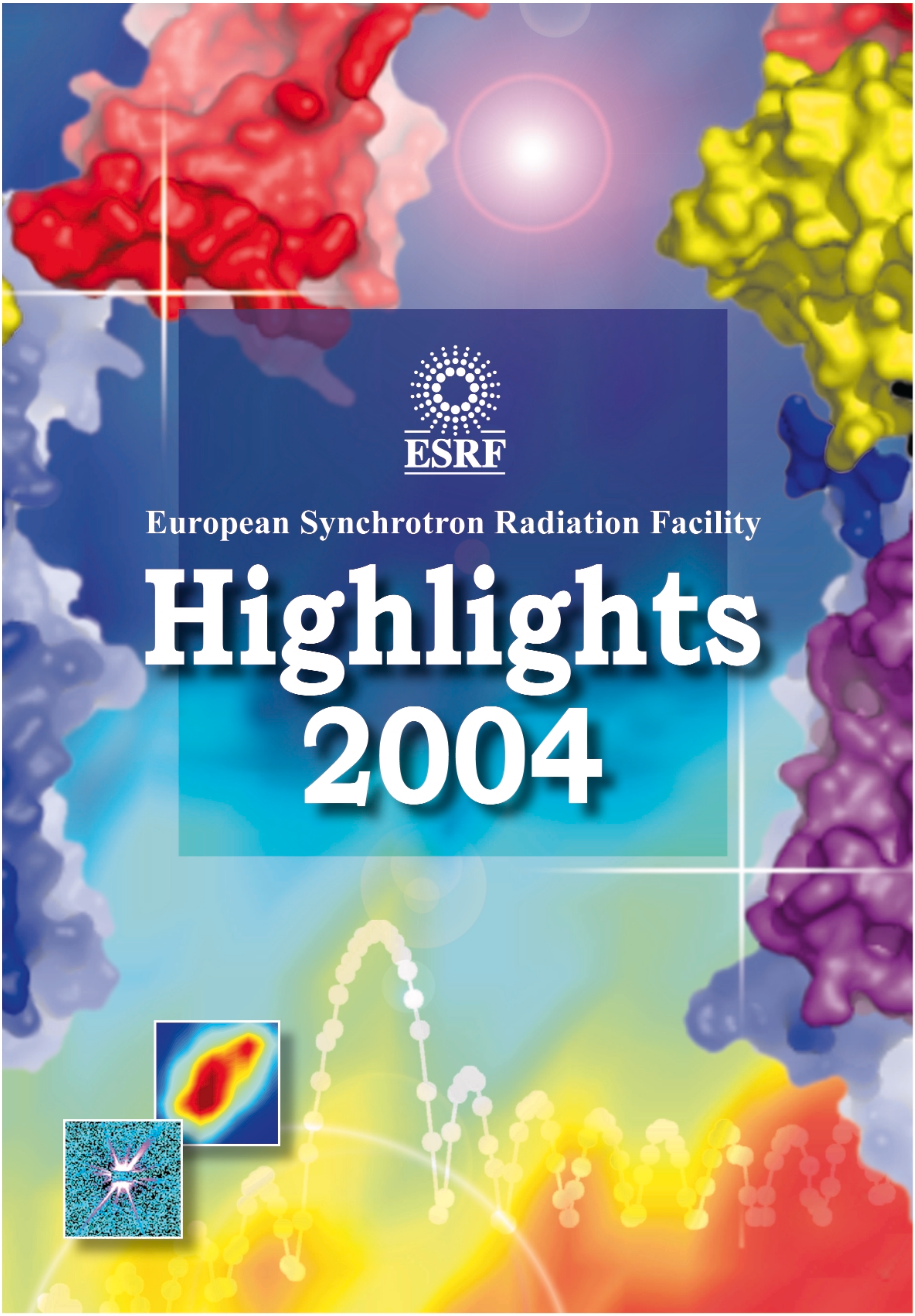

ESRF

European Synchrotron Radiation Facility

Highlights 2004

ESRF

European Synchrotron Radiation Facility

Highlights 2004

Contents

Pages

Introduction 2

Scientific Highlights 4

- *High Resolution and Resonance Scattering* 4
- *Materials Science* 22
- *Soft Condensed Matter* 40
- *Structural Biology* 55
- *Surface and Interface Science* 71
- *X-ray Absorption and Magnetic Scattering* 84
- *X-ray Imaging* 108

The X-ray Source 126

Facts and Figures 135

Introduction

This has been a year of records for the ESRF. In 2004, a record number (1675) of proposals was received by our User Office. This corresponds to a total of 26251 shifts requested across all of the ESRF's beamlines. Scientific output also continues to grow. Staff at the ILL-ESRF library have identified almost 1200 refereed articles published during 2003, referring to work carried out at the ESRF. These scientific achievements were supported by an excellent Machine performance, with the longest recorded period of beam delivery without interruption: during December, the beam was maintained in 16-bunch mode for 288 hours (12 days) without a single beam trip, despite 48 refills followed by beam cleaning. Beam availability in 2004 equalled that of 2003, reaching 97.95%. Industrial interest in the ESRF was also at unmatched levels with the highest number of requests for industrial beamtime and the largest turnover for the Industrial and Commercial Unit.

As in previous years a vigorous programme of beamline renewal and improvement was pursued. A noteworthy event was the installation of an infrared beam port on BM21. The "edge radiation", emitted when electrons enter the bending magnet, is collected and transmitted to the infrared microscopy station at ID21. The high brilliance of the edge radiation leads us to expect that this facility should be competitive with the new 2 to 3 GeV light sources, despite the higher electron energy at the ESRF. Full commissioning of the infrared microscopy station will take place during the early part of 2005.

Rapid progress has been made with the Partnership for Structural Biology. Not only are the scientific collaborations central to this partnership now producing new science, but also the second branch of the new beamline ID23 for high-throughput, microfocus-beam macromolecular crystallography is at a very

advanced stage of construction, and the shell of the PSB laboratory building is almost complete.

Records were also broken where computing resources are concerned. The 30 public and 11 CRG beamlines have again generated a record volume of data in 2004 with a total of about 110 Terabytes in some 55 million files. The daily data production reached 1 Terabyte/day at the end of the year, reflecting the increased efficiency of the beamlines and the use of high-resolution detectors.

This was also a year of anniversaries, foremost among which was the tenth anniversary, on 30 September, of the start of User operation. This important milestone for the ESRF was celebrated by a special edition of the Newsletter in December. Where administrative matters are concerned it is important to note that on 1 July, Poland became the latest Scientific Associate, bringing to 18 the number of national partners. During the year, extensions of the Arrangements with Israel and the Czech Republic were also signed. Furthermore, work continued apace on the development of the Long Term Strategy, an essential programme for renewal of the ESRF over the next five to ten years.

The PSB laboratory/office building on 10 January 2005.

The 2004 Christmas tree with, from left to right, Pascal Elleaume (Machine Director), Pierre Thiry (Head of Technical Services Division), Bill Stirling (Director General), Francesco Sette (Director of Research), Karl Witte (Assistant to the Director General, and Secretary of the ESRF Council), Helmut Krech (Director of Administration) and Rudolf Dimper (Head of Computing Services Division). Inset: Sine Larsen (Director of Research).

The Highlights 2004 document provides a comprehensive summary of the excellent science produced at the ESRF by scientists from around the world. While this is primarily a showcase for the remarkably wide variety of scientific topics investigated using synchrotron X-rays at the ESRF, there is also a final "Facts and Figures" section that provides a concise summary of activities at the ESRF throughout 2004. We hope that you enjoy reading the Highlights of 2004 and we look forward to a scientifically successful future for the ESRF.

W.G. Stirling, P. Elleaume, R. Dimper, H. Krech, S. Larsen, F. Sette, P. Thiry, K. Witte

(January 2005)

Highlights 2004

Scientific Highlights

High Resolution and Resonance Scattering

Introduction

The High Resolution and Resonance Scattering Group's activity comprises many more scientific topics and applications than can be reported here in sufficient detail. This year we are going to focus on two fields: Surface Science/Nano-structures and Earth Science. These are good examples that demonstrate the continual advances necessary to address the problems most relevant today. In addition, to the improvements of the quality and flux of the synchrotron radiation beam, we also witness better beamline optics and more sophisticated sample environments. Higher photon flux and a smaller X-ray beam allow high pressure and surface investigations with energy resolution down to the neV range and time resolution down to the ns regime. All these developments and investigations need the full dedication of the beamline staff and the expertise brought by our external users and collaborators.

The group is involved in two European projects: firstly VOLPE, which is nearing the end of a successful final year, and secondly DYNASYNC, which had only just started in 2004. In the framework of "Volume photoemission from solids" (VOLPE), the well-established surface sensitive technique of photoemission in the soft X-ray regime has been expanded to the hard X-ray regime being now bulk sensitive. First results on vanadium oxide have been achieved with an overall energy resolution of 70 meV at 6 keV [1]. With this resolution we are now looking forward to fully exploiting this new experimental environment. In the project on Dynamics in Nano-scale Materials Studied with Synchrotron Radiation (DYNASYNC) we apply nuclear resonance techniques in order to explore - under the same conditions and preferably in parallel - magnetic/electronic properties and slow (diffusional and rotational motions) and fast (phonons) dynamics in systems such as iron on tungsten, metal/oxide systems, and multilayers. Arriving too late to be reported on in these Highlights, the first measurements of the phonon density of states of monolayers, islands and bulk iron on tungsten have been conducted showing a tremendous difference in their phonon spectra and by this in their dynamical behaviour. Furthermore, magnetic properties could be followed during the growth process.

The emerging techniques of inelastic X-ray (IXS) and nuclear inelastic scattering (NIS) have again shown that their full potential has not yet been explored. First studies demonstrated that IXS has the capability to map not only dispersion curves but also to determine directly the density of phonon states. The very first experiments are reported on the model systems diamond and MgO [2]. In case of molecular systems, *i.e.* those with well-resolved optical/localised modes, NIS proved capable of separating the vibrational density of states of each phase in heterogeneous systems and also the (thermo-)dynamical quantities derived from it [3].

Finally, the study of glasses and disordered systems has continued. The following two examples on Basic Dynamics of Glasses demonstrate that the techniques have contributed to the fundamental understanding of these systems. Matic *et al.* compare the low energy dynamics of polymorphic ethanol in the glassy, rotationally disordered and crystalline phases and conclude on a common origin of the vibrational behaviour. The contribution by Chumakov *et al.* exposes the collective nature of the Boson peak in several systems and discusses a universal exponential "trans-Boson" behaviour in glasses.

R. Rüffer

References

[1] P. Torelli *et al., Rev. Sci. Instr.* **76**, 23909 (2005).
[2] A. Bossak *et al*., *submitted to PRL* (2005).
[3] A.I. Chumakov *et al*., *PRL* **92**, 243001 (2004).

Basic Dynamics of Glasses

Crystal-like Nature of Acoustic Excitations in Glassy Ethanol

It is well known that disordered materials exhibit anomalies in their dynamical and thermal properties compared to the Debye model and the behaviour of crystals. The anomalies are commonly linked to the nature of acoustic modes at wavelengths approaching typical distances of the disorder. However, the understanding of acoustic excitations in glasses is far from the level reached for crystalline solids due to both theoretical as well as experimental shortcomings. Recently there has been considerable experimental progress due to the development of high resolution inelastic X-ray scattering (IXS), enabling direct observations of longitudinal acoustic excitations in the region of the first Brillouin zone [1]. The common findings from these experiments on glasses are a linear dispersion of the acoustic modes at small wave vectors, with a slope of the dispersion corresponding to the longitudinal low frequency sound velocity, and a Q^2 dependence of the linewidth of the excitations.

In this work we investigate the influence of disorder on the nature of acoustic excitations directly by comparing IXS spectra from a monoclinic crystal, a rotationally disordered BCC crystal and a glassy phase of ethanol at wavevectors corresponding to the first and second

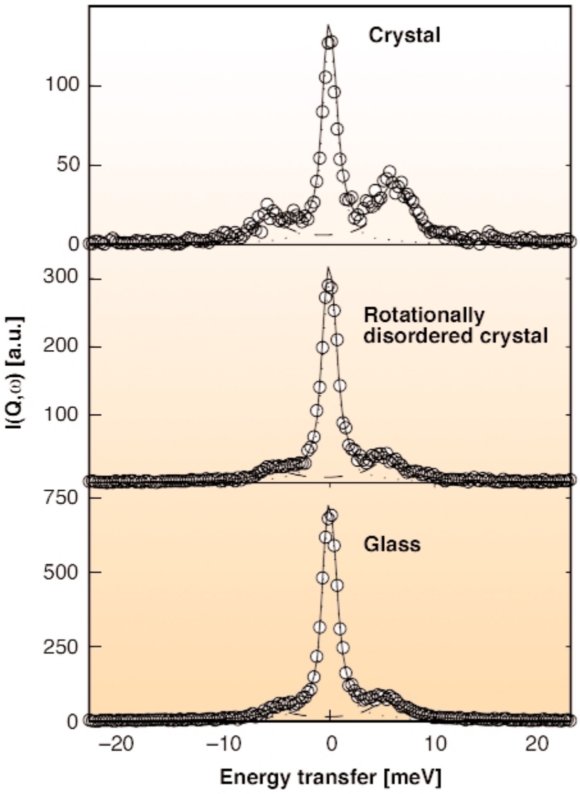

Fig. 1: IXS spectra from the three different solid phases of ethanol at $Q = 3\ \text{nm}^{-1}$.

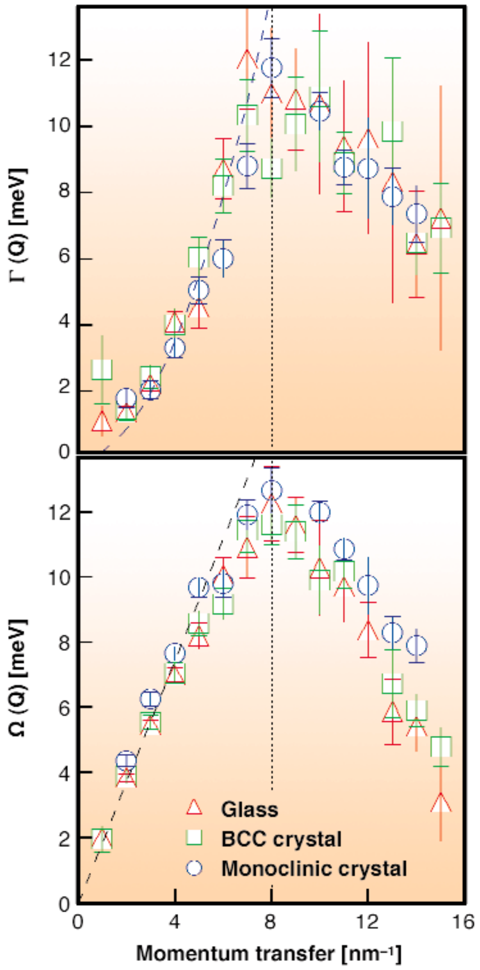

Fig. 2: Position, Ω(Q), and width, Γ(Q), of the acoustic excitations found from the IXS experiment. The vertical dotted line indicates the position of the average Brillouin zone. The dashed line in the lower panel corresponds to the sound velocity in the glass. In the upper panel the dashed line corresponds to a Q^2 behaviour of the width.

Brillouin zone of the crystal. Ethanol is one of a few polymorphic systems where glassy, rotationally-disordered, and crystalline phases can be investigated at the same temperature, enabling a direct comparison of the structural influence on the dynamical properties [2]. The different phases were prepared *in situ* in the cryostat using the same sample and all the measurements were performed at the same temperature, T = 86 K, at the **ID16** beamline. The diffracted intensity recorded simultaneously with the inelastic experiments confirmed the phase transformations.

An example of the experimental data is shown in **Figure 1**. At low momentum transfers, Q, one observes well-defined inelastic peaks, whereas at higher Q the inelastic component is broad and the peaks are ill-defined. The spectroscopic parameters, position, width and intensity, were extracted by fitting the spectra with a damped harmonic oscillator model for the acoustic excitations [1]. The results for the different phases are remarkably similar, as can be seen in **Figure 2**. They reveal an almost linear dispersion up to Q ~ 8 nm^{-1} in all three phases, and a linewidth that approximately follows a Q^2 behaviour. At higher Q the position of the excitation decreases in energy.

For a crystalline sample this picture is not surprising and can be understood in the well known terms of Brillouin zones and phonon dispersion curves. Since we have a polycrystal the dispersion represents the average of the dispersion relations in the different crystalline directions and the average Brillouin zone boundary is found at Q ~ 8 nm^{-1}. For the glass, the results are more surprising. Even though the material lacks translational order, we observe a crystal-like dispersion curve with a slope that agrees well with the low frequency longitudinal sound velocity. The maximum of the dispersion curve occurs at $Q = Q_P/2$ where Q_P is the main peak of the static structure factor, S(Q), and the dispersion curve goes towards a minimum at Q_P. Thus Q_P acts as a reciprocal lattice point for the glass defining a pseudo-Brillouin zone for $Q < Q_P/2$. This crystal-like behaviour provides evidence that we also have phonon-like excitations in the glass with wavelengths approaching the inter-particle distance in the material. The lack of influence of the structural disorder shows that the acoustic excitations are essentially of the same nature in the glass and in the poly-crystal, in the energy region of the excess in the vibrational density of states. Thus, the origin of the dynamical anomalies in the glass cannot be directly related to significant changes in the nature of these excitations.

From our results we can also offer an explanation of the universal Q^2 dependence of the linewidth for glasses [1]. Within the accuracy of the present experiment the width is the same in all three phases indicating a common origin. In the crystalline phases the increase of the width can be understood as a result of the increasing energy spread of the phonon branches in different crystalline directions. Along this line the observed linewidth in the glass can be attributed to an intrinsic averaging over different local structural orientations, and cannot be linked to the lifetime, or damping, of a single excitation, nor to the lack of short range order.

References

[1] F. Sette *et al*., *Science* **280**, 1550 (1998).
[2] M. Ramos *et al*., *Phys. Rev. Lett.* **78**, 82 (1997).

Principle Publication and Authors

A. Matic (a), C. Masciovecchio (b), D. Engberg (a), G. Monaco (c), L. Börjesson (a), S.C. Santucci (b) and R. Verbeni (c), *Phys. Rev. Lett.* **93**, 145502 (2004).
(a) Department of Applied Physics, Chalmers University of Technology, Göteborg (Sweden)
(b) Sincrotrone Trieste, Trieste (Italy)
(c) ESRF

Universal Dynamics of Glasses

The dynamics of glasses is considered to be more complicated than that of crystals. In some sense this is surprising, because order may have an infinite variety of forms whereas chaos should be universal. The universal trends of disorder, however, are obscured by particular molecular properties. Disregarding such molecular modes and focusing exclusively on collective vibrations, we found a universal law for the high-frequency vibrations in glasses.

In order to measure only the collective motions, we studied the glass dynamics using probe molecules. When the probe "swims" in a glass matrix without coupling to the host molecules, it follows the collective motions of the glass but is not sensitive to the local modes of the host molecules.

The isotope-selective technique of nuclear inelastic scattering was used to monitor the motions of the probes, which were molecules with a resonant nucleus in the centre of mass. With this approach, one monitors exclusively the motions of the central resonant nucleus. Furthermore, one selects pure translational motions of the probes: rotation is disregarded because the spectator nucleus is in the centre of mass; the few intra-molecular modes are separated in energy. The selected pure translational motions of the probe give the "density of states of collective motions" (CDOS) of the glass matrix.

We investigated toluene, ethyl benzene, dibutyl phthalate, and glycerol glasses. The probes were ferrocene molecules with the central resonant ^{57}Fe nucleus for the three first glasses and ^{57}Fe^{2+} ions for glycerol. The insensitivity of the probes to local vibrations is confirmed by comparison to the total DOS available from neutron data.

For all studied glasses, the reduced CDOS $g(E)/E^2$ clearly exhibits an excess of low-energy modes, the so called "boson peak" (**Figure 3**). The positions of the peak are consistent with the boson peak energies in the total DOS from neutron scattering data. The temperature evolution of the boson peak shows the same features as observed with other methods. This clear manifestation of the boson peak in the CDOS proves that the boson peak in the total DOS is largely composed of collective modes.

Beyond the boson peak, the reduced density of states of collective motions reveals a *temperature-independent exponential* behaviour:

$$g(E)/E^2 \sim \exp(-E/E_0)\ , \quad (1)$$

which, to our best knowledge, was not reported earlier. On a logarithmic scale, $g(E)/E^2$ follows a straight line over *three decades* of the reduced CDOS and starts to deviate from Eq. 1 only when obscured by the eigen mode of ferrocene at 22 meV (**Figures 4b-c**). Such a large "dynamical range" allows a clear identification of the CDOS behaviour with Eq. 1.

We also found this exponential behaviour in the *total* DOS available from neutron data for all studied here and other glasses. The most evident examples are shown in Figures 4b-d. In toluene, for instance, the total DOS follows Eq. (1) in the energy range up to 22 meV and over two decades of $g(E)/E^2$ (Figure 4c). In comparison to the total DOS, the CDOS exhibits slightly lower energy of the boson peak and a considerably steeper exponential

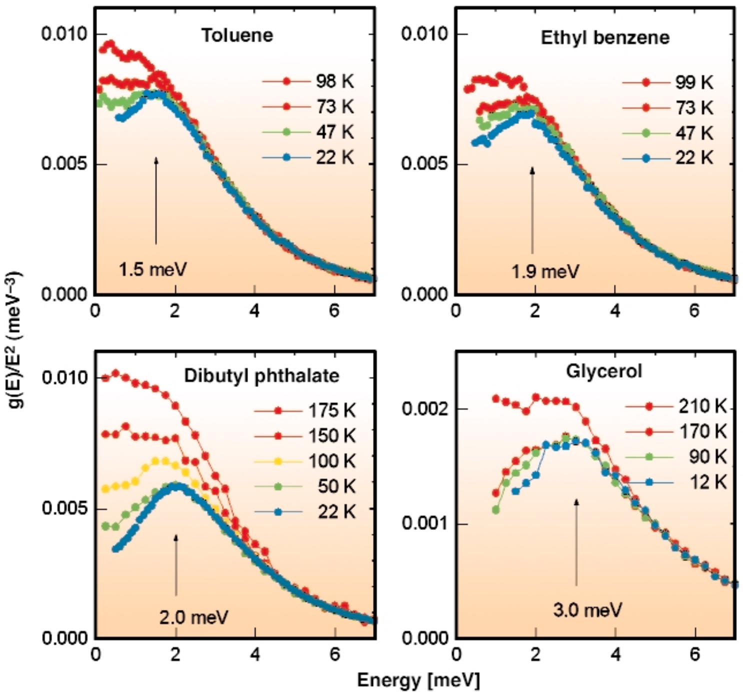

Fig. 3: Reduced DOS of collective motions in toluene, ethyl benzene, dibutyl phthalate, and glycerol glasses. Arrows indicate the energy of the boson peak estimated from the data at the lowest temperature.

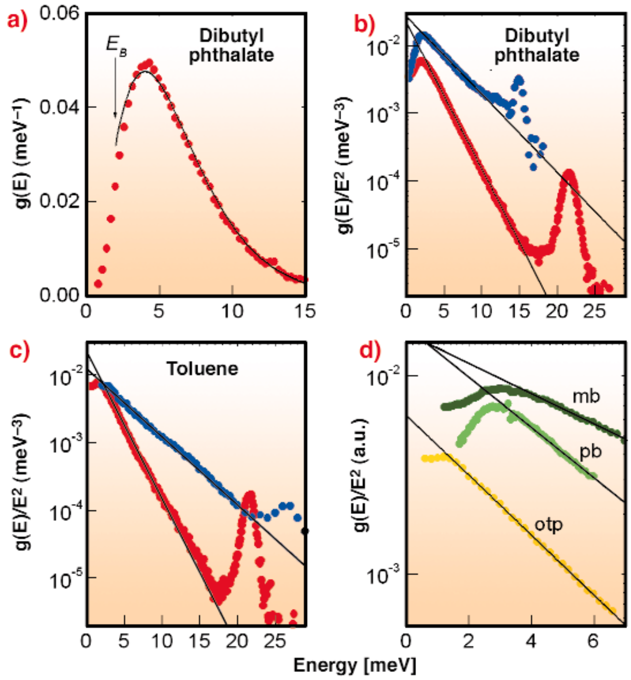

Fig. 4: (a) DOS of collective motions in dibutylphthalate at 22 K. Reduced DOS of collective motions in (b) dibutylphthalate and (c) toluene at 22 K (●) in comparison to reduced total DOS (●) from neutron data [1,2]. The neutron data are scaled to match our data at lowest energy. (d) Reduced total DOS from neutron data for orthoterphenyl (otp, ●) [3], polybutadiene (pb, ●) [4], and myoglobin (mb, ●) [5]. Solid lines show the fit according to Eq. 1. The arrow indicates the energy of the boson peak E_B.

slope. This difference can be explained by different correlation lengths accessible with various techniques.

In terms of fragility *m*, the studied glasses represent very fragile (toluene, *m* = 105), fragile (dibutylphthalate, *m* = 85), and intermediate (glycerol, *m* = 53) glass formers. The exponential behaviour of the reduced DOS is seen both in nuclear inelastic and inelastic neutron scattering data; it holds for molecular glasses, polymers, and proteins. These are strong indications that the *exponential behaviour* of the reduced DOS of collective motions is a universal feature for glasses.

References

[1] E. Duval *et al*, *J.Non-Cryst.Sol.* **307-310**, 103 (2002).
[2] I. Tsukushi *et al*, *J.Phys.Chem. Sol.* **60**, 1541 (1999).
[3] A. Tölle *et al*, *Eur.Phys. J. B* **16**, 73 (2000).
[4] R. Zorn *et al*, *Phys.Rev.E* **52**, 781 (1995).
[5] W. Doster, *et al*, *Phys.Rev.Lett.* **65**, 1080 (1990).

Principal Publication and Authors

A.I. Chumakov (a), I. Sergueev (a,b), U. van Bürck (b), W. Schirmacher (b), T. Asthalter (c), R. Rüffer (a) O. Leupold (a,d), and W. Petry (b), *Phys.Rev.Lett.*, **92**, 245508 (2004).
(a) ESRF
(b) TUM Physik- E13, Garching (Germany)
(c) Univ. Stuttgart (Germany)
(d) HASYLAB, DESY Hamburg (Germany)

Surface Science/Nanostructures

Introduction by J. Korecki, Institute of Catalysis and Surface Chemistry, Polish Academy of Sciences and AGH University of Science and Technology, Krakow (Poland)

Methods based on synchrotron radiation have contributed to surface and nanostructure sciences for a long time. In spectroscopic applications, however, synchrotron radiation was used mainly as the excitation source, with electron and ion spectroscopy constituting the traditional surface-sensitive tool. The situation has been changing rapidly over the last few years due to the development of high-resolution spectroscopy, which – thanks to the increasing synchrotron radiation brilliance – allows one to study diluted samples, typical for surface and nanoscience. An additional enhancement of surface sensitivity comes from the grazing-incidence (GI) geometry, often stimulating a sound methodological progress. Consequently, the spectroscopic methods – so vital for bulk materials – nowadays find broad applications in studying surfaces, interfaces and nanostructures.

One of the most important advantages of the applications described in the following pages is the possibility of applying different sample environments, allowing both *in situ* and *operando* spectroscopy, as well as variations of external parameters, such as pressure, temperature, or magnetic field. This opens new perspectives for studying not only the equilibrium, but also transient states, and even process dynamics, thus providing a common ground for the reported highlights.

Many studies of catalysts and sensors aim at correlating chemical activity and reactions paths with specimen structure and morphology. In heterogeneous systems, typical specimens consist of oxide-supported metallic nanoclusters. In order to determine their functionality, *operando* studies at elevated pressures and temperatures are necessary to bridge the gap between model studies and real working conditions. Safonova *et al.* report on such studies under reaction conditions for SnO_2-supported Pt and Pd nanoparticles. By combining quick EXAFS with *in situ* conductivity measurements for different compositions, as well as temperature and gas atmospheres, they convincingly reveal the relation between the gas sensitivity of the sensor system and the oxidation state of the nanoparticles.

The following two contributions are related to the activities pursued at the Nuclear Resonance Beamlines. The possibility of nuclear resonance scattering (NRS) to constitute an effective spectroscopy for ultra-thin films was demonstrated at the very early stages of the ESRF's operation [1]. Since then, the method - in its different experimental configurations and schemes – has gone far beyond the stage of proving its feasibility, becoming a standard tool at the ESRF for investigating structure, magnetism and phonons in nanostructures (the most representative examples of which can be found in [2-3]). The contribution by Klein *et al.* constitutes a good example of spatial sensitivity and capabilities of Grazing Incidence-NRS. NRS was used to probe the influence of the external magnetic field on the magnetisation structure of layers buried in thin coupled films, with the resolution of a few angstroms, using isotopic specificity given by ^{57}Fe probe layers.

True surface studies of diffusion in uncovered single crystalline iron films using NRS have been published recently [4]. A similar approach applied to studying diffusion and dynamics in submonolayer iron films on a tungsten substrate (single crystal W(110)) is reported by Sladecek *et al.*. The ultra-high vacuum (UHV) conditions, indispensable in such experiments, are now available at ID18. The UHV system allows one to measure NRS and nuclear inelastic scattering in a broad temperature range (**Figure 5**) for samples prepared not only *in situ,* but also at distant laboratories and subsequently transferred under vacuum conditions in a portable UHV chamber. Efficient NRS measurements need acquisition times shorter by two orders of magnitude and samples smaller by three orders of magnitude when compared to the UHV Mössbauer measurement results on similar Fe/W(110) samples [5]. The system is under further development and will evolve into complex surface-science equipment. This effort is part of a broad international cooperation under the Sixth EU Framework Programme's DYNASYNC project [6], which is aimed at studying different dynamical aspects at surfaces and in nanostructures, such as diffusion, phonons and magnetisation dynamics on carefully selected model nanostructures. It is my pleasure to mention that the project in question is under Polish coordination, which ties in well with Poland recently joining the ESRF.

References

[1] L. Niesen *et al.*, *Phys. Rev.* B **58**, 8590 (1998).
[2] R. Röhlsberger *et al.*, *Phys.Rev. Lett.* **86**, 5597 (2001); *Phys. Rev. Lett.* **89**, 237201 (2002).
[3] D.L. Nagy *et al.*, *Phys. Rev. Lett.* **88**, 157202 (2002).
[4] M. Sladecek *et al.*, *Surface Science*, 507-510, 124 (2002).
[5] J. Korecki and U. Gradmann, *Phys. Rev. Lett.* **55**, 2491 (1985).
[6] http://www.dynasync.kfki.hu/

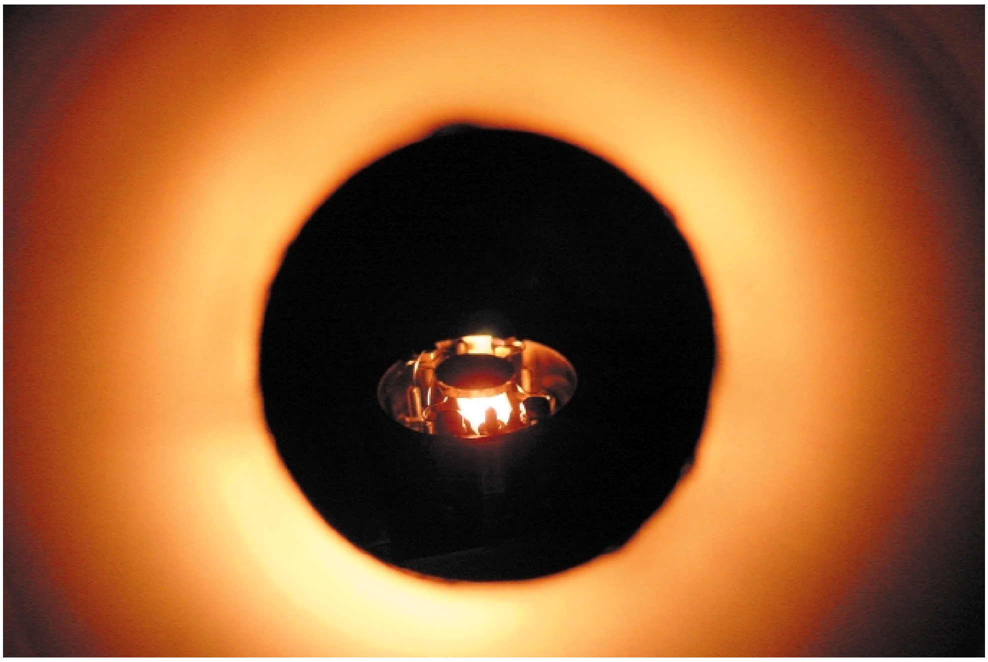

Fig. 5: Tungsten single crystal during the UHV diffusion experiment at the Nuclear Resonance Beamline.

Effect of Pt and Pd Nanoparticles on the Gas Sensitivity of Polycrystalline SnO_2 Thin Films: In situ XAS Study

Polycrystalline SnO_2 films are the materials of choice for the development of resistive gas sensors, which are used for the detection of toxic and explosive gases (CO, H_2, NO_x etc) [1]. The sensor properties are based on the fact that the electrical conductivity of SnO_2 films depends on the atmosphere composition. SnO_2 is an n-type wide band gap semiconductor. Adsorption of oxygen species creates trapped charges on the SnO_2 surface. Adsorption and consecutive redox reaction of a target gas with the adsorbed oxygen species leads to modulation of the quantity of charge and a variation of conductivity. Addition of noble metals modifies the electronic and catalytic properties of the SnO_2 by forming nanoparticles on the oxide surface. This process greatly enhances the sensitivity and decreases the working temperature.

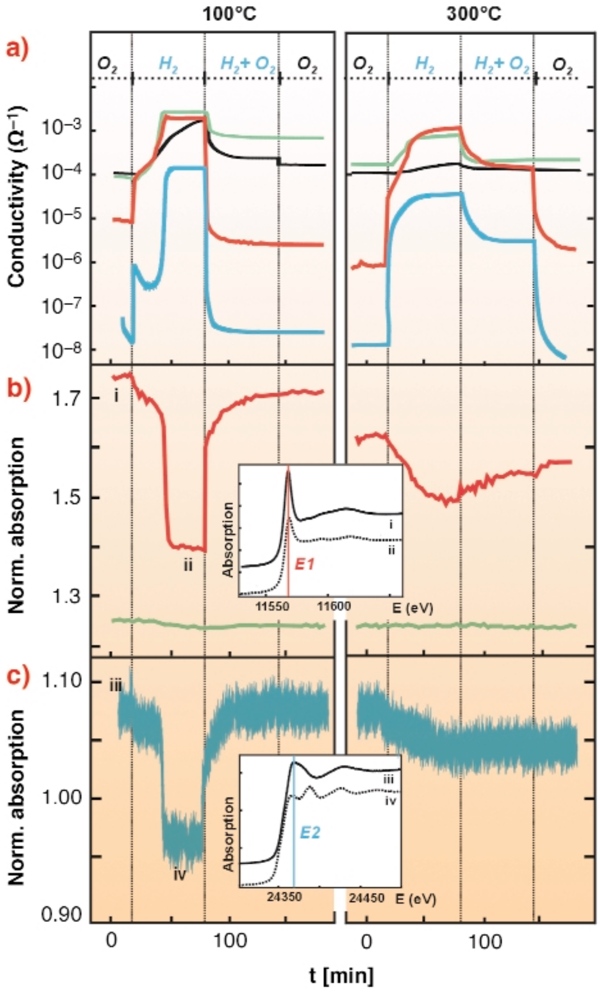

Fig. 6: Conductivity (a) and normalised absorption at E_1 = 11568.5 eV (b) and E_2 = 24368.6 eV (c) for Sn1 (black curve), Pt1 (red), Pt2 (green) and Pd1 (blue) in different atmospheres. The insets show the XANES region for Pt and Pd.

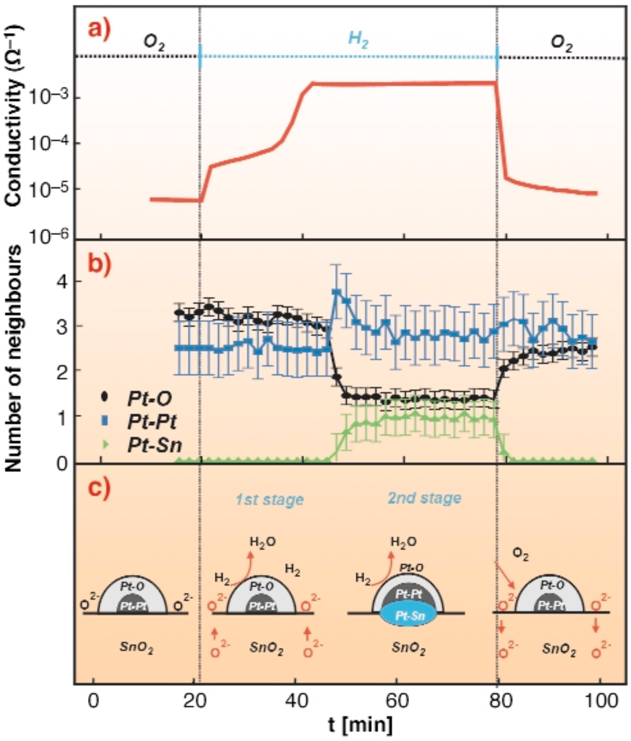

Fig. 7: (a) Conductivity; (b) the number of neighbours in the first shell of platinum calculated from EXAFS and (c) the proposed model for the Pt1 system at 300°C.

In spite of wide practical applications, the mechanism of resistive gas sensors is still under discussion. Most of the studies on the reactivity of sensor materials were done *ex situ*. This is not favourable since the chemical state of the sensor surface is extremely sensitive toward the atmosphere composition even at room temperature [1]. For SnO_2 films containing Pt nanoparticles it was previously observed using XANES spectroscopy that the Pt oxidation state strongly depends on the size of the nanoparticles and the presence of CO in the atmosphere [2]. In the present work the effect of Pt and Pd on the mechanism of SnO_2 gas sensitivity toward H_2 was studied at **ID26** by XAS *in operando* conditions.

The SnO_2 porous films (thickness 0.8-1.0 µm) were synthesised by aerosol pyrolysis [2]. Four systems were studied: pure SnO_2film (referred to as Sn1 in the following) and the SnO_2 films containing 2.0 at% Pt (Pt1), 6.3 at% Pt (Pt2) and 1.2 at% Pd (Pd1). The fluorescence XAS at Pt L_3- and Pd K-edges were acquired using quick EXAFS (30 s per spectrum) simultaneously with the conductivity measurements. The films were exposed to 20% O_2 in He (O_2), 1000ppm H_2 in He (H_2), and 1000ppm H_2 + 20% O_2 in He (H_2 + O_2).

We observed different mechanisms of gas sensitivity at high temperature (200°-300°C) and at low temperature (50°-100°C). We found that the Pt1 and Pd1 systems are much more sensitive to the presence of H_2 than Sn1 and Pt2 (**Figure 6**). The variation of normalised absorption at fixed energies near the Pt L_3- and Pd K-edges (Figures 6b and 6c) indicates the change of platinum and palladium oxidation states. Comparing experimental data with the spectra of reference compounds (metals and oxides) one can conclude that conductivity variations of Pt1 and Pd1 are accompanied by synchronous oxidation and reduction of platinum and palladium. Under the same conditions, platinum in Pt2 is almost metallic and non-reactive. This correlates with the fact that the Pt2 film contains bigger (2.3 nm) Pt nanoparticles than Pt 1 (1.7nm) [2].

The kinetics of the conductivity variation of Pt1 and Pd1 films in H_2 give a similar picture. Two stages of conductivity increase are observed at 300°C and only the second one is related to a variation of Pt and Pd oxidation state. For the Pt1 film, evaluation of the EXAFS data indicates not only the reduction of platinum but also of the SnO_2 matrix (Pt-Sn bonds in **Figure 7**). At low temperatures the conductivity of the Pt1 and Pd1 systems increases much faster than at high temperatures but the state of platinum and palladium varies very little. High sensitivity of Pt1 and Pd1 films towards $H_2 + O_2$ was also observed at 50-100°C.

We propose that the difference between the high temperature and the low temperature mechanisms is related to the oxygen mobility in the SnO_2 matrix. At low temperatures the redox reactions take place only at the SnO_2 surface that leads to the fast variation of the quantity of charge trapped at the SnO_2 surface by acceptor states including the states produced by Pt and Pd nanoparticles [1]. At high temperatures the participation of the bulk oxygen slows down the modulation of this charge.

References

[1] L. Moris, D.E. Williams, *J. Phys. Chem. B*, **105**, 7272-7279, (2001).

[2] M. Gaidi, J.L. Hazemann, I. Matko, B. Chenevier, M. Rumyantseva, A. Gaskov and M. Labeau, *J. Electochem. Soc*., **147**, 3131-3138, (2000).

Authors

O. Safonova (a), T. Neisius (a), B. Chenevier (b), A. Gaskov (c), M. Labeau (b).

(a) ESRF

(b) LMGP, Institut National Polytechnique de Grenoble (France).

(c) Chemistry Department, Moscow State University (Russia).

Imaging the Magnetic Structure of Exchange-coupled Thin Films

With the increasing complexity of layered magnetic nanostructures there is a growing need for experimental methods capable of imaging the depth dependence of their properties. Nuclear resonant scattering of synchrotron radiation from isotopic probe layers provides an excellent tool for this purpose. In a recent experiment [1], we have investigated the exchange coupling of a soft-magnetic Fe layer deposited on a hard-magnetic FePt film. At the interface between the two layers, the moments of the soft-magnetic film are pinned to the unidirectional magnetisation M_{FePt} of the hard-magnetic film. With increasing distance from the interface, the moments of the soft-magnetic film turn under the action of an external field H_{ext}, resulting in a spiral magnetic structure, see **Figure 8**.

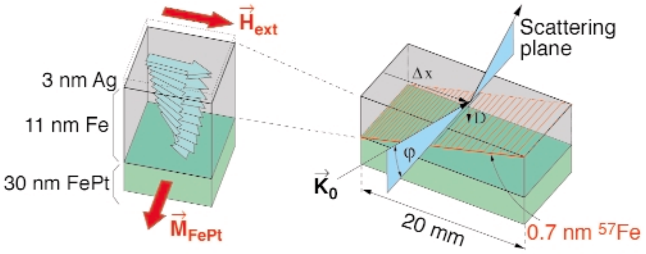

Fig. 8: Magnetic structure in the Fe layer of an Fe/FePt exchange spring as it forms in an external magnetic field of 160 mT. This image was obtained using an ultrathin probe layer embedded in the Fe film, shown on the right [1].

The structure of this spiral was imaged by employing a tilted ultrathin probe layer of ^{57}Fe, as shown in Figure 8. Thus, the transverse displacement of the sample relative to the horizontally focussed beam enables one to select specific depths in the sample. The measurements benefited from the sample acting as an X-ray waveguide. Data acquisition times could be reduced drastically thanks to a strong coherent enhancement of the signal [2], so that systematic studies as a function of external parameters like temperature and external field became possible. One of these studies was aimed at the investigation of the exchange coupling between two ferromagnetic layers through a nonmagnetic spacer layer. Due to the confinement of spin-polarised electron waves in the spacer layer one expects an oscillatory behaviour of the coupling strength. This manifests itself in a periodic ferromagnetic/antiferromagnetic coupling between the two films as a function of the spacer layer thickness.

The sample investigated here consists of an Fe layer on a hard-magnetic FePt layer ($L1_0$ phase) with unidirectional anisotropy, separated by a wedge-shaped Cu layer, as sketched in **Figure 9a**. To determine the coupling angle ϕ between the films, a ^{57}Fe probe layer is embedded in the centre of the Fe. Surprisingly, no variation of the coupling angle can be seen in remanence after saturation in an external field of 2.4 T. This situation changes drastically after application of a small external field in the reverse direction. Remarkably, one observes a modification of the *remanent* coupling angles, as illustrated in Figure 9. Below fields of 45 mT the strongest reorientation of the Fe moments occurs for thin spacer layer thicknesses, followed by a monotonous decrease with increasing Cu thickness. Above reverse fields of 50 mT an oscillatory behaviour of the coupling angle sets in. However, the coupling angles are below 40° and no evidence for an

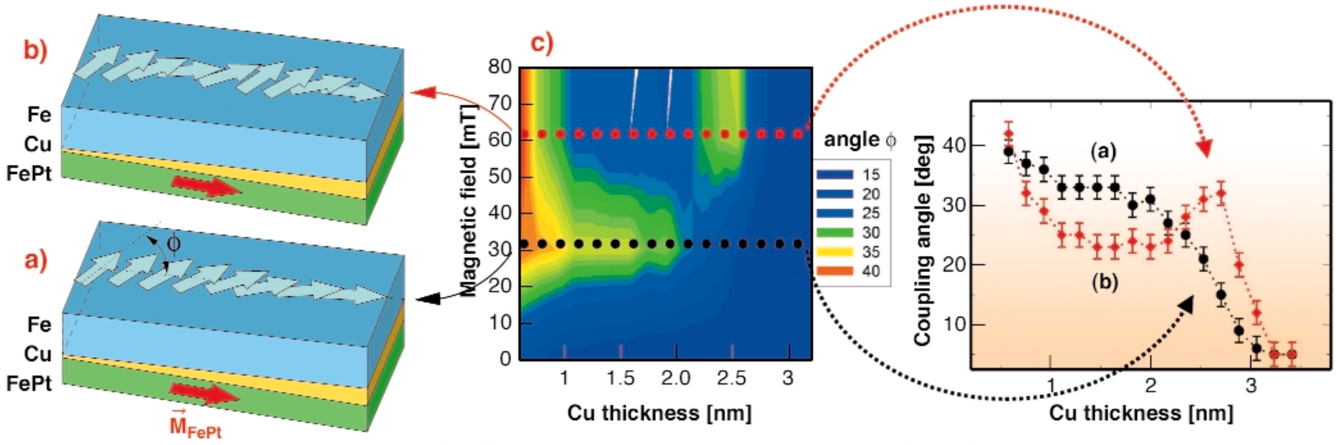

Fig. 9: Lateral remanent magnetic structure of the Fe layer in an exchange-coupled Fe/Cu/FePt trilayer. (a) After saturation in an external field of 2.4 T and application of a reverse field of 30 mT and (b) a reverse field of 60 mT. (c) Colour coded map of the coupling angle ϕ as function of the spacer layer thickness and the reverse external field.

antiparallel component of the Fe magnetisation was found. This interesting behaviour can be explained by the superposition of two coupling mechanisms in this layer system, *i.e.* dipolar coupling and interlayer exchange coupling. After saturation of the layer system the remanent state is determined by a dipolar coupling induced by interface roughness, resulting in a parallel alignment of both ferromagnetic layers. With increasing magnitude of the external field, this dipolar coupling is influenced by the external field, which leads to largest coupling angles at low spacer layer thicknesses. With further increase of the external field, another mechanism comes into play: small (*e.g.*, soft-magnetic) regions of the FePt film turn into the direction of the reverse field. The presence of these antiparallel domains leads to a frustration of the moments in the Fe film. In this case an alignment of the Fe film towards the perpendicular direction (biquadratic coupling) becomes energetically more favourable. Since this interaction is mediated by the interlayer exchange coupling, it carries an oscillating signature [3].

These studies show that remanent coupling angles between soft magnetic and hard magnetic thin films can be tuned by the application of external fields. It was found that such effects are even more pronounced if the external field is applied in a direction perpendicular to the unidirectional anisotropy of the FePt. This opens interesting perspectives for the manipulation of magnetic nanostructures with potential applications in magnetic data storage.

References

[1] R. Röhlsberger, H. Thomas, K. Schlage, E. Burkel, O. Leupold, and R. Rüffer, *Phys. Rev. Lett.* **89**, 237201 (2002).
[2] R. Röhlsberger, T. Klein, K. Schlage, O. Leupold, and R. Rüffer, *Phys. Rev. B* **69**, 235412 (2004).
[3] V. K. Vlasko-Vlasov *et al.*, *Phys. Rev. Lett.* **86**, 4386 (2001).

Principal Publication and Authors

T. Klein (a), R. Röhlsberger (b), K. Schlage (a), H. Thomas (a), O. Leupold (b), and E. Burkel (a), submitted to *Phys. Rev. Lett.* (2004).
(a) Institut für Physik, Universität Rostock (Germany)
(b) HASYLAB@DESY, Hamburg (Germany)

Diffusion in a Sub-monolayer Iron Film

Atomistic details of diffusion processes can be monitored by scattering methods [1]. Destructive interference of the scattered radiation occurs when either the emitting probe atoms change their sites or the vicinity of the atoms changes temporally due to diffusion. From the way the interference is destructed, the atomistic details of the diffusion mechanism can be deduced. This idea has been successfully applied to study the motion of atoms and defects in the volume, *i.e.* in bulk material. The spectrum of methods used ranges from neutron scattering and Mössbauer spectroscopy to nuclear magnetic resonance and interference of synchrotron radiation. For selected cases the atomistic jump process was revealed, and today bulk diffusion can be regarded as principally well understood.

Recently the question of how atoms diffuse in lower-dimensional systems has attracted more attention. The consequences of surface diffusion are easily seen in images taken by a scanning tunnelling microscope (STM), but its mechanism can hardly be determined because of the limited time resolution of the STM which is of macroscopic dimensions, *i.e.* a few hundredths of seconds. Here synchrotron radiation comes into its own: Using short synchrotron radiation pulses we get access to the nanosecond regime and by applying nuclear resonance scattering we are able to study the slow dynamics, which in our case is diffusion.

Nuclear resonance techniques are element and even isotope sensitive, which means we get selective access to a single layer on the surface. Now we can employ some of the methods successfully developed for bulk material. Although technically this is more laborious than bulk studies because of lower count rates, there is an essential advantage offered by surfaces: motion of surface atoms is always motion in the vicinity of a vacancy defect – the vacuum. For an atom embedded in the surface layer the broken symmetry at the surface induces an electric field gradient at the nuclear site with the main axis perpendicular to the surface. The orientation strongly depends on the nearest-neighbour co-ordination of the atom.

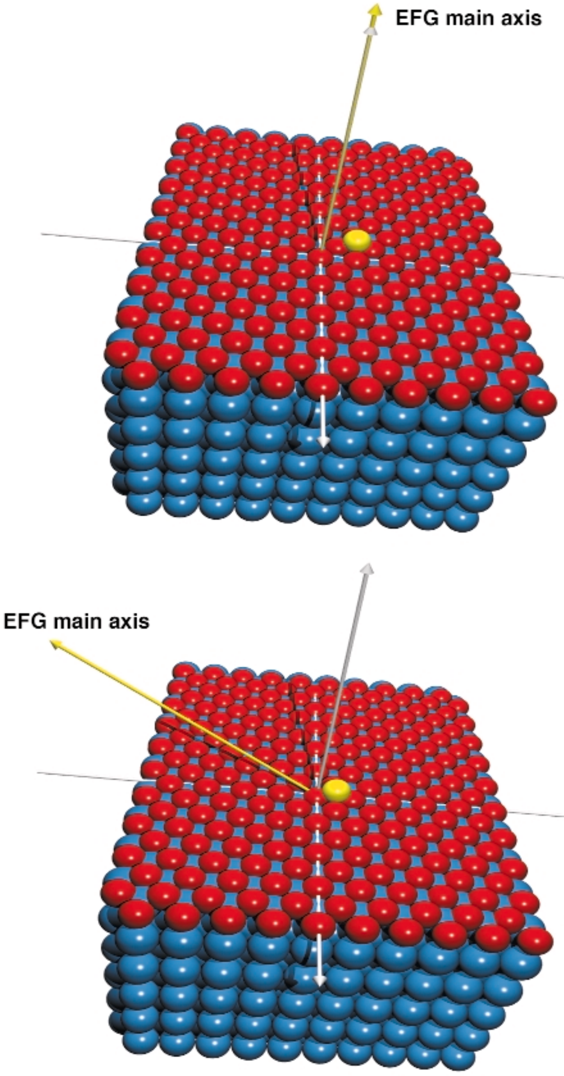

Fig. 10: Top: Model of a moving ad-atom on the surface. Perturbation of the intrinsic main axis of the electric field gradient (EFG) on an iron atom embedded in the uppermost layer. Bottom: The surrounding of the ad-atom changes with every jump. This causes a reorientation of the EFG main axis.

Exploiting this extreme case for the first time, we have studied surface diffusion by pursuing the fluctuation of the electric field gradient (**beamline ID18**). **Figure 10** shows how a perturbation by an additional defect, such an embedded vacancy or an ad-atom, moving on the layer will result in a reorientation of the main axis of the electric field gradient. If the reorientation is sufficiently fast, the atom will feel an effective decrease of the electric field gradient (motional narrowing).

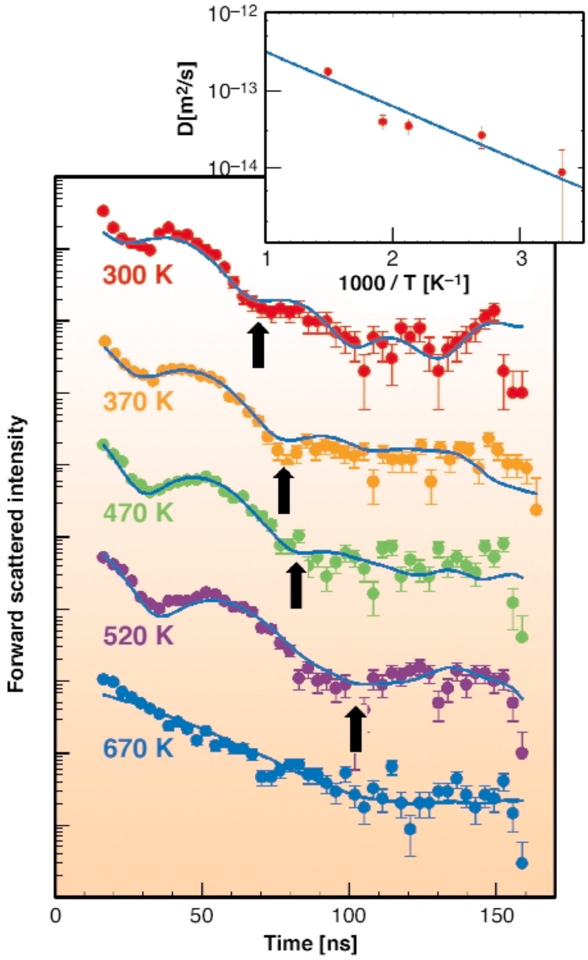

Fig. 11: Nuclear resonance scattering of synchrotron radiation: Time spectra for iron sub-monolayer (0.6 ML) on W(110) measured between RT and 670 K. The beat period indicated by black arrows increases clearly. The solid line is the fit achieved with an ad-atom model. The spectra are shifted relatively to each other in the vertical direction. The inset shows the calculated diffusion coefficient.

In nuclear resonance scattering, the electrical field gradient is manifested by a beat pattern in the measured time spectrum. **Figure 11** shows this pattern resulting from a sub-monolayer of iron on a tungsten substrate (single crystal W(110)). Arrows in Figure 11 indicate the clearly visible increase of the beat period after each temperature step between RT and 670 K. A RT spectrum was measured after each temperature step to check the structural stability of the sample and the reversibility of the effect. The analysis of the beat frequencies in the time spectrum favours the ad-atom diffusion compared to the vacancy exchange diffusion within the layer.

To connect the increase of the beat period with the fluctuation frequency and finally with the jump frequency of atoms, the theory of Dattagupta and Schroeder [2] developed for bulk materials was modified for surfaces.

In this way an Arrhenius diagram of the diffusion coefficient, assuming a nearest-neighbour jump diffusion mechanism of the ad-atoms, can be calculated. The Arrhenius plot with the activation energy 0.14(2) eV is shown in the inset of Figure 11.

Our study demonstrates the sub-monolayer sensitivity of the nuclear resonance scattering method and its ability to resolve fast (MHz) diffusion processes on surfaces with atomic resolution.

References

[1] G. Vogl and B. Sepiol, *"The Elementary Diffusion Step in Metals Studied by the Interference of Gamma-rays, X-rays and Neutrons"* in Diffusion in Condensed Matter, P. Heitjans and J. Kärger, (Eds), Springer (2005).

[2] S. Dattagupta and K. Schroeder, *Phys. Rev. B* **35**, 1525 (1987).

Authors

M. Sladecek (a), B. Sepiol (a), J. Korecki (b,c), T. Slezak (b,c), D. Kmiec (a), R. Rüffer (d), G.Vogl (a).

(a) University of Vienna (Austria)

(b) AGH University of Science and Technology, Krakow (Poland)

(c) Institute of Catalysis and Surface Chemistry, Polish Academy of Science (Poland)

(d) ESRF

Earth Science

Introduction by C. McCammon, Bayerisches Geoinstitut (Germany)

Processes that take place on the surface of the Earth and in its interior are intimately linked to the properties and structure of the Earth's materials down to the atomic scale. Probing the Earth's interior is challenging, since most measurements are constrained to be made from the Earth's surface. Much of what we know for certain about the Earth's interior is derived from seismology, which requires information on the structure and elasticity of Earth-forming minerals. Experimental studies therefore play a crucial role in constraining the properties of the deep Earth, since they allow measurements of the relevant properties at conditions appropriate to the Earth's interior. Pressure is a variable common to all studies of the deep Earth. Advances in technology have allowed experimental access to the pressures at the centre of the Earth, but at the cost of reduction in sample size. Synchrotron radiation is ideally suited to the study of these small samples, and allows the measurement of properties at the atomic level that can be related to properties and processes on a global scale.

The selected highlights showcase results on materials that have advanced our understanding of processes within the Earth. Gas hydrates such as methane hydrate have been found to occur in large quantities within the Earth's crust, and may represent the largest source of hydrocarbon on Earth. The release of methane from this reservoir may have contributed to variation in past atmospheric methane levels, with obvious consequences for past and future climate change. Seismic methods have been used to identify the existence of gas hydrate zones, for which elastic properties are an important parameter.

Iron is the most abundant element in the Earth's crust and mantle with a variable oxidation state. The electronic structure of iron, particularly its spin state, affects the degree to which different wavelengths of light are absorbed and hence the radiative thermal conductivity of the mantle. High-spin to low-spin transitions at high pressure can therefore influence the transport of heat in the mantle, and hence the dynamics of mantle convection. Iron is also the most abundant element in the core. The discovery of seismic anisotropy in the Earth's solid inner core, where seismic velocities are faster in N-S directions than along equatorial paths, has important implications for dynamic processes such as those that give rise to the Earth's magnetic field. On the horizon, the application of novel methods such as resonant X-ray emission spectroscopy (RXES) to samples under high pressure provides the chance for improved characterisation of the electronic structure of iron in relevant minerals at mantle conditions, and hence a better understanding of the properties and processes that occur within the Earth's interior.

Collective Modes and Localised Vibrations in Methane Hydrate

Methane hydrate [1] is an inclusion compound, in which methane molecules are trapped in an ice-like host lattice of water molecules. Three different crystallographic structures of methane hydrate are known: a low pressure phase MH sI, consisting of six large and two small cages in the unit cell, and two high pressure phases MH II and MH III. Methane hydrate structure I is of special interest as it forms at water-gas pressure conditions found in the world's oceans. Since large natural deposits have been discovered on the ocean floors, methane hydrate is considered as a potential future energy source. These hydrate deposits are detected by the difference in the sound velocities of the hydrate and gas baring sediments. Furthermore, the hydrate cemented sediments display mechanical properties, which are strongly dependent on the stability and the physical properties of methane hydrate. The unusually low and glass-like thermal conductivity observed in gas hydrates is therefore of special importance. This anomalous behaviour is thought to be attributed to a resonant scattering of the heat carrying acoustic lattice phonons by the localised guest vibrations, which should be observable in the phonon dispersion relation.

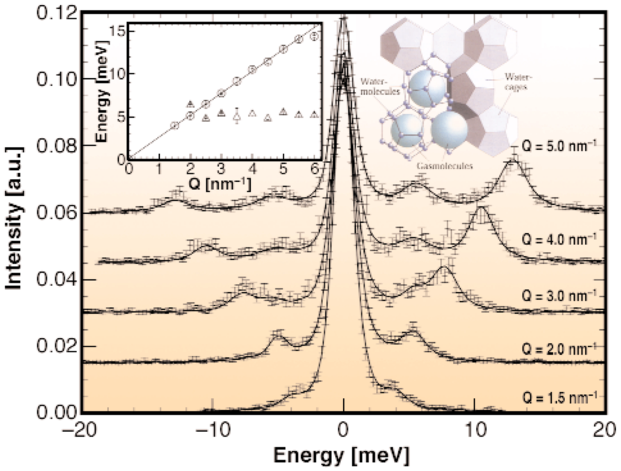

Fig. 12: Inelastic X-ray spectra of MH sI. The insets show the respective dispersion relation and a schematic of MH sI (provided by GEOMAR).

High energy resolution inelastic X-ray scattering (IXS) is therefore used to determine the collective dynamics of both the methane guest molecules and the host lattice. The phonon dispersion relation of methane hydrate was recorded at the beamline **ID28**. **Figure 12** shows a selection of the recorded IXS spectra, which display a well defined dispersive mode and a second non-dispersive peak from 3 nm^{-1} on. The dispersive excitation is identified with the longitudinal acoustic host-lattice phonon branch. From the slope of the dispersion an orientationally-averaged sound velocity $v = 3950 \pm 50$ m/s can be deduced. The peak at 5 meV is attributed to methane molecule vibrations inside the large cage. These vibrations become visible in the spectra after the intersection with the longitudinal acoustic mode at $Q \approx 2.5$ nm^{-1}, which points toward a coupling between the localised guest vibrations and the dispersive acoustic host lattice modes.

This interpretation is validated by the theoretical calculated dispersion relation and IXS intensities using lattice dynamical simulations. The resulting scattering function, which was orientationally averaged in order to simulate the powder sample, is shown in **Figure 13**. It shows two distinct excitations, a dispersive mode, which is the longitudinal acoustic lattice mode, and an optic mode corresponding to the localised methane molecule vibrations. The calculated longitudinal sound velocity is 3800 m/s in agreement with the experimental value. The calculated energy position of the guest mode is lower than the observed one, which points towards an underestimation of the methane-water interaction. Nevertheless, the combination of experimental and theoretical results shows that before the cross-over of the guest and host modes, the guest molecules are independent Einstein oscillators, leading to a negligible intensity in the IXS spectra. It is at the cross-over that the guest mode acquires a collective behaviour as it is modulated by the host lattice mode. This coupling of the guest and host vibrations leads to a transfer of scattered intensity from the acoustic lattice mode to the optic guest mode and thus to a damping of the intensity of the acoustic lattice phonons, which are closely related to the thermal conductivity.

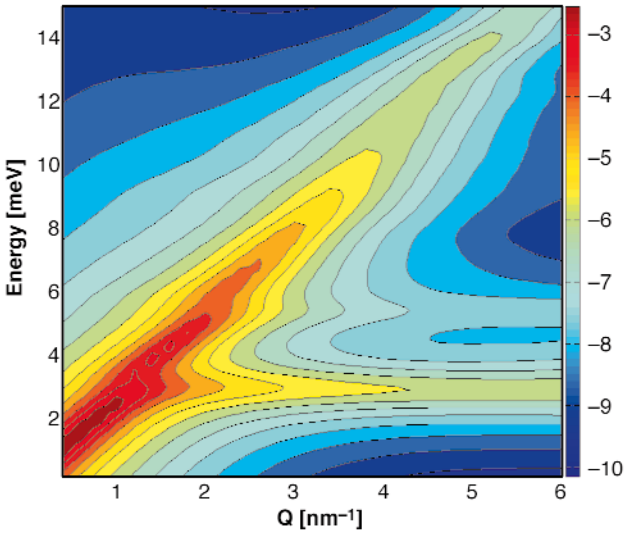

Fig. 13: Theoretical inelastic X-ray scattering function of methane hydrate. The longitudinal acoustic lattice mode and the optic guest mode can be observed.

This coupling is not observed for the high pressure structures of methane hydrate, as the guest molecules cannot be considered as independent oscillators anymore. Instead, especially for the "filled ice" MH-III, strong changes in the elastic properties of the ice host lattice are observed. These changes can be connected with the growing hydrophobic interaction between the methane and water molecules.

In conclusion, it was possible to gain insight into the origins of the anomalous thermal conductivity of methane hydrate. The results can be used as a starting point for a modelling of the thermodynamic properties of natural occurring hydrate deposits. The pressure dependent studies could also show that the hydrophobic interaction between the guest and host molecules is of fundamental importance for the elastic properties of methane hydrate.

References

[1] E.D. Sloan, Jr., *Clathrate Hydrates of Natural Gases* (Dekker, New York, 1998).

Principal Publication and Authors

J. Baumert (a), C. Gutt (b), V.P. Shpakov (c), J.S. Tse (d), M. Krisch (e), M. Müller (a), H. Requardt (e), D.D. Klug (d), S. Janssen (f), and W. Press (g), *Phys. Rev. B* **68**, 174301 (2003).

(a) Experimentelle und angewandte Physik, Universität Kiel (Germany)
(b) Experimentelle Physik I, Universität Dortmund (Germany)
(c) Chemistry Department, University of Western Ontario (Canada)
(d) National Research Council of Canada, Ottawa (Canada)
(e) ESRF
(f) Paul Scherrer Institute, Villigen (Switzerland)
(g) ILL

Electronic Transitions in Perovskite: Possible Nonconvecting Layers in the Lower Mantle

Earth's lower mantle is mainly composed of iron-bearing magnesium silicate perovskite $(Mg,Fe)SiO_3$, which is the most abundant phase (about 80% by volume), and magnesiowüstite (Mg,Fe)O. Iron in magnesiowüstite undergoes a spin-pairing transition between 60 and 70 GPa. We measured the spin state of iron in magnesium silicate perovskite $(Mg_{0.9}Fe_{0.1})SiO_3$ at high pressure and found two electronic transitions occurring at 70 and 120 GPa, corresponding to partial and full electron pairing in iron, respectively. The measurements were performed on beamline **ID16,** studying the Kβ emission line.

One of the main characteristics of low-spin (or spin-paired) iron-bearing minerals resides in the blue-shift of iron absorption bands (the absorption bands initially in the infrared and red region shift to the green-blue region). The proportion of iron in the low spin state thus grows with depth, increasing the transparency of the mantle in the infrared region, with a maximum at pressures consistent with the D" layer (the lowermost 300 kilometres of the mantle, a structurally and chemically complex layer sitting just above the core-mantle boundary). The resulting increase in radiative thermal conductivity suggests the existence of nonconvecting layers in the lowermost mantle.

Our experimental study of its major constituents suggests that the Earth's lower mantle is in a fundamentally different thermochemical state above 70 to 90 GPa, corresponding to depths greater than 1700 to 2000 km. This is due to a change in the electronic properties of iron in these phases at such pressures. The changes can have profound implications on the chemistry and dynamics of the lowermost mantle. They indicate that the lower mantle could be separated into three distinct regions in different thermochemical states (**Figures 14 and 15**):

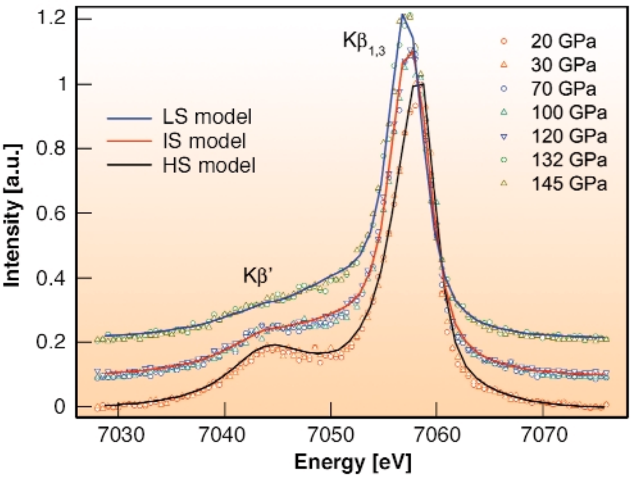

Fig. 14: X-ray emission spectra collected on magnesium silicate perovskite $(Mg_{0.9}Fe_{0.1})SiO_3$ between 20 and 145 GPa. The spin state of iron transforms twice at 70 and 120 GPa, as indicated by the changes in Kß' line intensity. Moreover, the position of the $Kß_{1,3}$ line shifts at each transition, and by a total of -0.75 eV between 20 and 145 GPa, which is in agreement with a high-spin to low-spin (HS–LS) transition in iron. The spectra have been vertically shifted (each group separately) for clarity; the first (bottom) group is characteristic of the HS state, the second (middle) is characteristic of the mixed state (mixture of HS and LS iron), and the third (top) is characteristic of the LS state. The solid lines are models constructed from reference molecular compounds, and are not fitted to the data.

- above 1700 km (below 70 GPa), the "normal" state, where iron is in the high-spin state in both lower-mantle compounds
- between 1700 and 2600 km (between 70 and 120 GPa), the "transitional" state, where iron can be in the low-spin state in magnesiowüstite, and partially in the high-spin state in perovskite
- below 2600 and to the core-mantle boundary (between 120 and 135 GPa), the "profound" state, where iron is in the low-spin state in both lower-mantle compounds

Interestingly, these distinct regions have geophysical signatures that have been previously reported. The "transitional" region corresponds to depths where chemical heterogeneities have been observed by seismic tomography. Thermodynamic modelling of the partitioning of iron in this state indicates that the spin transitions at 70 GPa could promote large scale chemical heterogeneities due to lateral temperature heterogeneities.

The depths and pressures of the "profound" region are in concordance with that of the D" layer. The transition pressure (120 GPa) is also in accord with a recently reported crystallographic transition in perovskite [1], and so is our estimated Clapeyron slope of 120 K/GPa [2]. The latter value is also in agreement with the seismically constrained [3] value of the Clapeyron slope at the D" layer of 170 K/GPa. All these concordances strengthen the suggestion that the present observation could

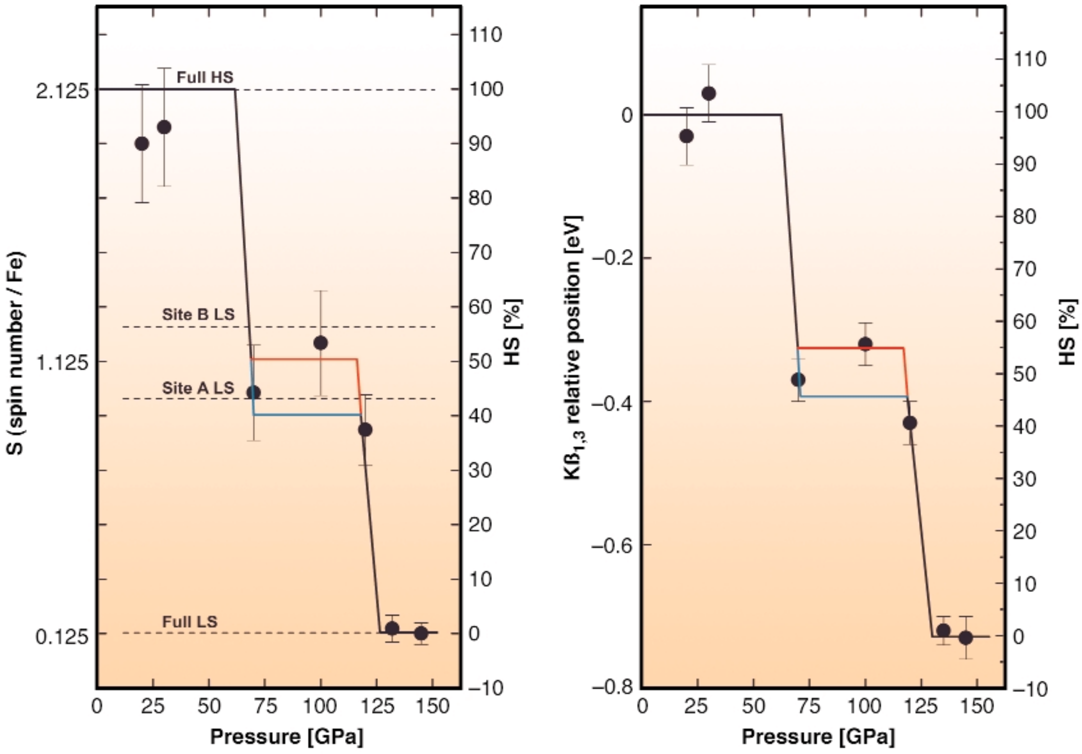

Fig. 15: Average spin number on the iron atom as a function of pressure, derived from the intensity of the Kß′ line (left) and the position of the $K\beta_{1,3}$ line (right). The blue and red lines are tentative curves (within the error bars) in the intermediate state plateau.

provide a mineral-physics basis for the Earth's D" layer. In the "profound" state, the lower-mantle mineralogical assemblage has an increased radiative conductivity, and should be associated with a strong dynamical signature since the increase in thermal conductivity may hinder convection and favour layering in the lowermost mantle.

References

[1] Murakami *et al.*, *Science* **304,** 855 (2004).
[2] Iitaka *et al., Nature* **430,** 442 (2004).
[3] Sidorin *et al., Science* **286,** 1326 (1999).

Principal Publications and Authors

J. Badro (a), J.-P. Rueff (b), G. Vankó (c), G. Monaco (c), G. Fiquet (a), F. Guyot (a), *Science* **305**, 383 (2004); *Science* **300**, 789 (2003).

(a) Laboratoire de Minéralogie Cristallographie, Université Paris VI, Institut de Physique du Globe, Paris (France)
(b) Laboratoire de Chimie Physique–Matière et Rayonnement, Université Paris VI, Paris (France)
(c) ESRF

Elasticity and Sound-wave Anisotropy in hcp Metals at High Pressure

Characterising the effect of pressure on the propagation of elastic waves in condensed matter is singularly important in many fundamental and applied research fields. An important case is related to the elasticity of hcp iron, the main constituent of the Earth's core. While the elastic anisotropy of Earth's inner core is now well established, its origin is still poorly understood. Theoretical predictions of the elastic moduli of iron yield very different results that are in disagreement with the scarce experimental results. Possible causes are: (i) the difficulty to perform reliable calculations at high pressures and temperatures, and (ii) the impossibility to carry out experiments on single crystal hcp iron.

Here we present the experimental determination of the five independent elastic moduli of hcp cobalt under hydrostatic compression to 39 GPa. Experimental and theoretical evidences suggest that hcp cobalt is a suitable analogue for hcp iron, with the advantage of being available as a single crystal. Thus, the knowledge of the elasticity of cobalt can be utilised to address the elastic anisotropy of hcp iron.

The experiments were carried out on the Inelastic X-ray Scattering (IXS) beamline II (**ID28**) utilising a focussed beam and an overall energy resolution of 3 meV. High quality single crystals (45 to 85 µm diameter, 20 µm thickness) were loaded in diamond anvil cells (DAC), using helium as pressure transmitting medium. The sound velocity of five independent acoustic phonon branches was determined as a function of pressure, permitting the derivation of the five independent elastic moduli. The results obtained compare well with ambient pressure ultrasonic measurements and, despite some discrepancies, an overall agreement with *ab initio* calculations [2] can be observed.

Determination of the full elastic tensor and its pressure evolution allows the mapping of the sound velocities in all along arbitrary directions in the crystal . The variation of the longitudinal acoustic sound velocity, $V_L\{\xi\}$, where ξ is the angle from the c-axis in the meridian (a-c) plane is, in the case of iron, related to the observed seismic-wave anisotropy in Earth's inner core. **Figure 16** shows $V_L\{\xi\}$, derived from IXS mesurements on cobalt, calculated at 0 K for cobalt and for iron [2], and derived from radial X-ray diffraction (RXRD) measurements on iron [1]. The results are compared at the same compression ratio $\rho_0/\rho = 0.86$ (P~36 GPa for Co and P~39 GPa for Fe). We note a substantial agreement between the IXS results and the calculations, even if in the calculations the magnitude of the anisotropy is underestimated. This comparison validates the theoretical results and suggests a sigmoidal shape for $V_L\{\xi\}$ in hcp iron as well, as indeed the calculations show.

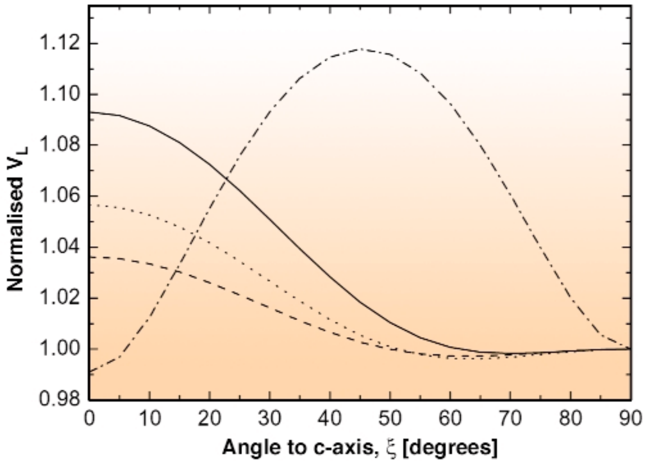

Fig 16: $V_L\{\xi\}$, from c- to a-axis. For a clear comparison, the velocities are normalised to one for $\xi = 90°$. Solid line: IXS measurements for hcp Co; dotted line: calculations for hcp Co [2]; dashed line: calculations for hcp Fe [2]; dash-dotted line: RXRD measurements for hcp Fe [1].

The above experiments on single-crystalline Co were complemented by IXS measurements on a textured polycrystalline Fe-sample at 22 and 112 GPa. The aggregate longitudinal acoustic (LA) phonon dispersions, determined at the two pressures for two different orientations of the diamond anvil cell (at 50° and 90° respect to the compression axis of the cell), are reported in **Figure 17**, together with the differences in the derived sound velocities. While at 22 GPa the two dispersions almost overlap, leading to velocities equal within the error bars, at 112 GPa the difference becomes significant. Considering the known texture, with the c-axis of the crystallites preferentially oriented along the main compression axis of the cell, we can conclude that at 112 GPa the sound propagates faster by 4 to 5% at 50° from the c-axis than at 90° (*i.e.* in the basal plane). The measured anisotropy on a textured polycrystalline sample at 112 GPa is of the same order of magnitude as the anisotropy of seismic waves in the Earth's inner core (3-4%).

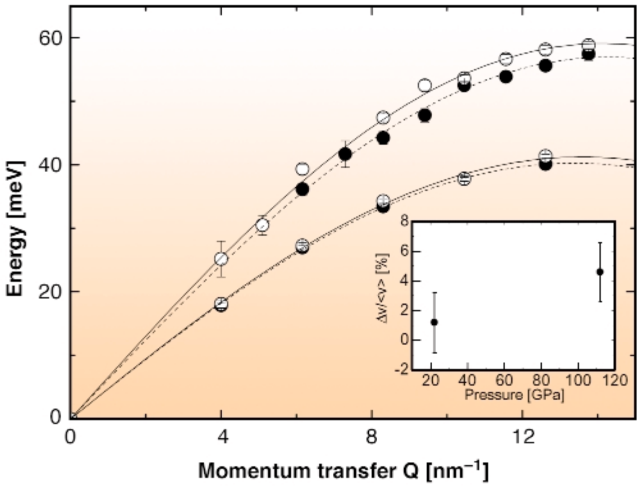

Fig 17: LA phonon dispersions of hcp Fe at room temperature and at pressures of 22 GPa (lower curve) and 112 GPa (upper curve) for the two orientations of the DAC; full (open) circles: sound propagation at 90° (50°) to the DAC loading axis. Where not visible the errors are within the symbols. The inset reports the relative difference in the sound speeds for the two orientations at the two pressures investigated.

Our results support the hypothesis of a sigmoidal shape of the longitudinal acoustic sound velocity in hcp iron at high pressure and ambient temperature, with a significant higher speed along the c-axis. A moderate alignment of the c-axis of the iron crystallites along the Earth's rotation axis, in an otherwise randomly oriented medium, can alone qualitatively explain compressional travel time anomalies observed in the Earth's inner core.

References

[1] H.K. Mao *et al.*, *Nature* **396**, 741 (1998); correction, *Nature* **399**, 280 (1999).

[2] G. Steinle-Neumann *et al.*,*Phys. Rev. B* **60,** 791 (1999).

Principal Publications and Authors

D. Antonangeli (a), M. Krisch (a), G. Fiquet (b), D.L. Farber (c), C.M. Aracne (c), J. Badro (b,c), F. Occelli (c), H. Requardt (a), *Phys. Rev. Lett.*, **93**, 215505 (2004); D. Antonangeli (a), F. Occelli (a), H. Requardt (a), J. Badro (b), G. Fiquet (b), M. Krisch (a), *Earth Planet. Sci. Lett.*, **225**, 243 (2004).

(a) ESRF
(b) Laboratorie de Minéralogie-Cristallographie de Paris, Institut de Physique du Globe de Paris (France)
(c) Lawrence Livermore National Laboratory (USA)

High-pressure Phonon Spectroscopy of Oriented hcp Iron

The hexagonal (hcp) high-pressure phase of iron (ε-Fe) is the most relevant constituent of the Earth's inner core. The thermodynamic and elastic properties of this phase are therefore of actual geophysical interest.

Using Nuclear Inelastic Scattering (NIS) with the 14.413 keV transition of Fe-57, the phonon density-of-states (DOS) in hcp iron was measured for the first time up to 42 GPa at ID22N of ESRF [1] and later up to 153 GPa at the APS [2]. Using the texture of the pressurised sample, we developed a new method to study the orientation dependence of the phonon density-of-states in ε-Fe up to 40 GPa [3]. The use of texture enables a search for a possible anisotropy in the sound velocity. Here we report on such a high-resolution NIS study of oriented ε-Fe up to 130 GPa.

Synchrotron radiation of 14.413 keV with a bandwidth of 3 meV was focused onto the sample of about 50 µm in diameter, contained in a Be gasket between the diamonds in the high-pressure cell [3]. NIS spectra were measured in two different directions, 0° and 75°, with respect to the axis of the diamonds, which is also the preferred c-axis orientation of the ε-Fe sample. NIS spectra of ε-Fe were recorded from 28 GPa up to 130 GPa. The phonon-DOS spectra, derived from the NIS spectra [1,3], are shown in **Figure 18**. They exhibit clear pressure-induced shifts of their characteristic peaks to higher energy as well as characteristic differences for the two orientations.

To explain the orientation dependence of the observed phonon DOS, theoretical calculations of the phonon dispersion relations and phonon-DOS were performed for ε-Fe at 40 GPa [3]. In addition, we demonstrated that the observed texture effects can be enforced by difference spectra, producing projected phonon-DOS as seen by NIS parallel and perpendicular to the hexagonal c-axis [3].

From the thermodynamic and elastic parameters derived from the phonon-DOS spectra of Figure 18 we concentrate here on the mean sound velocity v_m, connected in the Debye model with the longitudinal and transversal sound velocity, v_p and v_s, by $3/(v_m)^3 = 1/(v_p)^3 + 2/(v_s)^3$. The sound velocities v_m of ε-Fe, derived from the low-energy range (0 - 15 meV) of the DOS are shown in **Figure 19**. They exhibit a systematic difference between the two directions, increasing with pressure and amounting to about 4% at 130 GPa. One can use the known bulk modulus K and shear modulus G of ε-Fe to derive the corresponding v_p and v_s values from the measured v_m values [2]. The results for v_p are shown in Figure 19 and exhibit a smaller, but well-resolved

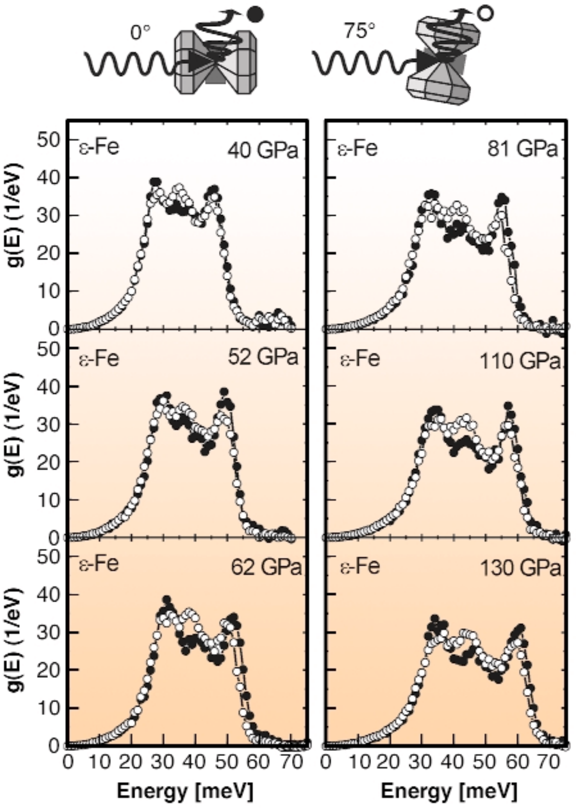

Fig. 18: (above) Transmission of the SR beam through the Fe sample at 0° and 75° with respect to the diamond anvil axis in the high-pressure cell. (below) Phonon-DOS g(E) of ε-Fe derived from NIS spectra at various pressures. Full dots correspond to the 0° direction and open dots to the 75° direction.

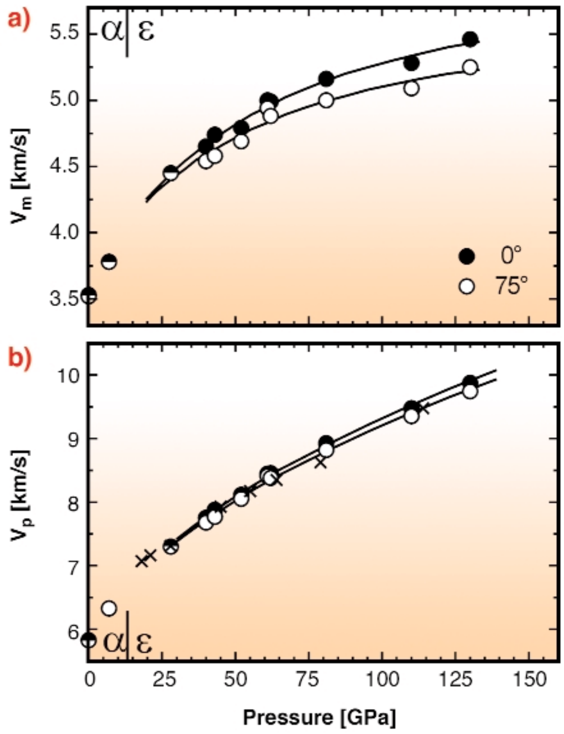

Fig. 19: a) Mean sound velocity v_m in ε-Fe derived from the phonon-DOS spectra shown in Figure 18. b) Longitudinal sound velocity v_p derived from v_m as explained in the text. Full and open dots have the same meaning as in Figure 18. The v_m and v_p data for α-Fe are also shown [3]. The crosses mark v_p values measured by IXS preferentially perpendicular to the c-axis.

difference. The 75° data agree nicely with v_p data obtained by IXS, a complementary technique (see D. Antonangeli *et al.*, preceding article). All other elastic parameters derived from the full phonon-DOS exhibit similar differences indicating that the lattice is stiffer parallel to than perpendicular to the hexagonal c-axis. One reason for this behaviour might be the observed decrease of the c/a ratio with pressure.

Bearing in mind that the present data of v_m and v_p were obtained from a textured sample (and not from a single crystal) and that the NIS probability varies with $\cos^2 \vartheta$, where ϑ is the angle between the k-vector of the incident synchrotron radiation and the polarisation vector of the excited or annihilated phonons, the experimentally observed v_m values at 0° and 75° provide only lower limits of the actual difference in v_m and the derived v_p and v_s values as seen parallel and perpendicular to the c-axis. When we derive v_m and, accordingly, v_p and v_s from the projected DOS, we obtain considerably larger differences, up to 10% for v_m and v_p at 130 GPa [4]. An exact determination of the difference depends on the degree of texture in the ε-Fe samples, which will be determined independently in future studies. The present data demonstrate the high-resolution power of NIS for precise determination of the sound velocities and other elastic parameters well above 100 GPa.

References

[1] R. Lübbers *et al.*, *Science* **287**, 1250 (2000).

[2] H.-K. Mao *et al.*, *Science* **292**, 914 (2001).

[3] H. Giefers, *et al.*, *High Pressure Research* **22**, 501 (2002).

[4] H. Giefers, PhD thesis (Paderborn, 2004); H. Giefers *et al.*, in preparation.

Authors

H. Giefers (a,b), G. Wortmann (a), A.I. Chumakov (c), D. Alfè (d).

(a) Department Physik, University of Paderborn (Germany)

(b) Present address: Department of Physics, University of Nevada, Las Vegas (USA)

(c) ESRF

(d) University College London (UK)

Fe K Pre-edges Revealed by Resonant X-ray Emission

The pre-edge structures at the K absorption edge of transition metals obtained from X-ray absorption spectroscopy (XAS) are known to be extremely sensitive to the chemical and structural local environment, and can be used as a fingerprint of the transition metal properties [1]. Compared to L edge measurements, this method is advantageously bulk-sensitive, because it is performed in the hard X-ray energy range, and can be applied to a vast variety of materials such as bio-complexes and Earth science related materials, under various sample environments.

In XAS, however, the pertinence of data analysis hinges on the broadening effect related to the 1*s* core-hole lifetime. This limitation can be overcome to a certain degree by using a second order process instead, namely resonant X-ray emission spectroscopy (RXES). This method consists of measuring a specific decay channel on resonance as the incident energy is tuned to an absorption edge. As a benchmark of this technique, we have applied RXES in a series of Fe-bearing minerals. We focused on the K_α emission line (2*p* → 1*s* transition) in the vicinity of the Fe-K edge (1*s*2*p*-RXES). In these model systems, Fe can be either of valence 2+ or 3+ and sits in a supposedly pure octahedral (O_h) or tetrahedral site (T_d). All the spectra were obtained on the **ID26** beamline using a Rowland circle spectrometer and a spherically-bent Si analyser.

Figure 20 shows the absorption edges obtained by RXES in the partial fluorescence yield mode (PFY). Here, the emitted energy E_2 is kept fixed at the maximum of the K_α

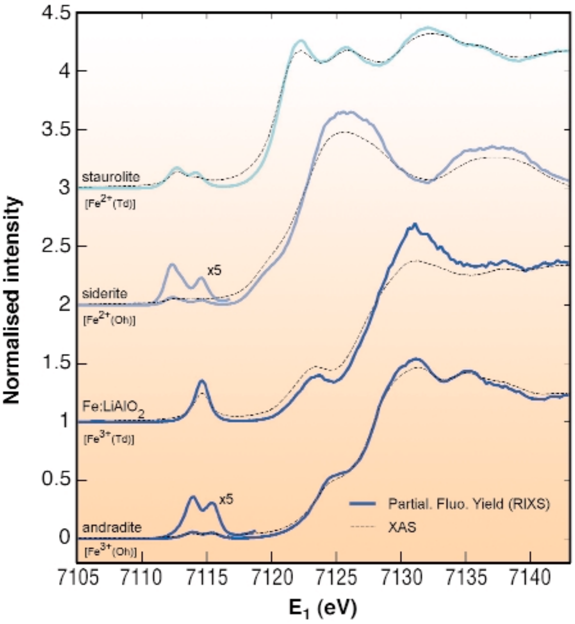

Fig. 20: High resolution absorption spectra at the Fe-K edge obtained by RXES in the PFY mode. The PFY-spectra are compared to conventional XAS (dotted lines).

line while the incident energy E_1 is varied through the Fe-K absorption edge. The presence of a shallower core-hole in the RXES final state, when compared to XAS, yields to a remarkable sharpening effect. Notably, the pre-edge exhibits a clear dependence on both Fe site-symmetry and valence. In a simple mono-electronic approach, this can be understood as due to the lift of degeneracy of the 3*d* states on the metal site, split by the crystal field of the surrounding ions. In octahedral environment, this would result in a mere doublet state, as observed in andradite. The absence of centre of symmetry in T_d ions leads to a more complicated picture: dipolar transitions to *d*-states hybridised with delocalised *p* electrons are now allowed. This yields an increase of intensity of the pre-edge by a factor of ~5.

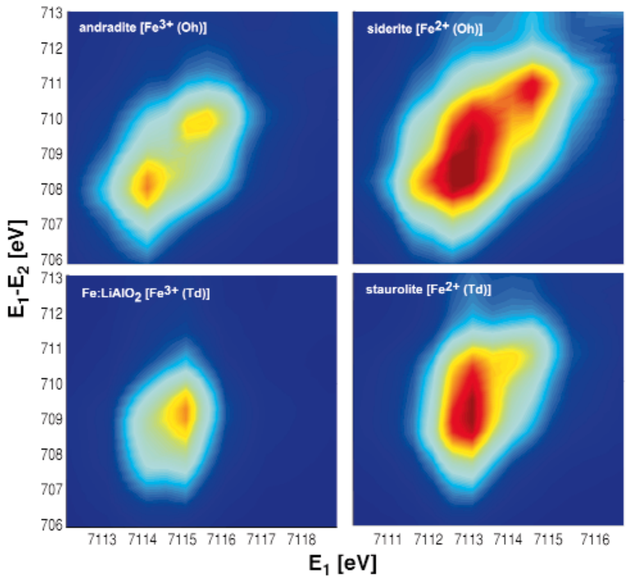

Fig. 21: RXES 2D-maps of the pre-edge region in the incident (E_1) vs transfer energy (E_1-E_2) plane for the four minerals.

Better insight can be gained by acquiring a complete map of the pre-edge region, in the RXES sense, as illustrated in **Figure 21** (see also [2]) for the four selected models. The colour-interpolated 2D-maps are reconstructed from series of RXES spectra, measured on a fine incident energy grid in the pre-edge region, and shown here as a function of the transfer energy E_1-E_2. In this plane, PFY absorption spectra correspond to cuts at 45°, while off-diagonal intensity reveals the spread of the 3*d* multiplet in the final state (in presence of a 2*p* core-hole), comparable to the Fe L absorption edges. Finally, XAS spectra can be recovered by integration over all transfer energies. RXES maps therefore provide a graphic and extensive representation of the Fe K pre-edge. In andradite, the distance between the two resonances (~1.6 eV) yields a direct estimate of the crystal field parameter (10Dq) in O_h symmetry. Similarly, in Fe:LiAlO$_2$ (T_d-Fe^{3+}), the asymmetric tail elongated towards to bottom left is reminiscent of the splitting of the *d* orbitals in T_d symmetry. Note that this 0.7 eV splitting would be entirely masked by lifetime broadening in XAS. Analysis of the pre-edge in Fe^{2+} compounds implies taking into account multiplet effects, as shown by strong off-diagonal resonances, *e.g.* in staurolite (T_d-Fe^{2+}).

In conclusion, the RXES method should be of particular interest for the field of mineralogy. It also merits broader interest for studying the electronic properties of complex materials in constrained environments.

References

[1] M. Wilke *et al.*, *Am. Mineral.* **86**, 714 (2001).
[2] P. Glatzel *et al.*, *J. Am. Chem. Soc.* **126**, 9946 (2004).

Principal Publication and Authors

J.-P. Rueff (a), L. Journel (a), P.-E. Petit (b), F. Farges (c), *Phys. Rev. B,* **69**, 235107 (2004).
(a) Laboratoire de Chimie Physique - Matière et Rayonnement, CNRS - Université Paris 6 (France)
(b) Institut des Matériaux J. Rouxel, CNRS - Université de Nantes (France)
(c) Laboratoire des Géomatériaux, CNRS - Université de Marne la Vallée (France), and Department of Geological & Environmental Sciences, Stanford University (USA)

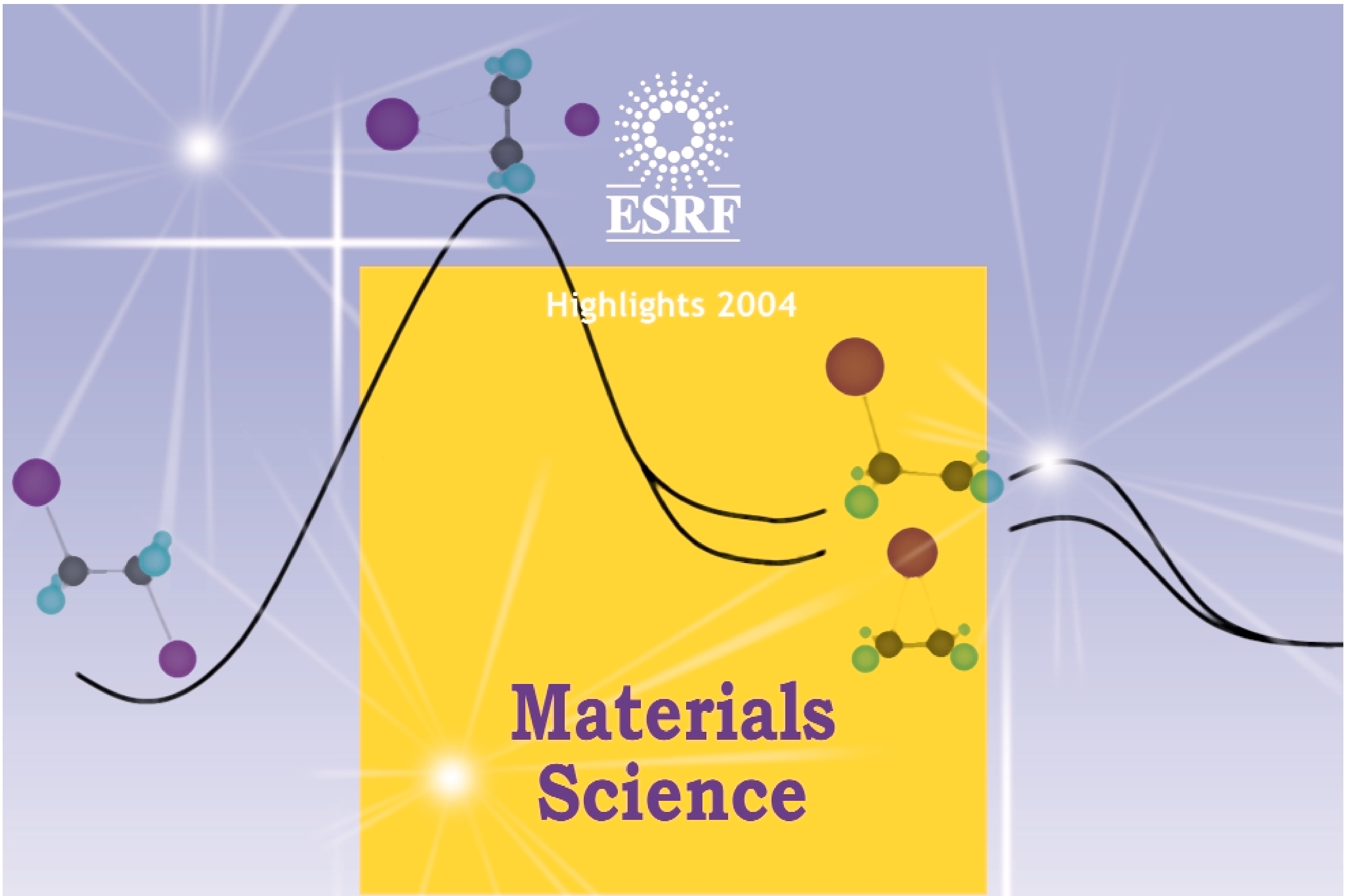

Materials Science

Introduction

Materials science plays a major role at the ESRF and spans a wide range of applications from chemical bonding, electronic applications, and novel synthesis to studies of grain growth and dynamic evolution of materials properties. The trend in materials science research at the ESRF is that micro focussing, time-resolved studies *in situ* and the application of combinations of techniques are on the rise. In order to illustrate these trends we have chosen a few examples in the categories: Materials and their Properties, Growth and Dynamics of Metals and Alloys, and Extreme Conditions.

The change of structure of molecules during chemical reactions is of fundamental importance for the understanding of reaction pathways. These often very fast processes can now be studied on the picosecond timescale by X-ray diffraction as illustrated by a study of photo dissociation of $C_2H_2I_2$ using pulsed picosecond lasers and X-ray beams (100 ps) showing the dissociation of the molecules including the time evolution of metastable complexes.

Porous solids are strategic materials for catalysis, separation and storage of gases and many other applications. One example illustrates the possibility of designing new porous materials by a combination of computer design and X-ray powder analysis with an example of the production of a new material from 1,3,5-benzene tricarboxylate and chromium trimers. A second example shows a combined X-ray and spectroscopy study of the stabilisation of Ag and Cu carbonyl clusters in the zeolitic nanochannels of the well-known zeolite ZSM-5.

Thin films are important for the production of superconducting and electronic materials. The control of the deposition procedure is essential for optimal performance of these materials. In one study the *in situ* evaluation of the deposition of superconducting $Yba_2Cu_3O_7$ films by pulsed laser deposition was followed by X-ray diffraction at high temperatures. The real-time evolution films of InO_3:Sn, an n-type semiconductor, was studied by X-ray diffraction. Films of this material are used in opto-electronics, solar cells and in liquid crystal displays. Annealing is known to improve the electrical and optical properties. The study correlates the changes of the film properties with its structure during annealing in vacuum.

Powder diffraction is becoming a very useful tool for a variety of studies at synchrotron facilities due to the excellent resolution. A novel application is presented to illustrate the use of powder diffraction even for very large structures such as proteins in the temperature dependence study of the hexagonal turkey egg-white lysozyme.

The properties of metals and alloys can be improved by addition of trace elements and by mechanical processing or annealing. The mechanisms for the improvements are, however, often not known in details. Four studies of these phenomena are given. In a small-angle

X-ray scattering experiment, the dynamic precipitation in an Al-Zn-Mg-Cu alloy was studied during quenching. It was shown that the precipitation process is much faster during straining of the materials as compared to static ageing. The 3D-XRD microscope at ID11 has been used to study the individual grain growth during annealing of Al single crystals. A movie of the grain growths of several grains in three-dimensions was produced. The third example presents a novel method to study stress and strain fields in amorphous materials. Previously only crystals could be characterised by diffraction, but now, by employing high-energy X-ray correlation functions, the strain tensors in a bulk metallic glass was determined. The dynamics of amorphous materials can also be followed using the coherence of the X-ray beam. The fourth example shows how the intensity fluctuations in the speckle pattern can be analysed by autocorrelation functions. In this example, X-ray photon autocorrelation spectroscopy was used to investigate the antiphase domain dynamics in the intermetallic phase $Co_{60}Ga_{40}$.

High-pressure studies are gaining in importance for a number of areas of materials science research. The new applications of laser heating have now opened up the field for studies both at high pressures and high temperature (> 5000 K). In one study the matter of electronic topological transitions due to distortions of the electronic band structure was studied in osmium by angle-dispersive X-ray diffraction. During the study of the equation of state it was found that the Fermi surface of osmium passes through a topologic singularity at 25 GPa. A second study deals with the synthesis of nitrogen. Nitrogen usually consists of dimers with strong triple bonding. In a synthesis above 2000 K and pressures above 110 GPa, a theoretically predicted cubic phase, polymeric nitrogen, was found as evidenced by a combination of X-ray diffraction and Raman techniques. The final example deals with the boundary between the earth's mantle and the core. In this region one notices a large contrast in the properties across the region. The interaction between iron and silica (SiO_2) was studied in an electrically and laser heated diamond anvil cell at pressures up to 140 GPa and temperatures over 3500°C. It was shown that iron and SiO_2 do not react at high pressures and iron-silica alloys dissociate into almost pure iron and a CsCl-structured FeSi compound. The existence of the FeSi at the base of the Earth's lower mantle could explain the anomalously high electrical conductivity of this region and provide a key to the understanding why the amplitude of the Earth's nutation is out-of-phase with tidal forces.

Å. Kvick

Materials and their Properties

Photodissociation of $C_2H_4I_2$ Studied by Picosecond X-ray Diffraction

How does the structure of a molecule change during a chemical reaction and how does the molecule interact with its nearest neighbours during the reaction? This is a very difficult question since most molecules are formed and broken extremely quickly. In fact the primary step in the formation of a molecule is the creation or breakage of chemical bonds or the transfer of electrons or protons. These steps are typically completed in 10-1000 femtoseconds, which is about 1000 times faster than the X-ray pulse from a synchrotron. A newly-formed molecule is usually created in a high-energy state, which relaxes into secondary structures by exploring all internal degrees of freedom in the molecule (turn angles, bond angles, bond lengths, etc). In this process, the molecule may reach a local minimum on the potential energy surface and later de-excite through collisions with its neighbours. These secondary structures, which typically have picosecond lifetimes in liquids, can be determined by single pulse X-ray diffraction from photosensitive molecules that can be activated by a short laser pulse. Here we report on the photo detachment of I_2 from diiodoethane $C_2H_4I_2$, see **Figure 22**. We now know that molecular iodine I_2 is formed in a two-step process, which involves the unstable C_2H_4I radical:

$C_2H_4I_2 + h\nu \rightarrow C_2H_4I + I \rightarrow C_2H_4 + I_2$

Note that quantum chemistry predicts two intermediate structures of C_2H_4I in methanol (CH_3OH) at nearly the same energy, the bridged and the anti structure. The experiment, which was done on beamline **ID9B**, shows that the bridged structure alone is formed in methanol, a fact that we ascribe to nearest neighbour interaction in liquid methanol.

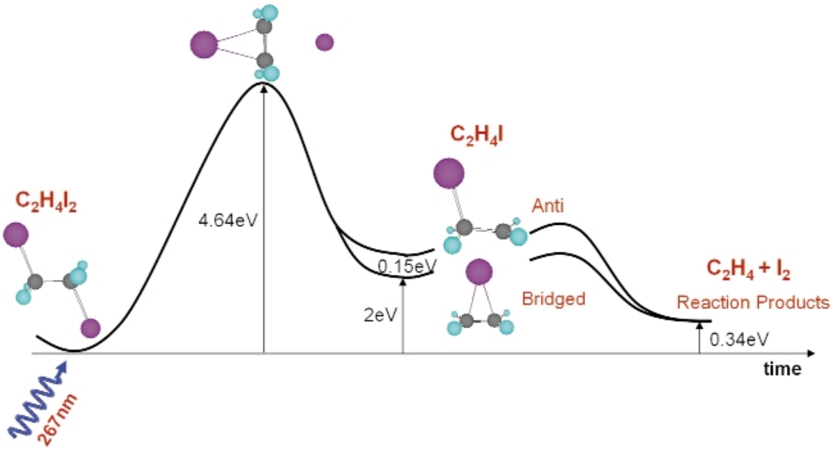

Fig. 22: Calculated energy landscape of the photoproducts of $C_2H_4I_2$. Iodine is pink, carbon gray and hydrogen blue.

The $C_2H_4I_2$ molecules were dissolved at a concentration of 1:400. The $C_2H_4I_2$ molecule is excited by the absorption of a UV pulse (2 ps, 267 nm) in the C-I stretched band, which leads to the emission of an iodine atom into the solvent. In 60% of the excited molecules, the freed iodine atom thermalises in the first solvation shell and recombines geminately. In 40% of cases, however, the C_2H_4I radical is formed and we would like to determine its structure, lifetime (decay mechanism) and the liquid structure around it. In the experiment, the pulsed laser beam (2 ps, 267 nm, 986 Hz) and the pulsed X-ray beam (100 ps, 0.07 nm, 986 Hz) were focused onto a 0.3 mm thick sheet of liquid formed by a sapphire nozzle. By suitably adjusting the speed of the liquid, a fresh sample was injected into the beam every millisecond. The time resolution is then simply the delay between the pump and the probe. The diffracted beam was recorded on a CCD detector and the images were recorded in pairs *with* and *without* excitation. The white beam from the single-harmonic undulator U17 was used to compensate for the low frequency of the experiment. The X-ray beam was focused by a toroidal mirror to 0.10 x 0.05 mm^2 and the flux was 5 x 10^{11} ph/s in a 2.5% bandwidth around 18.0 keV. The difference in the radial intensity $\Delta S(q, \tau)$, non excited – excited, is oscillatory and strongly dependent on the time delay. The associated Fourier transform is a measure of the change in the atom-atom pair distribution functions $g_{ij}(r)$ within the molecule [1,2], see **Figure 23.**

The negative peak at 5.1 Å coincides with the I..I distance in $C_2H_4I_2$. The measurements tell us that this correlation is reduced, *i.e.* at least one iodine atom has left the molecule after 100 ps. The second negative peak at 2.1 Å comes from a change in the C-I correlation. This feature is consistent with the formation of the bridged structure. The measurements at later times show, rather dramatically, that the liberated iodine atoms “swim” around the C_2H_4I radical and strips off the second iodine to form $C_2H_4 + I_2$. This diffusive process takes about 10 ns. Note finally that the radial curves $\Delta S(r, \tau)$ provide a 1-dimensional moving image of a chemical reaction in solution: it is probably the closest we get to film chemical reactions in disordered media with X-rays.

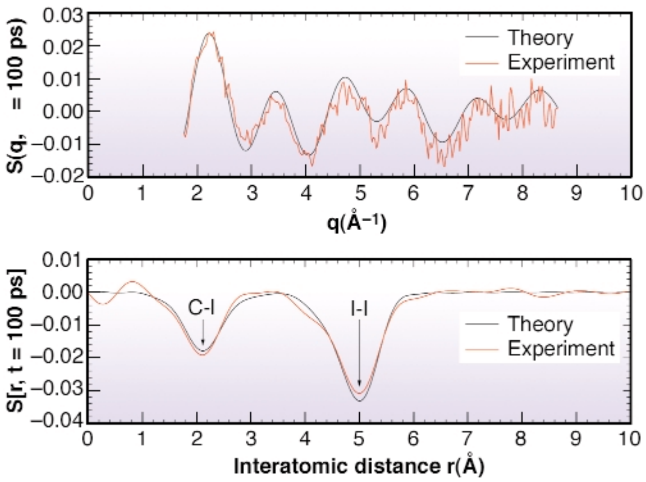

Fig. 23: The transition $C_2H_4I_2 \rightarrow C_2H_4I + I$ produces an oscillatory change $\Delta S(q)$ in the diffracted intensity measured here 100 ps after dissociation. The Fourier transform $\Delta S(r)$ is shown below.

References

[1] A. Plech, M. Wulff, S. Bratos, F. Mirloup, R. Vuilleumier, F. Schotte and P. A. Anfinrud, *Phys. Rev. Lett.*, **92**, 12, 125505-1 (2004).

[2] S. Bratos, F. Mirloup, R. Vuilleumier, M. Wulff and A. Plech, *Chem. Phys.* **304**, 245–251 (2004).

Principal Publications and Authors

H. Ihee (a), M. Lorenc (b), T.K. Kim (a), Q.Y. Kong (b), M. Cammarata (c), J.H. Lee (a) and M. Wulff (b), *submitted for publication*.

(a) Department of Chemistry and School of Molecular Science, Advanced Institute of Science and Technology (KAIST), 305-701, Daejeon (Republic of Korea)

(b) ESRF

(c) National Institute for the Physics of Matter and Department of Physical and Astronomical Sciences, Palermo (Italy)

Design of Crystallised Hybrid Solids with Giant Cells and Mesopores

Porous solids are strategic materials owing to their applications in petroleum chemistry, fine chemicals, catalysis, separation and storage of gases. They exist either as purely inorganic or hybrid organic-inorganic frameworks. The current challenge [1] is to obtain giant pores to use them also as nanoreactors.

For such a challenge, chance is not sufficient, and design procedures must be introduced [2]. This requires the combination of targeted chemistry and computer simulations. This is particularly possible with hybrid solids, which are constructed from inorganic building units and organic moieties. For design purposes, we need first to establish the synthetic chemical conditions corresponding to the existence of targeted inorganic units in solution. Second, we use computer simulations to explore in 3D space the possibilities of a connection between the above inorganic unit with the organic ligand (here 1,3,5-benzene tricarboxylate [BTC]). The simulations yield candidate crystal structures with their atomic coordinates and space groups. Then a comparison between the X-ray powder diffraction patterns of the different simulated models and the experimental one allows us to identify the correct candidate.

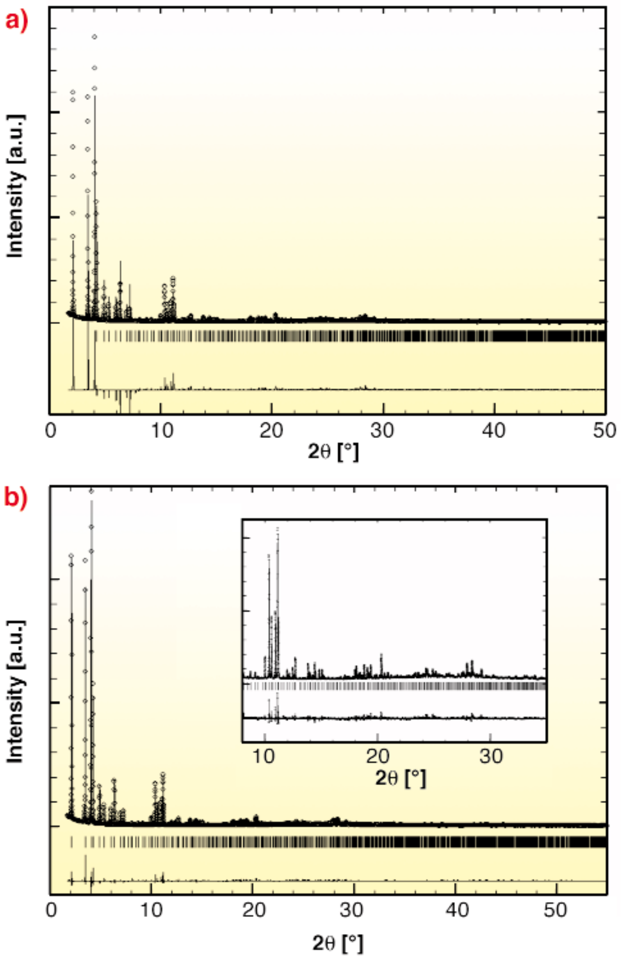

Fig. 24: Comparison of the theoretical (a) and refined experimental (b) patterns of MIL-100.

This new procedure was applied to μ_3-O chromium(III) octahedra trimeric building units with BTC. The resulting product (MIL-100) was a green powder with a Langmuir surface of ~ 3,100 m^2/g indicating its porous character. The chemical analysis of this product gave a ratio of 1:2 between Cr trimers and BTC. This information was used in the simulation program. The latter provided three candidate polymorphs with close lattice energies, together with their theoretical X-ray powder diffraction patterns. The position of the Bragg peaks of only one of them fit (**Figure 24**) those of the experimental product (labelled MIL-100). It consists of a cubic unit-cell (S.G. F*d-3m*, a = 72.26 Å, V = 387,000 Å^3) far beyond the current possibilities for solving the structure from *ab initio* procedures.

Starting from the coordinates provided by the simulations, the Rietveld refinement of the crystal structure (68 independent framework atoms) was performed from synchrotron data collected at 80 K on beamline **ID31** (λ: 1.55075 Å) and further allowed us to localize the extra-framework water molecules with good R values. The difference in intensities relates mainly to the fact that the simulation takes into account only the framework and not the species inserted in the cages.

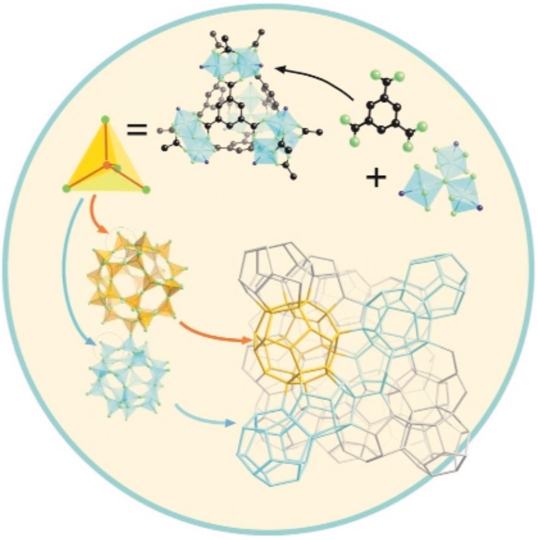

Fig. 25: Genesis of the structure from Cr(III) trimers and BTC forming first supertetrahedra which connect in three dimensions to give cages with 20- and 28 supertetrahedra.

Beside the originality of the method, the structure of MIL-100 itself is appealing. Indeed, the trimers and the BTC molecules (**Figure 25**) are first linked to each other via the carboxylate functions in order to build supertetrahedra whose corners are occupied by the trimers and the faces by BTC. These supertetrahedra are microporous with free diameters of ca. 6.6 Å. More interestingly, they connect to each other via the trimers in order to build a three-dimensional structure of corner-sharing supertetrahedra with two types of cages within the framework whose dimensions are now typically in the range of *mesopores*. The smallest, limited by 20 supertetrahedra and forming pentagon dodecahedra, has an internal *free* diameter of ≈ 25 Å and pentagonal windows: (~ 4.8 x 5.8 Å). The face sharing of these dodecahedra creates larger cavities, limited this time by 28 supertetrahedra. The polyhedron determined by the centres of the supertetrahedra has now 12 pentagonal and 4 hexagonal faces. The free aperture of the large hexagonal windows is ~ 8.6 x 8.6 Å and the internal free diameter close to ≈ 29 Å. In the as-prepared materials, the cavities are occupied only by water molecules, which evolve from room temperature to 100°C.

In conclusion, MIL-100 represents the largest non proteinic solid isolated to date, the structure of which could be solved only by applying an original method combining targeted chemistry, computer simulation and powder diffraction. Using this approach, the resolution of structures, even very complex ones, is restricted to a Rietveld refinement. Moreover, MIL-100 provides the first example of a mesoporous solid with crystalline walls, at variance to the usual mesoporous solids, with a unique hierarchical system of three types of cages of different dimensions. Also, MIL-100 may have outstanding applications in the domain of sorption/separation of species.

References

[1] G. Férey, A.K. Cheetham, *Science* **283**, 1125 (1999).
[2] M. Eddaoudi, D.B. Moler, H.Li, B. Chen, T.M. Reineke, M. O'Keeffe, O.M. Yaghi, *Acc. Chem. Res*. **34**, 319 (2001)

Principal Publication and Authors

G. Férey (a), C. Serre (a), C. Mellot-Draznieks (a), F. Millange (a), S. Surblé (a), J. Dutour (a), I. Margiolaki (b), *Angew. Chem. Int. Ed*. **43**, 6285, 6290, 6296 (2004) (3 articles).
(a) Institut Lavoisier, UVSQ, Versailles (France)
(b) ESRF

Heterogeneous Non-classical Cu(I)- and Ag(I)-carbonyls Stabilised in ZSM-5 Zeolite: Thermodynamic and Spectroscopic Features

The electrostatic, σ- and π-contributions in the formation of carbonyl bonding for the "*non classical*" Cu(I)- and Ag(I)- carbonyls hosted inside zeolitic nanocavities have been separated using a combination of thermodynamic and spectroscopic information. Adsorption of CO, at RT, on well-defined Cu(I) and Ag(I)-ZSM-5 systems was studied by the joint use of adsorption microcalorimetry and IR, EXAFS and XANES spectroscopies performed on the beamlines **BM8** (GILDA) and **BM29**, respectively. The formation in the zeolite pores of heterogeneous, $[Cu(CO)_2]^+$ and $[Ag(CO)]^+$ complexes, with a stoichiometry that agrees with the homogeneous "*non classical*" carbonyls, has been observed at p_{CO} = 40 Torr. A C-O stretching frequency higher than that of the free molecule (2143 cm^{-1}) has been observed: $\tilde{\nu}_{CO}$ = 2192 cm^{-1} for $[Ag(CO)]^+$, while the $[Cu(CO)_2]^+$ complexes (**Figure 26a**) result in a doublet at 2151 and 2178 cm^{-1} [1-3]. The number of CO molecules adsorbed per Cu(I) cations, obtained by volumetric measurements, agree fairly well with the local stoichiometry emerging from the EXAFS data analysis. As an example, Figure 26b reports the results of the EXAFS data analysis, performed with GNXAS software. Interaction with CO at RT causes a partial solvation of Cu(I) cations from the zeolite walls: the Cu-O_F distance (O_F = framework oxygen) is elongated by +0.11 ± 0.03 Å. The scattering due to the carbonyl ligands results in a coordination number for the CO molecules of 1.8 ± 0.3, in agreement with the $[Cu(CO)_2]^+$ stoichiometry suggested by IR spectroscopy and adsorption microcalorimetry. The Cu-C distance obtained for the $[Cu(CO)_2]^+$ complex is 1.88 ± 0.02 Å, while the C-O distance (1.12 ± 0.03 Å) is in good agreement with the gas-phase value (1.128 Å), and the Cu-C-O bond angle is linear within the error bars (170° ± 10°), in agreement with indirect IR evidences.

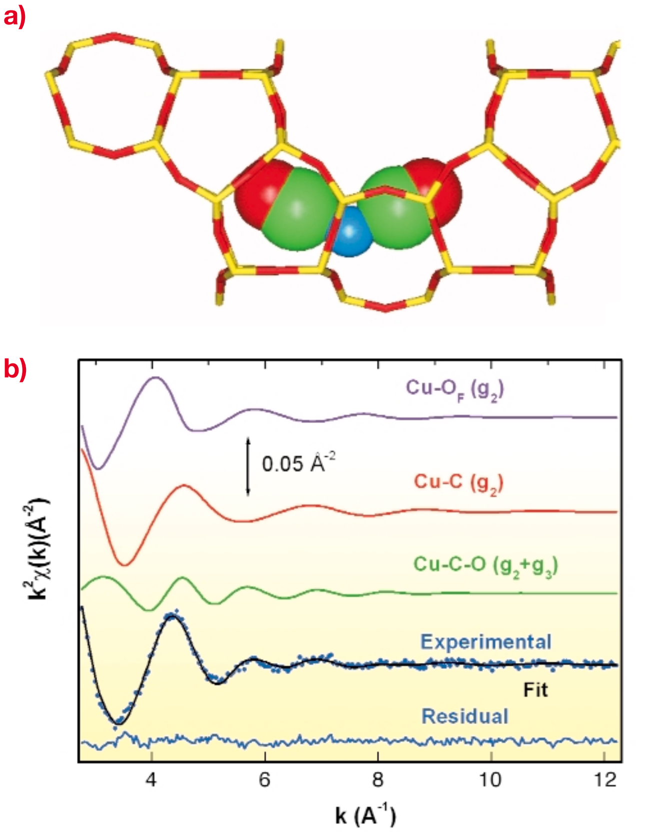

Fig. 26: (a) Pictorial representation of a $[Cu(CO)_2]^+$ complex (ball representation) hosted inside the ZSM-5 framework (stick representation: O red; Si or Al yellow). (b) The Cu-K edge EXAFS spectrum collected on Cu(I)-ZSM-5 zeolite in interaction with CO at RT (p_{CO} = 40 Torr: blue dotted curve) has been successfully simulated (black full line) as the superimposition of both framework oxygens (magenta line) and two adsorbed CO molecules (red and green curves).

The zero-coverage enthalpies of CO adsorbed on Cu(I)- and Ag(I)-sites (-Δ_{ads}H ~120 and ~100 kJ/mol, respectively) are much larger than the -Δ_{ads}H values measured for the Na^+ (~35 kJ/mol) and K^+ (~28 kJ/mol) sites hosted in the same zeolite pores in spite of the closeness of the charge/radius ratios of the two sets of metal cations [Na^+ and Cu(I); K^+ and Ag(I)]. The high -Δ_{ads}H values and the irreversible nature of (a fraction of) the *d*-block metal carbonyls implies the onset of a π-back donation reinforcing the carbonyl bond with respect to a pure σ-coordination.

Insertion of ammonia ligands results in the displacement of one CO molecule and in the formation of intrazeolitic $[Cu(NH_3)_n(CO)]^+$ complexes characterised by $\tilde{\nu}_{CO}$ = 2100 cm^{-1}, a value significantly lower than in the gas. This datum indicates that, in such $[Cu(NH_3)_n(CO)]^+$ complexes, the π-back donation dominates both in the electrostatic and σ-donation components. The charge releasing character of the amino ligand certainly plays a role in quenching the electrostatic component of the Cu(I)←CO interaction [1].

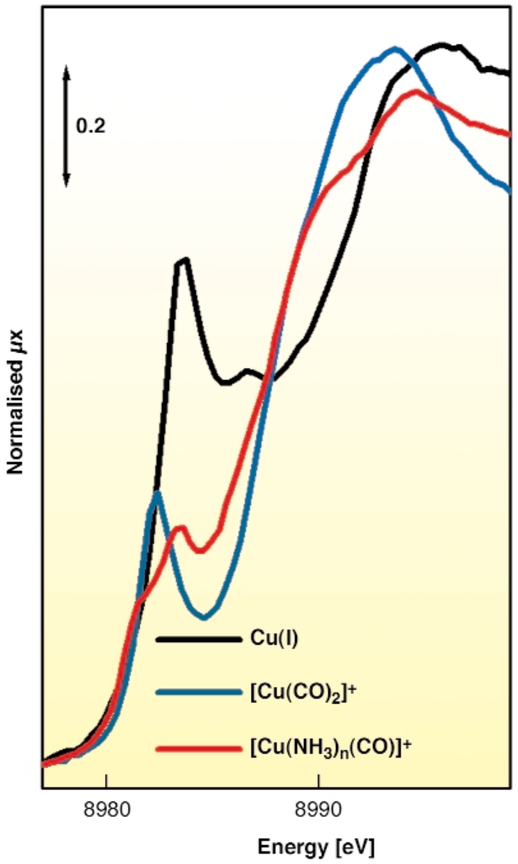

Fig. 27: Normalised XANES spectra of Cu(I)-ZSM-5 *in vacuo* (black line), after interaction with CO on samples activated (blue line) and previously in contact with NH_3 (red line).

Figure 27 reports the important modification of both electronic and geometric configurations of Cu(I) centres upon formation of $[Cu(CO)_2]^+$ (blue curve) and $[Cu(NH_3)_n(CO)]^+$ (red curve) complexes hosted in ZSM-5 zeolite (black curve: zeolite *in vacuo*). Significant red shift and shape variations of both edge and pre-edge features are observed. XANES data confirm the strong charge releasing character of the amino ligand and explains the low ν_{-CO} observed in the IR experiment.

References

[1] A. Zecchina, S. Bordiga, G. Turnes Palomino, D. Scarano, C. Lamberti and M. Salvalaggio, *J. Phys. Chem. B,* **103**, 3833-3844 (1999).
[2] V. Bolis, S. Maggiorini, L. Meda, F. D'Acapito, G. Turnes Palomino, S. Bordiga and C. Lamberti, *J. Chem. Phys.* **113**, 9248-9261 (2000).
[3] C. Lamberti, G. Turnes Palomino, S. Bordiga, G. Berlier, F. D'Acapito and A. Zecchina, Angew. *Chem. Int. Ed.*, **39**, 2138-2141 (2000).

Principal Publication and Authors

V. Bolis (a,b), S. Bordiga (b,c), A. Zecchina (b), C. Prestipino (b,c), L. Capello (d), F. D'Acapito (d), C. Lamberti (b,c), *J. Phys. Chem. B*, **108**, 9970-9983 (2004).
(a) University of Piemonte Orientale, and INSTM (Italy)
(b) NIS centre of excellence University of Turin, and INSTM (Italy)
(c) INFM UdR of Turin University (Italy)
(d) ESRF (France)

In situ X-ray Diffraction during Pulsed Laser Deposition

Pulsed Laser Deposition (PLD) has become a widespread technique for the fabrication of thin films [1]. A powerful pulsed laser is used to create a plasma off a target material, which is subsequently epitaxially deposited on a heated single crystal substrate. With each laser pulse, only a fraction of a monolayer is deposited, thereby making it possible to control the thickness very accurately. In between two individual laser pulses, the adatoms on the substrate are allowed to relax, which results in very smooth layers and interfaces. PLD is especially suited for the deposition of complex transition metal oxides and in particular for high-Tc superconductors owing to two different aspects. First of all, growth with PLD can take place at relatively high oxygen background pressures (up to 100 Pa), allowing for stoichiometric deposition of these materials. Second, the layered structure of high-Tc superconductors requires atomic control of deposition.

Although PLD is widely used due to the advantages over traditional molecular beam epitaxy (MBE) techniques, the processes governing the growth, *i.e.* nucleation and subsequent coalescence of islands are not yet understood. To accomplish a more detailed understanding of the PLD process, structural information during growth is needed. So far, mainly *in situ* Reflection High Energy Electron Diffraction (RHEED) measurements have been performed [2]. RHEED is a very useful technique to study the growth of the layer mechanism. However, a quantitative analysis of the structural data is hampered due to multiple scattering effects. In case of using X-rays, which interact much less than electrons in scattering events, kinematical theory applies. To study crystal growth using surface sensitive X-ray scattering techniques, high-brilliance X-ray beams, nowadays readily available at third generation synchrotron sources, are needed. In this way it is possible to investigate the growing interface/surface at an atomic scale.

To study thin film PLD growth *in situ* by X-ray diffraction, a special sample chamber was constructed [3]. A film of the high-Tc superconductor $YBa_2Cu_3O_{7-x}$ was grown on a substrate of $SrTiO_3$. The experiments were carried out by mounting the chamber on a 2+3 type surface diffractometer with vertical scattering geometry at **BM26** (Dubble) and focusing an excimer laser, having a wavelength of 248 nm, on the target. During deposition the substrate temperature was kept at 780°C and the oxygen pressure in the chamber at 0.03 mbar.

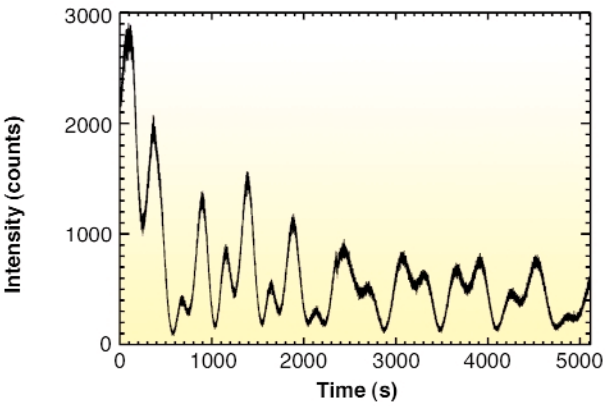

Fig. 28: Intensity oscillations of the (0,0,0.15) point as a function of time during growth of the $YBa_2Cu_3O_{7-x}$ thin film.

At a grazing angle for the incoming beam of 1 degree, the intensity of the reciprocal point (0,0,0.15) in STO lattice units is monitored during deposition (**Figure 28**). An oscillatory pattern is seen where each maximum corresponds to the completion of another monolayer, and therefore indicating so-called layer-by-layer growth. This is explained by considering the following: on an atomically flat surface, a fraction of a monolayer is deposited. Due to the increase of the surface roughness, the intensity will drop. When however the monolayer is completed, *i.e.* the whole surface is covered by the monolayer, the surface is atomically flat again and the intensity reaches a maximum.

Growth was stopped several times, allowing further characterisation of the grown film. **Figure 29** shows the 001 Bragg reflection of the film when it was 21.0(1) nm thick. The pronounced Kiessig fringes show that the surface is particularly smooth, which is to be expected in case of layer-by-layer growth.

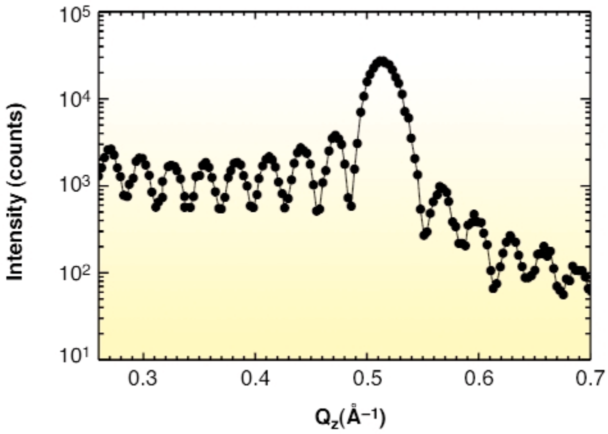

Fig. 29: The 001 Bragg reflection of the film at 21.0(1) nm thickness and 780 °C. Pronounced Kiessig fringes indicate a particularly smooth surface.

In conclusion, we were able to follow the PLD growth of a thin $YBa_2Cu_3O_{7-x}$ film *in situ* by X-ray diffraction. This opens the possibilities of performing detailed studies of complex oxide thin film growth on the atomic scale.

References

[1] D. Chrisey and G. Hubler, *Pulsed Laser Deposition of Thin Films* (John Wiley and Sons, New York, 1994).
[2] G. Rijnders,G. Koster, D. Blank, and H. Rogalla, *Appl. Phys. Lett.* **70**, 1888 (1997).
[3] V. Vonk, S. Konings, L. Barthe, B. Gorges and H. Graafsma, *J. synchr. Rad.* (in preparation).

Authors

V. Vonk (a,b), K. Driessen (a), M. Huijben (b), S. Harkema (b), B. Gorges (a) and H. Graafsma (a).
(a) ESRF
(b) Low Temp. Division and MESA+ Res. Inst., Univ. of Twente (The Netherlands)

Real-time Evolution of the ITO Film Properties and Structure during Annealing in Vacuum

Tin-doped-indium oxide In_2O_3:Sn (ITO) is an *n*-type semiconductor with high transparency and nearly metallic conductivity. Thin films of ITO find applications in optoelectronics, solar cells, and in the liquid crystal display industry. Annealing is a known way to improve the electrical and optical properties of ITO. The present investigation was performed to correlate changes of the film properties with its structural evolution during annealing in vacuum.

Amorphous 130 nm thick films were produced on Si(100) substrates covered with SiO_2 by reactive pulsed magnetron sputtering using the technology described in [1]. To study the real time evolution of the film structure with experiments at the ROBL beamline (**BM20**), a UHV annealing chamber with an X-ray transparent beryllium dome was installed on a six-circle goniometer. The XRD data were obtained in Bragg-Brentano geometry by a multichannel position sensitive detector allowing a fast acquisition time. In experiments carried out in the ITO deposition equipment at FZR (Forschungszentrum Rossendoorf) the optical properties of the films were monitored *in situ* by spectroscopic ellipsometry (SE). In both experiments the annealing temperature T_a was gradually increased from 20 to 330°C with a constant rate of 5°C/min and the film resistivity was measured *in situ* by a four-point probe technique.

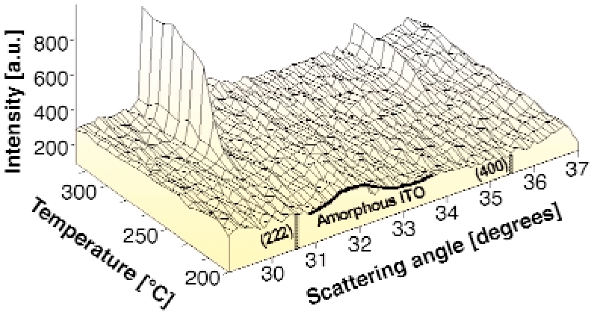

Fig. 30: Evolution of XRD patterns during annealing in vacuum.

At an increase of T_a up to 250 ± 10°C, the XRD patterns show only a broad amorphous peak around 32°. The evolution of the XRD patterns within the temperature range 200-320°C is shown in **Figure 30**. At $T_a \geq 250$°C, the (222) and (400) peaks of crystalline In_2O_3 phase start to appear. Their intensity increases strongly if T_a increases by approximately 30°C, pointing to a rapid crystallisation of the film. The film becomes completely crystalline at $T_a \geq 280$°C with a stable structure above, which exhibits a weak (222) fibre texture in this state. The size of coherently diffracting domains was estimated to 65 ± 4 nm. The temperature dependence of XRD integral intensity of the In_2O_3 (222) peak ($I_{(222)}$) (**Figure 31a**) shows an enhancement of the crystalline fraction during the amorphous-to-crystalline transition. Roughness growth observed by SE is correlated to the film crystallisation.

Using the Kolmogorov–Johnson–Mehl–Avrami equation for the time dependence of crystallisation degree $f = I_{(222)} / I_{C(222)} = 1\text{-exp}(-Kt^n)$, where $I_{C(222)}$ is the integral intensity at complete crystallisation, the kinetic exponent $n = 2.99 \pm 0.23$ was determined. Because the coherently diffracting domain size is smaller than the film thickness, this kinetic exponent indicates a three-dimensional crystallisation process.

The temperature dependence of the resistivity in Figure 31b indicates several stages with features at T_a = 110, 150, 280 and 310°C. The behaviour of the free electron density Ne in the Figure 31b qualitatively agrees with a decrease of the resistivity, excepting the temperature range of 280-310°C. The refractive index in Figure 31c decreases at increasing annealing temperature that relates to the free electron density behaviour. The stability of the film resistivity and refractive index at a temperature below $T_a \sim 120$°C indicates that neither the free electron density nor the structure of the ITO films change during the first annealing period. At temperatures (120-240°C) the resistivity improvement and free electron density increase in the amorphous ITO can be attributed to the creation of oxygen vacancies due to relaxation of distorted In-O bonds in the amorphous phase.

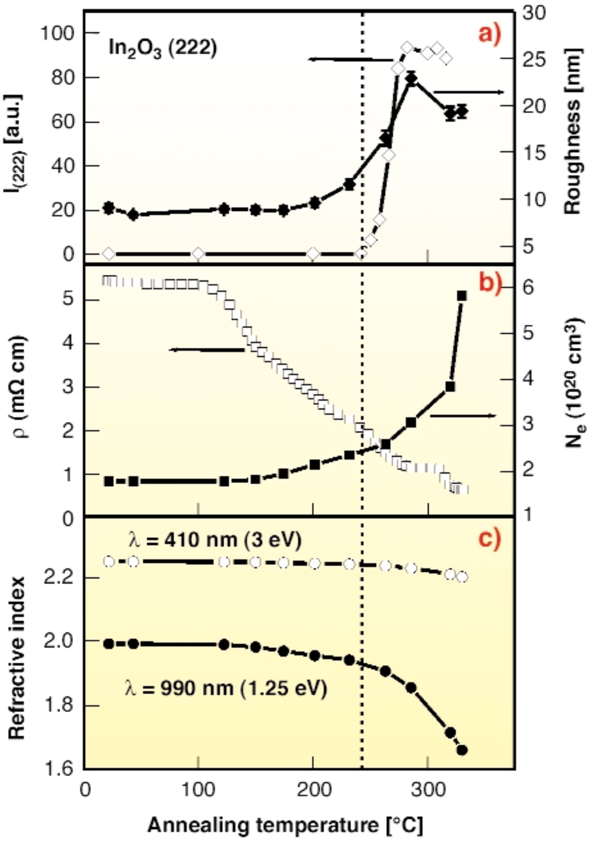

Fig. 31: The temperature dependence of the XRD integral intensity of the In_2O_3 (222) peak ($I_{(222)}$) and the film roughness (a); resistivity and free electron density N_e (b); refractive index (c).

The enhancement of the free electron density N_e after the beginning of crystallisation can be explained by the onset of Sn donor activation in a crystalline phase. However, the SE is sensitive to the free electron density enhancement even in crystalline grains, which are electrically insulated. These grains do not contribute to resistivity decrease until they are electrically connected. Maybe such connections are a reason for the drop of resistivity after a plateau observed within the temperature range 280-310°C. The comparison of the graphs in Figure 31 clearly shows that at constant heating rate the resistivity and optical properties depend non-linearly on the crystalline fraction.

In summary, the structure and properties dependency on temperature of ITO films have been monitored in real time during annealing in vacuum, using three complementary *in situ* techniques. The direct observation of the structure yields a crystallisation temperature of 250°C. Even in the amorphous state the film resistivity decreases significantly at increasing temperature, probably due to relaxation of distorted In-O bonds, which leads to a free electron density enhancement by the creation of oxygen vacancies. The rapid crystallisation is accompanied by film roughening and leads to a further decrease of the resistivity due to Sn donor activation.

References

[1] A.I. Rogozin, M.V. Vinnichenko, A. Kolitsch, and W. Möller, *J.Vac. Sci. Technol.* A**22**(2), 349-355 (2004).

Principle Publication and Authors

A. Rogozin (a), N. Shevchenko (a), M. Vinnichenko (b), F. Prokert (a), V. Cantelli (a, c), A. Kolitsch (a), and W. Möller (a), *Appl. Phys. Lett.* **85**(2), 212-214 (2004).
(a) Forschungszentrum Rossendorf, Dresden (Germany)
(b) University of Kyiv (Ukraine)
(c) ROBL-CRG, ESRF

X-ray Powder Diffraction Study of Hexagonal Turkey Egg-white Lysozyme

Obtaining the atomic structure of a large macromolecule like a protein depends upon the availability of good quality single crystals, the growth of which entails considerable skill and dedication. The conditions for optimal crystal growth must be painstakingly investigated, and a microcrystalline powder often precipitates instead of the sought-after crystal. Following the recent reports of crystal structure refinement [1] and solution [2] of some small proteins from powder diffraction data, the notion of obtaining at least some structural data from the powder looks potentially attractive, especially given the very high quality powder-diffraction patterns that can be measured at a modern synchrotron-radiation source. Despite all efforts, some materials of interest appear stubbornly to resist forming single crystals, the availability of the powder technique thus widens the spectrum of samples which might be investigated. Moreover, powder diffraction measurements can also give a range of complementary information beyond that which can be obtained from a single crystal. For example, the peak shapes depend on the microstructure of the material, accurate unit cell parameters can easily be determined, and the sample generally survives under more varied or extreme conditions. Here we report on our attempts to apply powder diffraction techniques to simple proteins.

In the present study, the structure of turkey egg-white lysozyme (TEWL) has been refined from high-resolution X-ray powder diffraction data. The sample was obtained in a polycrystalline form via rapid precipitation at high protein concentration using a 0.5 M NaCl solution (pH = 6) and the diffraction data were collected at room temperature employing the High-resolution Powder Diffraction (ID31) and the Materials Science (ID11) beamlines. Our structural analysis was initiated with a structural model that had previously been derived from single crystal data (PDB entry: 1TEW). Molecular replacement was shown to give a suitable starting point for refinement, illustrating that powder data can be sufficient for this approach. Crystallographic models were then refined by combined Rietveld and stereochemical restraint analysis of the powder data (d_{min} = 3.35 Å) resulting in the extraction of reliable lattice parameters and the refinement of the molecular conformation (**Figure 32**). The structure is hexagonal (Sp. group: $P6_122$; a = 71.0945(3) Å, c = 85.0371(5) Å) with 12 symmetry related molecules in the unit cell, in agreement with previous studies.

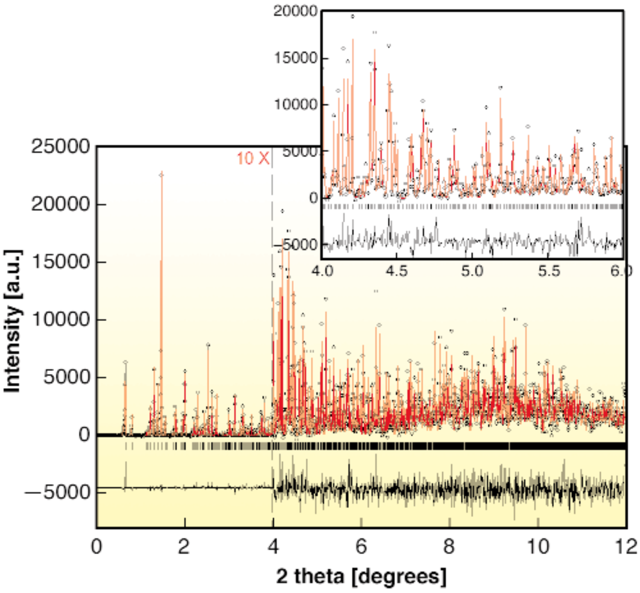

Fig. 32: The Rietveld fit for sample crystallised at pH 6 and 295 K (λ = 0.700667 Å, ID31 data). Open symbols: data, red line: final calculated pattern, black line: difference between the experimental data and the final refined model. The bars represent the Bragg reflections corresponding to the hexagonal structural model. The background intensity has been subtracted for clarity. The profile has been expanded by a factor of 10 at Bragg angles larger than 4°. Inset: Selected region of the Rietveld fit in the 2θ region, 4°-6°. The profile has been expanded by a factor of 10 for clarity.

TEWL is a relatively compact structure, comprising 8 helices and 4 anti-parallel ß-sheets. The overall and secondary structural topology of the powder structure are essentially the same as in the previously determined single-crystal structures with a few slight differences mainly in the regions of the flexible loops and the C and N-termini of the molecule. The average RMS deviation of the $C\alpha$ positions, after aligning the original (PDB entry: 1TEW) and refined structures, was determined to be 0.95 Å over

128 residues. The deviation between the structures may arise in part due to the differences in the structural resolution of the data (d_{min} = 1.65 Å for 1TEW and 3.35 Å for the powder structure). The Ramachandran plot for the main-chain torsion angles (ϕ,ψ) indicated that there were no torsion angles falling in disallowed regions.

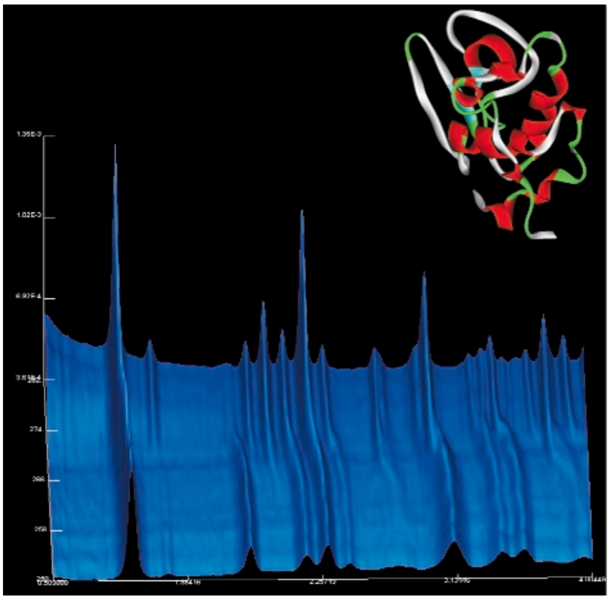

Fig. 33: Diffraction profiles plotted as a function of temperature (vertical axis) collected while warming the TEWL sample through the freezing transition at beamline ID11. Inset: Refined conformation of TEWL (pH 6.0) at RT illustrated as ribbon.

Low temperature experiments indicated how strategies for cryocooling and cryoprotecting samples might be more easily developed with powdered samples. In this case, we have observed a significant contraction in TEWL upon freezing (**Figure 33**). Interpretation of the very low-resolution data obtained below the freezing point of the mother liquor would seem to indicate that the channels in the structure expand significantly and the protein becomes packed much more closely together.

These results illustrate that powder diffraction methods can provide a wealth of complementary information about the structure of protein crystals. Molecular replacement techniques can be used to find out how the molecule packs into a unit cell for a particular structural modification. The molecular structure may also be refined by using stereochemical restraints in addition to the usual Rietveld method for powder profile refinement.

References

[1] R.B. Von Dreele, *J. Appl. Cryst.* **32**, 1084-1089 (1999).
[2] R.B. Von Dreele, *Acta Cryst.* D**56**, 1549-1553 (2000).

Principal Publications and Authors

I. Margiolaki, (a), J.P. Wright (a), A.N. Fitch (a), G.C. Fox (a) and R.B. Von Dreele (b), *Acta Cryst. D, accepted*.
(a) ESRF
(b) ARGONNE, IL 60439 (USA)

Growth and Dynamics of Metals and Alloys

In situ Measurement of Dynamic Precipitation in an Al-Zn-Mg-Cu Aluminium Alloy

Aluminium alloys are frequently alloyed to give rise to precipitation hardening, increasing the strength of these light alloys to more than 600 MPa. It is known that the presence of dislocations modifies the precipitation reaction profoundly in such materials, promoting heterogeneous precipitation of a stable phase, whereas the material free of crystalline defects experiences the formation of metastable precursors [1] such as the Guinier Preston (GP) zones in Al-Cu alloys.

When dislocations move into a supersaturated solid solution (when it is being plastically deformed), a significant acceleration of the precipitation kinetics can be observed. Although this phenomenon is well known at high temperatures (above 300°C) [2], where diffusion is very fast, it was not known whether this happens at ambient temperatures. In fact, the precipitates that form during static ageing (*i.e.* without plastic deformation) at room temperature are extremely small, and can only be observed using small-angle scattering techniques.

We have studied dynamic precipitation at ambient temperature in an Al-Zn-Mg-Cu alloy (alloy 7010, a type used for airplane wings), quenched from 475°C to room temperature. Precipitate size and volume fraction were determined by small-angle X-ray scattering (SAXS) performed on the D2AM (**BM02**) beamline at an energy of ~8 keV. Plastic deformation has been performed *in situ* on the 100 μm thick samples, controlling the amount of deformation by monitoring the sample transmission

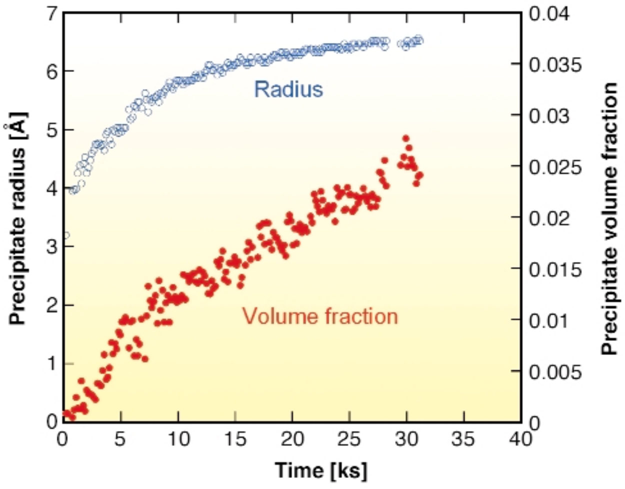

Fig. 34: Evolution of the precipitate size and volume fraction at ambient temperature following a quench from 475 °C (SAXS measurements).

during the test. X-rays are collected by a CCD camera and a radial average is performed to obtain normalised scattering intensity profiles.

After quenching, the material gradually evolves forming fine scale precipitates (GP zones containing all three alloying elements) ; the nucleation radius is about 0.5 nm, and the volume fraction evolves in an hour to more than 2% (**Figure 34**).

During straining, a fast increase in scattered intensity is observed (**Figure 35**), which is evidence for the occurrence of precipitation. However, this precipitation has to be compared to that which occurs if the sample is not deformed on the same time scale. Figure 35b shows that the dynamic precipitation process is almost an order of magnitude faster than static ageing. Moreover, we have characterised a strong negative strain rate sensitivity of this phenomenon: above a strain rate of ~ 5. 10^{-3} s^{-1}, it becomes almost negligible. This strain rate sensitivity is coherent with a mechanism similar to dynamic strain ageing [3]: precipitates form during the waiting time of dislocations at obstacles, which itself depends on the strain rate.

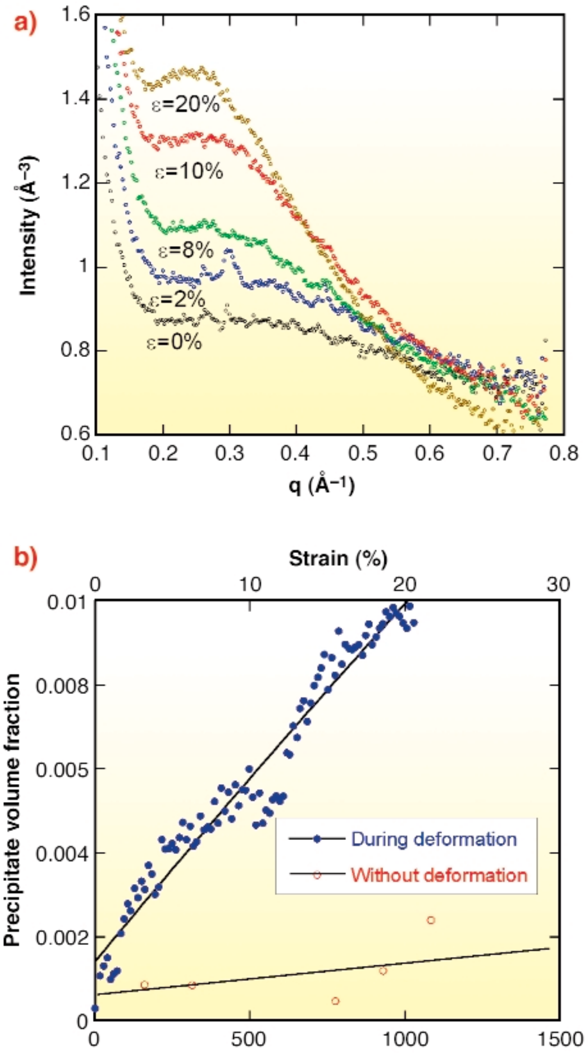

Fig. 35: (a) SAXS profiles as a function of plastic strain show evidence for the apparition of small precipitates; (b) the precipitate volume fraction is plotted both as a function of strain and time. The latter presentation enables the comparison with static precipitation (data from Figure 34), showing the large increase in precipitate kinetics associated with the dynamic precipitation.

The direct evidence of dynamic precipitation is an important step in understanding some remarkable properties of supersaturated solid solutions, and notably the very high strain hardening rate (slope of the stress-strain curve) observed [4], which is twice the value predicted by the accepted internal variable theory. Precipitates formed during straining participate subsequently to the flow stress. The negative strain rate sensitivity of dynamic precipitation also explains the corresponding negative strain rate sensitivity of the strain hardening rate.

References

[1] F.C. Larché, in *Dislocations in Solids*, North-Holland Publ. Co, Amsterdam, Netherlands, **4**, 135 (1979).
[2] E. Evangelista, H.J. Mcqueen, and E. Cerri, in *Proc. of the 13th Riso Int. Symp. on Mat. Sc.,* Risø National Laboratory, Roskilde, Denmark, 265 (1992).
[3] L.P. Kubin, and Y. Estrin, Y., *Acta Metall. Mater.* **38** (5) 697 (1990).
[4] W.J. Poole, and H.R. Shercliff, *Mat. Science Forum*, **217-222**, 1287(1996).

Principal Publication and Authors

A. Deschamps (a), F. Bley (a), F. Livet (a),D. Fabregue (a), L. David (b), *Phil. Mag. A* **83** (6), 677-692 (2003).
(a) LTPCM / INPG (France)
(b) GEMPPM, INSA Lyon (France)

Watching the Growth of Bulk Grains during Recrystallisation of Deformed Metals

When a material is deformed plastically, excess line defects (dislocations) and some excess point defects are introduced into the material. The density of these excess defects can be reduced by means of annealing. One of the basic processes taking place during annealing is recrystallisation [1]. Although resembling crystallisation, recrystallisaton is a very different process. The differences relate to the fact that recrystallisation occurs in an already solid crystalline material, and thus the atoms have to move from one lattice arrangement in the deformed material into a new and more perfect one.

The 3DXRD microscope [2] situated at beamline **ID11**, which has been developed in a collaboration between the ESRF and Risø National Laboratory, facilitates non-destructive observations of structural changes in the bulk of materials. Recently, the growth of individual

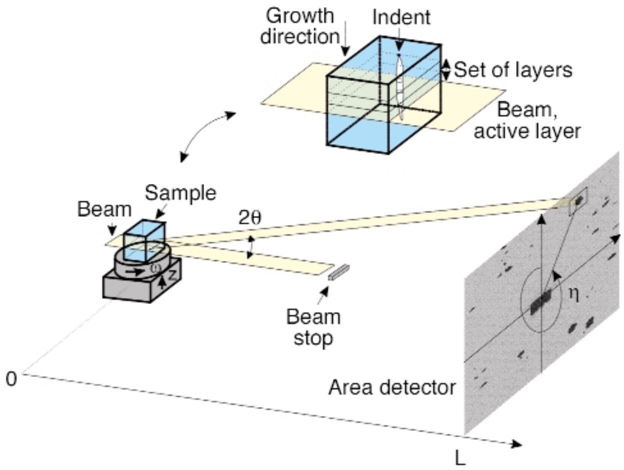

Fig. 36: Sketch of the experimental setup. Co-ordinate system (x,y,z) and angles (ω,2θ,η) are defined. The x-axis is along the beam direction, the y-axis is transverse to the beam direction and the z-axis is normal to the beam plane. The insert shows the principle of obtaining a "snapshot" of the grain by repeatedly recording an oscillation photograph followed by a vertical translation of the sample stage.

recrystallising grains have been filmed *in situ* as a function of annealing time in the bulk of deformed Al single crystals. A planar beam shape with dimensions 5 µm vertically and 600 µm horizontally was used to record a "snapshot", *i.e.* a stack of cross sections constituting the full three dimensional shape of the individual recrystallising grain (see schematic view of the experimental setup in **Figure 36**). By repeating this procedure during an annealing period, a four dimensional measurement, *i.e.* three spatial dimensions and one time dimension, of the recrystallising grain was obtained, as shown in **Figure 37**. All the grains measured so far exhibited irregular movements contradicting the assumption of smooth growth in the classical models of recrystallisation for the chosen sample system. The information content provided in this new type of measurement, given by the position of individual grain boundary segments, the crystallographic orientation of the recrystallising grain and the average orientation of the surrounding deformed microstructure, makes it possible to probe the mechanisms of recrystallisation locally.

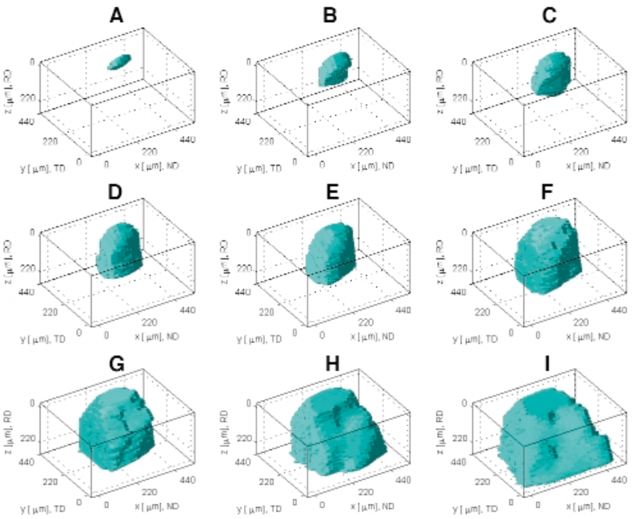

Fig. 37: Storyboard of the expansion of the grain in the sample reference system. In total 73 "snapshots" were taken during 30 hours of annealing at temperatures in the range 280°C to 310°C. The storyboard contain "snapshots" 1, 12, 17, 27, 39, 49, 59, 72 and 73 shown in figures A to I. At different times, different parts of the grain were leading in the expansion.

References

[1] E.g. "Recrystallisation – Fundamental Aspects and Relation to Deformation Microstructure", *Proc. 21st Risø Int. Symp. on Materials Science*, Edited by N. Hansen *et al.*, Risø, Denmark (2000).

[2] H.F. Poulsen *et al.*, *J. Synchrotron Rad.* **4**,147-154 (1997).

Principal Publication and Authors

S. Schmidt (a), S.F. Nielsen (a), C. Gundlach (a), L. Margulies (a,b), X. Huang (a), D. Juul Jensen (a), *Science* **305**, 229–232 (2004).

(a) Center For Fundamental Research: Metal Structures in Four Dimensions, Risø National Laboratory, Roskilde (Denmark)

(b) ESRF

Measuring Strain Distributions in Amorphous Materials

Diffraction methods have become standard in the characterisation of stress and strain fields in crystalline materials. To our knowledge, characterisation of strain in amorphous materials by diffraction methods has not been reported. This is remarkable, since their scope within materials science and engineering parallels that of crystalline materials. Most ubiquitously, polymer glasses are used in applications from medicine to transport to space flight. At present localised strain information is only available from surface probes such as optical or electron microscopy. This is unfortunate since surface and bulk characteristics in general differ. Hence, to a large extent, the assessment of strain distributions relies on untested models.

Here we present a universal diffraction method based on hard X-rays for characterising bulk stress and strain fields in amorphous materials. The transmission type set-up involves a focused monochromatic beam, an area detector and acquisition of images while rotating the sample around one axis. Using correlation functions, minute shifts in local maxima are determined in reciprocal space as well as direct space, that is in the S(Q) and g(r) profiles, respectively. The components of the strain tensor are determined with a resolution of 10^{-4}.

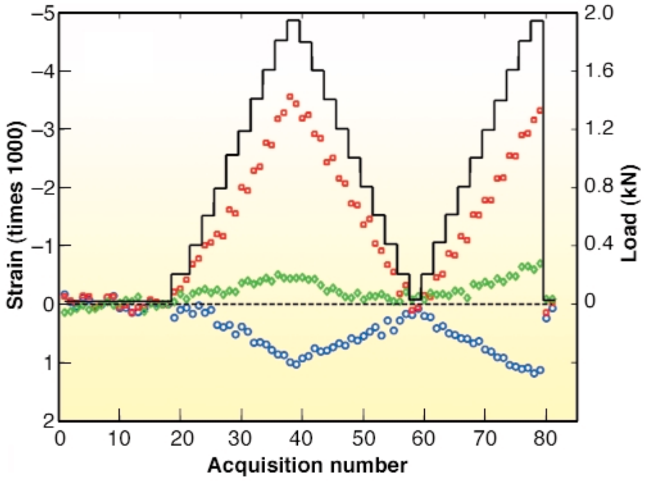

Fig. 38: Evolution of the axial (red), transverse (blue) and in-plane shear (green) strain components during compression of a homogeneous bulk metallic glass. The external load is indicated by the line and referring to the scale at the right.

The method was verified by *in situ* compression experiments on a bulk metallic glass (BMG) performed at beamline **ID15B**. Shown in **Figure 38** are the resulting axial, transverse and shear strains during two consecutive loading cycles, as derived from the first maximum in S(Q). Probing the strain on a length scale of ~10 Å in this way, the axial response for the homogeneous specimen is found to be identical to the macroscopic strain evolution. By comparison, similar plots based on the shifts of the first maxima in g(r) demonstrated that the atomic next-neighbour bonds are 2.7 times stiffer due to structural rearrangements at the 4-10 Å scale. Mapping strain fields is achieved by scanning the specimen, as illustrated in the example of **Figure 39**. Additional work on partially crystalline BMGs demonstrated that the method is applicable also to composites comprising an amorphous matrix and crystalline inclusions.

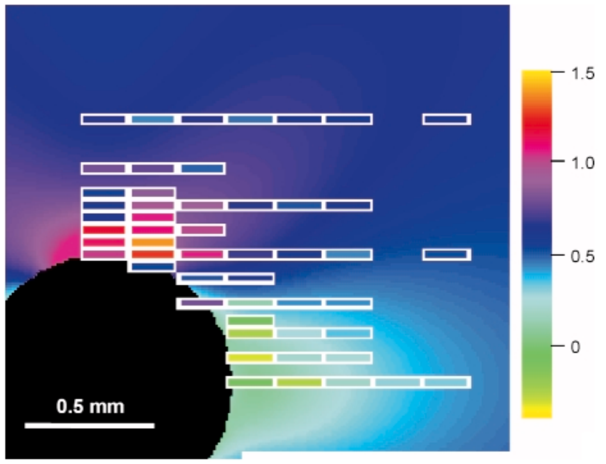

Fig. 39: The axial strain field around a circular hole in a 2 mm thick plate of a bulk metallic glass at a compressive stress of 390 MPa acting in the horizontal direction. Shown are the results from the X-ray diffraction experiment (boxes) as well as the result of an analytical model (background) – both with reference to the colour code to the right (lattice strain in %).

Authors

H.F. Poulsen (a), J.A. Wert (a), J. Neuefeind (b), V. Honkimäki (c) and M.Daymond (d). *Nature Materials* **4**, *33-36* (2005).

(a) Risø National Laboratory, Roskilde (Denmark)
(b) SNS, Oak Ridge National Laboratory (U.S.A.)
(c) ESRF
(d) ISIS, Rutherford Appleton Laboratory (U.K.)

Revealing Dynamics in Alloys by X-ray Photon Correlation Spectroscopy

Scattering of coherent X-rays at a disordered sample produces a highly-modulated diffraction pattern, a so-called speckle pattern. Such a graininess shows up in the superstructure peak of an alloy if antiphase domains are present in the coherently illuminated single crystalline sample volume [1]. Dynamics in the sample gives rise to intensity fluctuations *I(t)* in the speckle pattern that are measured and analysed by evaluating the correlations in the signal. Hence the name X-ray photon correlation spectroscopy. Usually the autocorrelation function of *I(t)* is calculated to gain information about the underlying dynamics, which works extremely well in the case of fast dynamics. In the case of slow dynamics, however, fluctuation analysis [2] and its extension, detrended fluctuation analysis (DFA), respectively, turns out to be a more appropriate approach. The big advantage of DFA is the ability to

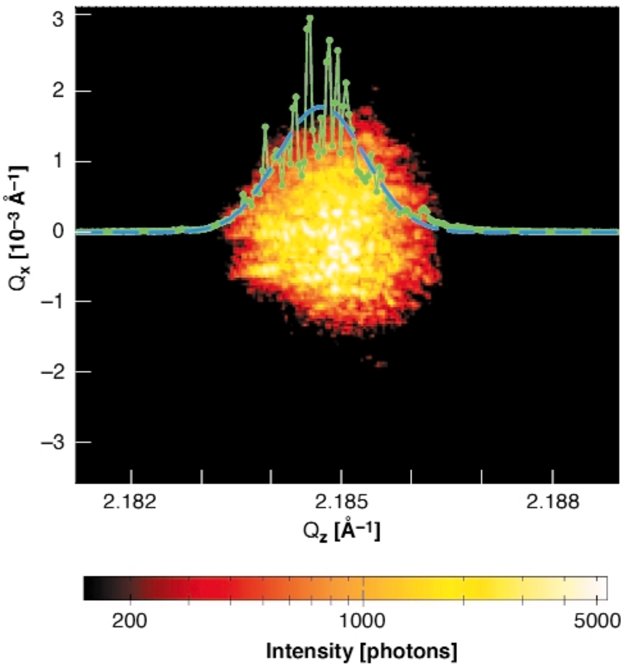

Fig. 40: Sum of two hundred CCD images of the (100) superstructure peak of Co$_{60}$Ga$_{40}$ at room temperature (no dynamics present). The green line shows a slice (Q_x = 0) through the peak exhibiting strong intensity fluctuations. The dashed blue line indicates a Gaussian fit to the intensity distribution – this would be the result of scattering with conventional, incoherent X-rays.

"detrend" the data, *i.e.* to account for spurious correlations caused, for example, by a non-constant overall intensity or small drifts in the experimental setup during the measurement. Thereby, trends of order *n-1* in the data are removed by DFA*n*, *i.e.* DFA*1* removes stepwise constant trends, DFA*2* stepwise linear trends and so on.

At **ID10A**, we performed XPCS measurements of antiphase domain dynamics in the B2-ordered $Co_{60}Ga_{40}$ intermetallic phase. **Figure 40** shows the (100) superstructure peak at room temperature, where no dynamics is measurable and thus a pronounced *static* speckle pattern is obtained. For investigating *dynamics* the sample was measured at temperatures between 690 K and 1060 K. Time series of CCD images were taken and evaluated using DFA up to the third order (DFA3). In doing so, so-called fluctuation functions *F(t)* are calculated. By fitting a power law $F(t) \propto t^{\alpha}$ the fluctuation exponent α is obtained, characterising the correlations. Here, we are mainly interested in distinguishing two types of fluctuation-scaling behaviour, uncorrelated behaviour ($\alpha = 0.5$) and random walk (RW) behaviour ($\alpha = 1.5$). The latter is introduced by the internal dynamics of the sample. Movement of antiphase boundaries is accomplished by diffusion of atoms at the antiphase boundaries. Since the diffusing atoms perform a RW the phases of successively scattered photons also perform a RW, which manifests in RW fluctuations of the speckle intensities.

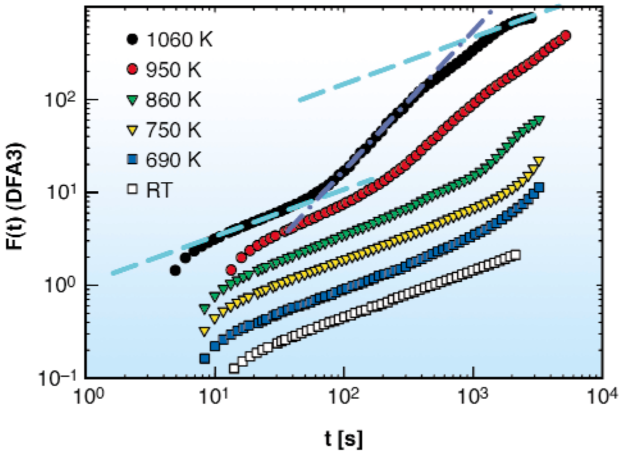

Fig. 41: Fluctuation functions *F(t)* from third-order DFA of speckle intensity fluctuations in the (100) superstructure peak of $Co_{60}Ga_{40}$ at increasing temperatures, double-logarithmic plot. Slope $\alpha = 0.5$ (denoted by the dashed cyan lines) indicates uncorrelated fluctuations, slope $\alpha = 1.5$ (denoted by the dash-dotted mauve line) indicates random walk fluctuations.

Figure 41 shows the DFA*3* fluctuation functions obtained for the (100) superstructure peak. For elevated temperatures RW behaviour is obtained on long timescales. Due to an incoherent background, uncorrelated fluctuations dominate on shorter timescales. At the three highest temperatures, a tendency for uncorrelated behaviour can also be found on the longest timescales measured. This is caused by the fact that every phase information is modulo 2π. Once an additional phase difference of 2π between interfering scattered waves is exceeded the situation becomes indistinguishable from the initial state and $\alpha = 0.5$ is obtained again.

The higher the temperature is, the earlier the RW correlations start to dominate the correlation behaviour. This temperature dependence gives access to the activation energy of the underlying process, the movement of antiphase boundaries. In good agreement with Monte Carlo simulation results, we find the migration energy for atoms diffusing at antiphase boundaries to be approximately a quarter of the migration energy for bulk diffusion of Co atoms that dominate the diffusion behaviour in the temperature range investigated.

In conclusion, we have successfully applied detrended fluctuation analysis to XPCS data. By following the dynamics in the superstructure peak of a $Co_{60}Ga_{40}$ single crystal as a function of temperature, we have determined the activation energy for the mobility of the antiphase boundaries. Our study underlines the potential of the method for investigations of slow dynamics in hard-condensed matter.

References

[1] M. Sutton, S.G.J. Mochrie, T. Greytak, S.E. Nagler, L.E. Bermann, G.A. Held, G.B. Stephenson, *Nature (London)* **352**, 608 (1991).

[2] L.-M. Stadler, B. Sepiol, R. Weinkamer, M. Hartmann, P. Fratzl, J.W. Kantelhardt, F. Zontone, G. Grübel, G. Vogl, *Phys. Rev. B* **68**, 180101(R) (2003).

Principal Publication and Authors

L.-M. Stadler (a), B. Sepiol (a), J.W. Kantelhardt (b), I. Zizak (c), G. Grübel (d,e), G. Vogl (a), *Phys. Rev. B* **69**, 224301 (2004).
(a) Universität Wien (Austria)
(b) Martin-Luther-Universität Halle-Wittenberg (Germany)
(c) Hahn-Meitner-Institut Berlin (Germany)
(d) ESRF
(e) Deutsches Elektronen Synchrotron, Hasylab (Germany)

Extreme Conditions

A New High-pressure Isostructural Phase Transition in Osmium

Recently, there has been much interest in the nature of Lifshitz [1] or electronic topological transitions (ETT). This type of phase transition arises when distortion of the electronic band structure results in a topological singularity of the Fermi surface. Interestingly, while the experimental data remain somewhat ambiguous, most simulations suggest that such an ETT in zinc does indeed exists in this pressure range. Thus, one might expect that other hcp metals should exhibit similar phenomena. Experimental and theoretical results have shown the existence of small local maxima in the band structure just above the Fermi energy near the high-symmetry point L on the zone boundary in osmium. Thus, the potential exists that these structures might fall below the Fermi energy upon compression and give rise to an ETT.

In order to clarify these points, we have undertaken an experimental study of the EoS (equation of state) of osmium using angle-dispersive X-ray diffraction with ultra-high accuracy.

Angle-dispersive X-ray diffraction measurements were recorded at the high-pressure diffraction beamline **ID09A**. In order to minimise the errors on the equation of state, a total of 33 diffraction patterns were recorded between 0 and 20 GPa, and 10 more points between 20 and 75 GPa in both Ne and He pressure generating media (**Figure 42a**).

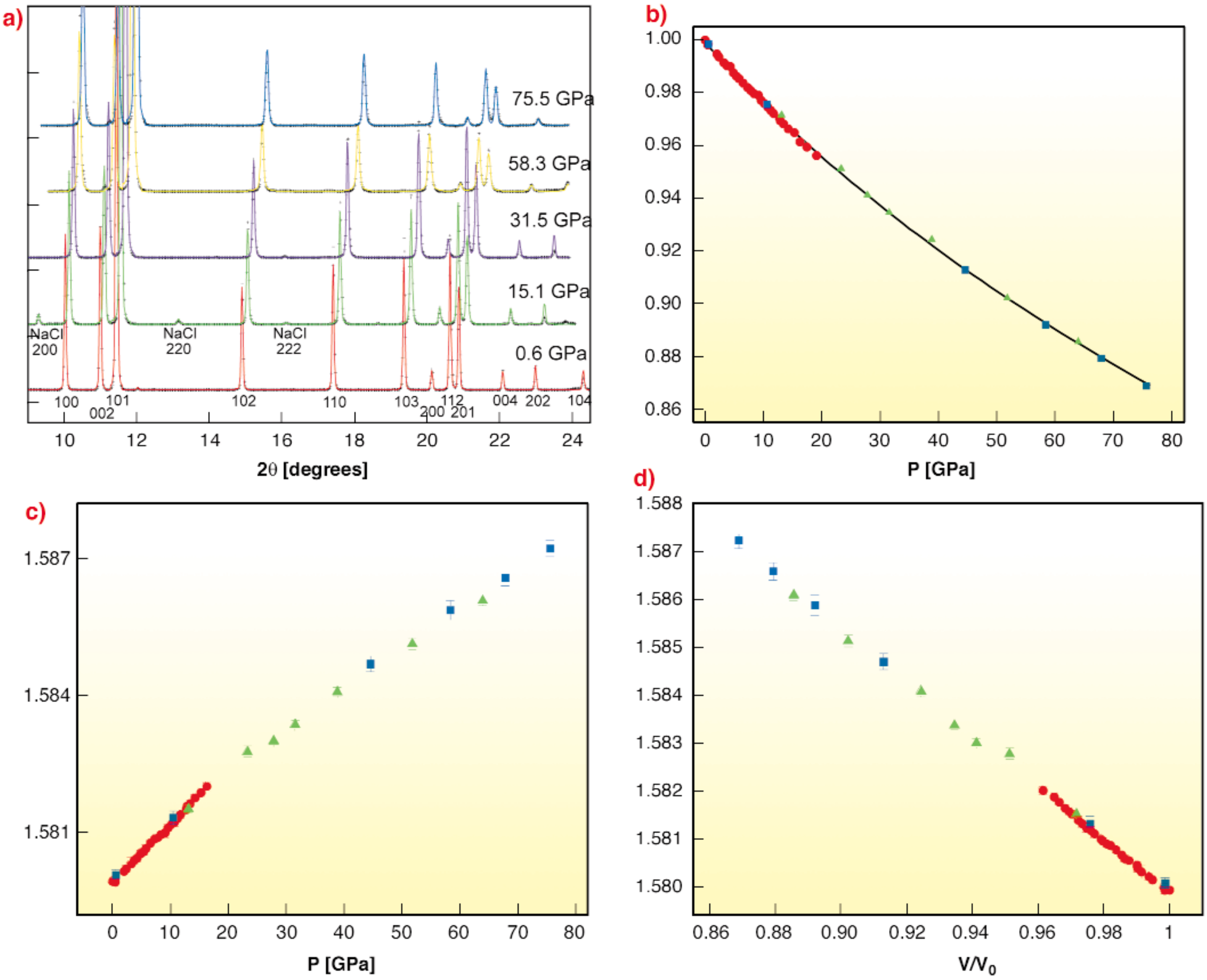

Fig. 42: a) Integrated angle-dispersive diffraction patterns recorded at various pressures. The experimental data is represented by a + symbol, and the curves are obtained from a Rietveld structural refinement of the data. The osmium reflections are labelled on the lowermost spectrum. NaCl reflections are labelled on the second spectrum. b) The isothermal equation of state of Osmium at 300 K. The different symbols correspond to the three independent loadings (the size of the symbol is greater than the experimental errors both on pressure and volume). The solid curve is a third-order Birch-Murnaghan fit to the data yielding $K_0 = 410.9 \pm 1.2$ GPa, $K_0' = 3.97 \pm 0.04$, and $V_0 = 27.949 \pm 0.002$ A^3. The c/a ratio of osmium versus pressure (c), and volume (d). The linear fits to the c/a vs. pressure data yield $c/a = 1.57993 + 1.25049.10^{-4}\ P + O(P^2)$ over the pressure range 0 to 25 GPa and $c/a = 1.58071 + 8.65348.10^{-5}\ P + O(P^2)$ from 25 GPa to the highest pressure achieved in the study. The linear fit to the c/a vs. reduced volume data yields $c/a = 1.63504 - 0.0552\ (V/V_0) + O(V^2)$.

The EoS derived from our data is shown in Figure 42b using the third-order Birch-Murnaghan equation; $P = 3/2K_0[(V/V_0)^{-7/3}-(V/V_0)^{-5/3}]\{1+3/4(K_0'-4)[(V/V_0)^{-2/3}-1]\}$, where V is the volume, V_0 is the zero pressure volume, K_0 is the isothermal bulk modulus and K_0' its first pressure derivative. Using a stochastic minimisation algorithm on the third-order Birch Murnaghan EoS, which gives a more robust estimate of the parameters as well as the correlation matrix in the case of incompressible materials at low volumetric compression, we find $K_0 = 410.9 \pm 1.2$ GPa, $K_0' = 3.97 \pm 0.04$, and $V_0 = 27.949 \pm 0.002$ A^3. Our new results show that the bulk modulus of osmium is actually 8% smaller than that of diamond, contrary to the conclusions of Cynn *et al.* [2], with K_0' close to 4 as is to be expected for a well-behaved incompressible material.

Our new data present a most surprising and novel result; although a simple analysis of the EoS indicates that there are no first order structural transitions, a more detailed analysis of the c/a ratio as a function of pressure (Figure 42c) shows an interesting feature around 25 GPa. Two distinct compression regimes can be identified below and above 25 GPa. Importantly, these two regimes are not resolvable as a function of volume (Figure 42d) but only as a function of pressure (Figure 42c). When plotted as a function of volume, the c/a ratio exhibits a monotonous and continuous behaviour (Figure 42d) over the entire pressure range, and can be approximated by a unique linear function within the error bars. This means that the modulus, namely $\delta P/\delta V$, must also exhibit the same discontinuity as seen in the function c/a (P). These effects likely arise for changes in the electronic structure on compression and could be the signature of a Lifshitz transition, where the first derivative of the compressibility presents a discontinuity at the transition pressure and the second derivative is not defined. Such transitions arise by the passage of the Fermi surface through a topologic singularity [1]. In the case of osmium, we suggest that the anomaly may arise from the passage of the maxima in band h_7 below the Fermi energy with compression resulting in the collapse of the small hole-ellipsoid. Finally, our findings show the importance of high-accuracy diffraction measurements and how these types of studies on third-generation synchrotron sources can help pinpoint, isolate, and even unveil peculiar behaviour in materials that could otherwise not be observed.

References

[1] I.M. Lifshitz, Zh. Eksp. Teor. Fiz. 38, 1569 *Sov. Phys. JETP* **11**, 1130 (1960).

[2] H. Cynn, J.E. Klepeis, C.-S. Yoo, and D.A. Young, *Phys. Rev. Lett.* **88**, 135701 (2002).

Authors and Principal Publication

F. Occelli (a), DL. Farber (a), J. Badro (a,b), CM. Aracne (a), D.M. Teter (c), M. Hanfland (d), B. Canny (e), B. Couzinet (e), *Physical Review Letters* **93** (10): Art. No. 109901 Sep 3 (2004).

(a) Earth Science Division, Lawrence Livermore National Laboratory (USA)
(b) Laboratoire de Minéralogie Cristallographie (UMR CNRS 7590), Institut de Physique du Globe de Paris, Université Paris VI (France)
(c) Organization 9753, Sandia National Laboratory (USA)
(d) ESRF
(e) Laboratoire de Physique des Milieux Condensés (UMR CNRS 7602), Université Paris VI (France)

Single-bonded Cubic Form of Nitrogen

Nitrogen usually consists of molecules where two atoms are strongly triple-bonded. Here, we report on a new form of nitrogen where all atoms are connected with single covalent bonds, similar to carbon atoms in diamond. The compound was synthesised directly from molecular nitrogen at temperatures above 2,000 K and pressures above 110 GPa using a laser-heated diamond cell. From X-ray and Raman scattering we have identified this as the long-sought-after polymeric nitrogen with the theoretically predicted cubic gauche structure (cg-N). This cubic phase has not been observed previously in any element. The phase is a hard substance with bulk modulus ≈ 300 GPa, characteristic of strong covalent solids. The cg-N represents a new class of single-bonded nitrogen materials with unique properties such as energy capacity: more than five times that of the most powerfully energetic materials.

It was predicted that at high pressure, solid molecular nitrogen would transform to an atomic solid with a single-bonded crystalline structure called polymeric nitrogen [1,2]. Experimentally, a new, dark, apparently non-molecular phase has been recently found above 180 GPa at 80 K [3] and then at room and elevated temperatures [4,5]. Some properties of this black phase are close to that predicted for the polymeric nitrogen; that is, the value equilibrium pressure (about 100 GPa), and a huge hysteresis enabling the black phase to be recovered at ambient pressure and low temperatures. However, there are no convincing data for cg-N or any other phase with an extending polymeric network.

We synthesised polymeric nitrogen in numerous runs at $T > 2{,}000$ K at $P > 110$ GPa. The cell was specifically designed for X-ray diffraction measurements of such a weak scatterer as nitrogen (**Figure 43a**). We used c-BN gasket which produces only a few weak peaks, and the 1-µm thick boron plate (a very weak scatterer) as an absorber of the laser radiation. The highly-focussed X-ray beam of bealine **ID09** was used to scan the sample. We fitted the measured spectra to a mixture of cg-N and c-BN (Figure 43b). Parameters from Rietveld refinement for cg-N were: space group *I* 213, $a_0 = 3.4542$ Å, sites 8*a*, $x = 0.067$. The cg-N structure is shown

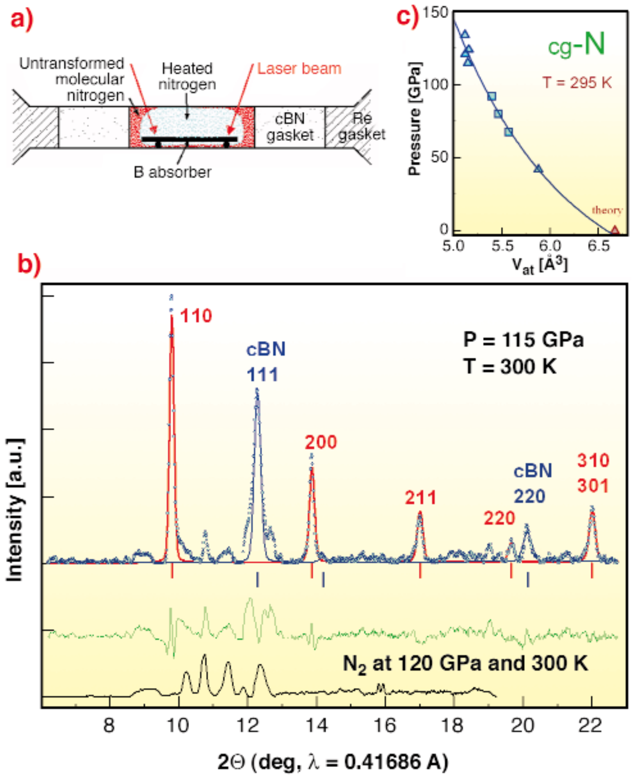

Fig. 43: X-ray diffraction measurements of nitrogen after heating to 2,600 K at 140 GPa. (a) A cross-section of the sample arrangement. X-ray diffraction was measured with a monochromatic X-ray beam with 0.4168 Å wavelength focused to a spot of ~5 x 5 μm. Diffraction spectra were taken across the culet in 5 μm steps. The spectrum shown in (b) was from the centre of the sample which was oscillated at ±1° around the vertical axis to average reflections. Positions and intensities of the peaks were fitted using Rietveld refinement for the cg-N phase (red line) and c-BN (blue solid line). The green spectrum is the difference between the refinement and the experimental spectrum. This molecular phase was not refined because its structure was not known. For comparison, a spectrum of another, unheated sample at 120 GPa is shown at the bottom. (c) The EOS of the cubic gauche structure (cg-N). The experimental points were fitted with BM EOS with B_{42} = 460.72 GPa, B'_{42} = 4.0, V_{42} = 5.878 Å^3 taken at 42 GPa. Extrapolation of this EOS to zero pressure gives a volume of cg-N structure about 6.6 Å^3 - in excellent agreement with theoretical predictions of 6.67 Å^3 [2]. The zero-pressure bulk modulus B_0 calculated using different forms of EOS was found to lie in the range 300 – 340 GPa.

schematically in **Figure 44**. All nitrogen atoms are three-fold coordinated and bond-lengths are the same for all pairs of bonded atoms. At a pressure of 115 GPa, the bond length is 1.346 Å. We also determined the cg-N structure on decreasing pressure and found its bulk modulus $B_0 \approx 300$ GPa.

References

[1] A. K McMahan, and R. LeSar *Phys. Rev. Lett.* **54,** 1929 (1985).
[2] C. Mailhiot, *et al Phys. Rev. B* **46,** 14419 (1992).
[3] M. Eremets. *et al Nature* **411,** 170 (2001).

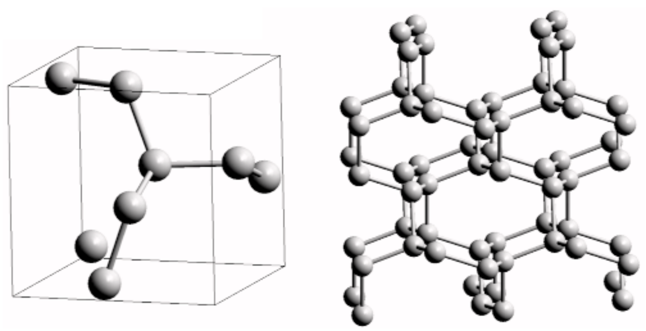

Fig. 44: The cg-N structure. Each atom of nitrogen is connected to three neighbours with three single covalent bonds. The primitive cell is shown on the left, and an extended structure of the polymeric nitrogen is shown on the right.

[4] A.F. Goncharov *et al Phys. Rev. Lett.* **85,** 1262–1265 (2000);
[5] E. Gregoryanz *et al Phys. Rev. B* **64,** 052103 (2001), ibid *B* **66,** 224108 (2002).

Principal Publication and Authors

M.I. Eremets (a), A.G. Gavriliuk (abc), I.A. Trojan (ac), D.A. Dzivenko (a), R. Boehler (a), *Nature Materials* **3**, 558 (2004).
(a) Max Planck Institute für Chemie, Mainz (Germany)
(b) A.V.Shubnikov Institute of Crystallography of Russian Academy of Sciences, Moscow (Russia)
(c) High Pressure Institute of Russian Academy of Sciences, Troitsk (Russia)

Reaction of Iron and Silica at Core-Mantle Boundary Conditions

The boundary between the Earth's mantle and core (so-called D" layer) is interesting because of the large contrast in properties across this region. The seismologically observed changes in density and sound wave velocities, for example, are significantly (2-3 times) greater than across the air-rock (or air-sea water) interface at the Earth's surface. Moreover, the difference in materials across the boundary, with predominantly crystalline rock above and liquid iron alloy below is among the most profound in the Earth. In this sense, the core-mantle boundary can be considered the primary "surface" of the planet, and is simply because of its remoteness that it has attracted less study than the top of the Earth's crust. There is a number of geophysical, geochemical, seismological arguments which link processes at D" layer and at the surface of the Earth. For example, super-plumes originated from the core-mantle boundary (CMB) manifested themselves as hot-spot volcanoes on Hawaii.

The Moon and Sun cause the Earth's lunisolar precession and a so-called nutation of the Earth's rotation axis, *i.e.* small variations in the position of the Earth's rotation axis. It was recognised recently that the amplitude of the Earth's nutation is out-of-phase with tidal forcing produced by the

Sun and Moon. A potential explanation for this observation could be the presence of a thin layer of a material with anomalously high electrical conductivity in the base of the Earth's mantle. What could be the nature of this layer?

To elucidate the composition and properties of the D" layer at the core-mantle boundary, understanding of chemical reactions between liquid iron and the complex Mg-Fe-Si-Al-oxides of the Earth's lower mantle is required. Experimental problems arise due to extremely high pressures (over 1 400 000 atmospheres, or 140 GPa) and temperatures (over 3000°C), which characterise this region. We studied an interaction between iron and silica (SiO_2) in electrically- and laser-heated diamond anvil cells and in a multianvil apparatus at pressures up to 140 GPa and temperatures over 3500°C, simulating conditions down to the CMB. At pressures below 40 GPa and high temperatures, iron and silica react forming iron oxide and iron-silicon alloy with up to 5 wt% Si (**Figures 45 and 46**).

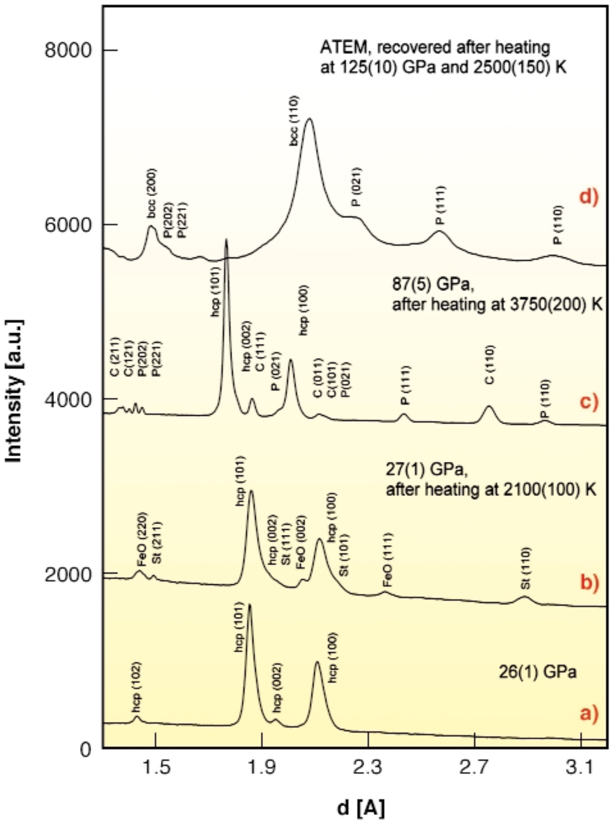

Fig. 45: Representative angle-dispersive X-ray (a-c) and electron (d) diffraction patterns obtained in experiments with iron and amorphous silica as starting materials. (a) At 26(1) GPa before heating of the sample only diffraction lines of ε-Fe (marked as hcp) are present. (b) After heating at 2100(100) K silica crystallised in stishovite (St) and new lines of wüstite (FeO) appeared. (c) Heating of iron and amorphous SiO_2 mixture at 85(5) GPa and 2400(150) K resulted just in crystallisation of silica phases ($CaCl_2$- and α-PbO_2-structured, marked (C) and (P), correspondingly, but wüstite was absent. (d) Selected area electron diffraction spectrum of the material recovered after heating at 125(10) GPa and 2500(150) K. Figure 45d shows only the presence of α-PbO_2-type (P) silica phase and iron (bcc).

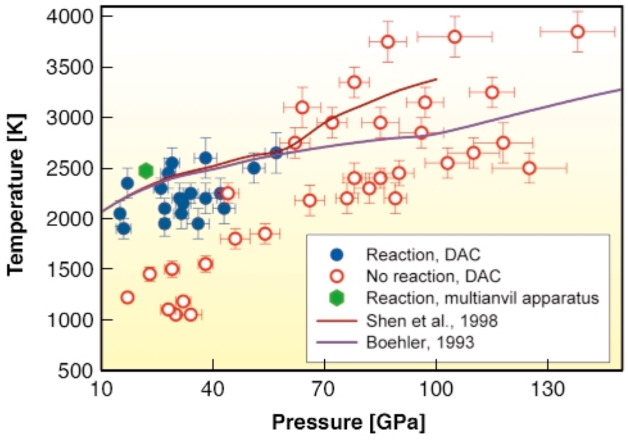

Fig. 46: Experimental results on the chemical interaction of iron and silica. Filled blue dots show P,T conditions at which the reaction between iron and silica was observed, and open red circles – conditions at which the reaction does not occur. Green hexagon corresponds to observation of the reaction in multianvil experiments. Solid lines shows melting curve of iron according to Boehler (1993) (pink) and Shen *et al.* (1998) (dark-red).

However, at pressures of 85-140 GPa, iron and SiO_2 do not react and iron-silicon alloys dissociate into almost pure iron and the CsCl-structured (*B2*) FeSi compound (Figures 1 and 2). Experimental observations suggest that during formation and differentiation of proto-Earth, iron alloy, segregating in a deep magma ocean and thus containing several wt% Si would subsequently decompose into a mixture of Si-poor iron phase and silicon-rich *B2* phase in the core. The metallic silicon-rich *B2* phase, produced by this reaction, or produced at the CMB due to reaction between iron and silicate, is denser than the material of lower mantle and lighter than liquid iron in the Earth's outer core. So, iron silicide should accumulate at the CMB. It was found that high-pressure iron silicide phase *B2* FeSi is an electrically conducting material. The presence of *B2* FeSi at the base of Earth's lower mantle could explain the anomalously high electrical conductivity of this region and provide a key for understanding why the amplitude of the Earth's nutation is out-of-phase with tidal forcing.

Principal Publications and Authors

L. Dubrovinsky (a), N. Dubrovinskaia (a), F. Langenhorst (a), D. Dobson (a), D. Rubie (a), C. Geßmann (a), T. Le Bihan (b), W.A. Crichton (b), I. Abrikosov (c), B. Johansson (d), Nature, 422, 58-61, 2003; L. Dubrovinsky, N. Dubrovinskaia, F. Langenhorst, D. Dobson, D. Rubie, C. Geßmann, T. Le Bihan, W. A. Crichton, Phys. Earth Planet. Inter., 146, 243-247, 2004.

(a) Bayerisches Geoinstitut, Universität Bayreuth (Germany)

(b) ESRF

(c) Department of Physics and Measurement Technology, Linköpings University (Sweden)

(d) Condensed Matter Theory Group, Department of Physics, Uppsala University (Sweden)

Soft Condensed Matter

Introduction

The soft condensed matter highlights demonstrate the diversity of research being carried out at the soft condensed matter (ID02, ID10A/B and ID13) and several CRG beamlines. This diversity has promoted links to several neighbouring disciplines such as materials science, biology, and engineering.

Developments at beamline ID02 have included advances in time-resolved small- and wide-angle scattering (SAXS/WAXS) techniques. Weiss *et al.*, have demonstrated SAXS combined with modelling at the millisecond scale for micellar self-assembly. This was achieved through the combination of stopped-flow techniques with a state-of-the art gas-filled detector. Close links to protein crystallography are evident in the experiments by Casselyn *et al.*, who studied the onset of BMV virus crystallisation down to the critical nucleus. Also recently, Stribeck *et al.*, have been able to determine the autocorrelation function during the onset of polyethylene crystallisation in real time. This allows the first steps of mesophase formation to be “visualised”, which is of particular technological importance.

Ultra-small volumes and beam sizes are the realm of the microfocus beamline, ID13. Inkjet printing technology can deliver water droplets of 65 picoliters to precise locations without splashing. Lemke *et al.*, have used this technique to study the onset of starch granule hydration by *in situ* WAXS. The observation of a fast volume hydration within a few seconds can be explained by the porous nature of this important biopolymer. Naturally, ID13 has also been closely involved in the development of nanobeams at the ESRF. The use of 100 nm beams is already current practice. The report by Loidl *et al.*, demonstrates how such a beam can be used to study the strain field in a single carbon fibre across a bending zone.

The technique of X-ray photon correlation spectroscopy (XPCS) has been pioneered at ID10A. The highlight example concerns the study of ferrofluids containing core-shell particles. Robert *et al.*, were able to extract the hydrodynamic function, which contains information on solvent-mediated interactions between the colloidal particles, from SAXS and XPCS data. The results challenge existing colloidal hydrodynamic theories, which cannot provide an adequate description of these interactions.

Grazing-incidence diffraction (GID) is the speciality of beamline ID10B. The X-ray optical system of ID10B allows *in situ* studies on liquid surfaces, for example in a Langmuir trough. Breiby *et al.*, have studied the molecular ordering of poly(alkylthiophene) films on water. This also allowed them to study *in situ* doping by PF_6^-, which results in an insulating-conducting phase transition. *In situ* GID was also used by Berman *et al.*, to study the nucleation of CdS and Ag_2S nanocrystals at the air-solution interface.

The highlight that seems to have appealed the most to the general public has been the work carried out on chocolate by Peschar *et al.*. This is demonstrated by the unusually high number of mainstream press articles concerning this study. The work is being carried out at several CRG beamlines and involves wide- and small-angle scattering techniques. These results are being used to elucidate the complex phase behaviour of chocolate. The example reported below concerns the crystal structures of several cocoa butter triglycerides by powder diffraction on BM16 and BM01B.

C. Riekel

Soft Matter Self-assembly: Structure and Dynamics

Micellar Self-assembly on the Millisecond Timescale

Amphiphilic molecules possess a unique architecture with a hydrophilic head group and hydrophobic tail(s). When suspended in water, above certain critical concentration these molecules self-assemble into micelles thereby minimising the contact between hydrophobic tail and water. Depending on concentration, temperature and other thermodynamic parameters, a large variety of equilibrium structures such as spherical, cylindrical or disk-like micelles, bicelles, vesicles, and liquid-crystalline phases such as smectic, cubic, hexagonal, and nematic phases can be observed [1]. More recently, these self-assembling properties of amphiphilic molecules have been increasingly exploited in the fabrication of nanostructured materials, *e.g.* mesoporous systems with well-defined pore sizes. Understanding the dynamical aspects of the micellar self-assembly is often pivotal in their applications because the final state can vary depending on the kinetic pathway. The timescales of the underlying structural organisation may range from a millisecond up to weeks. Small-angle X-ray scattering (SAXS) is a powerful tool that can be used to elucidate the nano-scale structure of these micellar entities. By combining the high brilliance with state-of-the-art detector (RAPID), the very early stages of this self-assembly process, hitherto inaccessible to structural investigations, can be probed.

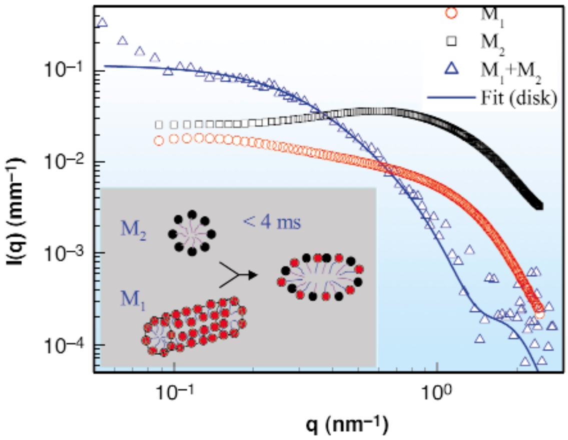

Fig. 47: SAXS intensities for 50 mM solutions of $C_{14}H_{29}N(CH_3)_2O$ (M_1) and $C_7F_{15}COOLi$ (M_2) and their mixture within the first 5 ms after rapid mixing. The continuous line represents a fit to disk-like mixed micelles. The inset depicts the corresponding structural change.

The micelle to vesicle transition is a typical example of micellar self-assembly [2]. For instance, the transition can be induced by rapid mixing (within milliseconds) of equimolar amounts of oppositely charged micelles with a stopped-flow device [3]. Quantitative SAXS data with millisecond range time resolution permits the intermediate states to be accurately modelled. **Figure 47** shows the very first step in the transformation of an equimolar mixture of zwitterionic and anionic micelles to vesicles (M_1 and M_2, respectively). The original micellar solutions contain short rod-like zwitterionic and spherical anionic micelles and they transform to disk-like micelles of twice the size within the mixing time (< 4 ms). **Figure 48** further depicts that the radius of these disk-like micelles evolves with time and they close to form unilamellar vesicles within a second. While the details of this transformation are beyond the scope here, it can be mentioned that the driving force is the unstable rim region of the disk-like micelles that generates a line tension which tries to bend the disk to a closed object. This tendency is counterbalanced by the bending energy of the amphiphilic bilayers that tries to keep them flat [2]. From the radius of the initial vesicles (or equivalently the final disk radius) the ratio between bending elastic constants and line tension of the bilayer can be determined.

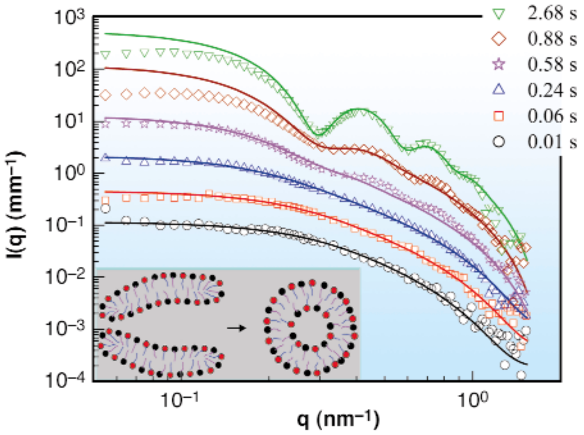

Fig. 48: The time evolution of SAXS intensity illustrating the growth of transient disk-like micelles over the first few hundred milliseconds after mixing and their transformation to unilamellar vesicles within a second. Continuous lines in each of three lower and upper curves represent disk-like micelles and unilamellar vesicles (shell), respectively. For the sake of clarity, the successive scattering curves have been multiplied by a factor √10. The inset depicts the corresponding structural change.

In summary, the original micelles transform to disk-like micelles in the mixing process. The disks grow in size over a few hundred milliseconds and then close to form vesicles within a second. At longer times the vesicles evolve further and become more polydisperse, but on a much slower timescale. The scattering data demonstrate that the structural changes occur in a very homogeneous and synchronised manner corresponding to a sharp transition. The millisecond time-resolution enables the identification of the different structural intermediates and their dynamics in this multi-step transition. The building blocks of many nano-structured systems are often templated vesicles whose structure is controlled by the dynamics of their formation. In this case for example the monodisperese vesicles are obtained within the first few seconds. Therefore, the micellar structural dynamics can be exploited for the fabrication of advanced complex colloidal materials.

References

[1] W.M. Gelbart, A. Ben-Shaul, and D. Roux, *Micelles, Membranes, Microemulsions, and Monolayers*, Springer-Verlag, New York (1994).
[2] H.T. Jung, B. Coldren, J.A. Zasadzinski, D.J. Iampietro and E.W. Kaler, *PNAS* **98**, 1353 (2001).
[3] S. Schmölzer, D. Gräbner, M. Gradzielski and T. Narayanan, *Phys. Rev. Lett.* **88**, 258301 (2002).

Principal Publication and Authors

T.M. Weiss (a), T. Narayanan (a), M. Gradzielski (b), C. Wolf (b), P. Panine (a), S. Finet (a) and W.I. Helsby (c), *Phys. Rev. Lett.* (2005), *accepted*.
(a) ESRF
(b) Lehrstuhl für Physikalische Chemie I, Universität Bayreuth (Germany)
(c) Daresbury Laboratory, Cheshire (U.K.)

Dynamic Behaviour of Magnetic Fluids

Magnetic fluids (ferrofluids) are suspensions of colloidal particles, bearing a giant magnetic moment, in a liquid carrier [1]. These systems are interesting for both fundamental (*i.e.* as model systems for dipolar fluids) and applied research and find numerous applications such as in loudspeakers and hard disks.

Dynamic Light Scattering (DLS) is a well-established technique used to investigate the dynamic behaviour of colloidal suspensions. However, it has two main limitations: multiple scattering (*i.e.* opacity to visible light) and a limited Q-range. These constraints render any DLS investigation on magnetic fluids impossible and consequently only a few experiments have been performed addressing their dynamic properties on mesoscopic length scales.

Dynamic X-ray techniques allow the limitations of DLS to be overcome. The dynamic behaviour of a novel magnetic fluid was studied on the Troïka beamline **ID10A**. The system investigated consists of charge-stabilised core-shell magnetic particles [2], with a $CoFe_2O_4$ magnetic core, surrounded by a silica (SiO_2) shell. **Figure 49** (left) shows a photograph of the opaque sample.

The system was initially studied by small-angle X-ray scattering (SAXS) in order to characterise the core-shell structure of the colloidal composite particles and to extract the static structure factor. The effective short-time diffusion coefficient D(Q) was then probed by X-ray Photon Correlation Spectroscopy (XPCS).

For interacting systems, the contribution of direct (Van der Waals, electrostatic and eventually magnetic dipolar interactions) to the static behaviour of the system can be determined by measuring S(Q). The dynamic behaviour is described by the Q-dependent diffusion coefficient D(Q) given by

$$D(Q) = \frac{D_0}{S(Q)} H(Q), \quad (1)$$

where D_0 is the Stokes-Einstein diffusion constant. D(Q) depends, via S(Q), on the direct interactions, but also on the indirect interactions mediated by the solvent. The indirect interactions are contained in the so-called hydrodynamic function H(Q).

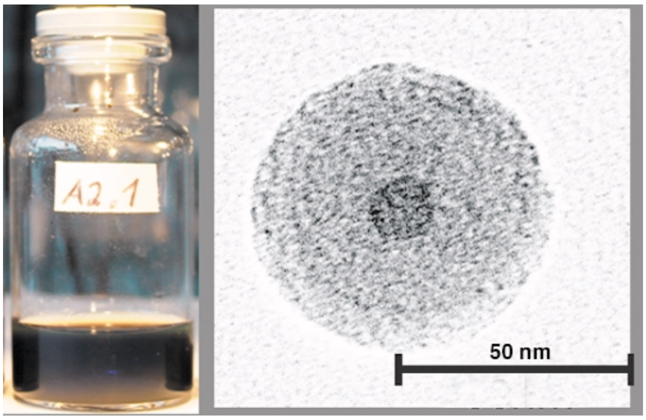

Fig. 49: (left) Photograph of the sample; (right) a TEM picture of a single core-shell particle.

The TEM image in Figure 49 (right) shows unambiguously the core-shell structure of a single particle. SAXS data provide a magnetic core-radius of 79 Å, a total core-shell radius of 356 Å and a size polydispersity of ΔR/R = 0.13. The static structure factor S(Q) without magnetic field (o in **Figure 50a**) is obtained from SAXS on a concentrated sample. The S(Q) peak indicates liquid-like ordering with a mean interparticle distance of 1550 Å. The Rescaled Mean Spherical Approximation (RMSA) was used to model S(Q), as indicated by the solid line, from which the effective number of charges per particle $Z = 250\ e^-$ was determined. Hence, as far as the structure is concerned, the system can be modelled by neglecting the magnetic dipolar interactions (without an external magnetic field, the magnetic moments are randomly orientated due to thermal agitation).

The dynamic behaviour was probed by XPCS. Figure 50a presents the inverse normalised effective diffusion coefficient $D_0/D(Q)$ (•). The diffusion constant D_0 was measured to be $5.56 \cdot 10^{-12} m^2 s^{-1}$. $D_0/D(Q)$ displays a peak at the same position as S(Q), thus indicating that the fluctuations of the most probable configurations decay the slowest. Using the measured S(Q) and $D_0/D(Q)$, the hydrodynamic function H(Q) was extracted by Equation 1, as presented in Figure 49b. H(Q) mimics the behaviour of S(Q) and presents in particular a peak located at the same position. Over the whole measured Q-range, H(Q) < 1, indicating that the indirect interactions act as an additional friction force slowing down the dynamics.

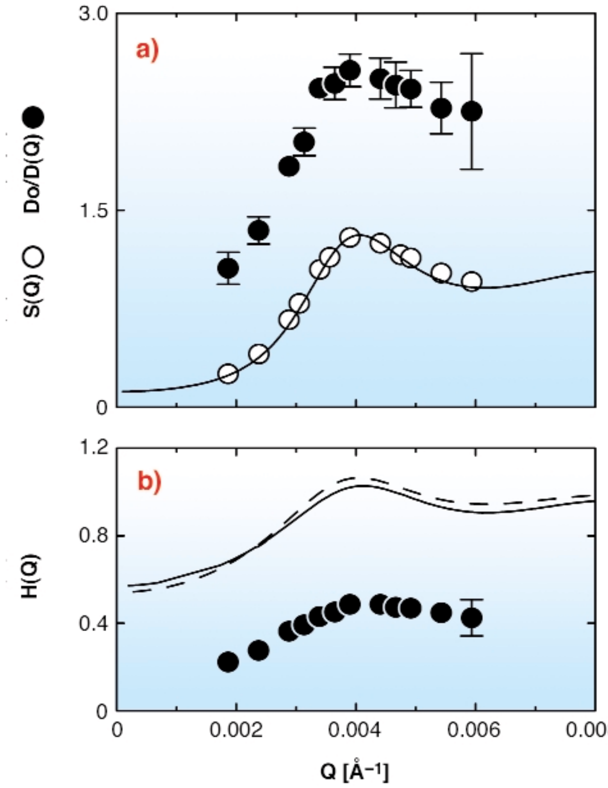

Fig. 50: (a) Measured static structure factor S(Q) (o). The solid line is a fit to the S(Q) using the RMSA. $D_0/D(Q)$ probed by XPCS (•) is shown for comparison. The extracted hydrodynamic function H(Q) is shown in (b) and is compared to existing models (δγ-expansion and pairwise additive approximation, solid and dashed line, respectively).

The behaviour of the extracted H(Q) cannot be described by any of the existing colloidal hydrodynamics theories (the δγ-expansion and pairwise additive approximation are shown in Figure 50b) and is more than a factor 2 smaller than expected over the whole Q-range. Whether or not these unexpectedly slow dynamics can be attributed to the presence of the magnetic dipoles anchored on each particle will be the subject of further investigations.

References

[1] E. Blums, A. Cebers and M. Maiorov, ed., *Magnetic Fluids* (De Gruyter, New York, 1997).

[2] T. Autenrieth, J. Wagner, R. Hempelmann, W. Härtl, A. Robert and G. Grübel, *Appl. Organometal. Chem.* **18**, 520 (2004).

Principal Publications and Authors

A. Robert (a), J. Wagner (b), T. Autenrieth (b), W. Härtl (c) and G. Grübel (a,d), *J. Chem. Phys*, in print; J. Wagner, T. Autenrieth, A. Robert, W. Härtl and G. Grübel, *J. Magn. Magn. Mat*, in print.

(a) ESRF
(b) Universität des Saarlandes, Saarbrücken (Germany)
(c) Wallburg-Realschule, Eltmann (Germany)
(d) DESY/HASYLAB, Hamburg (Germany)

Structural Evolution of Regenerated Silk Fibroin: Combined SAXS/WAXS Experiments

During the spinning process of spiders or silk worms, solvated random-coil fibroin protein is transformed into a dry, semicrystalline silk thread [1]. It is often assumed that a silk I structure is initially formed and subsequently transformed into the β-sheet type silk II structure [2] under the action of shearing forces in the tapered end of the spinneret. An experimental proof is, however, lacking and *in vivo* experiments on dragline silk production showed only the presence of the silk II structure.

In order to simulate the shearing forces occurring during the spinning process we have studied the solidification process of regenerated *Bombyx mori* silk using the Couette geometry on the rheometer (**Figure 51a**) at beamline **ID02** by an *in situ* SAXS/WAXS experiments.

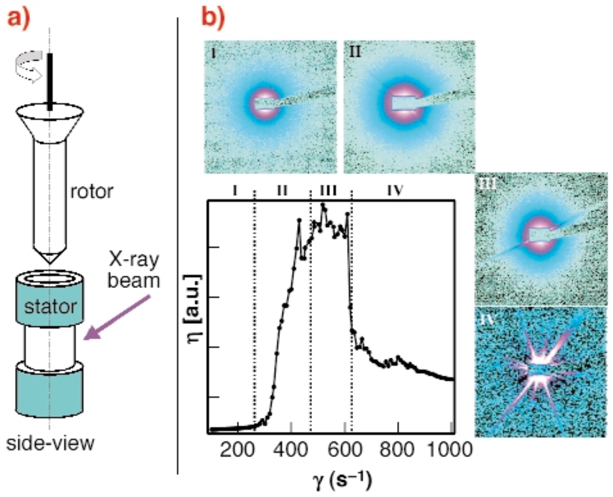

Fig. 51: a) Schematic design of the Couette cell geometry used at beamline ID02; b) change of the viscosity (η) upon increase of the shear rate (γ) and characteristic SAXS patterns recorded in four selected zones.

The change of viscosity with shearing rate can be roughly separated into four zones. A non-Newtonian behaviour was observed starting in zone II. Analysis of the scattering data suggests a transition of the random-coil fibroin into a more compact, folded fibroin, presumably due to an onset of hydrogen-bonding. Aggregation of fibroin starts in zone III as evidenced by streaks. Due to the formation of large fibroin aggregates in zone IV the viscosity is decreasing. WAXS data show that the precipitated fibroin is amorphous. Complementary ATR-FTIR data indicate the presence of β-sheet conformation.

The formation of the silk I/silk II structures during the drying process of a piece of precipitated fibroin (**Figure 52a**) was investigated by micro-SAXS/WAXS experiments at beamline **ID13**. Figure 52b shows a composite picture obtained by a 10 x 10 µm mesh-scan with a 5 µm beam.

The data (Figure 52c and 52d) agree to the presence of two phases: (i) a silk II phase with rather broad reflections and (ii) a second phase with narrow reflections corresponding probably to a hydrated silk I structure. As the two phases coexist in different ratios across the scanned zone one can assume that the drying process proceeds through an intermediate hydrated silk I phase, which is subsequently transformed into the unhydrated silk II structure.

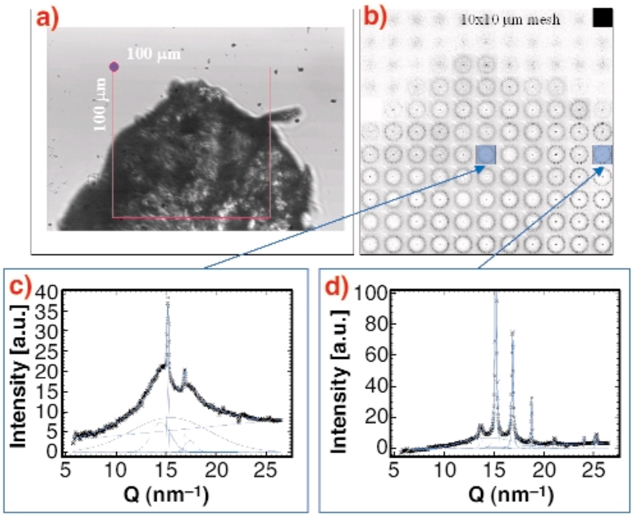

Fig. 52: a) Optical image of precipitated and partially dried sample. The 100 x 100 µm zone was mesh-scanned by a 5 µm X-ray beam; b) composite picture of the mesh-scan: the individual "pixels" correspond to SAXS/WAXS patterns recorded with a MAR CCD; c) azimuthally-averaged WAXS-pattern from the edge showing a mixture of broad reflections (silk II) and narrow reflections of a second phase, which probably corresponds to the silk I structure. The broad reflections of the silk II phase are identical to the reflections from a *Bombyx mori* fibre; d) practically pure second phase (silk I) reflections.

References

[1] F. Vollrath and D.P. Knight, *Nature* **410,** 541-548 (2001).

[2] R.D.B. Fraser and T.P. MacRae, *Conformations of Fibrous Proteins*, New York: Academic Press. (1973).

Principal Publication and Authors

M. Rössle (a), P. Panine (b), V.S. Urban (c) and C. Riekel (b), *Biopolymers* **74**(4), 316-327 (2004).
(a) EMBL Outstation Hamburg (Germany)
(b) ESRF
(c) Oak Ridge National Laboratory (USA)

Soft Matter: Microstructural Evolution

Visualisation of Nanostructure Evolution during Polymer Crystallisation

In the production of most textile fibres or plastics parts polymer melts are crystallised, and the developing nanostructure from crystalline domains in an amorphous matrix determines the materials properties. Engineers control temperature, composition and other parameters of the melt in order to tailor the product, but the mechanisms behind polymer crystallisation are not yet understood. We have developed a method of real-space visualisation of the domain arrangement from small-angle X-ray scattering (SAXS) patterns. *In situ* experiments were carried out at beamline **ID02**. Based on results of the new method we expect to elucidate the mechanisms which govern crystallisation and melting of polymers and their variation upon change of processing parameters.

The method combines modules from various fields of science such as beamline engineering, digital image processing, computer tomography, scattering theory and animation rendering. It extracts the information on the samples nanostructure from two-dimensional (2D) SAXS patterns with fibre symmetry using a topology $\rho(r) \in [\rho_{crys}, \rho_{amorph}]$ of phases with distinct densities. The SAXS patterns are collected by a low-noise CCD camera with fast readout that is coupled to an X-ray image intensifier (XRII–FReLoN, cycle time 7 s, exposure time between 0.1 s and 3 s). The exposure is continuously readjusted in order to keep the signal-to-noise ratio constant and high throughout the monitored process. As a result, the collected data in each image exploit the full dynamic range of the SAXS detector. 2D wide-angle X-ray scattering (WAXS) data are collected simultaneously with a second CCD camera that is coupled to a multi-channel plate (MCP-Sensicam CCD detector). Movies resulting from automatic data evaluation show an “edge-enhanced autocorrelation function” $z(r)$ — the autocorrelation of the gradient $\nabla\rho(r)$. This “chord distribution function” (CDF) shows peaks where ever there are domain surface contacts between domains in $\rho(r)$ and its displaced ghost as a function of ghost displacement. The movies exhibit the evolution of nanostructure and demonstrate the mechanisms of polymer crystallisation.

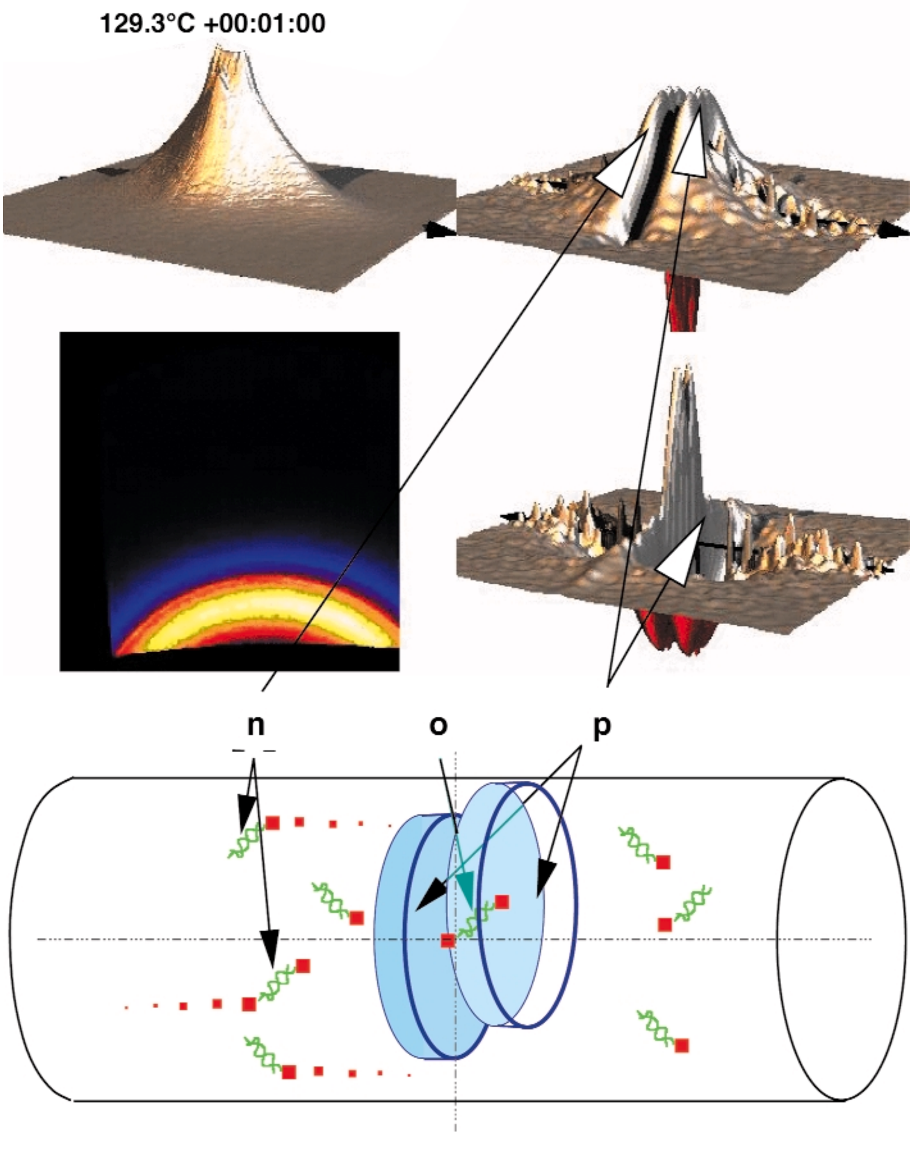

Fig. 53: Crystallisation of an oriented polyethylene melt. 1 minute after quenching to 130°C. Top: Movie frame with four panels: (left column) SAXS, WAXS; (right column) $z(r)$, $-z(r)$. Bottom: Sketch of the nanostructure. Off-meridional peaks (n) identified as entanglement strands and transverse shift (o) in twin-layers. Layer shape of crystals (p) from meridional peak in $z(r)$ and self-correlation triangle in $-z(r)$.

Figure 53 shows one movie frame representing the state 1 minute after quenching of an oriented polyethylene (PE) melt to 130°C. We observe primary, extended lamellae (stage "d" from **Figure 54,** which shows sketches of the observed phases of nanostructure evolution).

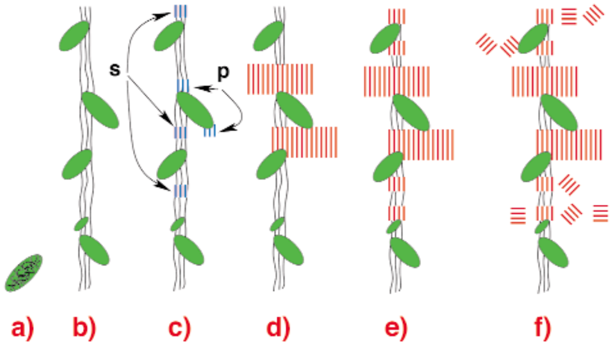

Fig. 54: Principal steps of crystallisation from a highly oriented, quiescent PE melt via a mesophase (a,b,c) coupled to primary (p) and secondary (s) crystal nuclei, extended crystalline layers (d), blocky crystals with longitudinal (e) and lateral (f) correlation.

In Figure 53 the layer character of the crystallites is demonstrated by the fact that the peaks in the CDF are extending in the direction transverse to fibre direction. The small number of peaks shows that only two layers (blue disks in the sketch) are correlated to each other. A transverse offset (p) between the members of the pair of correlated layers is induced by entities of a mesophase.

In conclusion, we found that PE crystallisation was always preceded by a mesophase structure. Based on the observed structure evolution it was suggested that its entities are entanglement-rich and disentangled regions in the melt, respectively. Extended lamellae prevail only at high crystallisation temperatures and become more perfect with time. Nevertheless, the majority of the crystallites formed during the final stages of crystallisation are small, imperfect and unoriented (*i.e.* "blocky" crystallites, Figure 54e,f). They are situated in the centre of free gaps so that correlations among crystallites are increased.

Principal Publication and Authors

N. Stribeck (a), P. Bösecke (b), R. Bayer (c), and A. Almendarez Camarillo (a) *Progr. Colloid Polym. Sci.*, (2005) in print
(a) Institute TMC, University of Hamburg (Germany)
(b) ESRF
(c) Institute of Mater. Science, GH Kassel (Germany)

Nucleation and Growth Kinetics of Brome Mosaic Virus Microcrystals

Understanding the interaction potentials that govern crystal formation is an essential step for X-ray structure determination. Brome Mosaic Virus (BMV) and polyethylene glycol (PEG) mixtures were chosen as a crystallisation model since their phase diagram presents a solid precipitated phase at high polymer concentration, known to be made of the synchronous formation of a large number of microcrystals [1]. Indeed, the addition of neutral polymers like PEG to biomacromolecular solutions results in an attractive potential (the depletion attraction) dependent upon polymer size and concentration. When the attraction increases, a fluid-fluid or fluid-solid phase separation eventually occurs.

The onset of BMV crystal nucleation and growth was observed for the first time using time-resolved X-ray scattering by the synchronisation of a fast stopped-flow mixing system (Bio-Logic) and the fast detector of **ID02**, for virus concentrations from 20 to 2.5 mg/ml and PEG concentrations down to 5% w/v. Due to the differences in molecular weights and contrasts of BMV and PEG, only the virus scattering was observed, in solution, in crystals and, possibly, in intermediary states. Twenty measurements of 50 ms each, exponentially spaced in time, were adequate to cover the process and avoid radiation damage.

Individual spots, *i.e*. Bragg peaks, arising from individual microcrystals appeared about one second after mixing (**Figures 55c-d**). After 20-60 seconds, the increasing number of spots built the diffraction rings of a crystal powder diagram as seen on the Figures 55e-f. The intensity of the rings grew for about ten minutes until there was almost no virus left in the solution. Interference rings, which would be a signature of an amorphous intermediate state, were not detected. This indicaties that only two phases were present during the time-resolved experiment: soluble viruses and microcrystals.

Dividing the intensity curves by the form factor to remove the contribution of the virus shape emphasised the structure factor (**Figure 56a**) and confirmed that only the crystallised form of the BMV was present.

The time evolution of the three parameters of Figure 56b was used to obtain the kinetic parameters of microcrystal nucleation and further growth. Both events induce a decrease in the concentration of soluble virus in solution and contribute to the increase of the peak intensities. The time lag necessary for Bragg peaks to become visible defines the onset of nucleation and varies from one to a few seconds according to the supersaturation, *i.e*. the BMV concentration. Then the diffraction peaks went on growing in essentially two steps corresponding to nucleation and crystal growth.

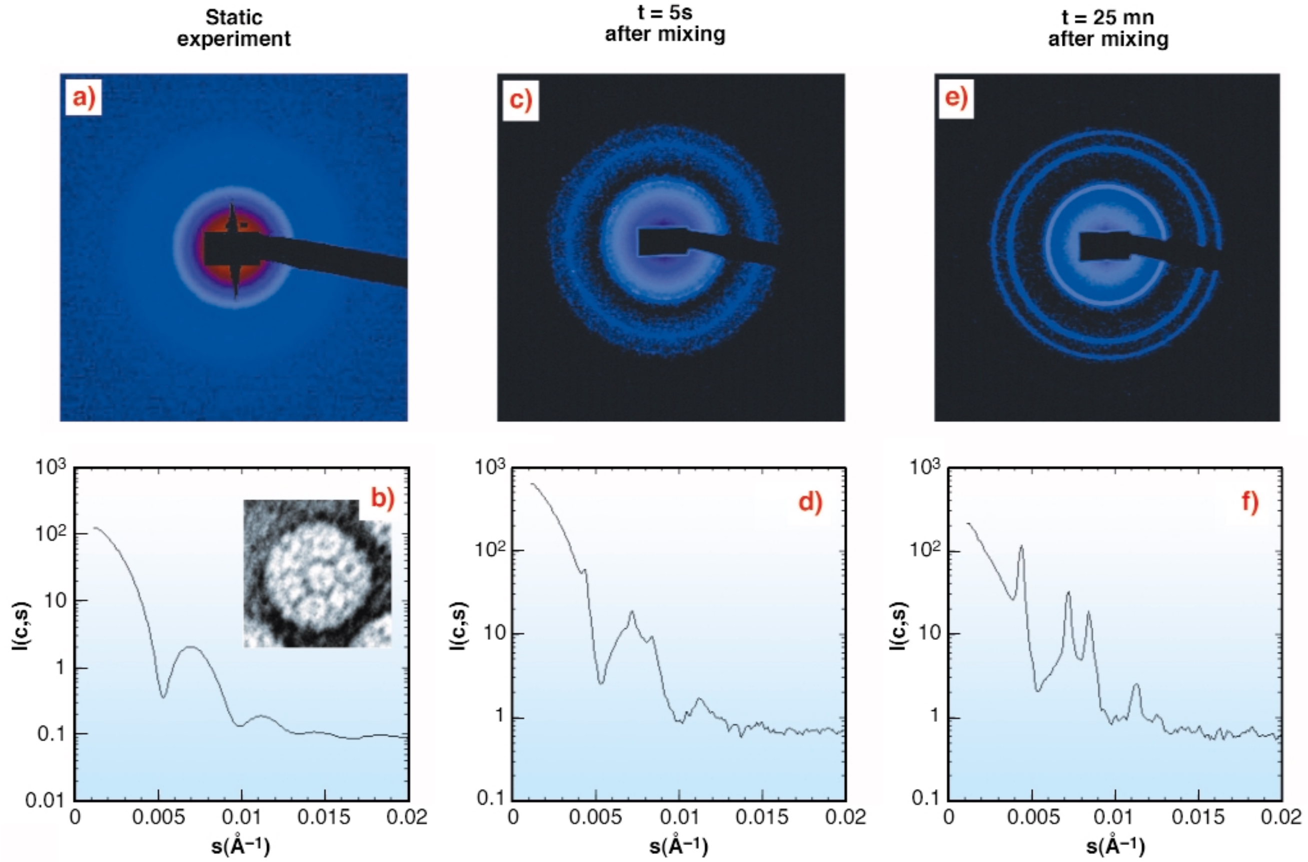

Fig. 55: Scattering intensities of Brome Mosaic Virus (top: 2D images; bottom: corresponding azimuthally regrouped and normalised scattered intensities); a,b: form factor obtained without PEG (20 frames at 2.5mg/ml). b-insert: electron micrograph of a negative staining BMV particle. The BMV is a T3 icosahedral RNA plant virus of 268 Å in diameter and a molecular weight of 4.6x10^6 Da. c-f: nucleation and growth of BMV crystals shows the appearance of individual microcrystal spots and Bragg peaks (BMV 10mg/ml and 5% PEG 20000).

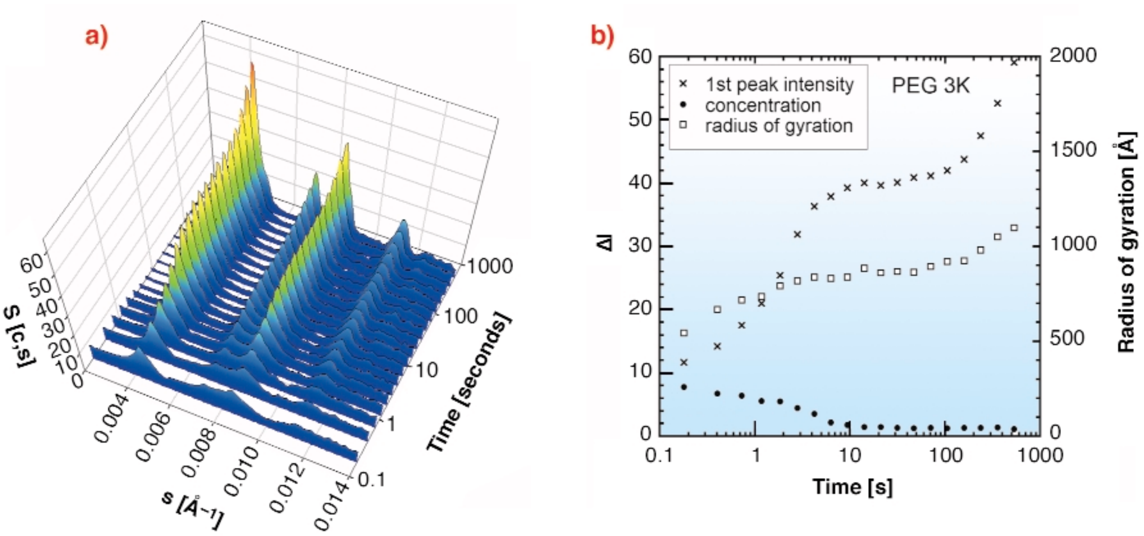

Fig. 56: BMV 20mg/ml and 10% PEG 3K evolution of a) structure factors and b) peak intensity, BMV concentration decrease (measured from the plateau value, from 0 to 0.0038 $Å^{-1}$) and microcrystal average radius of gyration (from the peak shape). Nucleation is achieved between 12 to 100 seconds after the mixing. The initial value measures the BMV concentration at the beginning of the experiment, while the final plateau value is close to the virus solubility. For each PEG the crystalline system was found to be face centered cubic (unit cell side close to 391 Å).

A higher PEG concentration was able to counterbalance a lower molecular range to produce crystals.

The size of the critical nuclei was evaluated with the PEG 3K conditions. Il should be equal to or smaller than the smallest microcrystal (radius of gyration of about 500 Å). Taking 276 Å as the virus diameter and assuming that 70 % of the nucleus volume is occupied by the virus in the fcc system, the number of viruses in the critical nucleus is therefore calculated to be ≤ 36.

These novel experiments were designed to address the question of whether the initial formation of dense liquid droplets could precede or favour nucleation. Our results demonstrate that in the case of BMV the formation of periodic order may take place without any long life concentrated "liquid-like" droplets.

References

[1] M. Casselyn, J. Perez, A. Tardieu, P. Vachette, J. Witz, H. Delacroix, *Acta Crystallogr.* D57:1799-1812 (2001).

Principal publication and authors

M. Casselyn (a), A. Tardieu (b), H. Delacroix (a) and S. Finet (c), *Biophys. J.* **87,** 2737 (2004).
(a) BioInformatique Structurale - Centre de Génétique Moléculaire, Gif-sur-Yvette (France)
(b) Laboratoire de Minéralogie et Cristallographie, Paris (France)
(c) ESRF

Structural Processes during Starch Granule Hydration by Synchrotron Radiation Microdiffraction

Starch granules are the most important energy reserve in higher plants. They are composed principally of amylopectin (major fraction) and amylose (minor fraction). Their structure is assumed to consist of concentric shells of alternating hard, semicrystalline, and soft amorphous layers. The starch granule organisation is, however, very complicated and many questions on the ultrastructure remain unsolved [1].

The microstructure of hydrated single potato starch granules had already been studied by X-ray microdiffraction in 1997 at beamline **ID13** [2, 3]. Radiation damage had, however, limited data collection to a few second per pattern [2]. Recent advances in microdiffraction techniques developed for biopolymers and protein microcrystals make revisiting this important biopolymer worthwhile. **Figure 57a** shows a single potato starch granule at 100 K in a cryoloop. A mesh-scan using a MAR CCD detector and a 5 µm beam is shown in Figure 57b with structural information in individual frames (Figure 57c) extending up to Q = 25 nm^{-1}. These data suggest an increase in crystallinity upon hydration of the granule and confirm the model of shells with a radial orientation of amylopectin fibrils. Preliminary evidence for a crystallisation of short-range ordered amylopectin towards the granule centre was also obtained.

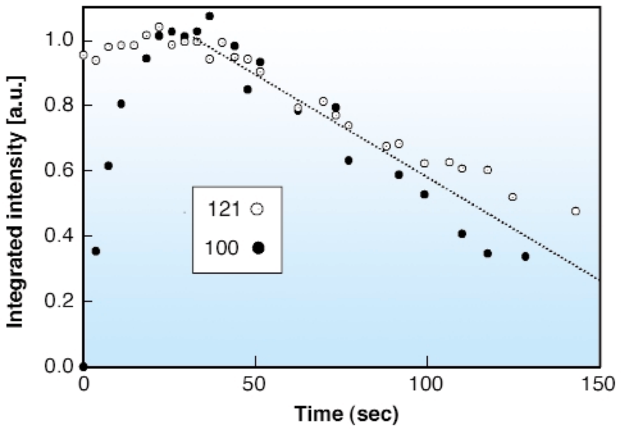

Fig. 58: Kinetics of evolution of integrated intensities of the 100 and 121 reflections (see Figure 57c). Both reflections were scaled to 1.0 at maximum intensity.

In order to advance the understanding of the structural steps involved in hydration and gelatinisation we studied the local hydration of single starch granules at room temperature by a drop-on-demand system using data collection times of 0.5 sec/frame. The time evolution of the 100 and 121 reflections is shown in **Figure 58.** Radiation damage is seen to be setting in for both reflections after the collection of 6-7 frames.

The 100 reflection is known to be particularly sensitive to hydration process [1] and suggests a half life of the hydration process of about 7 seconds. The unexpectedly rapid hydration reflects the porous nature of the starch

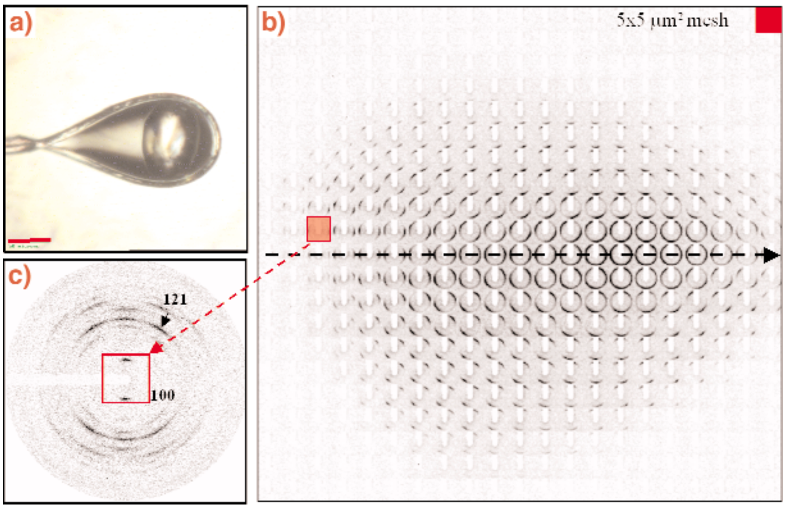

Fig. 57: a) A single potato starch granule in a cryoloop at 100 K using a glycol/water cryoprotectant; b) 5 x 5 µm² mesh-scan of single granule with a 5 µm beam. Note that the individual frames are rotated by 90°; c) single frame recorded in the outer parts of the granule showing a well-defined fibre diffraction pattern.

granules [1]. The size of the crystalline domains was found to increase from 5.7 nm (unhydrated) to 9.4 nm (≥10 sec hydration), which agrees well with the size of the proposed amylopectin side-clusters [1]. Larger domains of about 15 nm are only formed at longer hydration times. We plan to extend these experiments to combined SAXS/WAXS experiments and higher temperatures in order to study the onset of lamellar ordering and of gelatinisation.

References

[1] A. Buléon, P. Colonna, V. Planchot, S. Ball, *Int. J. Biol. Macrom*. **23,** 85-112 (1998).

[2] A. Buléon, B. Pontoire, C. Riekel, H. Chanzy, W. Helbert, R. Vuong, *Macromolecules* **30**(13), 3952-3954 (1997).

[3] T.A. Waigh, I. Hopkinson, A.M. Donald, M. Butler, F. Heidelbach, C. Riekel, *Macromolecules* **30**(13), 3813-3812 (1997).

Principal Publication and Authors

H. Lemke (a), M. Burghammer (b), D. Flot (c), M. Rössle (d) and C. Riekel (b), *Biomacromolecules* **5**(4), 1316-1324 (2004).

(a) Institut für Experimentelle und Angewandte Physik, University of Kiel (Germany)

(b) ESRF

(c) EMBL Outstation Grenoble (France)

(d) EMBL Outstation Hamburg (Germany)

Local Nanostructure of Single Carbon Fibres during Bending Deformation

Carbon fibres are especially suited for light-weight constructions in technical applications due to their low density (1.5 - 2.1 g/cm^3), the extremely high values of tensile strength (3 - 5 GPa) and Young's modulus (up to 900 GPa) and the outstanding high-temperature behaviour, superior to any other material. The fibres are very small (around 10 micrometres in diameter) and their structure and its development during the application of high loads as required in technical use is still largely unknown.

Single fibre bending experiments were designed to allow simultaneously scanning across the fibre from the tension to the compression range. **Figure 59** shows the experimental setup: Increased bending is achieved by decreasing the bending radius of the fibre, pulling its ends through a thin hollow needle. Quantitative strain distribution across the fibres was achieved by measuring the bending radius (with an online light microscope) and the fibre diameter (with SEM). Scanning X-ray microdiffraction experiments were performed by using the microbeam emanating from the waveguide structure available at **ID13** with a lateral resolution of 100 nm in one dimension [1]. The position dependence of two structural parameters under high load conditions are shown in **Figure 60**: The 10-band in the direction of the fibre axis yields the in-plane displacement d_{10} of the atoms in the hexagonal lattice planes of the graphene sheets, and thus the tensile strain at the level of the nanocrystallites. The second parameter is given by the azimuthal spread of the 002-reflection, its width χ_{002} being the most important parameter for the preferred orientation of the graphene sheets and thus the Young's modulus of the fibres.

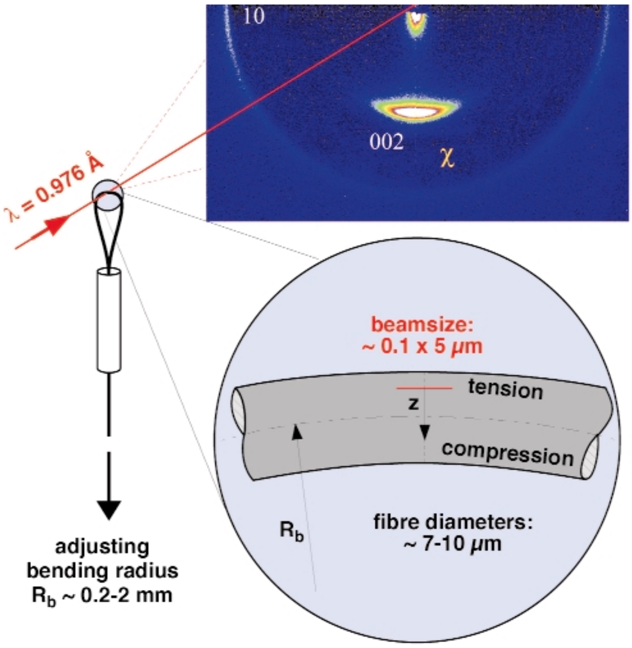

Fig. 59: Experimental setup: Bending is achieved by forming carbon fibre loops where the radius of the loop can be varied. The fibre is scanned by the X-ray beam from the waveguide structure with 100 nm lateral position resolution. 2D diffraction patterns were taken with a MAR-CCD detector.

Figure 60a shows the in-plane strain $\varepsilon_{10} = (d_{10}(z)-d_{10}(\text{unbent}))/d_{10}(\text{unbent})$ of the carbon atoms within those graphene sheets, which are perfectly aligned along the fibre axis. The symbols depict the results from scanning across the cross-section of the fibre, starting from the tension to the compression range. A perfectly linear dependence of the in-plane strain on the position across the bent fibre can be observed, shown for the case of very strong bending previous to rupture (squares, maximum tensile and compressive strain in the outer skin ε_{max} = 0.73%, fibre type HTA5131, Tenax industries, produced from PAN-precursor and subjected to a temperature treatment of 2100°C). However, a shift of the neutral axis from the centre towards the tension side reveals a stress re-distribution within the fibre, which is the consequence of an asymmetry of the tensile and the compression modulus. For comparison, the in-plane distances for a straight fibre are apparently constant (circles). In Figure 60b, the orientation distribution of the graphene sheets is visualised by the half-width at half-maximum χ_{002}. A more pronounced preferred orientation of the graphene sheets is observed in the tension zone, the opposite in the

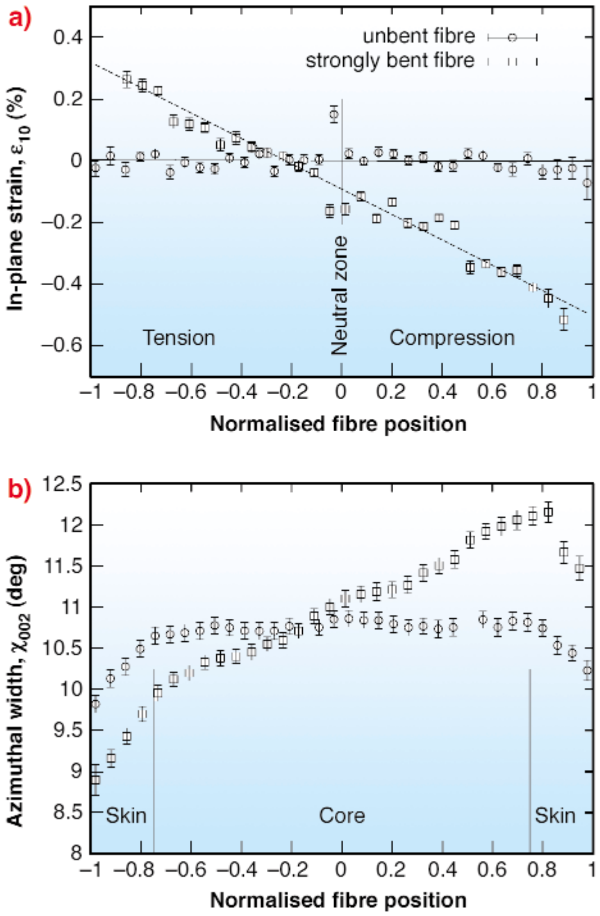

Fig. 60: (a) In-plane strain ε_{10} of the graphene sheets along the fibre axis and (b) orientation distribution of the graphene sheets with respect to the fibre axis. Circles, unbent fibre, squares, strongly bent fibre. Tension side is on the left.

compression zone. The same shift of the neutral zone towards the tension side suggests that buckling at the nanoscale of the graphene sheets is responsible for the different behaviour in tension and compression, since the decrease in orientation should result in a lower Young's modulus. Furthermore, a skin-core structure as proposed for this type of fibre already earlier in literature is clearly visible and can be quantitatively evaluated: A some 100 nm wide skin-region with a higher orientation (smaller χ_{002}) can be observed, visible towards the outer bounds of the fibre.

In conclusion, scanning microbeam diffraction on fibres with a position resolution of 100 nm allows a precise determination of their inner structure. When combined with the application of mechanical loads, the local structural development can be measured at an atomic level, allowing a deeper understanding of the complex structure-function relationship at the nanoscale.

References

[1] S. Lagormasino, A. Cedola, S. Di-Fonzo, W. Jark, V. Mocella, J.B. Pelka, and C. Riekel, *Cryst. Res. and Techn.*, **37**, 758 (2002).

Authors

D. Loidl (a), H. Peterlik (a), O. Paris (b), M. Burghammer (c).

(a) University of Vienna (Austria)
(b) Max-Planck-Institute of Colloids and Interfaces (Germany)
(c) ESRF

Structure of Chocolate Clarified with Synchrotron Powder Diffraction Data

Most chocolate eaters will have had the surprising experience that a newly opened bar of chocolate (pure or milk) has a greyish-white layer instead of the familiar chocolate colour (**Figure 61**). Most likely, this bar has fallen victim to the development of fat bloom. The cocoa butter in chocolate is responsible for chocolate's appearance. In most consumer chocolate the cocoa butter is in its second highest melting form, called ß(V). Storage of ß(V) chocolate at too high temperatures induces the transition to the most stable ß(VI) form and this transition is commonly associated with fat bloom. To understand the ß(V) → ß(VI) transition, crystal-structure knowledge of the principal components of cocoa butter is required. At room temperature solid cocoa butter consists mainly of three mono-unsaturated triglycerides, 1,3-dipalmitoyl-2-oleoylglycerol (POP), 2-oleoyl-1-palmitoyl-3-stearoylglycerol (POS) and 1,3-distearoyl-2-oleoylglycerol (SOS). The latter triglyceride comprises ~25% of cocoa butter and is known to play a major role in the crystallisation of cocoa butter into the ß forms. Good quality single crystals of SOS are extremely difficult to obtain so we resorted to synchrotron powder diffraction as an alternative.

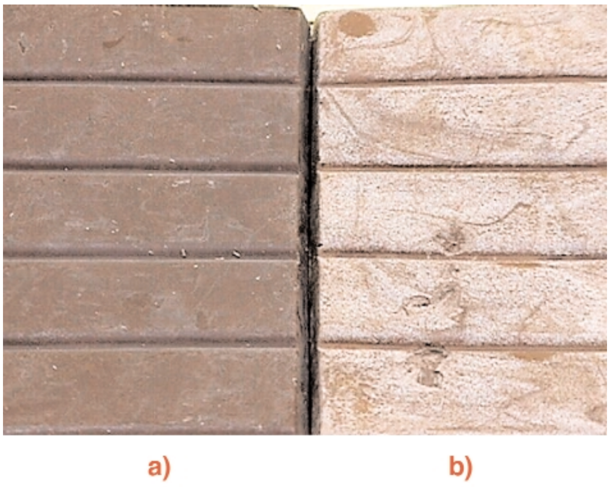

Fig. 61: a) Chocolate, b) Chocolate affected by fat bloom.

High-resolution powder diffraction data for ß$_2$-SOS, the second highest melting form of SOS, were collected at **BM16** and for cocoa butter from the Ivory Coast in the ß(V) phase at the Swiss-Norwegian CRG **BM01B**. Interestingly, both diffraction patterns are very similar, suggesting they share the same principal structural features. Unit-cell determination ('indexing') was a bottleneck for a long time but by developing our own indexing program this problem was overcome. In retrospect, the indexing problems were caused by the combination of a triclinic unit cell and exceptionally large differences of the cell-axis lengths, the shortest being ~5.45 Å, the longest ~ 65 Å. Also the pattern of ß(V) cocoa butter could be indexed, which is surprising because cocoa butter is a co-crystallised mixture of triglycerides. For crystal structure determination of ß$_2$-SOS we used the direct-space programs FOX and ORGANA that are both based on R-value minimisation and exclusion of chemically unfeasible types of packing. Starting from the SOS structural model, a crystal structure of ß(V) cocoa butter was found in a similar way, with the outer ethyl-groups in the saturated chains being partially occupied.

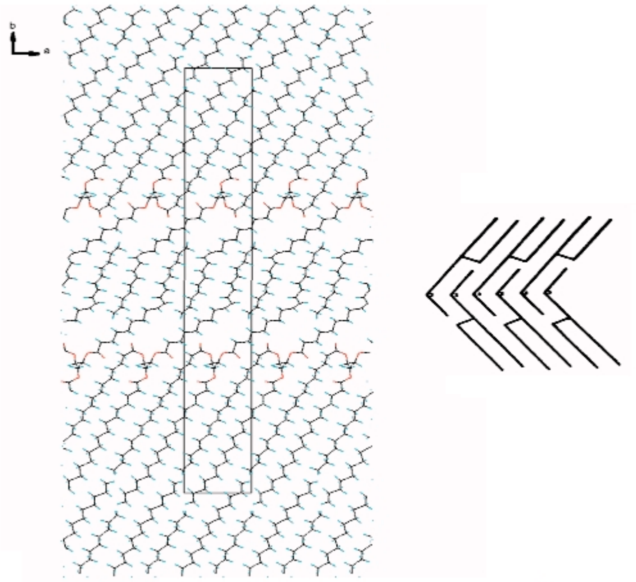
a) b)

Fig. 62: a) Crystal structure packing and characteristics of ß$_2$-SOS and ß(V)-cocoa butter. b) Packing of SOS proposed in the literature.

Both ß$_2$-SOS and ß(V) cocoa butter have a triple-chain length packing with alternating layers of saturated chains (being packed together) and mono-unsaturated oleoyl chains. With respect to the oleoyl layer, the crystal structures of ß$_2$-SOS and ß(V) cocoa butter differ considerably from the packing model for SOS proposed in the literature because of the absence of π-π interaction (**Figure 62**). This latter feature and the cocoa butter crystal structure model provide an explanation for the driving force behind the slow ß(V) → ß(VI) phase transition. The packing of SOS, POS and POP in ß(V)-CB has a ß$_2$-SOS like structure in which on average only 57% of the two carbon positions at the end of the saturated chains are occupied, while 43% are ethyl-end 'holes'. The absence of interactions at these 'holes', and the absence of π-π interaction in the oleoyl layer, causes ß(V) to be metastable and is likely to be the driving force for the transformation to the ß(VI) form, implying a structural re-organisation that reduces the amount of directly opposing 'holes'. It can be envisaged that this process may take place either via a solid-state ß(V) to ß(VI) transformation or via a melt-mediated process in which the ß(V) dissolves in the melt and ß(VI) crystallises. This fundamental knowledge concerning the stability of the cocoa butter ß phases has already led to the development of a new chocolate-manufacturing process technology in which crystallisation of chocolate into the ß(V) and also into the ß(VI) can be regulated by using the appropriate liquid seed crystals and temperature handling [1].

In conclusion, on the basis of high–resolution synchrotron powder data we solved the crystal structures of ß$_2$-SOS and ß(V) cocoa butter, and thus obtained the crystal structure of the most commonly produced form of chocolate. The packing of the crystal structure models provides an explanation of their metastability and it is expected that this will form the basis of an atomic-level description of the ß(V) → ß(VI) phase transition, which is associated with the occurrence of fat bloom.

References

[1] K.F. Van Malssen, A.J. Van Langevelde, R. Peschar, H. Schenk. *Patent WO 01/06863* (2001).

Principal Publication and Authors

R. Peschar, M.M. Pop, D.J.A. De Ridder, J.B. Van Mechelen, R.A.J. Driessen, H. Schenk, *J. Phys. Chem. B.* **108(40)**, 15450-15453 (2004).
Laboratory for Crystallography, HIMS, University of Amsterdam (The Netherlands)

Soft Matter: Surfaces and Interfaces

Self-organisation in Nanoscopic Poly(alkylthiophene) Films on Water

Conjugated polymers are promising for electro-optical applications like light emitting diodes, solar cells and lasers. These polymers are organic semi-conductors, which can be doped to yield conductivities approaching ordinary metals [1]. In order to fully exploit the properties of organic molecules, excellent control of the molecular orientation is required. To better understand the self-organisation observed in films of poly(alkylthiophenes), we have previously performed *in situ* studies of the drying process associated with solution casting [2]. In the present work, the Langmuir method was used in an attempt to obtain ultra-thin films. Regioregular poly(hexylthiophene) (R-PHT) with > 98% head-to-tail couplings, and poly(octylthiophene) (POT) with ~ 80%

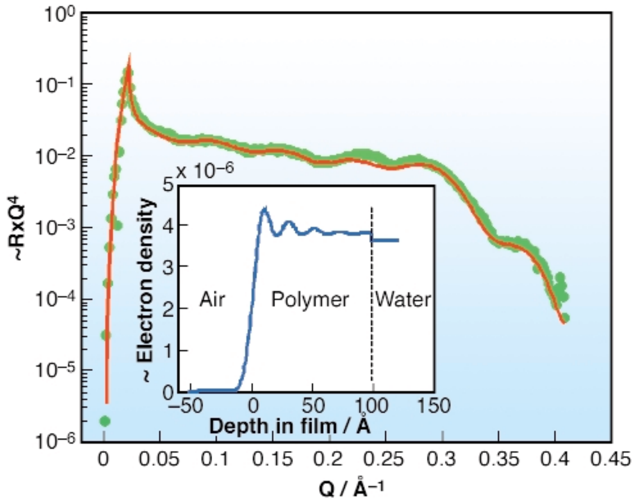

Fig. 63: Reflectivity data (green dots) obtained for a thin POT film floating on water versus scattering vector $Q = 4\pi\sin\theta/\lambda$. The solid red line is the fit. The inset shows the employed scattering density profile. Inside the polymer film, there is a periodic oscillation being damped towards the water subphase.

head-to-tail couplings were used. Closely analogous results were obtained for poly(dodecylthiophene) and other poly(thiophene) derivatives.

A few drops of low concentration (~ 1 mg/ml) solutions in chloroform were spread on a clean water surface in a shallow teflon trough. The films were studied with X-ray reflectivity and Grazing-Incidence Diffraction (GID) at the **ID10B** beamline. A vertical one-dimensional position sensitive detector was used for collecting the scattered intensity. *In situ* doping of the floating films was achieved by injecting $NOPF_6$ dissolved in acetonitrile into the water subphase.

X-ray reflectivity obtained from a POT film floating on the water surface is shown in **Figure 63**. The fitted curve is obtained by applying a standard matrix formalism from the optical theory of stratified media, applied to the density profile shown in the inset of the figure. The refractive indices of water and polymer were determined from tabulated values. The air-polymer interface was found to be graded, with a (Gaussian) width ~ 5.3 Å. This particular film had a thickness of about 10 nm, corresponding to five repetition units of the semi-crystalline *a*-axis.

The feature at scattering vector Q ~ 0.3 $Å^{-1}$ is a result of the semi-crystalline structure of the film. The best fit was obtained for a model with an exponentially damped harmonic variation of the electron density, a model sometimes used for smectic liquid crystals. The period of the modulation, 20.8 Å, is compatible with the *a* - parameter of solid POT, which is 20.4 Å. The model implies a well-developed layering near the air-polymer interface, decaying towards less pronounced ordering at the polymer-water interface, in qualitative agreement with the aliphatic side chains being hydrophobic (**Figure 64**).

GID gave complementary information to the laterally averaged density profile obtained from the specular reflectivity measurements. An important result was the observation of a large degree of anisotropy. The *100*-reflection is strongest for the scattering vector perpendicular to the film plane, whereas the *010* reflection could only be observed for scattering vectors parallel to the film plane. This implies that the unit cell *a*-axis tends to be parallel to the film normal. From the width of the *100* diffraction peak, the average dimension of the ordered regions could be estimated to about 10 nm, in agreement with the reflectivity data.

Structural changes associated with the insulating-conducting phase transition in conjugated polymers have been reported previously for PATs, notably an expansion of the *a*-axis. A change of the *100* peak position following *in situ* doping of the floating films was indeed observed, indicating an increase by as much as 15-20%. The doping could also be observed visually, as the film changed its colour from being weakly reddish to a hardly visible pale blue. Dedoping takes place; after 2 hours the film is regaining its original colour accompanied by a contraction of the *a*-parameter.

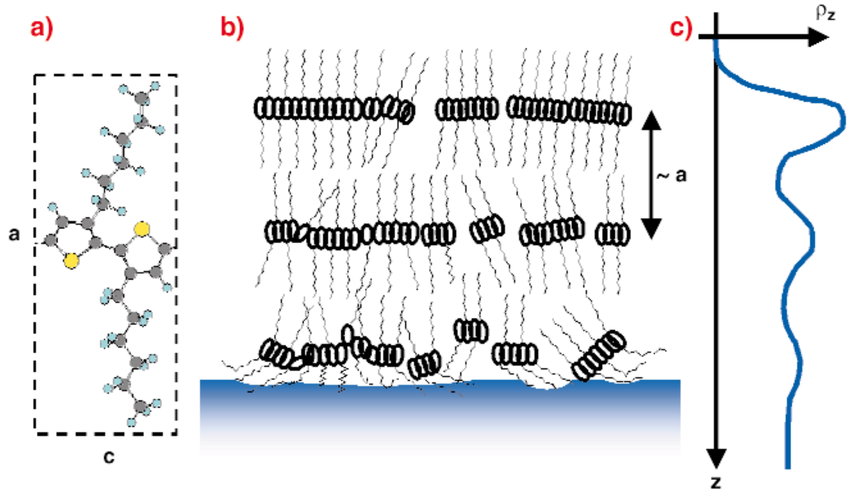

Fig. 64: a) The orthorhombic PAT unit cell, with a ~ 20.4 Å for POT, and c ~ 7.8 Å. In the b-direction (out of the paper plane), the aromatic rings form stacks. b) A sketch of the molecular ordering. c) The corresponding density profile.

In conclusion, we have demonstrated that the Langmuir technique can be used to obtain homogeneous ultrathin films consisting of a few molecular layers. A detailed model of the polymer conformation in these films accounting for all the observations has been established. These results are very interesting in view of the favourable molecular orientation and the thickness being appropriate for electronic logics nanoscale applications.

References

[1] G. Hadziioannou, P.F. van Hutten, (eds.), *Semiconducting polymers: chemistry, physics and engineering*, Wiley, Weinheim (2000).

[2] D.W. Breiby, E.J. Samuelsen and O. Konovalov, *Synth. Met.* **139**, 361 (2003).

Principal Publication and Authors

D.W. Breiby (a), E.J. Samuelsen (b), O. Konovalov (c) and B. Struth (c), *Langmuir* **20**, 4116 (2004).
(a) *The Danish Polymer Centre, Risø National Laboratory (Denmark)*
(b) *Dept. of Physics, Norwegian University of Science and Technology (Norway)*
(c) *ESRF*

GID Studies of Oriented Nucleation of Semiconductor Nanoparticles on Polyconjugated Langmuir Films at the Air-Solution Interface

Polyconjugated Langmuir films of polydiacetylene (PDA) are anisotropic, robust films that change their colour from blue to red upon thermal, mechanical, UV and shorter wavelength irradiation or chemical stimulation. Parallel polymer backbones are organised in 2-D crystalline domains whose typical size varies from several µm to several hundreds of µm. In previous work, we used TEM and AFM to evaluate the lateral ordering and crystallographic orientation of nanocrystalline PbS, CdS and Ag_2S deposited on PDA LF templates [1-4]. These studies involved transfer of the ultrathin films onto solid supports and their study *ex situ*. This may involve structural changes during the transfer. Evidently, *in situ* grazing-incidence X-ray diffraction (GID) structural studies at the air-solution interface can overcome this problem, elucidate the true structure of the films and allow the study of the factors affecting it. 10,12-pentacosadiynoic acid in chloroform solution was spread over an aqueous subphase in a Langmuir trough mounted at beamline **ID10B**. After the solvent has evaporated, the monomers were compressed to their stable trilayer structure and polymerised by ultraviolet irradiation.

We monitored the transition from the blue to the red forms of the PDA Langmuir films. Accurate control of radiation (combined synchrotron and UV) dose was achieved by lateral translation of the trough with respect to the beam during scans. Hence, any given area in the sample can be varied from very short to longer exposure time periods. GID maps (reflected intensity, vs q_{xy} and q_z) of the pure blue and red phases and their mixtures were obtained (**Figure 65a-c**). The pure blue phase, obtained by minimal exposure, is shown in Figure 65a. Continued exposure to X-ray radiation gradually increases the relative amount of the 'red' phase (Figure 65b). These GID maps depict coexistence of the two phases. Upon further increase in radiation dose, the entire film converts to the 'red' phase (Figure 65c). The transition between the phases appears to be discrete,

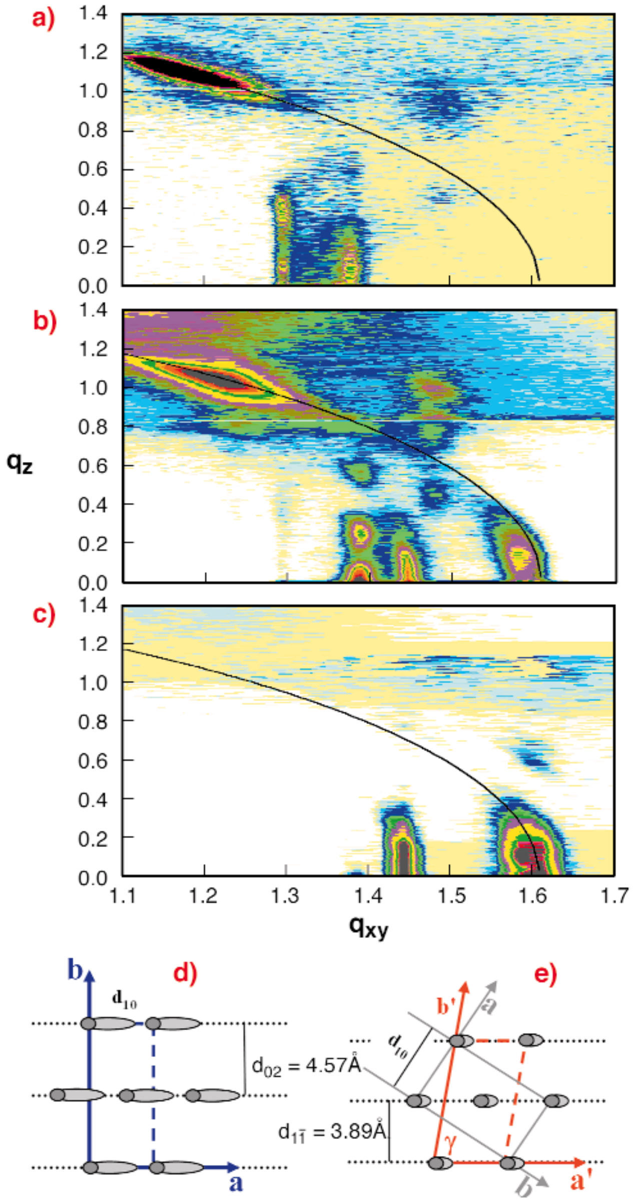

Fig. 65: GID maps depicting the gradual structural transformation of PDA blue phase (a), through coexistence situation (b) to a fully transformed 'red' phase (c). The black arc corresponds to $q_{total} = 1.6$ [$Å^{-1}$]. The reconstructed unit cell of the blue phase (d) and the red phase (e) are shown. The red phase is denser with the alkyl chains nearly vertical.

with no intermediate structures observed. The ‘blue’ to ‘red’ conversion is manifested in a shift of the q_{xy} and q_z position of the two Bragg peaks obtained from the centred rectangular structure to higher q_{xy} values. Note also the shift in position of the intense reflection at $q_{xy} = 1.18$ and $q_z = 1.1$ [Å^{-1}] along the same q_{total} arc to circa $q_{xy} = 1.60$ [Å^{-1}] and q_z close to zero (near-normal orientation of the alkyl side groups) from Figure 65a to Figure 65c. Based on these results, we constructed a model describing the crystallographic unit cells corresponding to each phase, as shown in Figure 65d,e.

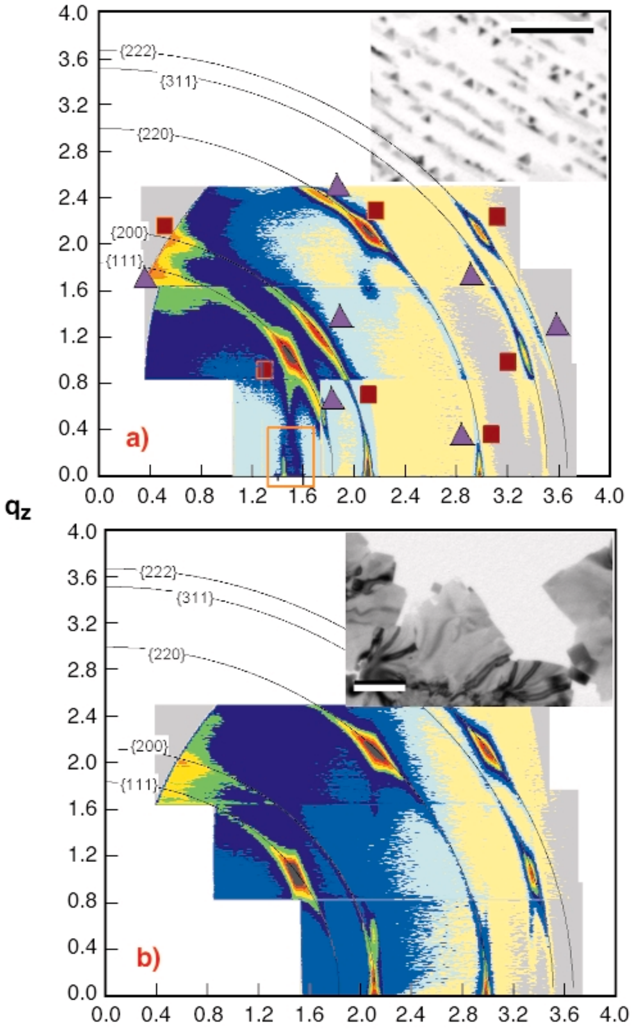

Fig. 66: GID maps of (a) PbS nanocrystals nucleated under PDA film. Reflections from the PDA layer are marked with a frame. Inset: TEM micrograph depicting the PbS on PDA. (b) GID map of PbS grown at the air-solution interface in the absence of PDA, indicating that all crystals are (100) oriented. Inset: PbS crystals in the absence of PDA.

PDA-PbS nanocrystal hybrid materials were produced by exchanging the pure water subphase with a solution containing Pb^{2+} cations and subsequently exposing the interface to controlled amounts of H_2S gas. This resulted in the formation of triangular and elongated PbS nanocrystals, aligned in linear rows along the polymer strands as shown in the TEM image in **Figure 66a**, inset. The equidimensional triangular crystallites are (111) oriented. The right angle and the elongated crystals are (100) oriented. Both crystal orientations are aligned with the [110] direction along the PDA backbone [4]. *In situ* GID studies were carried out in order to compare the orientation of the PbS nanocrystals in the presence or absence of PDA template films at the interface. GID diffraction pattern from the hybrid material depicts the contribution of the organic template and both (100) and (111) orientations of the incipient crystallites (Figure 66a). In the absence of PDA, only the (100) orientation is observed, as expected for crystals with the rocksalt structure (Figure 66b). The (111) orientation, directly induced by the PDA film, is a result of the strong interactions between the PDA carboxylic headgroups and the metal cations in solution. The GID study of templated crystallites under the film indicated strong association with the red phase of PDA. These metal cation – LF interactions are currently being studied in more detail by the authors.

References

[1] A. Berman, and D. Charych, *Adv. Mater* **11,** 296 (1999).

[2] N. Belman, A. Berman, Y. Lifshitz, V. Ezersky and Y. Golan, *Nanotechnology* **15,** S316 (2004).

[3] A. Berman, N. Belman and Y. Golan, *Langmuir* **19,** 10962 (2003).

[4] N. Belman, Y. Golan and A. Berman, *Crystal Growth and Design* (2004), in press.

Authors

A. Berman (a), Y. Lifshitz (a), O. Konovalov (b) and Y. Golan (a).

(a) Ben Gurion University (Israel)

(b) ESRF

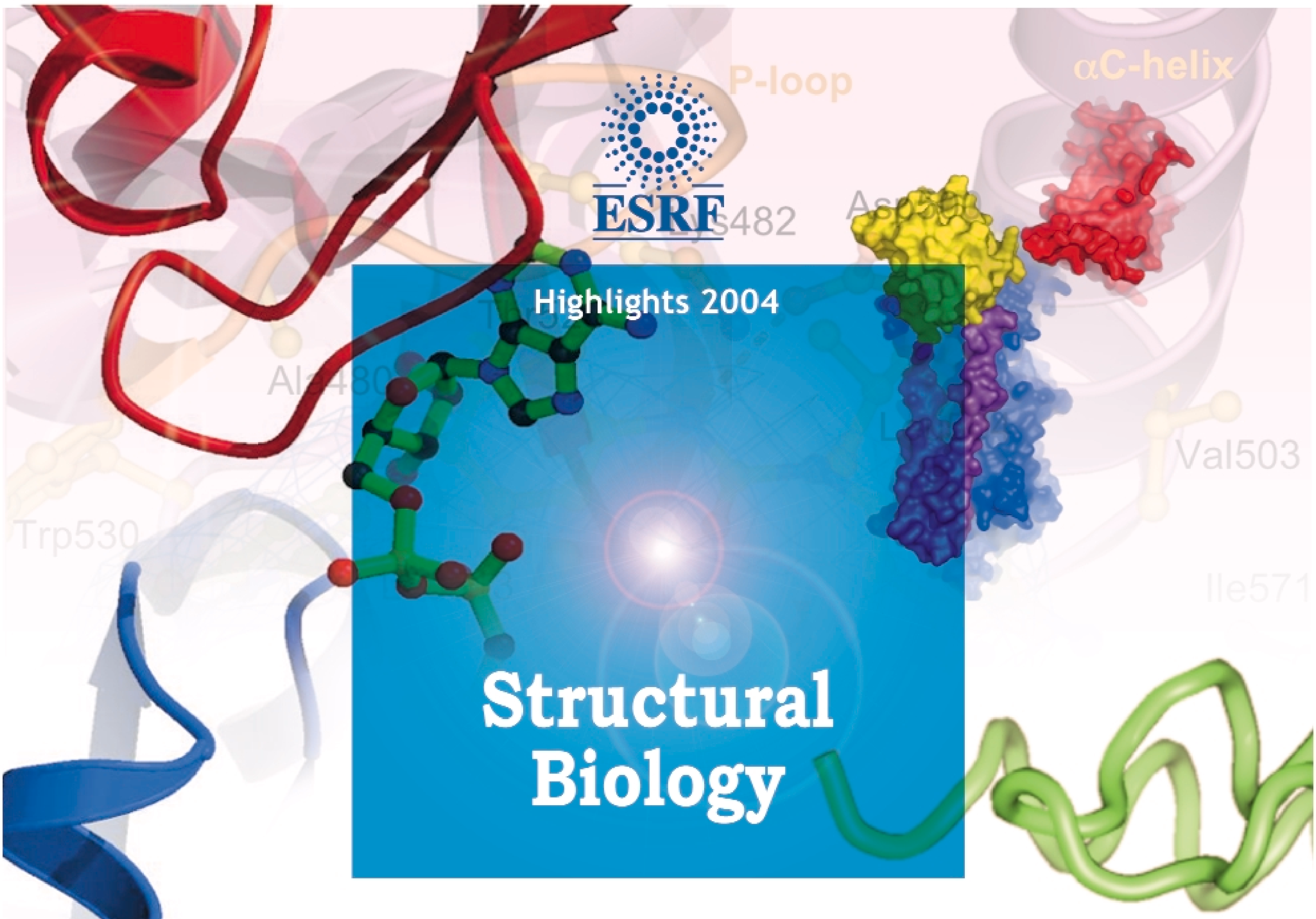

Highlights 2004

Structural Biology

Introduction

2004 was a very busy year at the Macromolecular Crystallography (MX) beamlines of the ESRF (ID14 A&B, ID29, ID23-1). Nearly 600 separate experimental sessions were used and more than 2000 visiting scientists performed experiments at the MX beamlines. About 20% of the experimental sessions involved industrially-related activities, in particular the MXpress service, which continues to go from strength to strength. As in previous years this high throughput of visits and experimental sessions could not be sustained without the excellent support provided by the User and Travel offices, Experiments Division secretarial support and the ESRF Support Groups and Services. Routine operation of the ID23-1 end-station began, as planned, in April 2004 and both provided a valuable new addition to the facilities in the MX beamline portfolio and allowed the number of shifts provided to the User Community to increase slightly at a time when several of our more well-established end-stations were briefly closed to allow the installation and commissioning of new equipment and software designed to further improve their user-friendliness and automation. Almost all the end-stations are now equipped with micro- or mini-diffractometers and, in our now annual review of progress towards full beamline automation, J. McCarthy summarises developments in this area (page 69).

The MX External Scientific Programme continues to provide research highlights resulting in publications in Journals of the highest quality and impact. The article by Sørensen *et al.*, page 56, summarises investigations of conformational changes in the structures of transmembrane cation pumps the results of which originally appeared in Science magazine as did the results of studies on bacterial nitric oxide (NO) signalling by Nioche *et al.*, page 58. As NO signalling is vital to the efficient functioning of drugs such as Viagra®, the interest in this latter work is perhaps understandable!

Also presented here are other examples of Structural Biology research, of interest to both the scientific community and the general public alike, such as the crystal structures of a human rhinovirus (the cause of the common cold) bound to a fragment of its cellular receptor (Verdaguer *et al.*, page 59) and those that allowed the elucidation of the structure of heamagglutinin of the 1918 Influenza virus (Gamblin *et al.*, page 60). The results of this latter work were extensively reported in the news media as they provided an explanation of the virulence of the 1918 'flu pandemic that caused the death of an estimated 20 million people. Also of general public interest was a report by the Cancer Genome Project (Wan *et al.*, page 62) describing investigations into the effects of point mutations on the activity of the product of the B-RAF gene. Several such mutations convert B-RAF into an oncogene and the results of this work provided structural reasons for this. This latter work was carried out on ID13 and illustrates how some ESRF beamlines that are not dedicated full-time to MX can also provide significant contributions to the field. The CRG beamlines BM14, BM16 and BM30A, also provided significant amounts of beamtime for use in the External Scientific Programme of the ESRF. An excellent example of the science performed on the these beamlines is the report by Stuart *et al.* (page 63), describing the analysis of the structures, in different catalytic states, of the virus motor protein P4 which packages RNA in bacteriophage Φ12. These studies provide the first insights into the mechanism of the active packaging of RNA in viral capsids.

The In-House research carried out by the scientists, post-doctoral researchers and Ph.D. students associated with the MX beamlines also continues to develop apace. As ever this is based upon three building blocks: methods development; collaboration with external groups and the ESRF MX Group's own projects centring on the structural genomics of the radiation-resistant bacterium *Deinococcus radiodurans*. Three reports included here illustrate the two former aspects: The report by Ravelli *et al.* (page 64) shows how methodological developments – particularly those exploiting radiation damage – can help tip the balance between success and failure for difficult, but biologically-interesting projects. That by Brzezinski *et al.* (page 65) is the first fruit of a collaboration between ESRF scientists and those at the University of Stockholm, the aim of which is the development of a bacterial biosensor that will allow the detection of carcinogenic nitroaromatic compounds. Finally, the article by Alzari *et al.* (page 67) sheds light on the structure and mechanism of Glycogen Synthase, an important enzyme involved in one of the metabolic pathways used for the catalytic conversion of glycogen which is the major source of energy in most living organisms.

What does 2005 hold in store for MX activities at the ESRF? The construction and commissioning of ID23-2 will be completed during the second half of the year. This microfocus beamline will provide a welcome and significant addition the facilities available at the ESRF. Additionally, the new laboratory building for the Partnership for Structural Biology (PSB) will be completed, providing a new focus for Structural Biology both for the ESRF in particular and the Grenoble campus in general. Finally, efforts in beamline automation will continue: During 2005 *all* the MX beamlines (including the new ID23-2 end-station) will be equipped with ESRF/EMBL sample changers. This represents another significant step to the full automation of the MX beamlines so eagerly awaited by both ESRF scientists and external users alike.

G. Leonard and S. McSweeney

Loading the Calcium Pump

Cation pumps maintain the electrochemical gradients of cations across biomembranes. These membrane proteins are also known as P-type ATPases due to their use of a phosphoenzyme intermediate in a functional cycle driven by ATP hydrolysis [1]. Prominent examples of cation pumps in higher organisms include the Na^+,K^+-ATPases, which maintain the membrane potential in animals and the ability to perform secondary transport, the H^+,K^+-ATPases which are the acid pump of the stomach, and the Ca^{2+}-ATPases, which maintain calcium levels as required for the use of this cation in signalling. We are studying rabbit SERCA1a, a 110 kDa Ca^{2+}-ATPase isolated from the membrane of sarco(endo)plasmic reticulum from fast-twitch muscle. This protein pumps Ca^{2+} from the cytoplasm to the lumen, thereby terminating the activity of myosin-actin filaments. It represents an attractive model system of the P-type ATPases. Our aim is to obtain crystal structures of its defined functional states and thus to address the general question on how Nature has devised a cation pump running on ATP.

The functional cycle of SERCA, and the P-type ATPases in general, is typically depicted by E1 and E2 states. A Ca_2E1 state is adopted upon binding two cytoplasmic Ca^{2+} ions [2]. When further supplied with ATP, γ-phosphoryl transfer to the conserved Asp351 residue takes place and the $Ca_2E1{\sim}P$ state is reached representing the high-energy intermediate state of the cycle. Formation of this state is coupled with the occlusion of the two bound Ca^{2+} ions, thereby preventing an unprofitable backflow to the cytoplasm once energy is being spent. This coupling mechanism is probably general in the P-type ATPases. From the

$Ca_2E1{\sim}P$ state the cycle proceeds through downhill transitions associated with the release of the two Ca^{2+} ions on the other side of the membrane in the E2P state, binding of counter-cation (protons for Ca^{2+}-ATPase) and an auto-catalysed dephosphorylation leading to the E2 state.

We have studied the transition to the $Ca_2E1{\sim}P$ state by determining the crystal structures of calcium-bound complexes with *i)* the non-hydrolysable ATP analogue AMPPCP, and *ii)* ADP:AlF_4^- which mimics the γ-phosphoryl transfer reaction. Data extending to 2.6 Å resolution on the Ca_2E1-AMPPCP form was obtained at beamline **ID29** allowing proper density modification of experimental phases (derived from a lead-derivative crystal), and refinement of the structure. Our biochemical data further show that the ADP:AlF_4^- complex mimics the true $Ca_2E1{\sim}P$ state very closely, as indicated by the efficient occlusion of bound Ca^{2+}. Based on the crystal structures we are therefore in a position to study the general mechanism of phosphoryl transfer and its coupling to cation occlusion in the P-type ATPases.

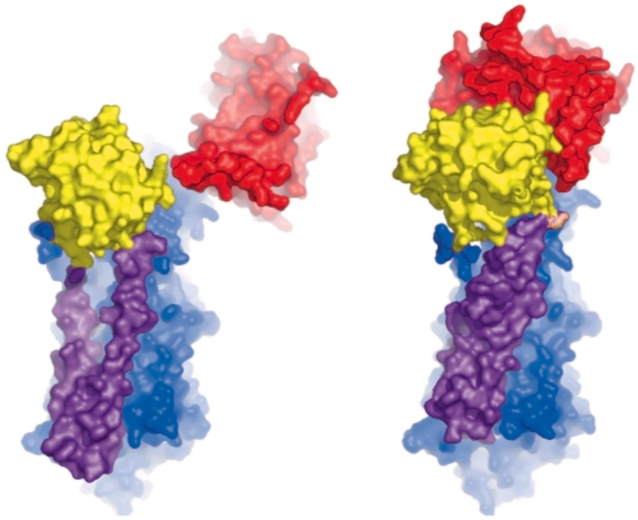

Fig. 67: Comparison of the Ca_2E1 state (left [2]) and the $Ca_2E1{\sim}P$ state (right). The A- and N-domains are shown in red and yellow, respectively, and the P-domain as well as the M3-M10 segment in blue. The mobile M1-M2 segment is shown in purple. The large conformational changes result from ATP binding and phosphoryl transfer, and close the cytoplasmic entry to the Ca^{2+} binding sites.

The overall structures of the AMPPCP and ADP:AlF_4^- complexes are similar showing a compact arrangement of the three cytoplasmic domains (A, P and N) relative to the 10 transmembrane segments (M1 through M10) as seen in **Figure 67**. A comparison with the nucleotide-free Ca_2E1 state reveals that large domain movements are induced upon ATP binding leading to a compact arrangement. A closer look at the nucleotide binding pocket in the AMPPCP complex reveals the rationale of phosphoryl transfer as the result of an octahedral coordination to a Mg^{2+} ion involving the γ-phosphate group and the Asp351 side chain as ligands. This arrangement places the side chain of Asp351 in a position for in-line attack (**Figure 68**). The conformational changes associated with the assembly of the phosphoryl transfer site are transmitted via a rotation of the A-domain to translation of the M1-M2 segments relative to M3 through M10. In this way a cytoplasmic entry to the two Ca^{2+} binding sites in the membrane is sealed off and occluded by residues of M1 and M2 (Figure 67). Our structure thus explains the coupling mechanism of P-type ATPases.

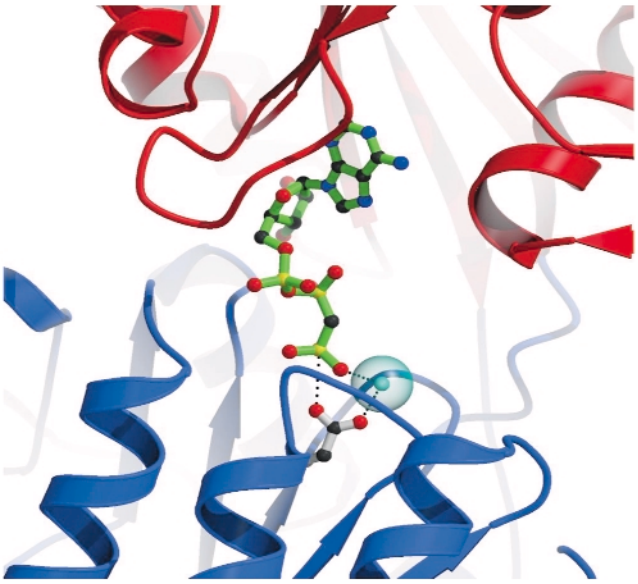

Fig. 68: Details of the nucleotide binding pocket in the Ca_2E1-AMPPCP complex showing that ATP binding (represented by AMPPCP in green sticks) joins the cytoplasmic N and P-domains (red and blue ribbons, respectively). The γ-phosphoryl transfer from ATP to the Asp351 side chain (white sticks) is facilitated by coordination of these groups as ligands to a Mg^{2+} ion (cyan sphere).

References

[1] J.V. Møller, B. Juul, M. le Maire, *Biochim. Biophys. Acta* **1286**, 1-51 (1996).

[2] C. Toyoshima, M. Nakasako, H. Nomura, H. Ogawa, *Nature* **405**, 647-655 (2000).

Principal Publication and Authors

T.L. Sørensen, J.V. Møller, P. Nissen, *Science* **304**, 1672-1675 (2004).

University of Aarhus (Denmark)

Crystal Structure of a Bacterial Sensor: Nitric Oxide Signalling Unveiled

Nitric oxide (NO) has emerged as an important gaseous molecule that can influence a plethora of cellular functions [1]. Specifically, NO signalling is indispensable for the proper functioning of drugs like Viagra® and Cialis® used in the treatment of erectile dysfunction. In humans, NO is generated from the amino acid L-arginine by the enzyme nitric oxide synthase [2]. Physiological actions of NO are mediated by its heme protein sensor, soluble guanylyl cyclase (sGC), which gets activated upon binding NO –up to 400-fold above basal level– and catalyses the conversion of guanosine triphosphate to cyclic 3',5'–guanosine monophosphate (cGMP) [3]. The primary function of sGC-derived cGMP is to trigger smooth muscle relaxation. Nearly 150 million men worldwide suffer from erectile dysfunction due to decreased NO production in the penile tissue and, therefore, fail to generate adequate amounts of cGMP. Both Viagra® and Cialis® enhance the erectile response by inhibiting the penile tissue-specific enzyme, phosphodiesterase-5, from breaking down cGMP. Although the basic mechanisms have been worked out, the structural basis for how NO activates sGC has remained elusive for nearly three decades.

Whereas the function of NO in humans is well established, its signalling role in bacteria is incompletely understood. Some bacteria generate NO from nitrite during a distinctive mode of respiration known as denitrification. Those lacking the machinery to produce NO find it to be toxic and utilise a molecular armamentarium to protect them from this poison. Indeed the century-old practice of nitrite curing of meats derives from the fact that NO is extremely toxic to *Clostridium botulinum* – the etiological agent of Botulism. The molecular strategies utilised by *C. botulinum* to detect and avoid NO in its natural habitats are unknown.

We have succeeded in discovering the link between cGMP generation in humans and bacterial NO sensing mechanisms. We accomplished this by first proving the hypothesis that some bacteria harbour a NO sensing protein (SONO, sensor of NO) with striking resemblance to the NO-binding heme domain of sGC. Overexpression and purification of SONO resulted in a red-coloured protein containing a heme prosthetic group. Our work further demonstrated that SONO from *C. botulinum* has femtomolar affinity for NO. SONO purified from other bacteria (cyanobacteria and *Vibrio cholerae*), however, do not exhibit this extreme binding affinity. In light of its sequence similarity with sGC and specificity for NO, SONO is an excellent model system to understand the structural basis of gaseous messenger signaling.

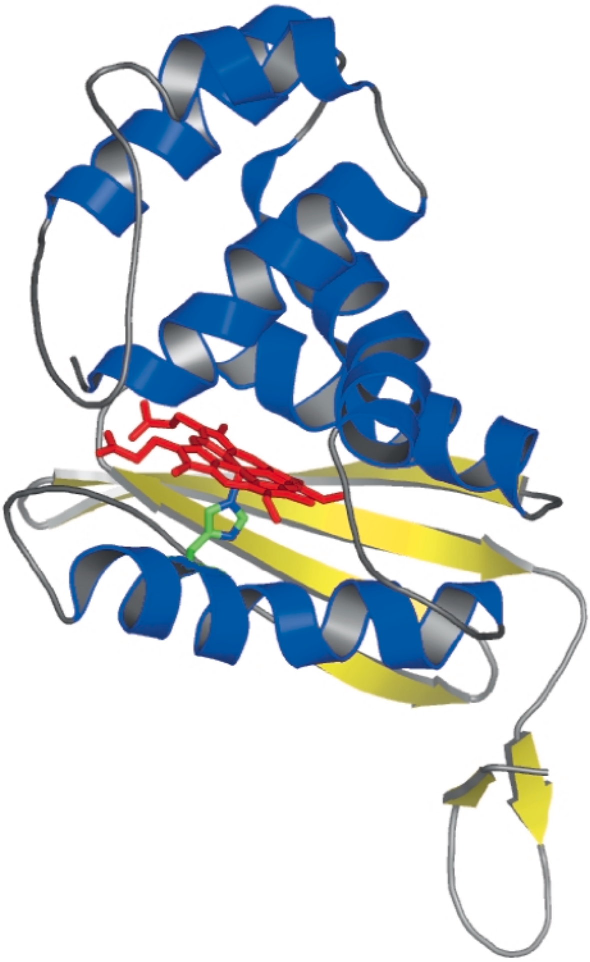

Fig. 69: Crystal structure of *T. tengcongensis* SONO. The heme group is shown as a stick model.

We have determined the X-ray structure of *Thermoanaerobacter tengcongensis* SONO (39% sequence identity to *C. botulinum* SONO), at 2.5 Å resolution, using multiwavelength anomalous dispersion data from cubic crystals collected at the Fe *K*-edge at beamline **ID29** of the ESRF. The three-dimensional structure of SONO is novel. It comprises an α-helical distal domain and ß-strand-rich proximal domain (**Figure 69**) with the heme nestled in between the two domains. The heme iron is coordinated by a highly-conserved histidine residue in the protein (**Figure 70**). Molecular recognition of heme is mediated by the electrostatic interaction between the propionate groups and conserved protein side chains. The structure also reveals a strategically located tyrosine side chain in the distal heme pocket for hydrogen bonding to NO (Figure 70). This residue is conserved in the *C. botulinum* protein and explains its strong binding affinity for NO. However, SONO from other bacteria and mammalian sGC have a hydrophobic distal pocket. Based on the high overall temperature factors for the distal domain, we posit that it undergoes conformational changes when NO binds to the heme.

Our structural analyses advances the conclusion that this domain's counterpart in mammalian sGC is poised

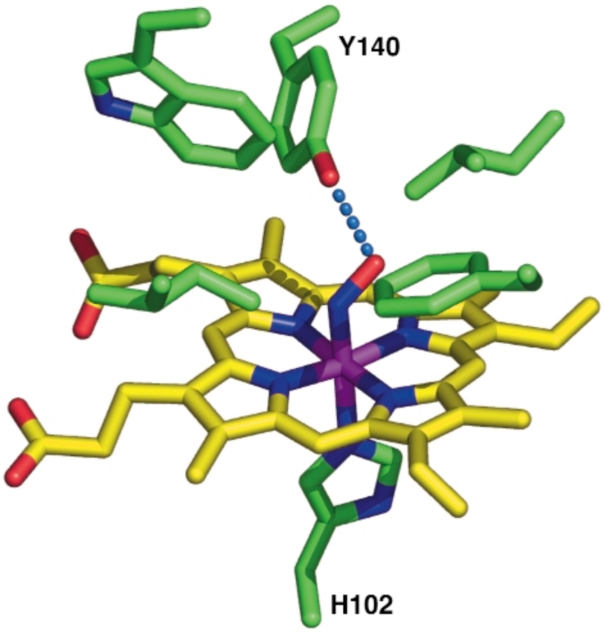

Fig. 70: A close-up view of the distal heme pocket highlighting the tyrosine side chain, which interacts and stabilises the heme-bound NO.

to interact with the cyclase for signal transduction. By determining the crystal structure of a closely related bacterial sensor, we have gained insights into the inner workings of sGC and its ability to get activated by NO. Our structure will also help with identifying novel binding modes of activators that function independently of NO. Furthermore, our work provides clues to the 75-year old question: How does *C. botulinum* recognise and shun NO? In the grand scheme of things, this study has opened new vistas for additional research into signalling by gaseous messengers.

References

[1] F. Murad, *Angew. Chem. Int. Ed. Engl.* **38**, 1856 - 1868 (1999).
[2] C.S. Raman, P. Martásek, and B.S.S. Masters *The Porphyrin Handbook,* **4**, 293 – 340 (2000).
[3] D. Koesling, M. Russwurm, E. Mergia, F. Mullershausen, A. Friebe, *Neurochem. Int.* **45**, 813 – 819 (2004).

Principal Publication and Authors

P. Nioche (a), V. Berka (a), J. Vipond (b), N. Minton (c), A.L. Tsai (a), and C.S. Raman (a), *Science* **306**, 1550 – 1553 (2004).
(a) University of Texas – Houston Medical School (USA)
(b) Health Protection Agency (UK)
(c) University of Nottingham (UK)

X-ray Structure of a Minor Group Human Rhinovirus Bound to a Fragment of its Cellular Receptor Protein

Human rhinoviruses (HRVs) are the main cause of mild upper respiratory disease, usually termed the common cold. The infectious agent is a small icosahedral particle ~300 Å in diameter, composed of a protein shell that encapsidates a single positive RNA strand. The capsid is built from sixty copies, each of four viral proteins VP1, VP2, VP3 and VP4. The first three form the external surface, whereas VP4 is an internal protein in contact with the viral RNA. With more than one hundred immunologically distinct serotypes, HRVs form the largest genus amongst the *picornaviridae* family. About ninety percent of the HRV serotypes, the major group, use intercellular adhesion molecule 1 (ICAM-1) for cell entry. The remaining serotypes, the minor group, bind to different members of the low-density lipoprotein receptor (LDLR) family. Both receptors are functionally and structurally unrelated. ICAM-1 belongs to the immunoglobulin (Ig) superfamily of proteins whereas the ligand binding domains of LDL receptors are composed of several imperfect direct repeats of about 40 amino acids in length, stabilised by three disulfide bonds and containing a conserved cluster of acidic residues near its C terminal end that coordinates a Ca^{2+} ion.

The first X-ray structures of intact picornavirus particles, those of a major group rhinovirus HRV14 and of a human poliovirus, revealed a deep cleft or ‘canyon’ surrounding each pentagonal vertex of the icosahedral shells. This ‘canyon’ is used by most picornaviruses as an attachment site for binding to their receptors, which typically have Ig-like domains. Three-dimensional electron microscopy image reconstruction techniques provided low resolution images of different rhinovirus-receptor complexes that illustrate this mode of receptor recognition for the major group human rhinoviruses and enteroviruses [1]. In contrast, the receptors for minor group rhinoviruses were shown to bind on a star-shaped dome at the tip of the five-fold vertex [2]. However, high-resolution structures of virus-receptor complexes are required in order to identify the critical interactions that determine the receptor recognition specificity.

We determined the co-crystal structure of a minor group human rhinovirus HRV2 with a fragment of one of its receptors, modules 2 and 3 of the very-low density lipoprotein receptor (VLDR). We collected data from three crystals on beamlines **ID14-4** and **ID29** to a resolution of 3.5 Å and solved the structure by molecular replacement. The averaged maps of the complex showed the presence of only one module of the receptor contacting the viral

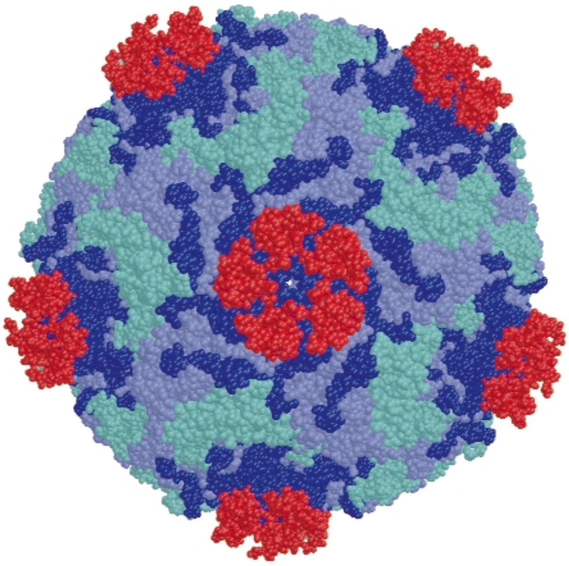

Fig. 71: The structure of the HRV2-V3 complex, shown in a space filling representation. Viral subunits VP1, VP2 and VP3 are in blue cyan and lilac respectively and the bound V3 modules are displayed in red. V3 binds outside the "canyon" and close to the virus five-fold vertex. The proximity between the N and C terminal ends of neighbour V3 modules is apparent.

surface. In this structure the C-terminus of one module is situated very close to the N-terminus of the adjacent module around the five fold axis (**Figure 71**) suggesting that more than one repeat in a single receptor molecule might attach simultaneously. The binding face of the receptor module is defined by the acidic calcium-chelating residues and, in particular, by an exposed tryptophan that is conserved in a majority of the modules (**Figure 72**). The attachment site on the virus involves the exposed surface loops BC, DE and HI, derived from two adjacent VP1 subunits, contacting each receptor module at the tip of the fivefold vertex, and one lysine residue in the HI loop, which plays a key roll in receptor recognition. Comparison of the VP1 sequences of all serotypes showed the strict conservation of this lysine in minor group HRVs. The unique combination of hydrophobic and ionic interactions of this lysine seems to be the basis of virus-binding specificity. Nevertheless, other residues in the vicinity must contribute and it is likely that these modulate the affinity of the receptors for the different serotypes.

Fig. 72: Intermolecular interactions between the V3 module of the receptor (red) and the viral VP1 proteins from two adjacent protomers (dark blue and turquoise, respectively). The Ca^{2+} ion is represented as a yellow sphere while chains of the residues directly involved in the virus-receptor interactions are shown as sticks.

References

[1] M.G. Rossmann, Y. He and R.J. Kuhn, *TRENDS in microbiology*, **10**, 324-331 (2002).
[2] E.A. Hewat, E. Neumann, J.F. Conway, R. Moser, B. Ronacher, T.C. Marlovits, and D. Blaas, *EMBO J.* **19**, 6317-6325 (2000).

Principal publication and authors

N. Verdaguer (a), I. Fita (a) , M. Reithmayer (b), R. Moser (b), and D. Blaas (b). *Nat. Struct. Mol. Biol*. **11,** 429-434 (2004).

(a) Institut de Biologia Molecular de Barcelona, CSIC Barcelona (Spain)
(b) Vienna Biocenter, University of Vienna (Austria)

The Structure and Receptor Binding Properties of the 1918 Influenza Haemagglutinin

An estimated 20 million people died in the influenza pandemic of 1918. The virus responsible probably originated from an avian virus that was introduced into the human population. The ability to be passed from human to human, coupled with a novel antigenicity, was a crucial factor in this virus being able to cause such devastation. Haemagglutinin (HA) is a surface glycoprotein of Influenza A viruses that mediates both viral binding to host cells and the subsequent membrane fusion required for virus invasion. Antibodies that block these activities neutralise virus infectivity. So HA plays an important role in defining the characteristics of the 1918 virus. Therefore, we have structurally characterised the 1918 HA to investigate features of the molecule that may have contributed to the explosive nature of the 1918 pandemic. We have also determined the structures of HA from the first swine influenza virus that was isolated in 1930, and from one of the first human influenza viruses that was isolated in 1934.

There are 15 antigenic subtypes of HA (H1-H15) all of which are found on influenza viruses that infect avian

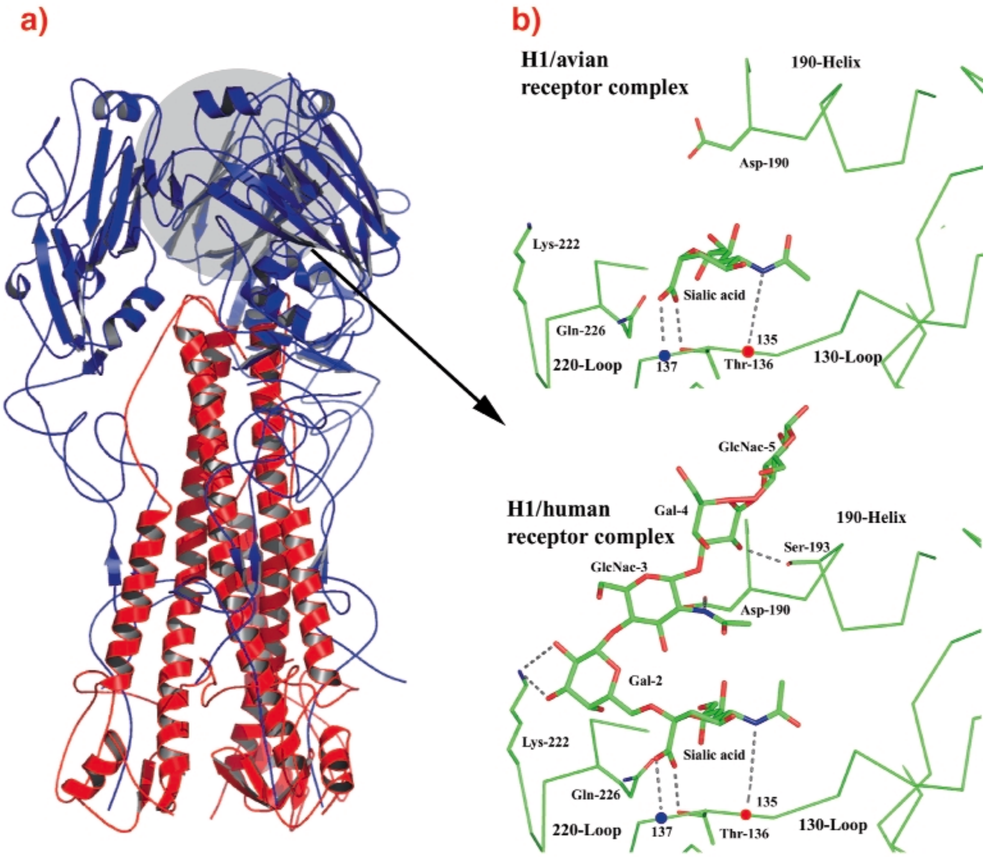

Fig. 73: a) Ribbons diagram of the trimer of 1918-human HA, coloured blue and red for the two polypeptides that form each subunit. b) 1930-swine HA receptor-binding site in complex with avian receptor and with human receptor. Two of the five HAs reported from 1918 viruses have receptor-binding sites indistinguishable from those of 1930-swine HA. The other three 1918 HAs differ only at residue 225.

species. Only three human influenza viruses have caused pandemics in the last century and each contained a different HA (H1 in 1918, H2 in 1957 and H3 in 1968).

The cellular receptors that HAs recognise are sialic acids linked to cell-surface glycoproteins and glycolipids. All subtypes of HA found in avian species prefer binding to sialic acid in an α2,3-linkage to galactose. In contrast, the HAs of human viruses recognise sialic acid in α2,6-linkage. As a consequence, the cross-species transfer of avian viruses into humans that results in pandemics requires a change in binding specificity.

The mechanism that human viruses have used to achieve these changes appears to be different for different subtypes. For the HAs of the H2 and H3 human viruses a minimum of two changes in binding site amino acids, Gln-226->Leu and Gly-228->Ser, correlate with the shift from binding avian to binding human receptors. In contrast, HAs of human H1 viruses (including the 1918 virus) acquire binding to human receptors whilst retaining Gln-226 and Gly-228.

To analyse the mechanisms of receptor binding and the structural basis of receptor specificity in the H1 subtype we determined the structures of α2,3- and α2,6-linked sialyl pentasaccharides as analogues of avian and human receptors respectively, in complex with the 1934 human HA and the 1930 swine HA. We then compared these structures to the 1918 HA (**Figure 73**).

Overall, the results suggest that the ability of the 1918 virus to bind human receptors, and thus its ability to spread in the human population, is attributable to the distinct geometry of the 1918 HA receptor binding site and the novel positioning of residues 226 and 228.

By recognizing human receptors, the human-1918 HA fulfils the first requirement of an epidemic virus – the ability to spread in the human population. The importance of this requirement is emphasized in the 1997 and 2004 outbreaks of H5 "chicken" influenza in Asia where the virus is extremely virulent for both chickens and humans, but has not acquired the ability to bind α2,6-linked sialosides and is therefore unable to spread. With the ability to ensure the efficiency of the initial stages of virus infection, coupled with novel antigenicity, the human-1918 HA may alone have been sufficient to generate the high pathogenicity of the 1918 pandemic virus.

Principal Publication and Authors

S.J. Gamblin (a), L.F. Haire (a), R.J. Russell (a), D.J. Stevens (a), B. Xiao (a), Y. Ha (b), N. Vasisht (a), D.A. Steinhauer (a), R.S. Daniels (a), A. Elliot (a), D.C. Wiley (b) and J.J. Skehel (a), *Science* **303**, 1838-1842 (2004).

(a) Medical Research Council (MRC) National Institute for Medical Research, London (UK)
(b) Howard Hughes Medical Institute, Harvard University, Cambridge, MA (USA)

Investigating the Molecular Mechanism of Oncogenic Mutations of B-RAF

Cancer is a genetic disease in which changes in the DNA of a gene cause alterations in the properties (or amounts) of the encoded protein, disrupting its normal function in the regulatory processes that control the homeostasis and development of a healthy cell. The Cancer Genome Project is a systematic effort to identify all the genetic abnormalities that contribute to the development of cancer.

In the first stage of this genome-wide screen for mutated genes, Futreal and colleagues identified somatic mutations in the *B-RAF* gene [1]. This discovery was significant because *B-RAF* encodes a serine/threonine protein kinase that is a critical component of a signalling pathway (the MAP kinase pathway) that promotes cell growth and proliferation. In healthy cells, this is activated only in response to growth signals. Furthermore, the gene encoding the RAS protein, which activates normal B-RAF, is itself mutated to an oncogene in 15% of human cancers. *B-RAF* mutations are particularly prevalent in cutaneous malignant melanoma, being associated with 60% of such tumours, and also occur with moderate to high frequency in colorectal, ovarian and papillary thyroid carcinomas. These findings implicate activating oncogenic mutations of *B-RAF* as critical promoters of malignancy. Since the initial discovery [1], extensive analysis of the *B-RAF* gene associated with human cancers has identified over 30 single site missense mutations, mostly located within the kinase domain, clustered to two regions; the glycine-rich P-loop of the N-lobe, and the activation segment. Significantly, a glutamate (E) for valine (V) substitution at residue 599 in the activation segment accounts for 90% of *B-RAF* mutations in human cancers. The V599E mutant of *B-RAF* possesses the hallmarks of a conventional oncogene. The kinase activity of this mutant protein is elevated greatly, it constitutively stimulates the MAP kinase pathway *in vivo* independent of RAS, and potently transforms NIH3T3 cells. Similarly to the ^{V599E}B-RAF mutant most other, although significantly not all, B-RAF mutants that have been characterised biochemically, have elevated kinase activity.

To understand how activating mutations alter the conformation of B-RAF, and hence stimulate its kinase activity, we crystallised the B-RAF kinase domain and determined its structure with X-ray diffraction data collected at the microfocus beamline (**ID13**). The protein was crystallised in complex with a small molecule inhibitor of B-RAF termed BAY43-9006 developed by Bayer pharmaceuticals, and which is currently undergoing phase III clinical trials. Our structural information revealed a unifying hypothesis for the activation of B-RAF kinase activity by diverse B-RAF oncogenic mutations, and provided the first quantitative insights into the mechanism of inhibition of B-RAF by BAY43-9006. The structure we solved of normal B-RAF showed that the kinase domain adopts an architecture characteristic of other members of the protein kinase family, containing two lobes termed the N- and C-lobes (**Figure 74**). Kinases are regulated by changes in their conformation, and the structure of B-RAF revealed that the kinase domain adopted an inactive conformation, being incapable of binding ATP and catalysing MEK phosphorylation. The protein was inactive because a key regulatory region of the enzyme, termed the activation segment, was held in an inactive conformation as a

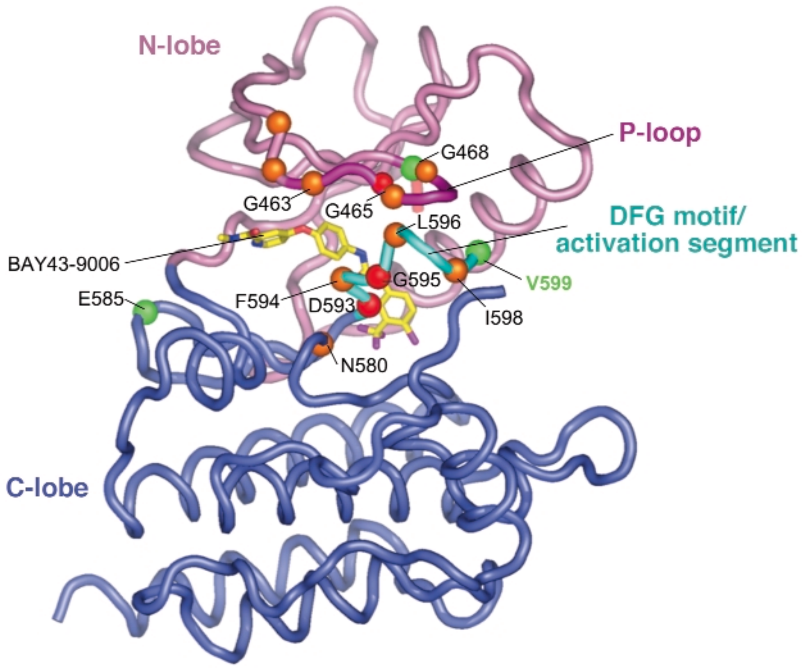

Fig. 74: Overall view of B-RAF kinase domain showing position of mutations (green, orange and red spheres, for high, intermediate and lower activity mutants) located at the P-loop/activation segment interface.

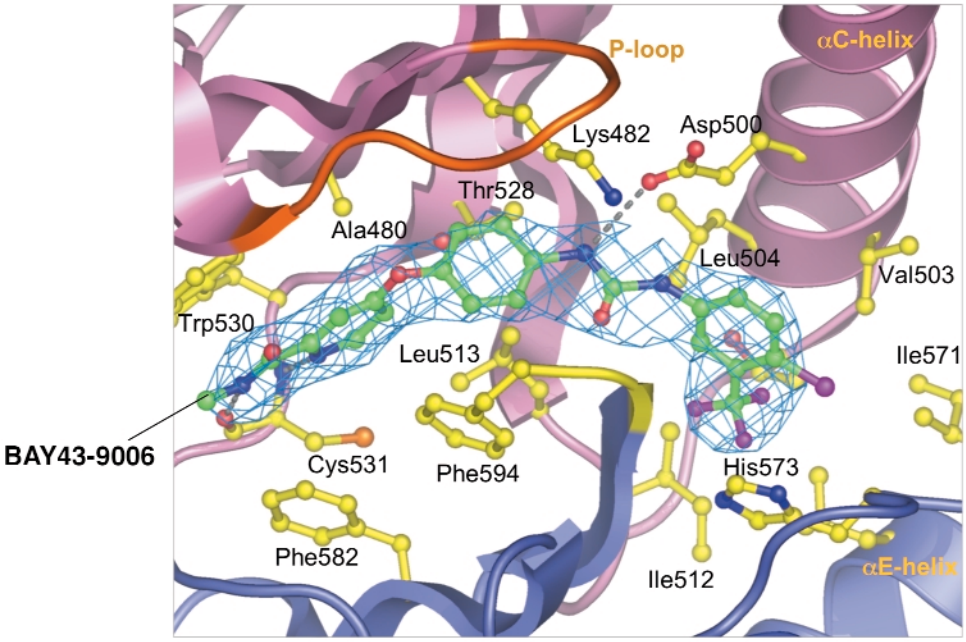

Fig. 75: Close-up view of BAY43-9006 bound to B-RAF.

result of hydrophobic interactions with the P-loop. Significantly, the regions of the activation segment and P-loop that interact with one-another, restraining the activation segment in an inactive conformation, are precisely where the majority of B-RAF oncogenic mutations are clustered. For example, the hydrophobic side chain of valine 599 of the activation segment contacts the side chain of phenylalanine 467 of the P-loop. This indicated that as a result of B-RAF mutations the inactive B-RAF conformation is destabilised thereby promoting an active B-RAF conformation. In addition, we proposed that a glutamate residue at position 599 (accounting for 90% of *B-RAF* mutations) promotes the active conformation by forming favourable electrostatic interactions with a lysine side chain of the αC-helix of the N-lobe (**Figure 75**).

Our structural studies of B-RAF provide new intellectual insights for drug development. In future work we plan to use the structure of B-RAF to develop more specific inhibitors of the kinase, and also to explore the conformations of mutant activating forms of the kinase.

References

[1] H. Davies *et al*., *Nature,* **417**: 949-954 (2002).
[2] P.T.C. Wan, M.J. Garnett, S.M. Roe, S. Lee, D. Niculescu-Duvaz, V.M. Good, C.M. Jones, C.J. Marshall, C.J. Springer, D. Barford, and R. Marais, *Cell,* **116**: 855-867 (2004).

Authors

P.T. Wan, S.M. Roe and D. Barford,
Section of Structural Biology, Institute of Cancer Research, Chester Beatty Laboratories, London (UK)

The Structure of Bacteriophage ϕ12 Packaging ATPase: An RNA Packaging Motor Caught in Action

Genome packaging is an essential step in the life cycle of all viruses. Different strategies ranging from co-assembly of the coat protein with the nucleic acid (like in HIV) to active packaging into pre-assembled capsids have been demonstrated. The dsRNA bacteriophage Φ12 of the *Cystoviridae* family utilise the latter mechanism. The packaging is performed by a virus motor protein P4 at the expense of ATP hydrolysis. The hexameric packaging motor resides at the five-fold vertices of the procapsid (**Figure 76**) and serves as the portals for RNA entry. The role of P4 in the packaging of genomic RNA resembles that of the portal complex encountered in dsDNA bacteriophages. While the dsDNA portal complex relies upon a transiently associated terminase complex for ATPase activity, P4 acts as both the ATPase and the portal ring making it one of the simplest viral packaging motors.

In order to better understand how P4 couples ATP hydrolysis to RNA translocation during genome packaging, we have collected data from a selenomethionine-substituted P4 protein crystal in complex with ADP on ESRF beamline **BM14** to 2.5 Å resolution and solved the structure by the Multi-wavelength Anomalous Diffraction (MAD) method. The P4 subunit is composed of three domains and belongs to the α/β -fold family. The central domain of P4 is a Rossmann-type nucleotide binding domain which is

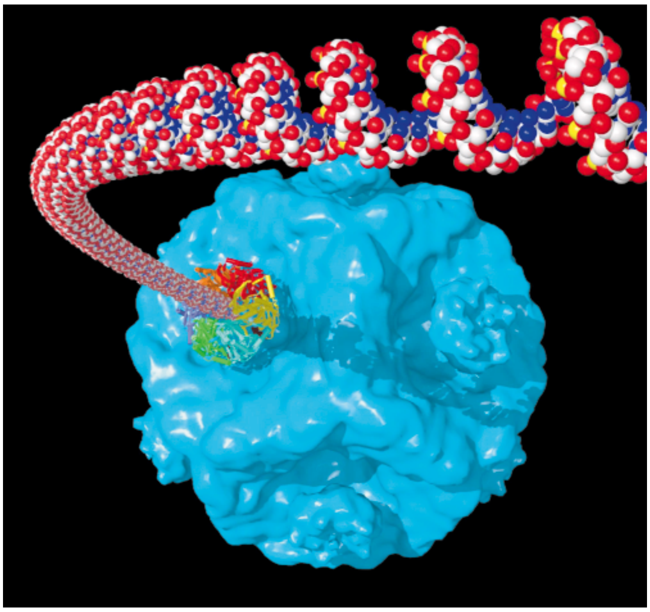

Fig. 76: Illustration of the hexameric ATPase P4 in the act of packaging ssRNA into the procapsid of bacteriophage φ12. A 20 Å icosahedral reconstruction of the φ12 procapsid complex (proteins P1, P2, P4 and P7) is shown in a blue isosurface representation. Density for one of the P4 turrets has been removed and substituted by a subunit coloured P4 hexamer. A-form ssRNA is shown as a cpk model.

structurally similar to that of a large class of hexameric helicases and oligoucleotide translocating enzymes.

To obtain snapshots of the motor protein at different steps on the catalytic pathway we have subsequently generated crystals of φ12 P4 in complex with a panel of different nucleotides (ADP and ATP analogues) and divalent cations. Since the motor is very active, even turning over supposedly non-hydrolysable analogues of ATP at room temperature, some of this work required a careful coordination of low temperature crystallisation and data collection. These structures revealed how ATP, activated by RNA binding, drives RNA translocation through cooperative conformational changes and provided the first insights into the mechanism of active packaging in atomic detail. Furthermore, this provides a model for chemomechanical coupling of this ubiquitous family of proteins of hexameric helicases.

Principal Publication and Authors

E.J. Mancini (a), D.E. Kainov (b), J.M. Grimes (a), R. Tuma (b), D.H. Bamford (b) and D.I. Stuart (a), *Cell* **118**, 743-55 (2004).

(a) Division of Structural Biology, The Henry Wellcome Building for Genomic Medicine, Oxford University (UK)

(b) Institute of Biotechnology, University of Helsinki (Finland).

A Structural Journey into Tubulin Regulation

Microtubules are dynamic components of the cytoskeleton. They rearrange continuously. In particular during cell division, cytoplasmic microtubules depolymerise and reassemble into the mitotic spindle. The heterodimeric $\alpha\beta$ tubulin proteins are the microtubule building blocks. Microtubule dynamics is regulated by intracellular proteins. Among them, stathmin-like domains (SLDs) of stathmin family proteins sequester two tubulin molecules per SLD in a tight complex (T2-SLD). Stathmin phosphorylation destabilises the complex and releases tubulin. Relatedly, phosphorylation of overexpressed stathmin is required for cells to go through mitosis. Microtubule dynamics is also hindered by exogenous ligands, some of which are anti-cancer drugs.

In the course of our structural studies of tubulin regulation, we have reported a partial structure of a T2-SLD complex [1] at 4 Å resolution, determined by molecular replacement using an electron microscopy model of polymerised tubulin. The limited resolution of the data did not allow us to refine the structure free from model bias. We therefore chose to redetermine the structure from scratch, using experimental phases. Combining a large number of native and derivative data sets measured on **ID14-4**, careful data collection taking radiation decay into account [2] and improved crystals, we now have a better defined picture of the complex at 3.5 Å resolution. Three main features have emerged from an analysis of this recent structure.

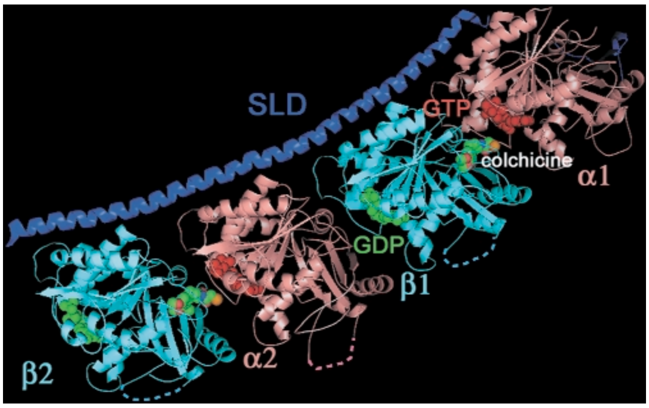

Fig. 77: Overview of colchicine-bound T2-SLD.

In the complex, the two tubulins are in a curved head-to-tail assembly (**Figure 77**). In contrast, tubulins are in a straight conformation in microtubules, in which SLD-bound tubulin is not incorporated. Tubulin monomers comprise three domains: N-terminal, intermediate and C-terminal. A comparison of tubulin monomers in the straight and curved structures reveals that they are related by a 10° rotation of their intermediate domains, which drives a translation of the long central helix connecting the N-terminal and intermediate domains. This translation leads to the steric clashes between adjacet tubulin subunits in the microtubules. To avoid these clashes, the neighbouring subunits reorient to yield a curved structure. These rearrangements form the basis of one of the key features of microtubule dynamics, the fast depolymerisation rate. In microtubules, the intermediate domains are locked in place through lateral contacts between neighbouring tubulins. As tubulin molecules start to disassemble, the lateral contacts neighbouring molecules had established with the leaving ones are lost. Their intermediate domains will rotate, lead to curvature and to further loss of longitudinal and lateral contacts. Microtubule destabilisation ensues as well as accelerated depolymerisation.

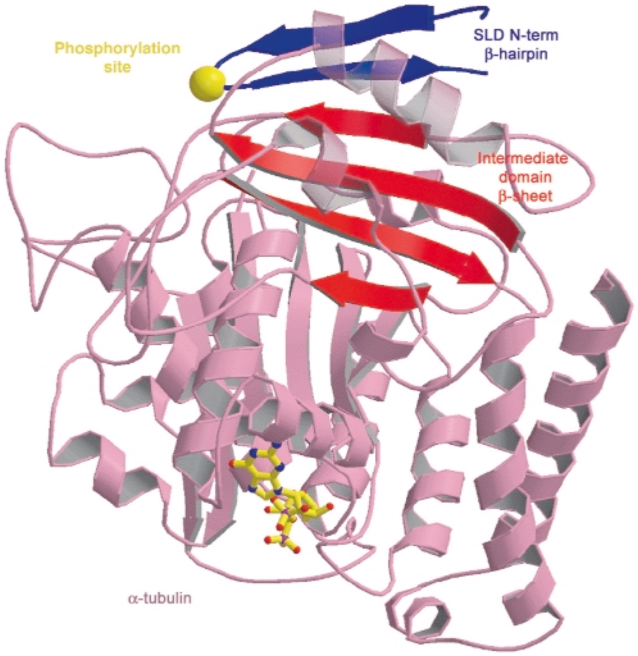

Fig. 78: The SLD N-terminal region caps the α-tubulin end of the T2-SLD complex.

The long C-terminal helix of SLD holds the two tubulin heterodimers together while its N-terminal region provides additional stability to the assembly by interacting with the α monomer located at one end of the complex. The N-terminal region forms a β-hairpin which extends the β-sheet of the intermediate domain of this α subunit (**Figure 78**). The N-terminal region will block, together with the curvature of the complex, incorporation of T2-SLD in microtubules. Interestingly, one of the regulatory phosphorylation sites of stathmin is located in the turn of the N-terminal β-hairpin. An incorporated phosphate group lowers the affinity of stathmin for tubulin, perhaps by destabilising the hairpin.

The structure also elucidates features of the mechanism of colchicine interference with microtubules, as the T2-SLD complex was co-crystallised with this small-molecule tubulin ligand. Colchicine is extracted from the crocus flower *Colchicum autumnale*, whose name derived from Colchis, the living area of the mythical witch Medea. It was widely used to block dividing cells in metaphase well before tubulin was identified as its target. We have localised the colchicine site in the β tubulin subunit at its interface with the α monomer (Figure 77). Colchicine acts as a wedge that prevents tubulin from adopting a straight conformation and thus inhibits microtubule growth. The structure also accounts for the tubulin stabilising effect of colchicine as it crosslinks the α and β monomers, rendering tubulin less prone to inactivation. The identification of this binding site and the light we shed on tubulin regulation opens the way for structure-based design of compounds interfering with microtubule dynamics.

References

[1] B. Gigant, P.A. Curmi, C. Martin-Barbey, E. Charbaut, S. Lachkar, L. Lebeau, S. Siavoshian, A. Sobel, M. Knossow, *Cell*, **102**, 809-816 (2000).

[2] K. Diederichs, S. McSweeney, R.B.G. Ravelli, *Acta Cryst. D*, **59**, 903-909 (2003).

Principal publication and Authors

R.B.G. Ravelli (a), B. Gigant (b), P.A. Curmi (c), I. Jourdain (c), S. Lachkar (c), A. Sobel (c), M. Knossow (b), *Nature*, **428**, 198-202 (2004).
(a) EMBL, Grenoble (France)
(b) Laboratoire d'Enzymologie et Biochimie Structurales, CNRS-UPR9063, Gif-sur-Yvette (France)
(c) U440 INSERM/UPMC, Institut du Fer à Moulin, Paris (France).

Development of a Bacterial Biosensor for Nitrotoluenes: the Crystal Structure of the Transcriptional Regulator DntR

The aim of this project is to develop a whole-cell bacterial biosensor for detection of nitroaromatic compounds, specifically, 2,4-dinitrotoluene (DNT). The sensor is based on a soil bacterium, *Burkholderia sp.* strain DNT, which is capable of using DNT as the sole source of carbon [1]. To digest this compound the bacterium produces enzymes (proteins) upon appearance of the chemical in its environment. The "device" that is used by the bacterium to detect DNT is also a protein, called a transcriptional regulator, in this case DntR. When DNT (the inducer) appears in the bacterial cell it binds to an inducer-binding cavity in DntR, which results in the initiation of reading of a DNA segment (transcription) that codes for an enzyme that is involved in the digestion of DNT. Thus, the bacterium has a feedback system, which is able to sense the compound and, as a result, synthesize enzymes that can degrade the compound. In the prototype biosensor the DNA segment coding for the enzyme was replaced by a segment coding for a green fluorescent protein. Consequently, bacteria containing this construct develop a fluorescent response in the presence of an inducer [1].

The prototype biosensor is sensitive to salicylic acid, which is an intermediate in the oxidative degradation of the aromatic ring in the bacterium. Because its sensitivity and specificity to DNT is too low, the inducer-binding cavity of DntR must be re-designed. One method to achieve this goal is to determine the three-dimensional structure of DntR and then exchange specific amino-acid residues within the cavity such that DNT would fit better.

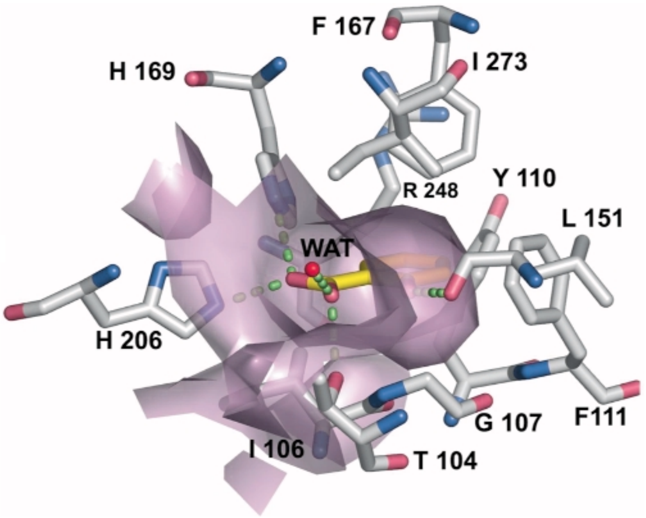

Fig. 79: DntR containing salicylate in the inducer-binding cavities. The surface defined by protein residues is shown in purple. Carbon atoms of amino-acid residues and salicylate are coloured grey and yellow, respectively. Water molecules are shown as red spheres. Hydrogen-bond interactions are shown as green dashed lines.

We determined two crystal structures of DntR, with acetate and thiocyanate respectively, occupying the inducer-binding cavity. In both cases DntR crystallises as a homodimer with a "head-to-tail" arrangement of monomers in the asymmetric unit. The inducer-binding domain of the DntR monomer consists of two sub-domains, each having a Rossman-fold topology. The inducer-binding cavity, with the polar entrance and the largely hydrophobic interior, is found at the interface of the sub-domains. We have positioned salicylic acid in the cavity using the positions of the acetate ions as markers. The model shows that a number of hydrogen bonds and hydrophobic interactions with the side-chains defining the surface of the cavity contribute to the specificity of the salicylate binding (**Figure 79**). Modelling of DNT into the inducer-binding cavity revealed several unfavourable interactions with the cavity surface and points to a number of residues that must be mutated in order to enhance the binding of DNT.

Although the asymmetric units of the crystal structures of DntR contain a homodimer, gel filtration studies demonstrate that DntR is a tetramer in solution. Examination of the packing between molecules in the crystals reveals the structure of a homotetramer in which the inducer-binding domains of DntR adopt a 'head-tail-head-tail' arrangement, similar to that recently reported for CbnR [2], which belongs to the same family of transcriptional regulators (LysR) as DntR and is the only other full-length transcription factor that has been crystallised.

A comparison of the structures of the full-length model of DntR (**Figure 80a**) and that of CbnR shows a difference in the positions of their DNA-binding domains (Figure 80b). This difference is presumably due to an active (DntR) and an inactive (CbnR) conformation of the regulator, with occupied and empty inducer-binding domains, respectively. The observation is in accord with the hypothesis that transcription activation is a result of a decrease in the bend of DNA.

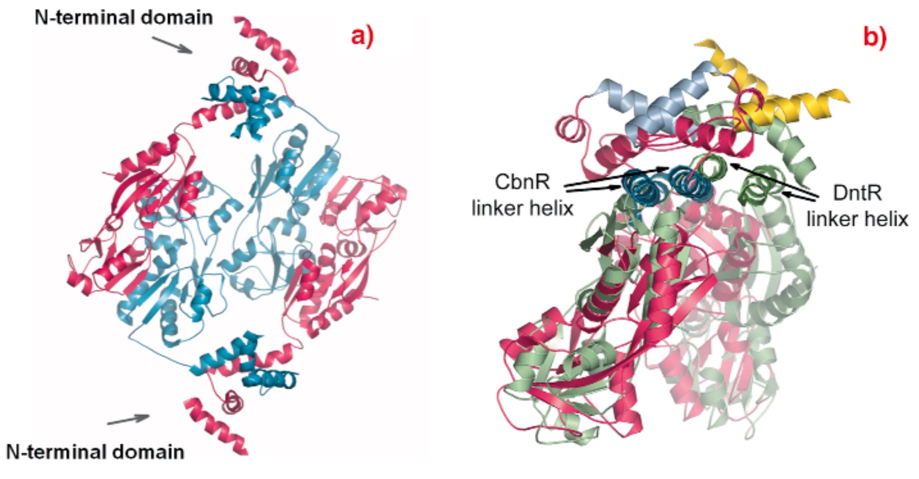

Fig. 80: The structure of the full-length homotetramers. (a) DntR with the inducer-binding domain refined and the N-terminal DNA-binding domains modelled. The monomers in the head-to-head dimers are shown in red and blue. (b) A superposition of the DntR dimer (green ribbons with recognition helices coloured yellow) and the CbnR dimer (red ribbons with recognition helices coloured blue).

In conclusion, we have solved the structure of DntR, which paves the way for the design of a bacterial biosensor for nitrotoluenes. In addition, the structure provides insights into the mechanism of transcription regulation by the LysR regulatory proteins.

References

[1] L.C. Ng, M. Forsman, FOI Research Report (2000) (http://www.foi.se/english/).

[2] S. Muraoka, R. Okumura, N. Ogawa, T. Nonaka, K. Miyashita, T. Senda, *J. Mol. Biol.* **328**, 555-66 (2003).

Principal Publication and Authors

I.A. Smirnova (a), C. Dian (a,b), G.A. Leonard (b), S. McSweeney (b), D. Birse (a,c), P. Brzezinski (a), *J. Mol.Biol.* **340**, 405-418 (2004).

(a) Department of Biochemistry and Biophysics, Stockholm University (Sweden)

(b) ESRF

(c) TGN Biotech Inc., Québec (Canada)

The Crystal Structure of Glycogen Synthase

Glycogen and starch, megadalton-sized glucose polymers, are the major reservoir of readily-available energy and carbon compounds in most living organisms. In mammals, glucose uptake and utilisation are under tight control. Defects in normal glucose handling are associated with a variety of human pathologies such as glycogen storage diseases and diabetes, in which persistent hyperglycemia is correlated with an early onset and increased severity of the disease. The metabolic pathways for the catalytic conversion of glycogen involve several enzymes, among these glycogen synthase catalyses the elongation, and glycogen phosphorylase the breakdown, of α(1,4)-linked glucans. A great wealth of information has been gained on glycogen degradation through the biochemical and structural studies of glycogen and maltodextrin phosphorylases in the last 30 years [1]. These studies have shown that glycogen phosphorylase regulation is a fascinating example of covalent and non-covalent allosterism, exquisitely coordinated by hormonal control. Information describing the tertiary and quaternary structures is now available for practically all the enzymes directly involved in glycogen processing. Surprisingly, very little structural information has been reported on glycogen synthase, which catalyses glycogen elongation through the successive addition of α-(1,4)-linked glucose residues to the polymer's non-reducing end, using ADP/UDP-glucose as glucose donor.

We have now determined the crystal structure of the glycogen synthase from *Agrobacterium tumefaciens* (AtGS) at 2.3 Å resolution, both in its apo-form and in the presence of ADP. The data were collected on **ID29**, and the structure solved using the SAD technique (single wavelength anomalous diffraction), followed by density modification procedures. The protein is found as a dimer in the asymmetric unit, with each monomer comprised of two 'Rossmann-fold' domains (**Figure 81**) that are organised as in the structures of glycogen phosphorylase and other glycosyl transferases of the GT-B superfamily [2]. A deep fissure between both domains contains the catalytic centre. A major difference between mammalian (family GT3) and bacterial (GT5) glycogen synthases, is that only GT3 enzymes are tightly regulated by phosphorylation and non-covalent allosteric modulation. According to the

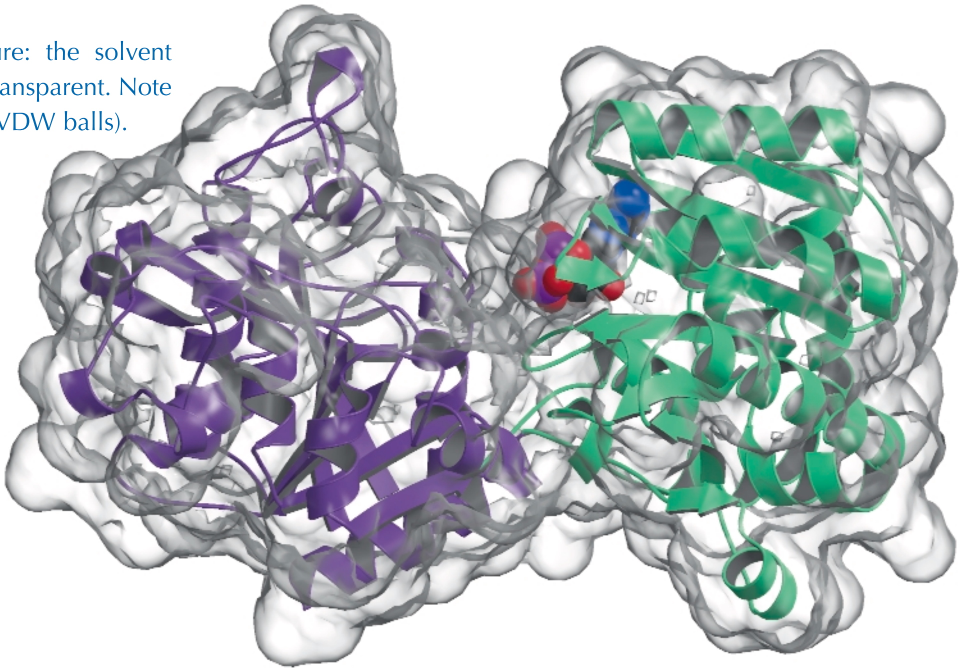

Fig. 81: Glycogen synthase structure: the solvent accessible surface is represented in transparent. Note the bound ADP molecule (drawn as VDW balls).

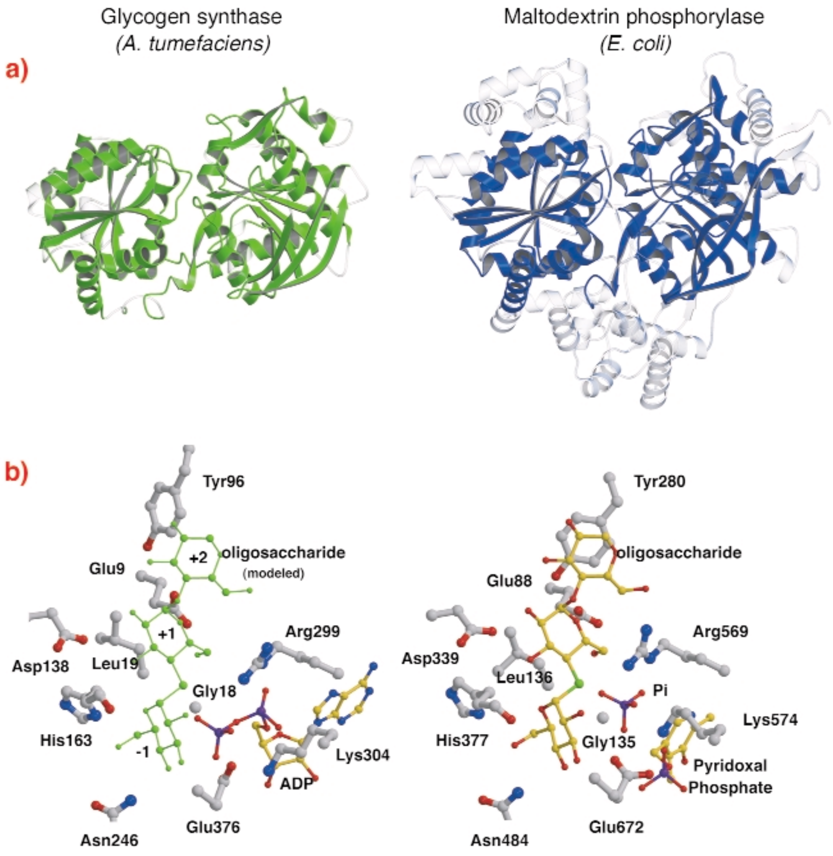

Fig. 82: Homology to glycogen phosphorylase: (a) after structural alignment, superimposed equivalent residues between AtGS and *E. coli* maltodextrin phosphorylase MalP, are represented in solid material (non-aligned regions, in transparent); (b) the catalytic sites of AtGS and MalP.

structure-based multiple sequence alignments among GT3, GT5 and glycogen phosphorylase sequences, the regulatory phosphorylation sites in human glycogen synthase are probably located in the 25-residue N-terminal and 120-residue C-terminal insertions, outside the non-regulated GT-B core of bacterial glycogen synthases. Mutagenesis studies had previously identified two conserved Arg clusters in GT3 enzymes as part of the allosteric site(s) for both the phospho-Ser/Thr residues and the non-covalent activator Glc-6P. The equivalent residues in AtGS are located at one end of the C-terminal domain, far from the reaction centre, indicating a long-distance regulatory effect.

The structure of AtGS shows a striking topological resemblance with the core structures of glycogen/ maltodextrin phosphorylases (family GT35) (**Figure 82a**), even though sequence identities are low (~14%). The structure of each Rossmann-fold domain of AtGS is significantly closer to those of phosphorylases from the GT35 family than to any other nucleotide-dependent glycosyl transferase. Glycogen synthase and phosphorylases also exhibit a strong resemblance at their catalytic sites (Figure 82b). The ADP ribose and the pyridoxal groups lie in equivalent positions, as do the distal phosphate of ADP in AtGS and the inorganic phosphate substrate in phosphorylases. Furthermore, critical amino acids that interact with the substrates' glucose moieties are also conserved. The catalytic mechanism used by glycogen synthases and phosphorylases is therefore probably similar, with subtle changes in structure explaining their overall different functional properties.

The initial suggestion that glycogen synthesis simply represented a reversal of its degradative phosphorolysis was demonstrated to be flawed as Leloir showed that UDP-Glc and glycogen synthase, not Glc-1-P and glycogen phosphorylase, were responsible for polysaccharide elongation [3]. Our work now demonstrates however, that the opposite independent reactions in glucose-glycogen interconversion are catalysed by closely-related homologous enzymes.

References

[1] J.L. Buchbinder *et al.*, *Annu Rev Biophys Biomol Struct* **30**, 191-209 (2001).
[2] P.M. Coutinho *et al.*, *J Mol Biol* **328,** 307-317 (2003).
[3] L.F. Leloir and C.E. Cardini, *J Am Chem Soc* **79**, 6340-6341 (1957).

Principal Publication and Authors

A. Buschiazzo (a), J.E. Ugalde (b), M.E. Guerin (a), W. Shepard (c), R.A. Ugalde (b) and P.M. Alzari (a) *EMBO J*, **23**, 3196-3205 (2004).
(a) Unité de Biochimie Structurale, Inst Pasteur, Paris (France)
(b) Inst de Inv Biotecnológicas, Univ de Gral San Martín, San Martin (Argentina)
(c) ESRF

Beamline Automation

The production of three-dimensional crystallographic structural information of macromolecules can now be thought of as a pipeline that is being streamlined at every stage from protein cloning, expression and purification, through crystallisation to data collection and structure solution. Synchrotron X-ray beamlines are a key section of this pipeline as they are where the X-ray diffraction data are collected, which ultimately leads to the elucidation of macromolecular structures. The throughput of macromolecular crystallography (MX) beamlines may be enhanced significantly with the automation of both their operation and of the experiments carried out [1].

Any automation procedure should include all of the steps shown in **Figure 83**: provision of a suitable X-ray beam onto the sample, the mounting, dismounting and storage of the sample, reduction (integration and scaling) of any data collected, initial structure solution and refinement processes and the linking of synchrotron radiation macromolecular crystallography (SRMX) experiments with home laboratory information management systems. The automation of SRMX facilities can thus be split neatly into two different aspects: those which the user sees and feels directly such as robotic sample changers and information management software, and those hidden from view such as automatic beamline validation and alignment routines. Both aspects are being addressed at the ESRF.

Protocols and software for the automatic alignment of the optical elements of a SRMX facility are essential to ensure its smooth and efficient operation. Automatic beamline alignment (ABA) procedures to achieve this and a historical database that allows monitoring and correction of the optical element positions have been developed. The ABA routines currently implemented or under development on the MX beamlines include calibrating, selecting and maintaining the X-ray energy, focussing the X-ray beam onto the sample position [2] and maintaining the integrity of the X-ray beam by monitoring its position and intensity using X-ray beam position monitors (XBPMs). For efficient automated beamline alignment, it is essential that the position and status of all beamline elements are monitored, stored and compared with those corresponding to an optimum alignment of the beamline. Any significant deviation from this ideal configuration should then trigger a re-alignment of the beamline. At the ESRF, a historical database has been modelled on the comprehensive database that is used in tracking the performance of the storage ring.

The high throughput demanded of today's MX beamlines can only be accomplished by the integration of an automatic sample changer as a beamline component. When installing a sample changer on the beamline one has to consider the automation of all aspects of a MX data collection experiment in order to maximise the benefit from the device:

- Sample identification, tracking and the handling of sample information known before an experiment commences, should allow automatic beamline preparation.
- Characterisation of each sample held in the sample changer (including the determination of unit cell dimensions, Laue Group, orientation matrix and data collection strategy).

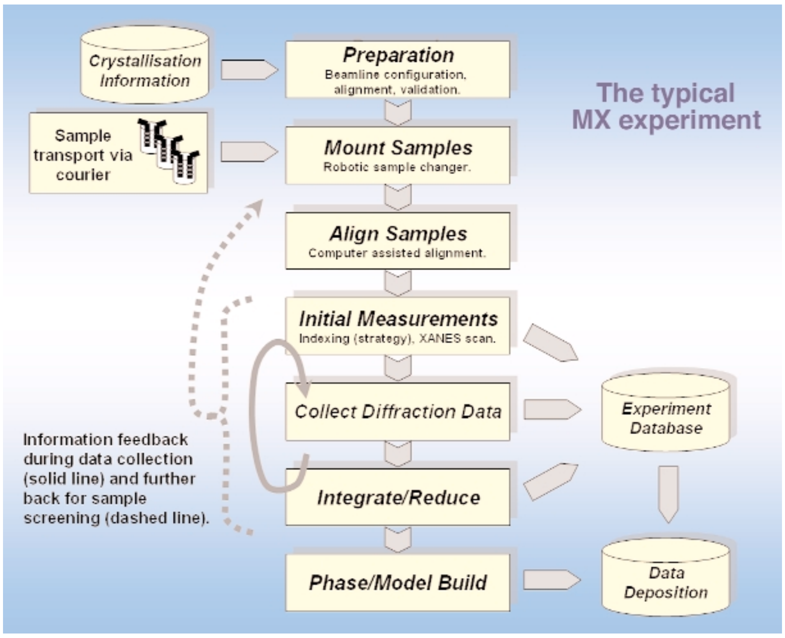

Fig. 83: A typical MX experiment. Each step may be automated and the steps must be linked for a fully automatic experiment.

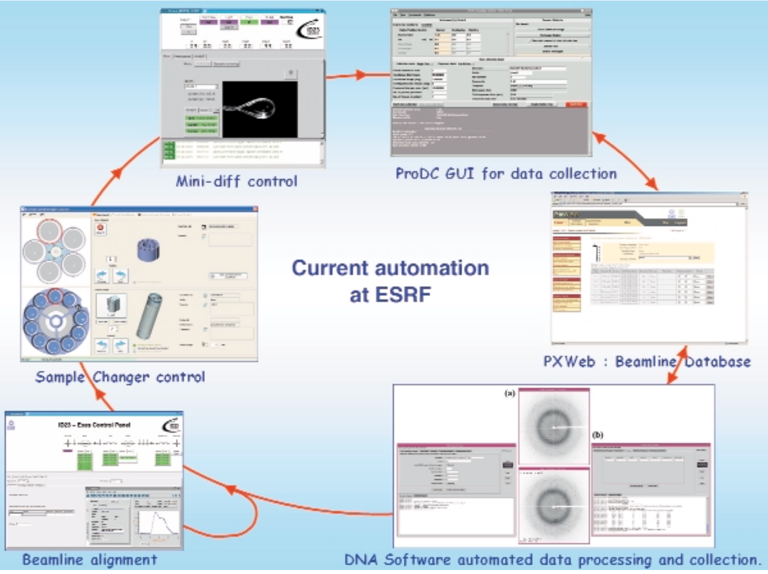

Fig. 84: The current status of automation at the MX beamlines. Each automated step is controlled via different software interfaces.

- Scoring and ranking of the samples contained in the sample changer and the collection and processing of diffraction data.
- Feedback, where intermediate results suggest strategic modifications to the on-going data collection should also be possible.
- Sample and information tracking inevitably involves the use of databases.

The EMBL Grenoble Outstation and the ESRF have developed sample changer robots that can hold up to 50 frozen samples. They will be installed on all ESRF MX beamlines by the end of 2005. The DNA software [3] for automatic crystal characterisation, determination of optimal data collection parameters and the processing of diffraction data is already available on all MX beamlines. The beamline experiment database (PXWeb/ISpyB) allows the submission and tracking of sample information and the exchange of data between the ESRF and the user home laboratory. Extensive tests of this data exchange pipeline are currently ongoing.

The sample changer robots are compatible with the mini- and micro-diffractometers that have been installed on nearly all of the MX beamlines (ID14-2,-3,-4, ID23-1, ID29). These diffractometers incorporate on-beam-axis visualisation of the sample, a high-precision air-bearing phi spindle and automatic sample centring and sample-to-beam alignment capabilities. A motorised mini-kappa system is under development as an add-on for the diffractometer.

The automation effort on the MX beamlines is continuously advancing and the links between each individual module of the MX experiment becoming seamless (**Figure 84**). This push towards increased automation will provide an efficient and effective environment for high-throughput MX.

References

[1] S. Arzt *et al*, *Prog. Biophys. Mol. Biol*. in press.
[2] O. Hignette *et al*, X-Ray Micro- and Nano-Focusing: Applications and Techniques II, *Proceedings of SPIE*, **4499** 105-116 (2001).
[3] http://www.dna.ac.uk

Author

J. McCarthy on behalf of the Joint Structural Biology Group (JSBG) of the ESRF and the EMBL Grenoble Outstation.

Surface and Interface Science

Introduction

While investigations relating to surfaces and interfaces are performed at a number of beamlines around the ESRF storage ring, the three beamlines ID01, ID03, and ID32 of the surface and interface science (SIS) group are highly specialised in this area of research. Resolving structural properties is the predominant goal, because the structure determines many other properties of a material. The X-ray tools are diffraction in grazing incidence geometry at all three beamlines and X-ray standing waves (XSW) at ID32. Work at ID03 and ID32 is mostly concentrated on the picometer scale, *i.e.* the precise atomic structure, whereas investigations at ID01 are more focused on the nanoscale. However, chemical composition as well as electronic and magnetic properties of surfaces and interfaces are also within the reach of the capabilities of the three beamlines. The method of choice is anomalous scattering at ID01, photoelectron- and fluorescence spectroscopy at ID32, and magnetic scattering at ID03.

At the tenth anniversary of the start of user operations in 1994, ID03 could look back at ten years of successful user experiments. ID32 will also celebrate its tenth anniversary of user mode this year, while ID01 will have to wait for another five years until 2010. Some exciting results obtained during the last year are presented in the following pages. They should give a taste of the diversity of scientific applications and the rapid evolution of novel techniques in the SIS group.

An example of “pushing back the limits” is given by the work of S. Ferrer *et al.* showing that hydrogen atoms adsorbed on a metal single crystal can be "seen" by surface X-ray diffraction (SXRD) at **ID03**. Subsequently, they followed the reaction of the Ni(111) surface when exposed to high H_2 pressure under real, catalytic conditions.

The contribution by H.L. Meyerheim *et al*. aids our understanding of the magnetic anisotropy in layered structures, which are used in recording devices and are thus of crucial importance. In the system Ni on W(110), the spin orientation can be changed by a single layer of Fe, while it is reoriented again by the deposition of an additional, single monolayer of Ni. At **ID03** the group found that the spin reorientation is not magneto-elastically driven, because the structural changes are much too small.

X. Torrelles *et al.* used crystal truncation rod measurements to determine the atomic structure of the vicinal "terraced" $SrTiO_3$ (106) surface under UHV conditions at **ID03**. They find an extraordinary order of the surface on the long-range, established by “charge undulations” of neighbouring terraces of opposite electrical polarity, while the surface is disordered on the short range.

Unravelling structural changes at electrode surfaces in contact with aqueous electrolytes is important for the understanding of processes such as corrosion, crystal growth, metal plating, and semiconductor processing. A.H. Ayyad *et al*. applied grazing incidence diffraction at **ID32** to study *in situ* the surface reconstruction before and after homoepitaxial growth of Au on Au (111) from electrolytes. They find an unexpectedly strong compression of the surface layer at certain Au-electrode potentials.

A layer of aluminium oxide on the NiAl(110) surface was investigated using X-ray diffraction by A. Stierle *et al.* at **ID32**. The sample was prepared in their home-lab in Stuttgart and shipped to the ESRF inside the UHV chamber, which was then mounted on the diffractometer. The complexity of the structure of the ultra-thin Al_2O_3 layer, which this experiment revealed, sheds light on the atomic mechanisms acting in corrosion protection or catalysis.

At **ID01**, S. Hazra *et al.* investigated the relationship between the surface morphology, modified by ion-bombardment, and the crystalline interface below, using depth-resolved grazing-incidence diffraction. With increasing dose of the Ar^+ ions they found that the buried subsurface layer is eventually rendered completely amorphous, but retaining a ripple structure that is well replicated at the surface. These results illuminate the ion-solid interaction processes responsible for the formation of nanostructures on metal and semiconductor surfaces. T.U. Schülli *et al.* employed anomalous diffraction at **ID01**. They analysed the (111) superstructure reflections at two complementary energies to study the near surface structure of an EuSe/PbSe epitaxial multilayer. The scattering factor of the thicker PbSe layer, dominating the diffraction pattern at other energies, was suppressed at the Pb MV edge such that the corresponding (111) Bragg intensity of this compound almost vanished. This study convincingly demonstrates the sensitivity of anomalous diffraction to strain and interdiffusion in heteroepitaxial systems with very small lattice mismatch.

Tien-Lin Lee *et al.* combined XSW with photoemission at **ID32** for investigating the room temperature structure of the Ge(111):Sn-√3×√3 surface. The existence of two components in the Sn core level photoemission spectra had given rise to extensive discussions. The work of Lee et al. establishes a link between the chemical state of Sn and the structure. The result supports molecular dynamics simulations that predict a very rapid oscillation of the Sn atoms between two vertical positions.

Finally, we want to briefly comment on the future of the SIS beamlines. ID01 is enjoying successful routine operation and for ID32 a rigorous refurbishment process is almost finished that has dramatically enhanced its potential and attractiveness to users. ID03 has been the world-wide undisputed benchmark beamline for surface X-ray diffraction over the years. A refurbishment is now pending. Furthermore, both scientists at ID03, S. Ferrer and O. Robach, left the ESRF at about the same time. This was an opportunity to review the scientific direction of the SIS group in general. To poll the interest and needs of the SIS user community, a round table discussion and a workshop on surface and interface science was organised in 2004, centred around three issues: 1) surface X-ray diffraction (on ideal and real surfaces) 2) further development of X-ray Standing Wave (XSW) methods for surface and interface structural characterisation (also in combination with XPS) and 3) the possibility of developing hard X-ray photoelectron spectroscopy (HAXPES) at the ESRF. The unanimous opinion of the users and thus the conclusion of the workshop was that no major change in the program of ID01 should be envisaged and the ongoing refurbishment of ID32 should be completed, further enhancing the spectroscopic capabilities of the beamline. The SIS community expressed very strong interest in keeping ID03 as the leading beamline for surface X-ray diffraction. This view was adopted by the ESRF management and a refurbishment of ID03 will be carried out during the next two to three years.

T. Metzger / J. Zegenhagen

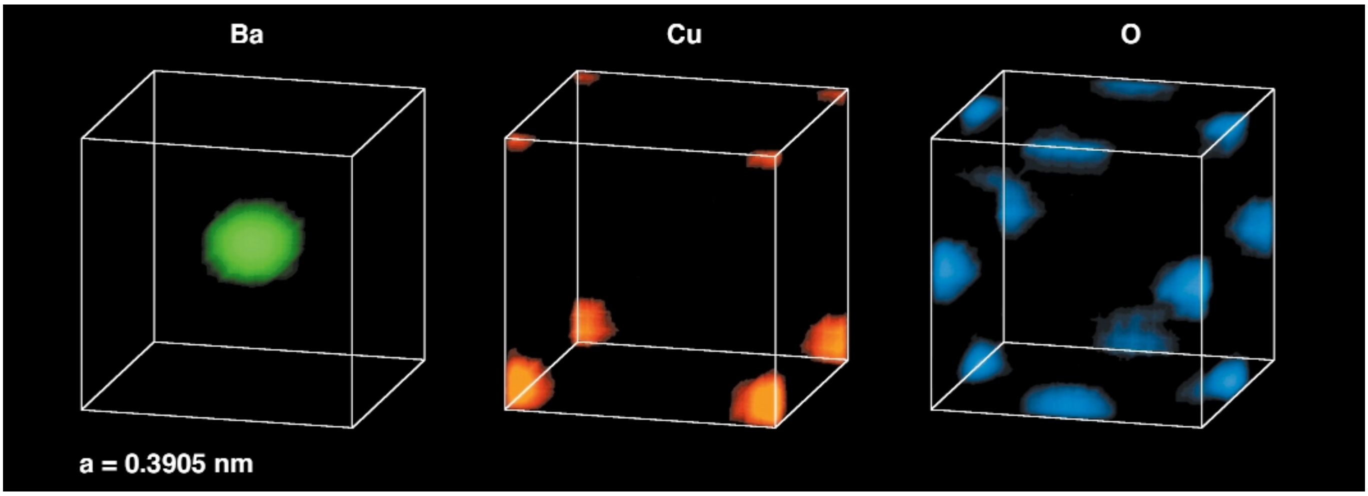

Fig. 85: Element specific X-ray standing wave imaging: Image of three elements of a monolayer of the superconductor $YBa_2Cu_3O_{7-\delta}$ on $SrTiO_3(001)$ (projected into the cubic $SrTiO_3$ unit cell). Measurements done at ID32.

Surface X-ray Diffraction: Atomic Structure

Seeing Adsorbed Hydrogen Atoms on Metals with Surface Diffraction: Towards Catalytic Conditions

One of the reasons for the quite late appearance of *in situ* studies of model catalysts "in action" by Surface X-ray Diffraction (SXRD) [1] is the widespread belief that surface diffraction can not "see" light adsorbed atoms and molecules, coming from the gas phase above the catalyst. This belief was already undermined by articles showing that the diffraction signals from an ordered layer of adsorbed CO molecules [2] or from a light oxide surface (the "zero electron" signals, which are proportional to (fMg^{2+}-fO^{2-}), from a MgO(001) surface) [3], could easily be detected.

Here we present further evidence of the sensitivity of SXRD to light atoms, on the textbook case of a p(2x2) ordered overlayer of hydrogen atoms on Ni(111). We also briefly describe the effect, relevant for catalysis, of exposure of the Ni(111) surface to one bar of H_2.

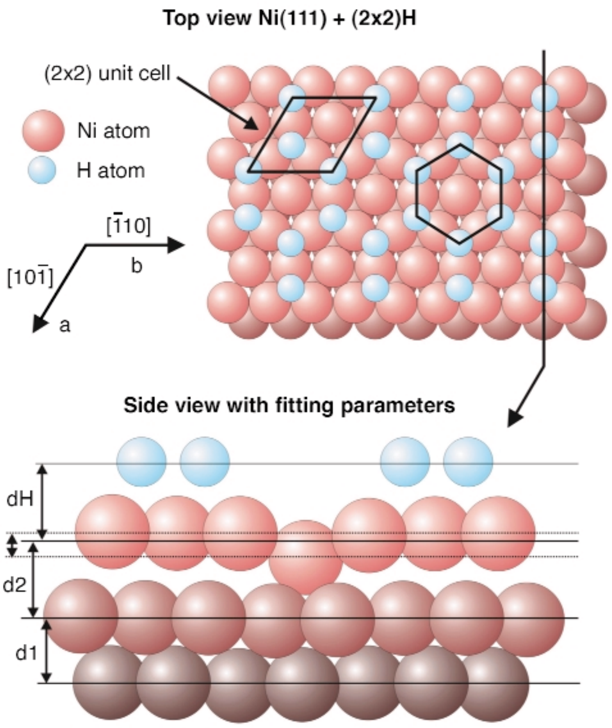

Fig. 86: The model of the UHV low-T p(2x2) structure of H adsorbed on Ni(111) proposed in [4]. The fitting parameters of the atomic model are shown. The values of these parameters found from our SXRD dataset compare well with the ones found from the LEED study [4].

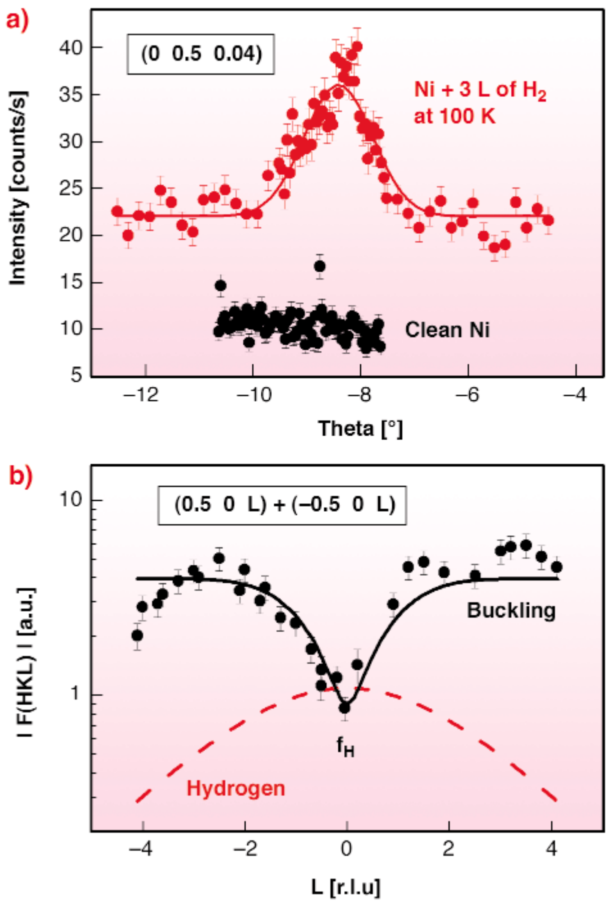

Fig. 87: (a) rocking scan around one of the SXRD peaks from the p(2x2) H-layer at 100 K. The scan after adsorbing H (top) is compared to the scan on the clean Ni (bottom). At this low L value, the peak comes purely from scattering by H atoms. (b) One of the fractional order reconstruction rods. The data (points) are compared to the calculated rod (solid line). The contribution of H atoms is shown by the dashed line. It is the main contribution at low L.

Figure 86 shows the atomic model proposed by Hammer *et al.* [4] for the Ultra-High Vacuum (UHV) low-temperature p(2x2) structure of H_2 on Ni(111), using quantitative Low Energy Electron Diffraction (LEED). This structure consists of half a monolayer of H atoms, with the Ni atoms located below the H atoms moving upwards (buckling). **Figure 87** shows a part of the SXRD dataset collected on **ID03** for this same structure. This structure is a good test-case of the sensitivity of SXRD to H atoms, because there are locations in reciprocal space where the diffracted intensity is purely due to H scattering. The low-L part of the fractional order rods (Figure 87a) is one such location, for two reasons. First the buckling (z-motion of the Ni atoms) of the last Ni plane contributes only at non-zero L's (Figure 87b), and secondly, the symmetry of the model (Figure 86) forbids x-y motions of the Ni atoms. The intensity due to H scattering in Figure 87a is 20 cts/s above background, with a full-width of 1°. The fitting of the structural parameters shown in Figure 86, using the SXRD data, gives values that agree well with the ones of [4]. The biggest error bar, as in the LEED study, is on the z-position of the H atoms, due to the very small L-range of proper interference between Ni and H scattering.

Room temperature exposure to H_2 at pressures ranging from 10^{-8} mbars to 1.1 bar was also studied. In this case, the surface stays (1x1) upon adsorption, *i.e.* there is no ordered superstructure of the H atoms. The surface structure remains practically the same as under UHV up to 300 mbar. Above 300 mbars, a slight decrease (max -40%) of the Ni crystal truncation rods occurs, interpreted by a mixture of surface disorder and/or roughness, possibly due to H embedding. This is an important result as it predicts a possible change at 300 mbars in the catalytic properties of Ni for the methanation reaction.

References

[1] M.D. Ackermann, O. Robach, C. Walker, C. Quirós, H. Isérn, S. Ferrer, *Surf. Sci.* **557**, 21 (2004).
[2] I.K. Robinson, S. Ferrer, X. Torrelles, J. Alvarez, R. Van Silfhout, R. Schuster, R. Kuhnke, K. Kern, *Europhys. Lett.* **32**, 37 (1995); C. Quirós, O. Robach, H. Isérn, P. Ordejon, S. Ferrer, *Surf. Sci.* **522**, 161 (2003).
[3] O. Robach, G. Renaud, A. Barbier, *Surf. Sci.* **401**, 227 (1998).
[4] L. Hammer, H. Landskron, W. Nichtl-Pecher, A. Fricke, K. Hein, K. Müller, *Phys. Rev. B* **47**, 15969 (1993).

Principal Publication and Authors

S. Ferrer (a,b), C.J. Walker (a), M. Ackermann (a,c), C. Quirós (a,d), H. Isérn (a), O. Robach (e), *submitted to Phys. Rev. B.*
(a) ESRF
(b) ALBA - Edifici Ciéncies, Bellaterra (Spain)
(c) Kamerlingh Onnes Laboratory, Leiden University (The Netherlands)
(d) Depto. de Física, Facultad de Ciencias, Universidad de Oviedo (Spain)
(e) CEA-Grenoble, DRFMC/SI3M/PCM (France)

Spin Reorientation and Structural Relaxation of Atomic Layers: Pushing the Limits of Accuracy

The direction of the magnetisation in magnetic materials is pinned along certain crystal directions. In addition to its fundamental interest, this magnetic anisotropy is important for technological applications. For example, in future high-density magnetic recording devices, magnetic alloys will be used where the easy magnetisation direction is perpendicular to the disk plane.

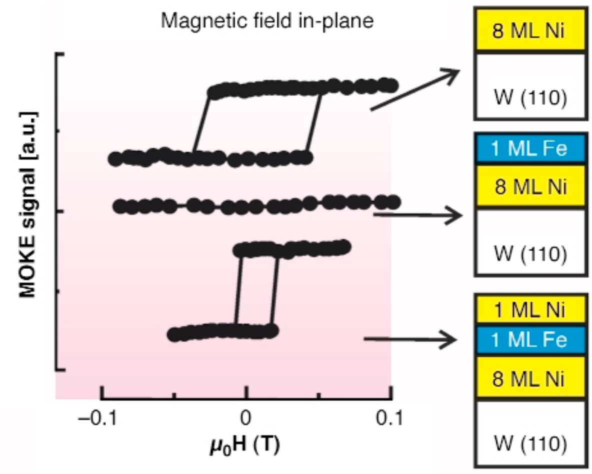

Fig. 88: In-plane magnetisation curves for Fe/Ni/W(110). Sample structures are shown schematically on the right.

In ultra-thin films, only several atomic layers thick, it is often observed that the easy magnetisation direction changes with adsorption of a single atomic layer of ad-atoms. One example is Ni/W(110). Magneto optic Kerr effect (MOKE) measurements indicate that, after deposition of several layers of Ni, the magnetisation lies in the plane as shown in **Figure 88** by the magnetisation curve with almost full remanence when measured in the longitudinal geometry (upper panel). Deposition of a single layer of Fe switches the easy axis to the normal direction (no hysteresis observed, centre), while another layer of Ni reverts it back to in-plane (lower panel).

In general, adsorbate-induced spin reorientations are explained by an anisotropy change due to surface modification. However, quantitative estimations indicate that the change of the magnetisation direction can also be induced by changes of the interlayer spacing in the percent range [1]. Here, a lattice spacing change of only 0.015 Å would be sufficient to induce a spin reorientation. Since this is in the limit of accuracy of surface structure analysis techniques, the magneto-elastic contribution is generally not discussed and analysed in detail.

In order to study the adsorbate-induced structural change, and its impact on the magnetic anisotropy, surface X-ray diffraction experiments were carried out at

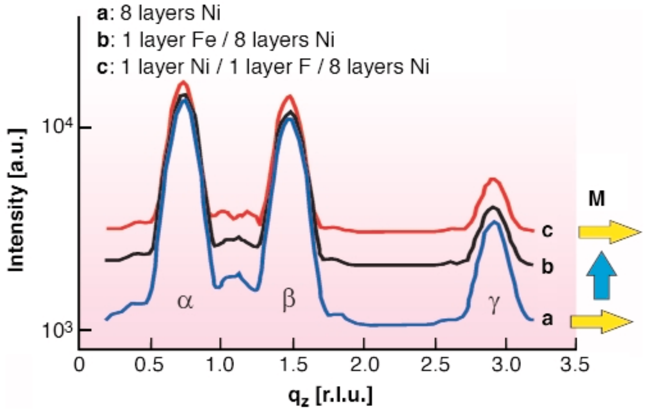

Fig. 89: X-ray scans along the surface normal after subsequent deposition of 8 layers of Ni (a),one layer of Fe (b) and another layer of Ni (c). Arrows indicate the easy magnetisation direction. Peak shifts are smaller than $5x10^{-4}$ reciprocal lattice units corresponding to changes of the interlayer spacing below about 0.002 Å.

the beamline **ID03** and combined with MOKE. Our experimental approach is based on the determination of *relative* peak shifts before and after layer deposition as shown in **Figure 89**.

Surface X-ray diffraction measurements along the sample normal were carried out probing the vertical lattice spacing of the Ni film. Scans were measured after subsequent deposition of eight Ni- layers (a), one Fe-layer (b), and another Ni-layer (c). Three Bragg-peaks are observed, where the first (α) and the third (γ) are related to the (101)- and (104) reflection of the fcc-like Ni-structure, while the second (β) represents the reflection from the crystallographic twin.

Detailed analysis of the peak positions and the profiles indicate that adsorption of one layer of Fe does not result in changes of the average interlayer distances larger than 0.002 Å. This is roughly one order of magnitude smaller than calculated (0.015 Å) necessary for a magneto-elastic driven switching of the easy axis. Therefore, the change of the easy axis must be attributed to the modification of the electronic structure of the surface layer due to adsorption, and this changes the magnetic surface anisotropy.

Our experimental procedure as well as the result have far reaching implications for the preparation of suitable magnetic systems, since the unprecedented accuracy of the near-surface structure determination allows a clear unravelling of the different factors contributing to the magnetic anisotropy.

References

[1] D. Sander, *Rep. Prog. Phys* 62, 809 (1999).

Principal Publication and Authors

H.L. Meyerheim (a), D. Sander (a), R. Popescu (a), J. Kirschner (a), O. Robach (b), S.Ferrer (b, c), *Phys. Rev. Lett.* **93**, 156106 (2004).
(a) MPI für Mikrostrukturphysik, Halle (Germany)
(b) ESRF
(c) also at: ALBA, Barcelona (Spain)

Atomic Structure of a Long-range Ordered Vicinal Surface of $SrTiO_3$

At the surface of a crystal, the atoms are missing some of their neighbours. For metals and semiconductors the atoms overcome this chemically frustrating situation by rearranging into a different short range order, *i.e.* the surfaces reconstructs. Reconstructions of semiconductors, for example, are mostly driven by rehybridisation and saturation of dangling bonds. Self organisation and long range order is initiated by the resulting stress. However, $SrTiO_3$ (STO, **Figure 90a**) is an insulator and characterised by strongly ionic bonds. The real charges of Sr, Ti, and O differ from the formal charges shown in Figure 90a and thus both (001) faces of STO (the SrO and TiO_2 low-index faces) are weakly polar [1], each carrying a charge of almost ± 1/2 e_0 per unit cell.

The STO(106) surface, which is vicinal to STO(001), exhibits an unusual morphology. In the low energy electron

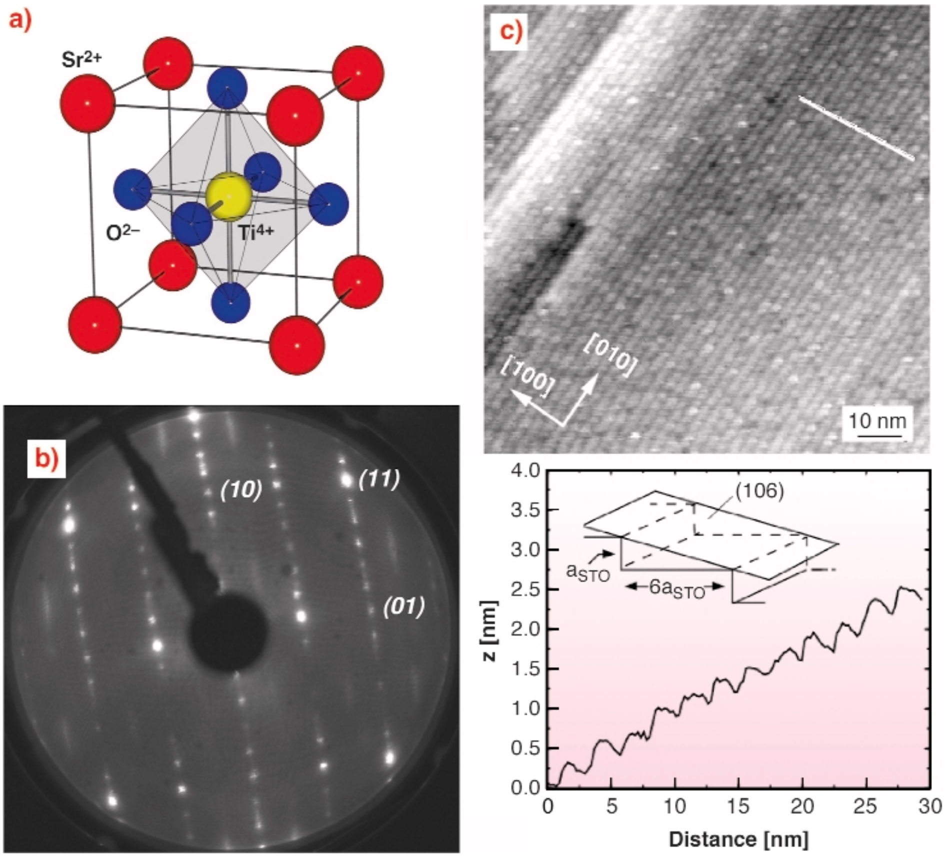

Fig. 90: a) The 0.391 nm long STO unit cell; b) LEED image of the STO(106)-p(1x2) reconstruction. Extra lines and spots between [01] and [10] indicate a (1x2) reconstruction; c) Corresponding STM image (+1.5 V sample bias and 0.2 nA) and cross-section along the indicated line.

diffraction (LEED) image of STO(106) in **Figure 90b**, besides the integer order reflections, spots at n/6 in the [10]-direction are due to the step structure and their sharpness is indicative of a very smooth (106) surface. The scanning tunnelling microscopy (STM) image in **Figure 90c** shows a very regularly "terraced" surface with an astonishing degree of long-range order. On the shorter length-scale, many uncorrelated contrast variations indicate substantial short-range disorder. The cross section of the STM image reveals rounded step edges.

The structure of STO(106) was solved by diffraction measurements at beamline **ID03** using X-rays of 20 keV energy. The surface was prepared in UHV by annealing only. Integrated intensities were recorded for 84 crystal truncation rods and the total number of non-equivalent reflections was 1644. From the widths of several reflections, the domain size was determined to be between 35 and 50 nm along the "step-edges", and close to 400 nm in the perpendicular direction, which represents a remarkable degree of long-range order. Utilising a "direct method", which has been developed for solving surface crystallographic problems [2], a starting model was obtained: a regularly stepped (106) surface with reduced site occupancies of the constituent atoms, varying as function of their proximity to the surface (**Figure 91**).

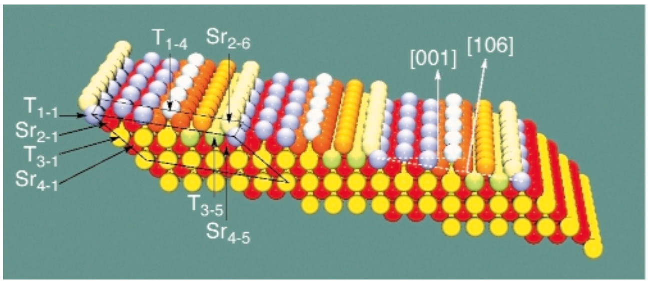

Fig. 91: Resulting model of the STO(106) surface. The oxygen atoms, which are in bulk like positions, are not shown for clarity. Fully occupied Ti and Sr sites are represented by yellow and red colours, respectively. Lighter colours indicate lower occupancies. The continuous line defines the monoclinic surface cell used in the data analysis.

The refinement of the surface structure yielded atomic coordinates very close to the corresponding bulk values and average occupancy values of the topmost Ti atoms (Ti_{1-1}, Ti_{1-2}, Ti_{1-3}) of 0.5, compatible with a (disordered) p(1x2) surface cell, which explains the observed (1x2) LEED image (Figure 90b). The Ti and Sr population factors of deeper layers decrease gradually as a function of their atomic z-coordinates toward the surface. Figure 91 shows the resulting (106) surface with Ti and Sr atoms in an ordered p(1x2) surface cell. The Ti/O and the Sr/O- ratios of the two topmost surface layers are of 0.60 and 0.94, respectively, so both layers are less polar than in the bulk. The Ti/O ratio of the third surface layer is 0.47 and thus very close to the bulk value (0.5). The decrease in the site occupancy increases roughness/disorder on a short length scale, but renders the surface smoother on the long range.

The surface structure derived from the best fit exhibits STO(106) terraces, which are (001) planes, but with an alternating $SrO_{1+\delta}$ and $TiO_{2-\varepsilon}$ termination and thus alternating surface charges. This "charge undulation" represents the driving force behind the observed remarkable degree of long-range order. However, the adjustment of the cation/oxygen stoichiometry in conjunction with the varying cation site occupancy obviously decreases the "charge undulation" in order to further reduce the surface energy, rendering the surface more stable than exclusively SrO or TiO_2 terminated STO(106) terraces.

References

[1] J. Goniakowski, C. Noguera, *Surf. Sci.* ***365***, L657 (1996).
[2] see *e.g.*: D.K. Saldin, R.J. Harder, V.L. Shneerson, W. Moritz, *Condens. Matter* **13**, 10689 (2001).

Principal Publication and Authors

X. Torrelles (a), J. Zegenhagen (b), J. Rius (a), T. Gloege (c), L.X. Cao (b) and W. Moritz (c), *to be published*.
(a) Institut de Ciència de Materials de Barcelona (C.S.I.C.), Bellaterra (Spain)
(b) ESRF
(c) Department für Geo- und Umweltwissenschaften, Universität München (Germany)

Potential-dependent Surface Compression during Au Electrodeposition

Electrochemical metal deposition processes have been a subject of substantial basic research during the last few years, motivated by current technologies as well as future applications. To obtain a better fundamental understanding of electrodeposition processes the homoepitaxial growth of Au on Au(111) in aqueous electrolyte solutions was studied. This is particularly interesting due to the complex, potential-dependent in-plane structure of Au(111) surfaces. The Au surface structure was monitored *in situ* during growth by grazing incidence X-ray diffraction (GID), performed at beamline **ID32** using a photon energy of 20 keV. In contrast to most previous diffraction studies of electrochemical interfaces, which were performed in a "thin layer geometry", a newly developed "hanging meniscus" transmission X-ray cell was used, where the beam passes through 5-6 mm of electrolyte solution. The minimised cell resistance and nearly unrestricted mass transport in this cell allows a combination of *in situ* surface X-ray diffraction studies of rapid structural changes with high quality electrochemical measurements.

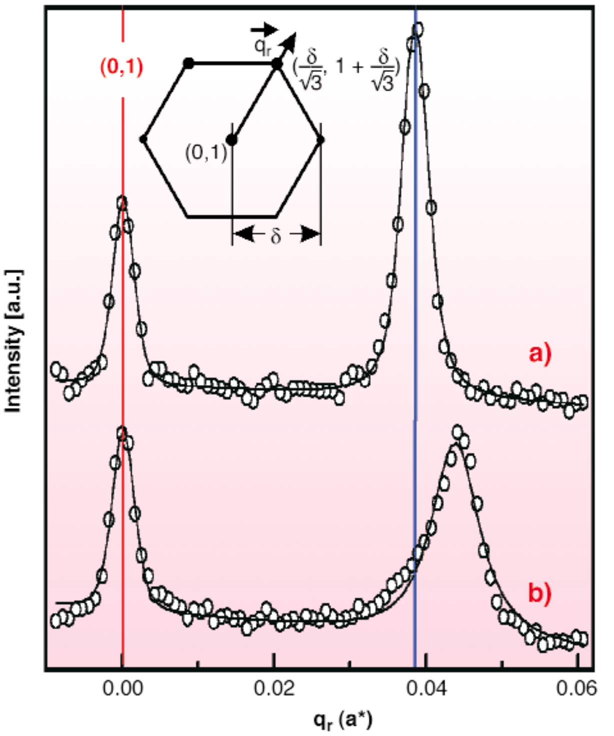

Fig. 92: X-ray scattering profiles along the $\vec{q}_r$ direction (in units of a* = 2.5 Å^{-1} , L = 0.15) recorded at –0.3 $V_{Ag/AgCl}$ in 0.1 M HCl (a) and 0.1 M HCl + 50 µM $HAuCl_4$ (b). The inset shows the schematic diffraction pattern of the (p×√3) reconstruction.

First the potential-dependent Au(111) surface structure in Au-free solution was investigated. In accordance with previous results obtained in "thin layer geometry" [1] a hexagonal pattern around the integer crystal truncation rods is found at potentials negative of a critical value (for 0.1 M HCl at 0.1 V vs. a Ag/AgCl reference electrode), indicative for the well-known ($p\times\sqrt{3}$) surface reconstruction (**Figure 92a**). p saturates at ≈ 22 at the most negative potentials. Subsequently the electrolyte was exchanged with a solution containing 5-200 µM $HAuCl_4$, resulting in the diffusion-limited electrodeposition of Au with deposition rates of 0.25 to 1 ML/min. As before, reconstruction peaks were found, however, shifted outwards by up to 20% (Figure 92b). This corresponds to a compression of the reconstructed surface layer down to $p \approx 19$ or a surface strain $\varepsilon = -p^{-1} = -5.3\%$, respectively. To date, a similar deposition-induced Au(111) surface compression has neither been reported in electrochemical environment nor under UHV conditions.

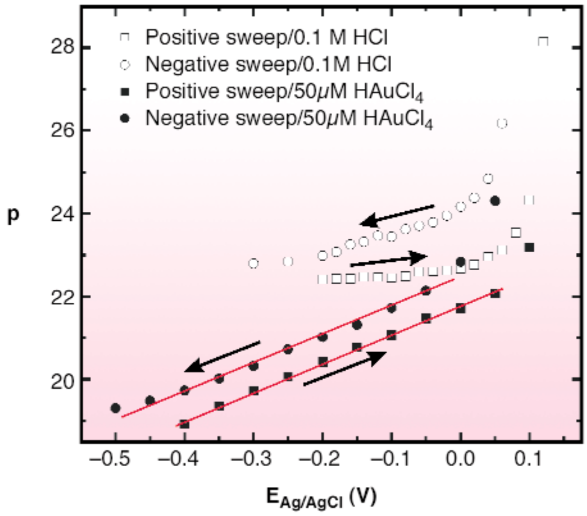

Fig. 93: Potential-dependent surface compression for the reconstructed Au(111) surface in 0.1M HCl (open symbols) and 0.1M HCl + 50 µM $HAuCl_4$ (solid symbols).

Systematic studies revealed a pronounced potential-dependence of this effect (**Figure 93**). At potentials in the vicinity of the ($p\times\sqrt{3}$) → (1×1) phase transition the surface compression is close to that in Au-free electrolyte (*i.e.*, $p \approx 22$). p decreases approximately linearly with the potential E. This behaviour was observed in HCl, KCl, and H_2SO_4 solution, indicating that cation and anion species as well as $HAuCl_4$ concentration (*i.e.* deposition rate) do not substantially influence the compression. To explain this phenomenon we suggest that the surface compression observed during Au deposition is closer to equilibrium in an electrochemical environment, whereas it is kinetically limited to $p \geq 22$ in Au-free electrolyte. Using a simple thermodynamic model, the slope $\delta\varepsilon/\delta E$ can be rationalised by the potential-dependent change in surface stress, found at the Au(111) - electrolyte interface [2].

In summary, the potential dependent surface compression, observed in the presence of Au electrodeposition, may be viewed as a characteristic parameter of charged Au electrode surfaces, which may help to refine theoretical models of the reconstructed Au(111) surface and of metal surfaces in general, respectively.

References

[1] J. Wang, A.J. Davenport, H.S. Isaacs, B.M. Ocko, *Science*, **255**, 1416-1418 (1991).

[2] C.E. Bach, M. Giesen, H. Ibach, T.L. Einstein, *Phys. Rev. Lett.*, **78**, 4225-4228 (1997).

Principal Publication and Authors

A.H. Ayyad, J. Stettner, O.M. Magnussen, *Phys. Rev. Lett.*, *in press*.

Institut für Experimentelle und Angewandte Physik, Universität Kiel (Germany)

Surface X-ray Diffraction of an Ultra-thin Al_2O_3 Layer on NiAl(110)

Aluminium oxide, a seemingly unimportant powder, plays a key role as an ultra-thin ceramic film in a variety of high-tech applications, such as high temperature corrosion protection in space, highly active catalytic materials and new types of permanent memory chips. The structure of ultra-thin, ordered Al_2O_3 layers has puzzled surface scientists for more than a decade [1]. Ultra-thin, well-ordered Al_2O_3 layers can be prepared by controlled oxidation of NiAl(110) single crystals. As the main result of this study it was found that the thinnest, stable aluminium oxide layer consists of only two oxygen and two aluminium ion layers, which are strongly distorted by the interaction with the NiAl substrate.

To unravel the structure of the Al_2O_3 layer, a surface X-ray diffraction experiment was performed at the ESRF surface science beamline **ID32** and at BW2 at HASYLAB. The oxide layer was prepared in the home lab in Stuttgart and was then shipped to the ESRF in a surface X-ray diffraction baby chamber under UHV conditions. **Figure 94a** shows one half of the in-plane diffraction pattern obtained at a photon energy of 10.5 keV (the second half can be obtained by rotation of 180°). The huge in-plane unit cell of the oxide layer (a = 10.59 Å, b = 18.01 Å as compared to the NiAl substrate a = 4.083 Å, b = 2.887 Å) gives rise to a large number of reflections, which can be mapped out by surface X-ray diffraction. From such an in-plane diffraction pattern model, independent real space information may be obtained directly by the calculation of the so-called Patterson map, presented in Figure 94b. The Patterson map yields direct information about the sum and difference vectors of different atoms in the surface plane. Close to the border of the unit cell (indicated by the black line), a pattern with locally hexagonal symmetry prevails,

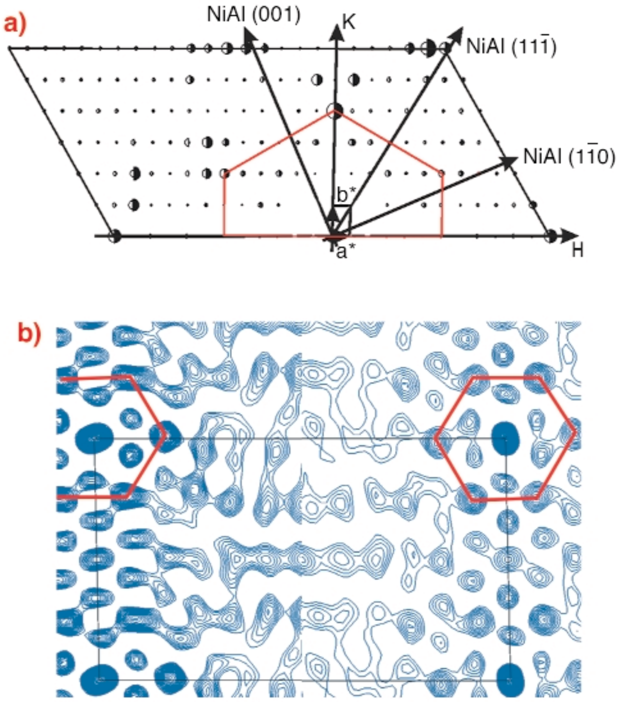

Fig. 94: a) One half of the measured structure factors (full half circles) together with the best fit structure factors (open half circles). The oxide layer H and K directions are indicated together with the NiAl substrate coordinates. The oxide layer is only commensurate along the NiAl(1-10) direction. b) Comparison between experimental (left part) and theoretical (right part) Patterson maps.

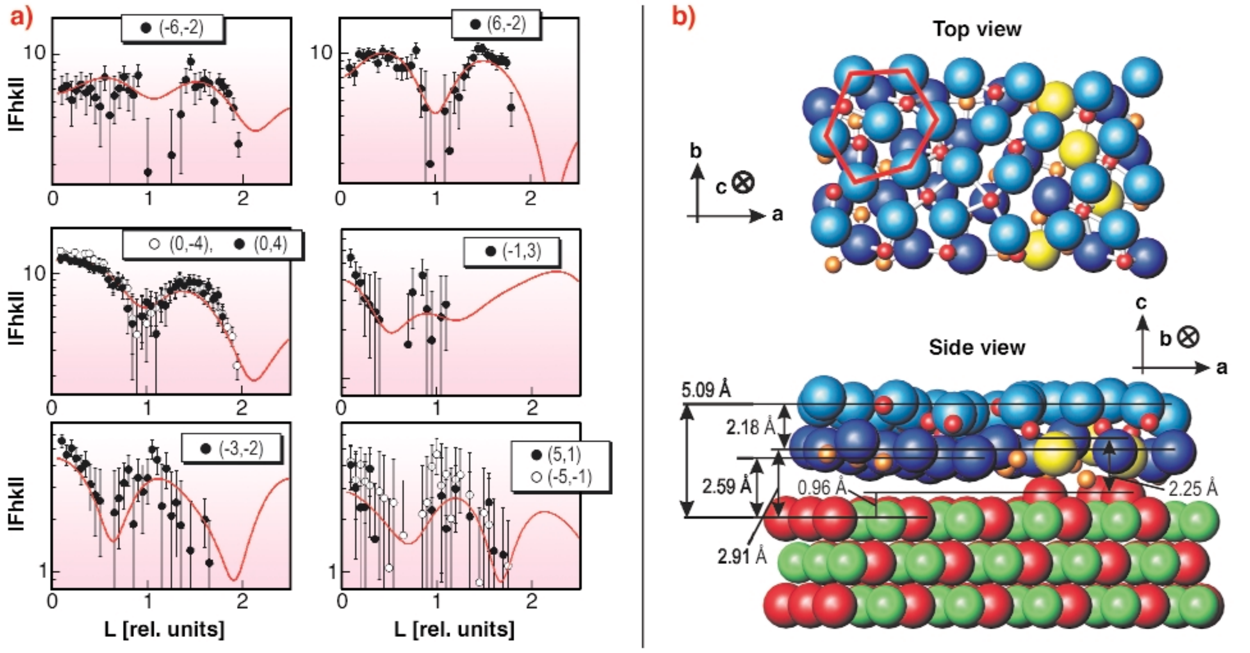

Fig. 95: a) Structure factors for different in-plane momentum transfers with varying momentum transfer L perpendicular to the surface in units of 2π/2.887 Å. Open and filled circles: data points, red lines: best fit structure factors. b) Best fit structural model side view and top view. Oxygen ions are plotted as blue or yellow spheres, Al ions as small spheres in red or orange, Al metal atoms as red spheres and Ni metal atoms as green spheres.

which is an indication that hexagons with 0.3 nm side length are an element of the structure. A hexagon with 0.3 nm side length would give rise to the diffraction spots in Figure 94a, which are connected by the red lines.

To get information about the full 3D structure of the layer, surface rods with momentum transfer perpendicular to the surface were examined. In **Figure 95a** the surface rods for different in-plane momentum transfers are plotted together with the best fit result. The surface rods show a characteristic modulation along L, which clearly indicates that the film must consist of more than one atomic layer. To find a structural model, which fits the diffraction data, different starting structures were considered, based on hexagonally closed packed planes of different Al_2O_3 phases. For the different starting structures a local variation of the atomic positions was performed to achieve a χ^2 minimisation, under the constraint that atoms are not allowed to overlap within their ionic radii.

The best fit structural model is sketched in Figure 95b. It was derived from a (00-1) oriented slab of κ-Al_2O_3 consisting of an oxygen ion and an aluminium ion double layer, originally occupying octahedral and tetrahedral sites between the two oxygen ion layers with equal probability. For the refined structure, a distance of 2.18 Å between the oxygen ion layers is found, in good agreement with Al_2O_3 bulk phases. The Al ions in between the oxygen ion layers sit on tetrahedral sites, octahedral sites, or sites with a fivefold coordination. At the interface, one sixth of the oxygen ions (plotted in yellow) are aligned with respect to the NiAl substrate. The oxide layer exhibits a buckling of 0.3 Å and a distance of 5.09 Å from the oxygen top layer to the first NiAl substrate layer.

References

[1] R. Franchy, *Surf. Sci. Rep.* **38**, 195 (2000).

Principal Publication and Authors

A. Stierle (a), F. Renner (a,b), R. Streitel (a), H. Dosch (a), W. Drube (c), B.C.C. Cowie (b), *Science* 303, 1652 (2004).
(a) MPI für Metallforschung, Stuttgart (Germany)
(b) ESRF
(c) HASYLAB, Hamburg (Germany)

Grazing-incidence and Anomalous Diffraction: Nanostructures

Ion Beam Induced Ripple Structure of Crystalline Layers in Si Wafers

The formation of a ripple-like pattern with a spatial periodicity varying from nm to mm on obliquely ion-bombarded solid surfaces has become a topic of intense research because of its potential as templates for the fabrication of nanoscale structured materials [1]. The ion-induced ripples are produced by interplay between a roughening process caused by the ion beam erosion (sputtering) of a surface and a smoothening process caused by thermal or ion-induced surface diffusion [2]. The ion-beam modified ripple structure on a semi-conducting surface such as silicon wafer has been studied in recent years mainly using microscopy, which provides images of the top surface morphology. In order to understand the ripple formation mechanism the amorphous-crystalline interface and the structure below have also been studied.

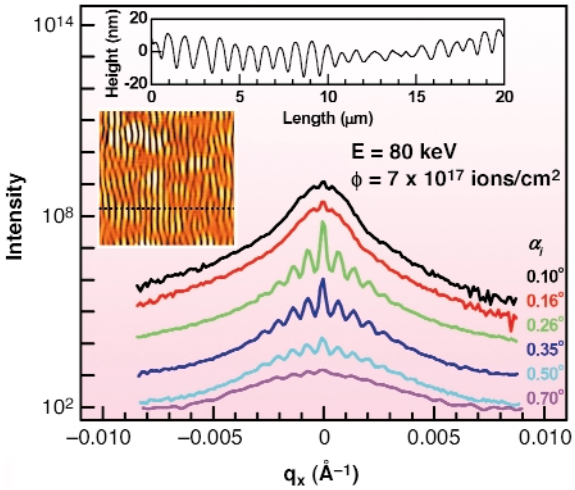

Fig. 96: Transverse GID curves perpendicular to the ripple structure around (220) Bragg peak of a ion-beam modified Si(001) wafer. Insets: AFM image (20 μm x 20 μm) and corresponding height profile.

Si(001) wafer surfaces were bombarded with $^{40}Ar^+$ beam of varying energy and dose at fixed incidence angle (60°) to form the rippled surfaces, which were characterised by atomic force microscopy (AFM) at the Saha Institute of Nuclear Physics [2]. The near surface structural studies were performed by depth-resolved X-ray grazing-incidence diffraction (GID) at the **ID01** beamline using a wave length λ = 1.55 Å. Typical GID curves for a sample show the presence of satellite peaks on both sides of the main (220) Bragg peak (**Figure 96**). The appearance of satellite peaks confirms the existence of lateral undulation of the buried crystalline part of the sample. The separation between the satellite-peaks is inversely proportional to the subsurface crystalline ripple wavelength, which agrees well with the ripple-like structure on the top surface observed through AFM measurements. At a certain value of *incident angle* the shape of the curve changes from a narrow to a broad one, indicating the onset of defect formation.

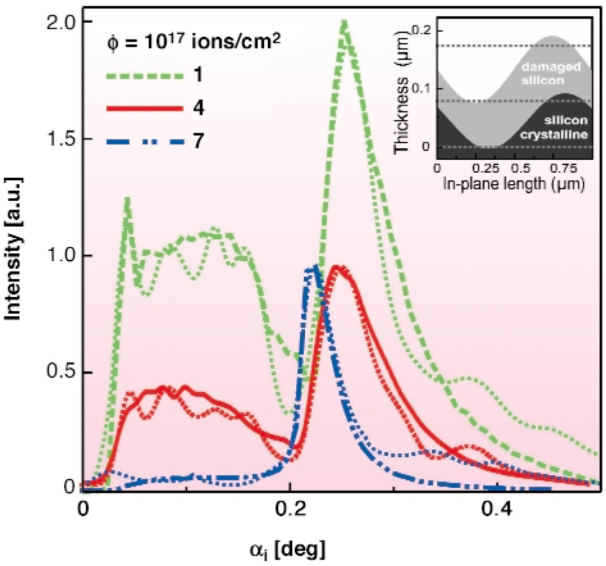

Fig. 97: Experimental and simulated (dotted) α_i scans measured at (220) Bragg peak for samples irradiated with different dose ϕ at E = 80 keV. Inset: Schematic Cross-section of the sample used for the simulations.

The Bragg intensity as a function of the incidence angle α_i (Vineyard profiles) for samples bombarded with different dose are shown in **Figure 97**. The plateau below $\alpha_{c,\,Si}$ at about 0.23° (instead of a single peak at $\alpha_i = \alpha_{c,\,Si}$) seen here, corresponds to materials of low density, gradually decreasing towards the top. Since the measurements are on an in-plane Bragg peak, intensities at all incident angles stem from crystalline material. Note that the onset angle, the shape and height of the plateau are a function of the implantation dose. For low doses there are two distinct critical angles; the appearance of a peak at 0.05° is attributed to the existence of a partially crystalline top layer with much lower density compared to crystalline silicon. For increasing dose the intensity of the plateau-region decreases. In the case where the dose was 7×10^{17} ions/cm^2, the plateau-region almost disappears and the shape of the α_i scan curve turns into a Vineyard profile expected for a sample with a non-scattering (amorphous) top layer. The reconstructed depth profile obtained from the simulation of the Vineyard profile (dotted lines in Figure 97) shows that the material density of the subsurface layer is very low (about 15% of the crystalline Si bulk density); at the same time the rippled, modulated crystalline part underneath is damaged and has a reduced density. The partially crystalline top layer at low dose, transforms to a completely amorphous layer for high doses and the surface morphology was found to be conformal with the underlying crystalline ripples.

In conclusion, by a combination of GID and AFM measurements we have characterised the relation between the formation of ripple-like structure at the surface and the crystalline material in the subsurface region of the silicon wafer due to ion bombardment. The wavelength of the buried crystalline ripple structure is well replicated at the top surface as observed by AFM measurements.

References

[1] U. Valbusa, C. Boragno, and F.B. de Mongeot, *J. Phys.: Condens. Matter* **14**, 8153 (2002).
[2] T.K. Chini, M.K. Sanyal, and S.R. Bhattacharyya, *Phys. Rev. B* **66**, 153404 (2002).

Principal Publication and Authors

S. Hazra (a), T.K. Chini (a), M.K. Sanyal (a), J. Grenzer (b) and U. Pietsch (b), *Phys. Rev.* B **70**, 121307 (2004), and H. Metzger (c).
(a) Saha Institute of Nuclear Physics, Kolkata (India)
(b) Institut fur Physik, Potsdam (Germany)
(c) ESRF

Strain Determination in Multilayers by Complementary Anomalous X-ray Diffraction

Strain and interdiffusion in multilayered semiconductor devices are crucial features for their functionality. The band structures as well as the 2D confinement effects depend on these properties. For EuSe/PbSe$_{1-x}$Te$_x$ multilayers a sensitive tuning of the EuSe lattice parameter by epitaxial strain additionally allows an influence on the magnetic behaviour of thin EuSe films. In heteroepitaxial structures, X-ray diffraction is usually the tool of choice to determine lattice parameters and hence strain. For the case of overlapping intensities from similar lattice parameters of two distinct materials the precise determination of their strain state and discrimination between strain and composition remains rather ambiguous. We show here, that anomalous diffraction applied to superstructure reflections of compound materials can overcome this problem.

The **beamline ID01** is ideally suited for anomalous X-ray diffraction at complementary energies yielding a selective suppression of Bragg reflections from compound semiconductor multilayers. The method is applied to a study of single crystal multilayers of EuSe and PbSeTe grown by solid source molecular beam epitaxy. In the vicinity of the Pb M_V- and Eu L_{III} absorption edges, strong resonances can be exploited, to measure separately, either the lattice parameter in the EuSe or in the PbSeTe layers, respectively. Furthermore, the enhancement of the chemical contrast by anomalous X-ray diffraction and the high resolution is exploited to achieve sensitivity for interdiffusion on an Ångstrom

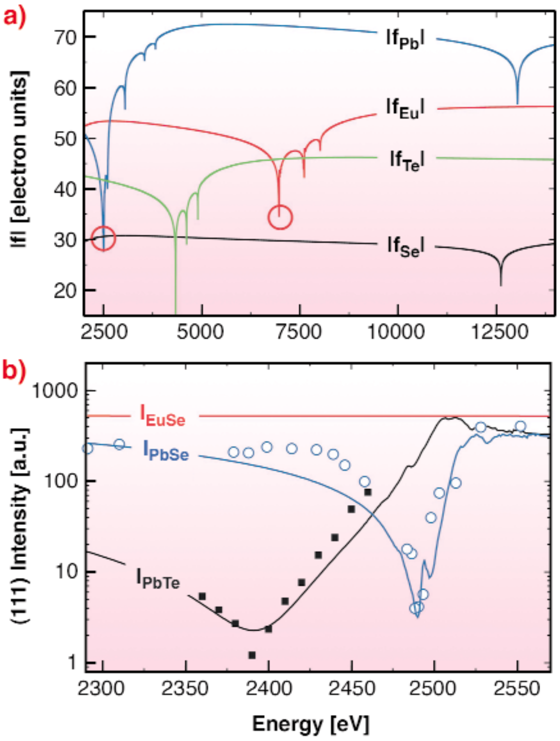

Fig. 98: (a) Real part of the atomic scattering factors of $|f_{Pb}|$ (blue line), $|f_{Eu}|$ (red), $|f_{Te}|$ (green) and $|f_{Se}|$ (black) for a momentum transfer corresponding to the PbSe and EuSe (111) Bragg reflections (values from www-phys.llnl.gov); (b) Calculated (lines) and measured (symbols) (111) Bragg intensity from EuSe (red) PbSe (blue) and PbTe (black) in the vicinity of the Pb M_V-edge.

scale. The lead and europium chalcogenides crystallise in the rock salt structure. The structure factor of the (111) reflections thus reads $f_{PbSe} = 4(f_{Pb}-f_{Se})$. f_{Pb} and f_{Se} are the complex atomic scattering factors. An equivalent expression holds for EuSe or $PbSe_{1-x}Te_x$. Exploiting the strong resonance at the Pb M_V edge, the momentums of the scattering factors of elements such as Se and Pb become comparable and the (111) Bragg intensity of this compound almost vanishes. The real parts of the complex atomic form factors of the four elements concerned, as well as the calculated and measured evolution of the (111) Bragg intensity from PbSe and PbTe are plotted in **Figure 98** as a function of energy. The red circles in 1(a) mark the complementary energies where either EuSe or PbSe have a minimum in the (111) structure factor.

All diffraction experiments were carried out in specular reflectivity geometry, up to scattering angles of 140°. This high angular range was required in order to achieve the necessary momentum transfers for the (111) reflection at X-ray energies as low as 2500 eV. We have recorded line scans across the specular (111) Bragg reflection of EuSe/PbSe and $EuSe/PbSe_{1-x}Te_x$ multilayer superlattices grown in the <111> direction. For the EuSe/PbSe sample the measurements (black lines) together with numerical best-fit simulations (red lines) are shown in **Figure 99**. The two complementary energies used were 2490 eV ((a), PbSe suppression) and 6975 eV ((b), EuSe-suppression). The multilayers are sketched in the insets. The EuSe layers are presented in blue, the thicker PbSe spacers in green. For 2490 eV, the scattering stems mainly from the thin EuSe layers leading to a broad envelope centred at 1.76 Å^{-1}. At 6975 eV, the scattering is largely dominated by PbSe spacer layers, which are about ten times thicker, and thus the envelope shape changes significantly. The centre positions that refer to the different lattice parameters are indicated by perpendicular blue (EuSe) and green (PbSe) lines. The differences in the spectra recorded for the two energies clearly shows that different parts of the sample are dominating the diffraction pattern for these two energies. From the fits the average thickness results in 47 Å for the EuSe and 427 Å for the PbSe layers. The interdiffusion length at the interface, as determined from numerical simulation of the data, is about 1.5 Å. The presumed exponential decay of the interdiffusion profile underlines the high quality of the growth. The experiments thus demonstrate the sensitivity of anomalous diffraction to strain and interdiffusion in heteroepitaxial systems with very small lattice mismatch.

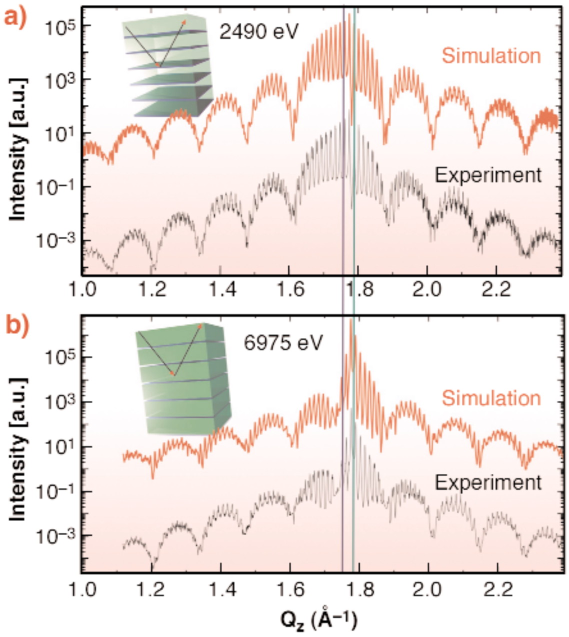

Fig. 99: Specular scans across the (111) reflection of a 100 x 427 Å PbSe / 47 Å EuSe multilayer at two energies together with the best fitting simulations.

Principal publication and authors:

T. U. Schülli (a,b), R.T. Lechner (a), J. Stangl (a), G. Springholz (a), G. Bauer (a), M. Sztucki (b), T.H. Metzger (b), *Phys. Rev. B*. **69**, 195307 (2004).

(a) Institute for Semiconductor Physics, Johannes Kepler University Linz, (Austria)

(b) ESRF

X-ray Standing Waves: Chemistry and Structure

Chemically-resolved Structural Analysis of Sn/Ge(111) Surface

For tetrahedrally coordinated semiconductors, the various reconstructions commonly observed at their surfaces can be largely understood through the effect of Jahn-Teller or Peierls distortion, which suggests that a metallic termination is unstable against a lattice distortion that turns the surface semiconducting. Known examples include surface unit cells containing even numbers of unpaired electrons, such as the tilted dimers of the Si(001)-(2x1) surface.

The α phase of the Sn/Ge(111) surface (and a few others), on the other hand, represents a less clear but interesting case. The seemingly simple structure (**Figure 100a,** [1]) contains 1/3 of a monolayer (ML) of Sn, all occupying the T_4 sites with one unfilled dangling bond per adatom. Depending on their vertical positions, the surface can exhibit a √3x√3 (*e.g.*, $h_1 = h_2$) or 3x3 ($h_1 \neq h_2$) symmetry. Low energy electron diffraction (LEED) shows that the former exists at room temperature (RT) and the latter appears upon cooling to temperatures below 200 K. Since the two phases have an odd number of half-filled dangling bond states per unit cell, they are both expected by a simple electron counting to be metallic. This immediately raises the question regarding the nature of this reversible transition, which has drawn broad attention in the past few years.

Despite extensive studies a complete understanding of the surfaces is not yet established. It was initially considered that the formation of surface charge density waves or a Mott insulator may explain this low temperature (LT) phase transition. But this has become questionable due to the lack of evidence supporting an energy gap opening at LT and Fermi surface nesting between the two phases.

Other observations were made by scanning tunnelling microscopy (STM) and core-level photoemission. For the 3x3 phase, bias-dependent STM reveals two types of Sn adatoms, which are also suggested by photoemission through the detection of a Sn 4*d* core-level shift. For the √3x√3 phase, the Sn 4*d* line shape remains unchanged, while all the adatoms appear equivalent in the STM images. These differences have led to a new model [2] proposing a buckled Sn layer for the RT phase, where the adatoms fluctuating vertically between the two equilibrium positions they are frozen into at LT. Such fluctuations do not necessarily change the √3x√3 symmetry in LEED, but imply that only time-averaged structures can be imaged by STM. However, surface X-ray diffraction study [1] has concluded with only one vertical Sn position for the RT phase.

In the present study we focus on exploring the Sn adatom structure behind the 4*d* core-level shift for the RT √3x√3 phase (Figure 100b) by measuring the photoelectrons excited by an X-ray standing wave (XSW) field. In addition to the high spatial resolution and chemical sensitivity, our approach also takes advantage of the fast process of photoemission in probing the equilibrium structures. Using this unique combination available at **ID32** we succeeded in resolving *simultaneously* the core-level shift and the vertical split of the Sn positions. Our results provide clear evidence that directly links the chemical states of the adatoms with the structures.

Figure 101a shows a typical photoemission spectrum recorded from a √3x√3 surface at an incident energy E_γ

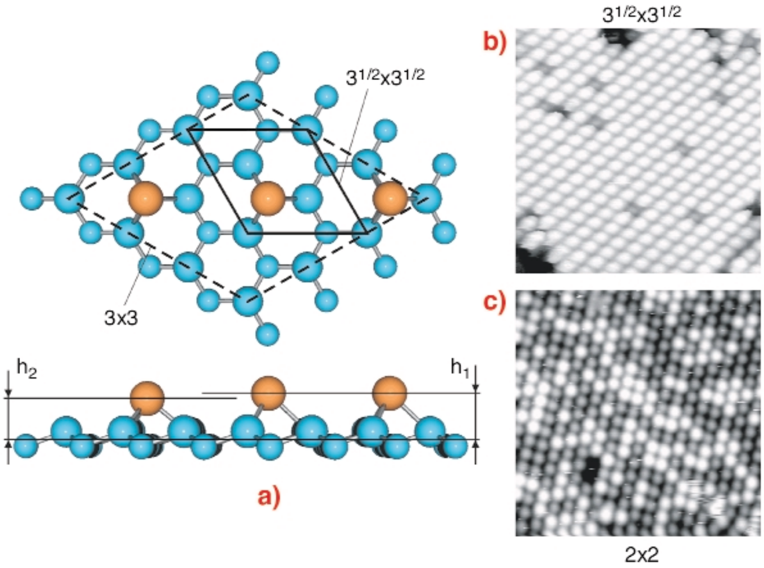

Fig. 100: Structural model (a) and STM images (b, c) for the α phase of the Sn/Ge(111) surface.

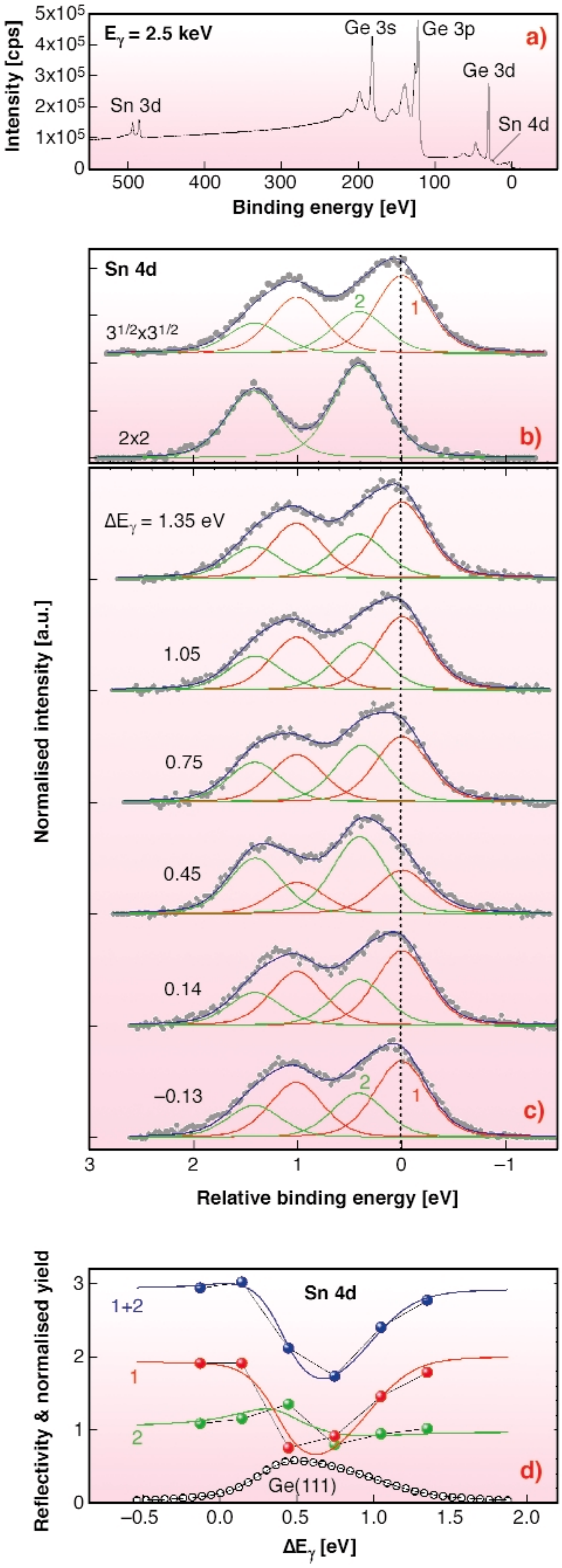

Fig. 101: Photoemission survey scans (a, b), XSW-modulated spectra (c) and XSW analysis of the integrated peak intensities (d).

of 2.5 keV. To reliably analyze the 4*d* core-level shift for the √3x√3 phase, we use the 2x2 surface (Figure 100c), which forms at a Sn coverage below 0.2 ML and is known to have only one chemical component in the 4*d* spectrum, as a reference. A line-shape comparison between the two surfaces is presented in Figure 101b. The broadening of the peaks is clearly visible and thus confirms the presence of a second component for the √3x√3 phase. Figure 101c shows the XSW-modulated Sn 4*d* spectra recorded at six incident energies over 1.5 eV centered around the Ge(111) reflection. The XSW-induced line-shape variation in Figure 101c provides the first concrete evidence that links directly the origins of the two Sn 4*d* components to two non-equivalent sites. Further analysis of the integrated peak intensities (Figure 101d) unveils unambiguously that it is the lower (higher) binding energy component that is associated with the higher (lower) Sn (Figure 100a). We determine the vertical separation h_1 to h_2 to be 0.23 Å, in good agreement with the previous theoretical calculations.

Our present XSW analysis supports a fluctuating Sn layer for the RT phase, as predicted by molecular dynamics simulations [2]. It also suggests that, as compared with the existing first-principle calculations, the lower (higher) binding energy 4*d* component has a filled (empty) state character. The core-level shift can be therefore explained as the result of a common initial-state effect.

References

[1] O. Bunk *et al*., *Phys. Rev. Lett.* **83**, 2226 (1999).
[2] J. Avila *et al*., *Phys. Rev. Lett.* **82**, 442 (1999).

Principal Publication and Authors

T.L. Lee, S. Warren, B.C.C. Cowie, and J. Zegenhagen, (2005) *to be published.*
ESRF

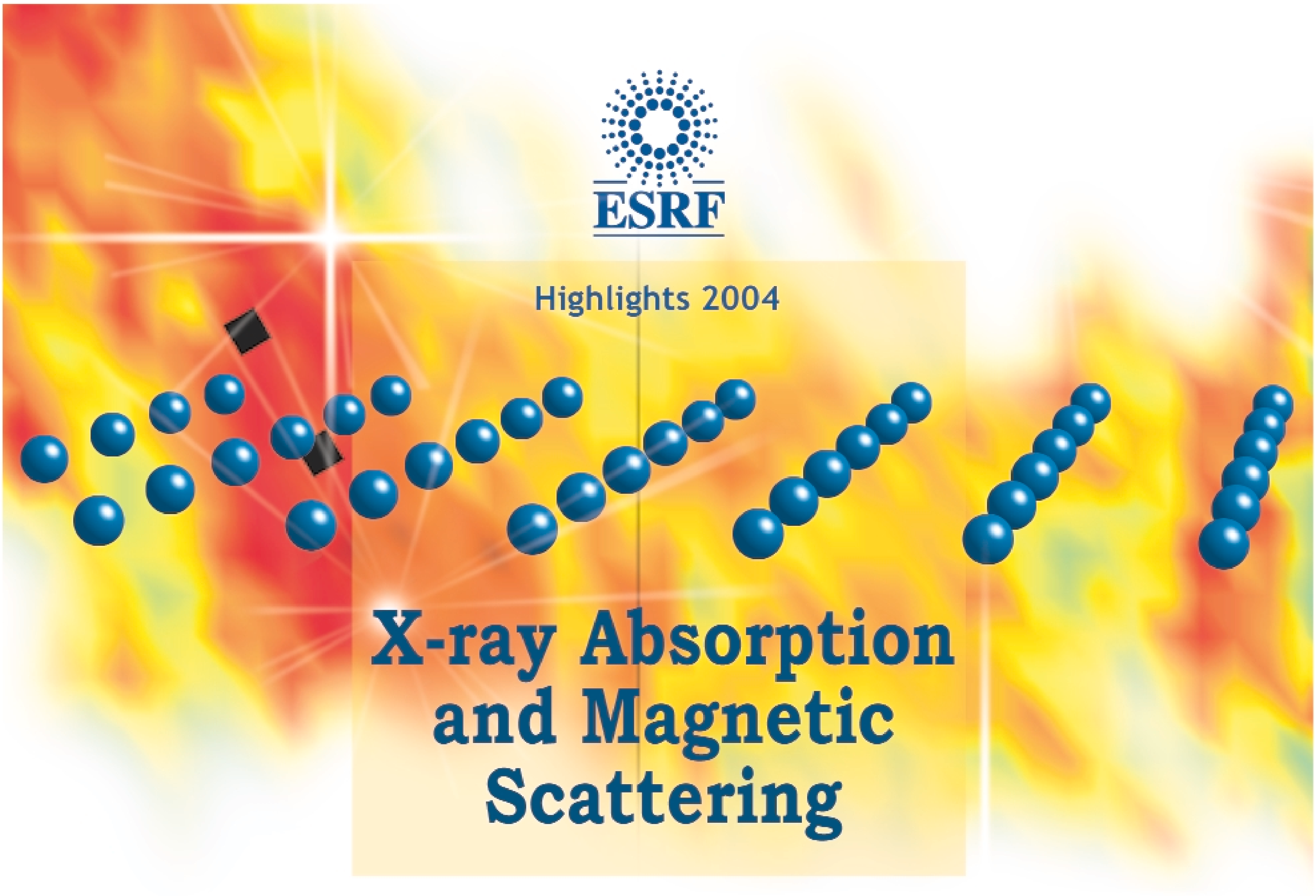

Highlights 2004

X-ray Absorption and Magnetic Scattering

Introduction

In the following articles the breadth and diversity of the research carried out during the last year can be seen. The chapter is divided into three sections, each with a short introduction: X-ray Absorption Fine Structure (EXAFS); X-ray Magnetic Circular Dichroism and Magnetic Scattering; Electronic Structure. However, in some senses this segregation is arbitrary, as the more general trend that is becoming evident is the combination of methods. This applies to both X-ray methods (e.g. EXAFS and diffraction; structural and magnetic measurements etc.) and to X-ray probes combined with laboratory techniques but applied *in situ* (*e.g.* Scanning tunnelling microscopy (STM); Infra-red or Ultra-violet spectroscopy, etc.). This is true in many disciplines, including Chemistry, Physics, and Magnetism, where one often needs to measure complementary information at the same time to address a problem. For example, having structural (both local and long range) and electronic information measured under the same conditions is becoming of paramount importance. As one pushes the limits of the possibilities of the X-ray methods by going to more extreme conditions, whether it be higher pressures, lower temperatures, faster time scales, smaller samples or higher magnetic fields, having a complete picture becomes imperative and will be a challenge for the coming years.

N. Brookes

X-ray Absorption Fine Structure

Introduction by S. de Panfilis, ESRF

X-ray Absorption Fine Structure (XAFS) spectroscopy is a structural probe for the local atomic environment around selected chemical species. This unique and powerful technique has recently been used in combination with other structural or chemical methods, providing an improved comprehension of the observed phenomena. The scientific issues addressed by these studies cover many different domains and it is well beyond the scope of this text to cite all of them. A few of these are reported in the following pages. Here we would like to present the general trend which has emerged in the last year.

On the X-ray absorption beamlines of the ESRF, the simultaneous usage of X-ray diffraction (XRD) and absorption spectroscopy (XAS) has become more and more routine. Thanks to the availability of novel experimental apparatus [1] designed to collect both XAS and XRD, XAFS measurements of systems under extreme conditions of high pressure and high temperature provide novel insight into the local atomic interactions as a function of thermodynamic parameters. This is very clearly demonstrated in the following articles from A. Filipponi *et al.* and D. Testemale *et al.* on aqueous solutions, and from A. San Miguel *et al.* on open clathrate Si crystals. Along the same lines, other interesting experiments have also been carried out in recent months. Among these, a study on the structural investigation of liquid Ga droplets dispersed in an epoxy matrix [2] revealed an extraordinary extension of metastable liquid Ga up to 2.3 GPa at room temperature. These measurements also showed the possible appearance of different Ga liquid polymorphs as a function of pressure. In another study on the structure of cubic ReO_3 by means of simultaneous XAFS and XRD over a wide range of temperatures [3], it was possible to reveal anomalies in the Re local environment, known to be responsible for the negative thermal expansion observed in this system. The high quality of the data allowed the scientists to determine the thermal evolution of Re-O distances with subpicometer sensitivity.

The usage of conventional laboratory techniques (UV-Vis, IR, FT-IR, DRIFTS, mass spectroscopy, galvanostatic electrochemistry) applied in combination with XAS in chemical experiments is also becoming an asset for the understanding of complex chemical reactions. Indeed, *in situ* time-resolved UV-Vis spectroscopy and dispersive XAFS were simultaneously applied to investigate homogeneous catalytic reaction mechanisms, as it is clearly shown in the following article from M. Tromp *et al.*. Analogously, synchronous, time-resolved, infra-red, XAFS, and mass spectroscopies were used to investigate the dynamic behaviour of Rh/Al_2O_3 catalysts during NO reduction by CO [4]. As a result, it has been found that the NO conversion, and its kinetic character are closely correlated to the conversion of Rh(I) to Rh(0). In a study on the intercalation of oxygen into the $SrCoO_{(2.5)}$ system, the covalence from the starting compound to the final $SrCoO_3$ reaction product was measured by XAFS during charge transfer under galvanostatic controlled conditions [5]. The Co oxidation was found to occur following a double step process, and an ordered intermediate phase was identified by X-ray and neutron diffraction at the corresponding charge transfer.

Another novel issue that deserves to be highlighted is the usage of very high photon energies for recording XAS spectra at high Z element K-edges. Exploiting the high photon flux from the source at very high energies, XAFS data collected at the lanthanides K-edges [6] were able to shed new light on the so-called “gadolinium brake” in the coordination of water molecules around rare-earth ions in aqueous solutions. In a different study, new results on the local coordination of trace rare earth cations in garnets were obtained by means of Dy K-edge XAS [7]. Different local environments were observed in distinct garnet compositions. This result, in contrast to what was previously believed on the basis of atomistic simulations of garnet structure, is of relevance for modelling petrologic and geochemical processes.

References

[1] For example, A. Filipponi *et al.*, *Rev. Sci. Instrum.* **74**, 2654 (2003).
[2] R. Poloni *et al.*, *submitted* (2004).
[3] J. Purans *et al.*, *in preparation.*
[4] M.A. Newton *et al.*, *Chem. Comm.*, **21**, 2382 (2004).
[5] R. Le Toquin *et al.*, *submitted* (2004).
[6] A. Abassi *et al.*, *in preparation*.
[7] S. Quartieri *et al.*, *Phys. Chem. Minerals* **31**, 162 (2004).

Newly-developed in situ Time-resolved Spectroscopic Techniques to Reveal Homogeneous Catalytic Reaction Mechanisms

The formation of aryl-aryl bonds and aryl-hetero-atom bonds are among the most important reactions in organic synthesis. C_{aryl}-N containing structures are important in biological systems and are common moieties in pharmaceuticals. Although in many cases palladium is a more active and selective catalyst under milder conditions compared to copper, some reactions

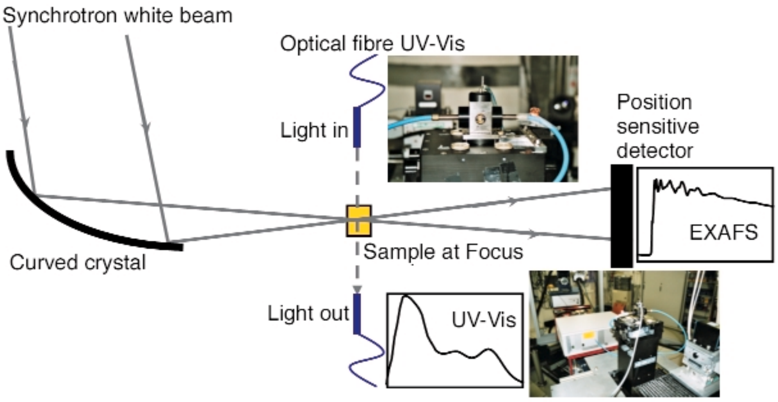

Fig. 102: Schematic representation of the combined ED-XAFS/UV-Vis setup. The insets display the complete setup and the cuvette in the observation head of the stopped flow module.

only proceed with copper. Moreover, because of its lower costs, copper is preferred for industrial processes. The mechanisms proposed for the Cu catalysed reactions are as yet reasonable guesses, because none of the intermediates have been isolated or characterised. Detailed structural information about catalysts in their active phase is in general the missing link in explaining structure-performance relationships in homogeneous catalysis.

X-ray absorption fine structure (XAFS) spectroscopy is a powerful technique for determining the local structure of metal complexes, such as the type and number of neighbouring atoms, distances and electronic properties. XAFS can be applied *in situ* and, using an energy dispersive data acquisition setup (ED-XAFS), spectra can be obtained in the sub-second range during reaction. With the use of ultraviolet and visible absorption spectroscopy (UV-Vis), the electronic absorption by molecules can be detected *in situ* and with time-resolution.

In collaboration with the ESRF staff at **ID24**, we have developed a novel setup (**Figure 102**) which enables the simultaneous acquisition of time-resolved *in situ* XAFS and UV-Vis data on homogeneous catalytic systems. A stopped-flow module is used to perform the reactions. Special cuvettes have been designed, in which the X-rays and UV-Vis light traverse perpendicular to one another. Different path lengths enable the simultaneous ED-XAFS and optical fibre UV-Vis experiments on the reaction mixture.

The Cu(II)-catalysed arylation reaction of phenylboronic acid and imidazole to *N*-phenylimidazole was studied at ambient conditions, with a time resolution of 10-200 milliseconds. Stoichiometric reactions were performed to decrease the number of reaction intermediates. The reactions were conducted using 20 mM of the dinuclear tetramethylenediamine bis-μ-hydroxy copper(II) complex $[Cu(OH)(TMEDA)]_2Cl_2$ as homogeneous catalyst.

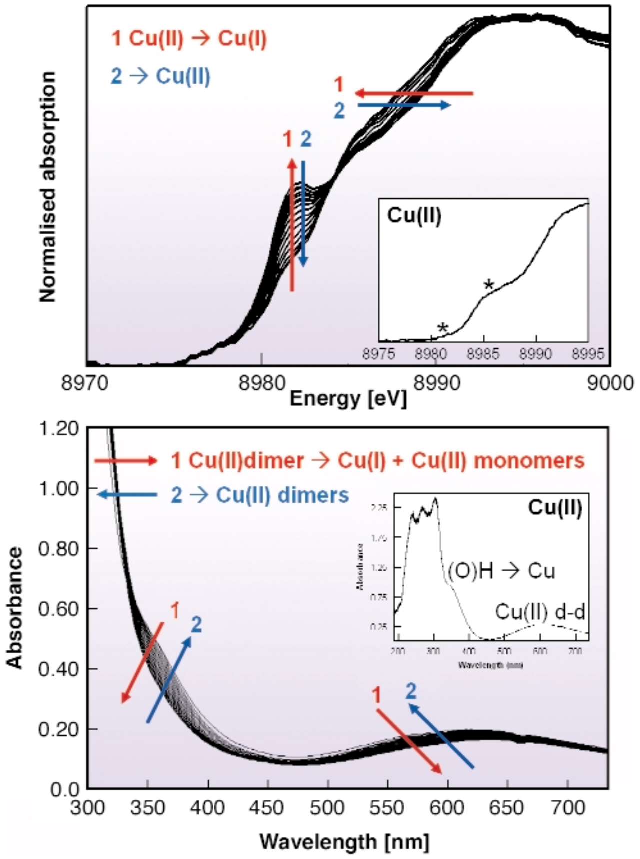

Fig. 103: Simultaneous (a) EDXAFS and (b) UV-Vis spectra of the Cu(II) catalysed arylation reaction. The insets show the starting dimeric Cu(II) catalyst in solution.

In **Figure 103** examples of the simultaneous ED-XAFS and time-resolved UV-Vis spectra of the arylation reaction are shown. The dinuclear Cu(II) structure of the starting Cu catalysts is confirmed. During reaction, the starting Cu(II) peaks disappear and an immediate formation of a pre-edge at ~8982 eV (Figure 103a) indicates the formation of a Cu(I) species. Simultaneously, UV-Vis spectra show the disappearance of the band at ~355nm and the decrease of the d-d transition band at ~620 nm, *i.e.* the dissociation of copper dimers and the disappearance of Cu(II) species respectively. These spectroscopic results thus suggest the formation of a monomeric Cu(I) species. In time, both ED-XAFS and UV-Vis results display the disappearance of Cu(I) species and the regeneration of Cu(II) species, both in monomeric and dimeric form.

Single step reactions were performed to mimic subsequent individual steps in the catalytic cycle and using these complementary techniques, the different reaction intermediates have been characterised in detail. In combination with catalytic results, a novel and unexpected mechanism for the Cu(II) catalysed arylation reactions has been proposed, **Figure 104**, which is in accordance with the simultaneously acquired ED-EXAFS results and with results from other characterisation techniques (*e.g*. EPR, NMR, XRD).

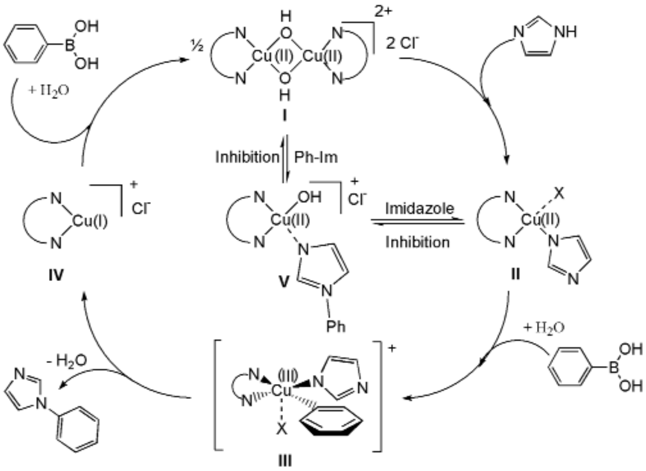

Fig. 104: Proposed reaction mechanism for the Cu(II) catalysed arylation of imidazole and phenylboronic acid.

The first and selectivity determining step in the catalytic cycle is the reaction of the Cu(II) dimer with imidazole, forming a monomeric Cu(II)(imidazole) intermediate. Upon subsequent addition of the phenylboronic acid reactant, a transient Cu(III) intermediate is formed which after reductive elimination forms the phenylimidazole product and a Cu(I) monomeric species. Finally, the Cu species is reoxidised forming again the Cu(II) mononuclear and dinuclear complexes. Inhibition by imidazole and phenylimidazole is observed. The phenylboronic acid is, in combination with H_2O, involved in the oxidation and reoxidation steps, whereas O_2 is not necessary for the reaction to proceed.

In summary, we have developed a new combined spectroscopic setup, which is a powerful tool for the *in situ* and time-resolved characterisation of reaction intermediates and therefore for the determination of reaction mechanisms. In principle every metal can be studied, however, the time resolution and quality of the data are dependent on the metal and its concentrations used.

Principle Publication and Authors

M. Tromp (a), G.P.F. van Strijdonck (b), S.S. van Berkel (b), A. van den Hoogenband (c), M.C. Feiters (d), B. de Bruin (d), S.G. Fiddy (e), A.M.J. van der Eerden (a), J.A. van Bokhoven (a), P.W.N.M. van Leeuwen (b), D.C. Koningsberger (a), *submitted*.
(a) Utrecht University (Netherlands)
(b) University of Amsterdam (Netherlands)
(c) Solvay Pharmaceuticals (Netherlands)
(d) University of Nijmegen (Netherlands)
(e) ESRF

Structural and Electronic Evolution of $As(OH)_3$ in High Temperature and High Pressure Aqueous Solutions by X-ray Spectroscopy

Intermolecular interactions in aqueous solution under conditions of elevated temperature and pressure are related to the structure of the solvent and in particular to the strength of the hydrogen bonding. Therefore, studying the structural and electronic evolution of solute particles with changing conditions of temperature and pressure is a way of obtaining information about the solvent itself [1].

The aim of our studies is to understand the relation between physical properties and structural organisation of liquids under conditions of elevated temperature and pressure, up to and beyond their critical point. These studies are possible thanks to a combination of the extremely bright and well-focused X-ray beams at the ESRF with specially-developed high-temperature and high-pressure cells. Recently we have investigated the molecular structure of the hydration of ions and molecules in supercritical water and aqueous solutions.Several techniques were used: X-ray Absorption spectroscopy (XAS at the FAME BM30B and ID26 beamlines) and X-ray Raman Inelastic Scattering to determine local structures of solvation around solute and solvent molecules, and Small Angle X-ray Scattering (SAXS) to determine the structure of the mesoscopic inhomogeneous distribution of water molecules in the compressible regime.

The molecule aqueous arsenious acid, $As(OH)_3$, is a very good candidate as a probe: it possesses a nonzero dipole moment that may evolve with the solvent permittivity ε and three OH groups likely to establish hydrogen bonds with solvent water molecules. The geometrical and electronic structure of the arsenious acid molecule $As(OH)_3$ in aqueous solutions was investigated by XAS. A new optical cell (**Figure 105**) developed for fluorescence spectroscopic studies permitted conditions from ambient to supercritical (0.3 m, $P = 250$ and 600 bars, $T < 500$°C) to be employed.

EXAFS analysis shows the constancy of the As-O distance, which remains about 1.77 Å in all conditions. These new results confirm that the As-O bonding has a strong covalent character, which remains under the supercritical temperature conditions. In the XANES region, new first principle calculations using the

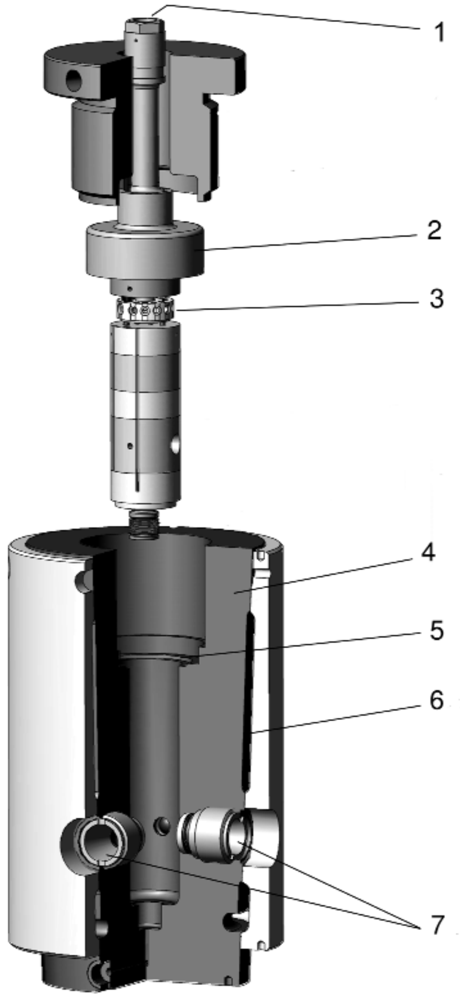

Fig. 105: 3D drawing of the high pressure (HP)-high temperature (HT) setup: (1) He inlet through the HP vessel plug; (2) HP vessel plug; (3) thermocouples and electrical connections; (4) HP vessel (150mm); (5) viton seal; (6) water cooling circulation; (7) thin beryllium windows.

FDMNES code [2] reveal an enlargement of the intramolecular O-As-O angles when temperature increases (**Figure 106**), coupled with a small reduction of the atomic partial charge magnitude. The changes in the solvent structure, such as the weakening of the hydrogen bonded network concomitant with the decrease of the solvent dielectric constant, are believed to explain the structural and electronic modifications in the $As(OH)_3$ molecule with increasing temperature. Indeed, a weakening of the hydrogen bonding between the As hydroxide complexes and water molecules, releases the molecule from the hydrogen-bonded network and allows it to open its structure to a more tetrahedral configuration (consistent with the sp^3 hybridisation of the As electronic orbitals). At the same time, the decrease of the bulk water dielectric constant results in the reduction of the partial atomic charges. The combination of EXAFS analysis with realistic XANES simulations is demonstrated to be a powerful tool, sensitive to both the 3D geometrical and electronic structures of aqueous complexes and on the solvent itself, in high temperature/high pressure fluids.

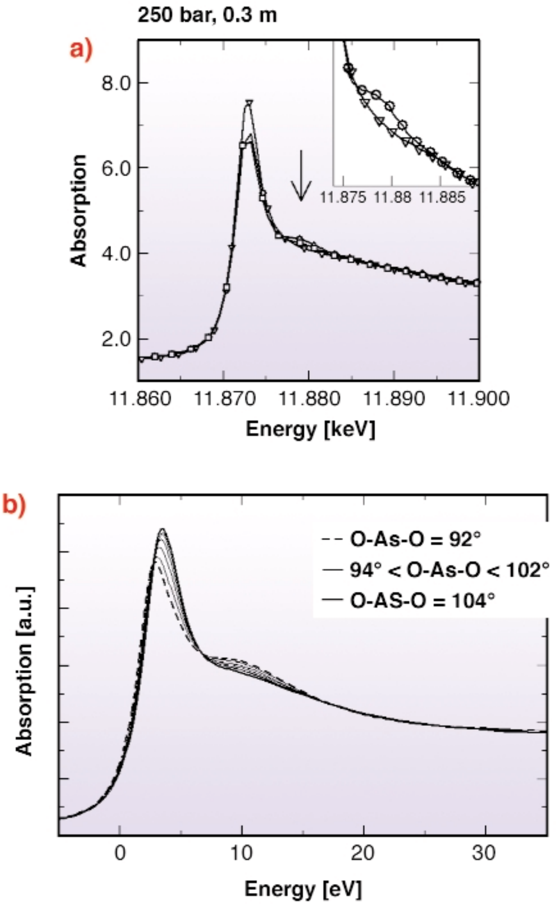

Fig. 106: a) Xanes spectra of arsenious acid solutions (0.3m) at 250 bars (30°C, 100°C and 425°C). The vertical arrow denotes a resonance at 8 eV above the edge which is damped with temperature. b) Simulated spectra (distances As-O=1.77 Å, As-O-H=120°) for O-As-O angles varying from 92° to 104° with a 2° step. The 8 eV resonance is also damped.

References

[1] V. Simonet, Y. Calzavara, J.-L. Hazemann, R. Argoud, O. Geaymond and D. Raoux, *J. Chem. Phys.* **116**, 2997 (2002) and *J. Chem. Phys.* **117**, 2771 (2002).

[2] Y. Joly, *Phys. Rev.* B **63**, 125120 (2001).

Principal Publication and Authors

D. Testemale (a, b), J.L. Hazemann (a), G. Pokrovski (c), Y. Joly (a), J. Roux (d), *J. Chem. Phys.* **121**, 8973 (2004).

(a) Laboratoire de Cristallographie, CNRS, Grenoble (France)
(b) SNBL/ESRF
(c) Laboratoire de Géochimie, CNRS, Toulouse (France)
(d) Institut de Physique du Globe, CNRS, Paris (France)

Water Solvation of Ions at High Pressure

High pressure water is a fundamental constituent of the Earth crust and upper mantle. Based on space probe observations and planetological models it has been proposed that water may even exist in the form of buried salted oceans under a deep ice crust on certain giant planet satellites and in particular on Europa [1]. There, a pressure of several kilobars (kbar) may be reached as compared with the ~1 kbar of the oceanic troughs on Earth.

These findings stimulate fundamental questions on whether, and to what extent, these harsh environments could support life. It is known that barophilic bacteria may survive pressures in the kbar range, but protein denaturation will take place at some point. In other scientific contexts, water, in the high pressure undercooled liquid range, has been predicted to display a liquid-liquid phase transition line ending in a critical point [2], as a result of the disruption of the hydrogen bonded network upon increasing pressure. These transformations will also affect the behaviour of water as a solvent which is relevant to biochemical sciences. Understanding the behaviour of water at high pressure is therefore a fundamental achievement with an interdisciplinary scientific relevance.

In addition to the possibility of investigating the structure of pure water under pressure [3], the ESRF facility allows us to conceive experiments where we investigate the behaviour of water around "impurities" present in a sample in the 1% concentration range, which is a fundamental step for the understanding of the water behaviour as a solvent at high pressure. This is possible using the so called "large volume" high pressure technique associated with the Paris-Edinburgh press [4] shown in **Figure 107** and available at **BM29**.

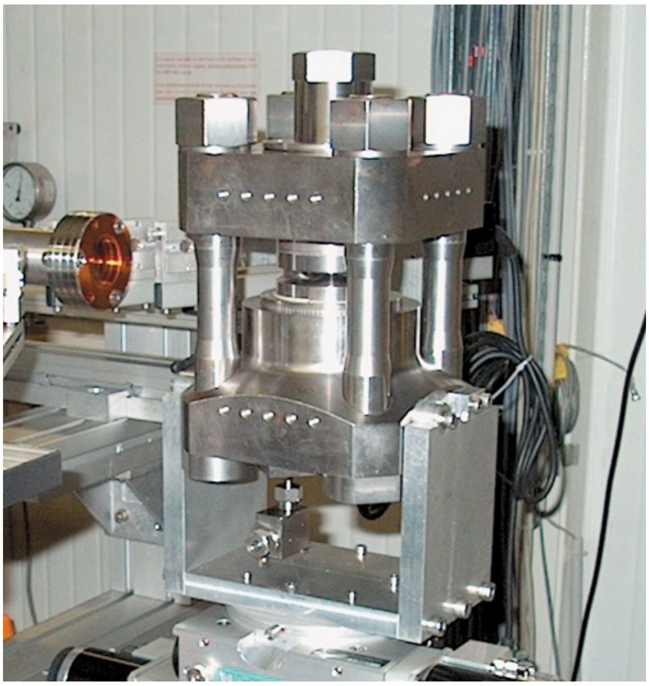

Fig. 107: The BM29 Paris-Edinburgh press.

With this equipment it is possible to create extreme conditions up to about 100 kbar and up to 1000-2000 K in a volume of about 1 cubic mm that can be filled with an aqueous solution sample. An X-ray absorption spectroscopy (XAS) experiment can be tuned to (and above) the threshold for the transitions of the 1s electron of a selected ion, into continuum states. Therefore the X-ray absorption signal will be only be determined by the environments of those atoms selected by the absorption edge being investigated. Such sensitivity cannot be achieved by any other experimental technique.

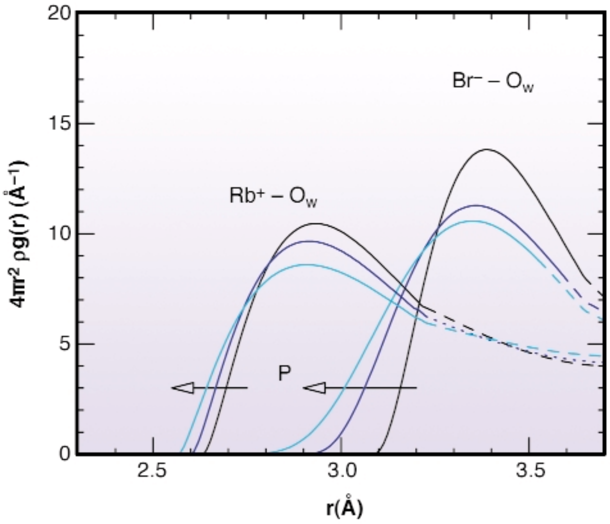

Fig. 108: Ion-water oxygen radial distributions as a function of pressure at ambient pressure, 14 kbar, and 28 kbar.

We have performed an experiment of this kind on a RbBr 0.92 molal aqueous solution measuring high quality X-ray absorption spectra at the Br and Rb K-edges as a function of pressure, following the pure water melting line. We have obtained the first experimental results for the pressure dependence of the radial distributions of the water oxygen atoms around the two ionic species. These functions, shown in **Figure 108**, indicate that the O distribution associated with the hydration shell of the negative ion is compressed remarkably with the application of pressure. In comparison, the O distribution around Rb ions appears to be less affected thus indicating the occurrence of a considerable molecular reorientation around the ions in the investigated pressure range. These results provide evidence that the water's structural transformation with pressure heavily affects its behaviour as a solvent. These findings, which are relevant to the planetological chemistry of high-pressure water, may also have implications on the ability of apolar solutes to develop a hydrophobic interaction under high pressure.

References

[1] J.S. Kargel, J.Z. Kaye, J.W. Head, G.M. Marion, R. Sassen, J.K. Crowley, O.P. Ballesteros, S.A. Grant, and D.L. Hogenboom, *Icarus* **148**, 226 -265 (2000).

[2] O. Mishima and H. E. Stanley, *Nature* **396**, 329-335 (1998).

[3] J.H. Eggert, G. Weck, and P. Loubeyre, *J. Phys.: Condens. Matter* **14**,11385 -11394 (2002).

[4] J.M. Besson, R.J. Nelmes, G. Hamel, J.S. Loveday, G. Weill, and S. Hull, *Physica B* **180-181**, 907 (1992).

Principal Publication and Authors

A. Filipponi (a), S. De Panfilis (b), C. Oliva (c), M.A. Ricci (c), P. D'Angelo (d), D.T. Bowron (e), *Phys. Rev. Lett.* **91**, 165505 (2003).
(a) INFM and Dipartimento di Fisica, Università dell' Aquila (Italy)
(b) ESRF
(c) Dipartimento di Fisica "E. Amaldi", Università degli Studi Roma Tre and INFM, Roma (Italy)
(d) Dipartimento di Chimica, Università di Roma "La Sapienza", Roma (Italy)
(e) ISIS Facility, Rutherford Appleton Laboratory, Didcot (UK)

Pressure-induced Homothetic Isostructural Volume Collapse in the Open Clathrate Crystals

Pressure induced isostructural transitions showing a homothetic volume contraction are extremely unusual. In fact, the usual pressure-induced phase transitions in crystalline solids are first order type, having a displacive nature associated with a change of structure. What are the necessary elements for a homotethic volume collapse of isostructural nature? First of all, the homothety constraint makes cubic structures the only good candidates for such an isostructural transition. But as the atomic structure is not varied, the only way to modify the properties of the crystal to allow for a volume collapse is "to modify the atoms". This is in fact what has been proposed for the few cases where pressure-induced isostructural volume collapse of cubic structures have been observed (Sm chalcogenides, Ce). This original idea was first proposed by E. Fermi for the Cs case, in which pressure gives rise to an inversion between the s and d atomic orbitals of the atom. Finally, for this particular case, recent work has shown the non-isostructural character of the transition.

The structure of the Ba_8Si_{46} type-I silicon clathrate can be viewed as the arrangement of face sharing "super-atoms" made of nano-cages of 20 or 24 silicon atoms each containing one guest Ba at the centre (see **Figure 109**). It constitutes an open form of sp^3 silicon allowing for endohedral intercalation. The application of pressure modifies the size of the nano-cages. This opens the way for the existence of a critical size by which the nature of the "super-atom" can be varied due to a modification of the hybridisation between the guest atom and the host cage.

We have performed high-pressure X-ray absorption and X-ray diffraction studies on the Ba_8Si_{46} clathrate. The experiments were performed at beamlines **ID24** (Ba L-III edge), **BM29** (Ba K-edge) and **ID30** (angular dispersive X-ray diffraction). The main conclusion has been the unambiguous determination of the homothetic character of the volume collapse transition [1] taking place at 11.5-14.0 GPa (**Figure 110**). The comparison of our results with high-pressure Raman experiments [2], allowed us to explore the details of the driving mechanism of such an original phase transformation. A change of hybridisation in the Ba@Si_{20} "super-atom" between Si-p and Ba-d orbitals appears as the most probable mechanism.

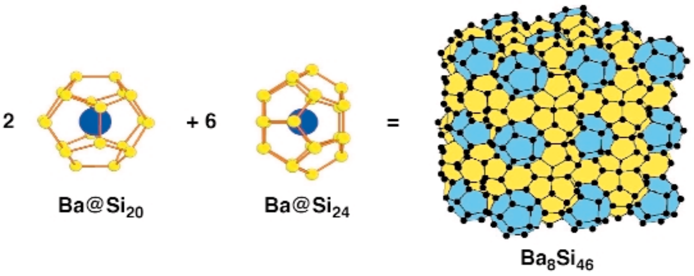

Fig. 109: The cubic type-I clathrate structure of Ba_8Si_{46}.

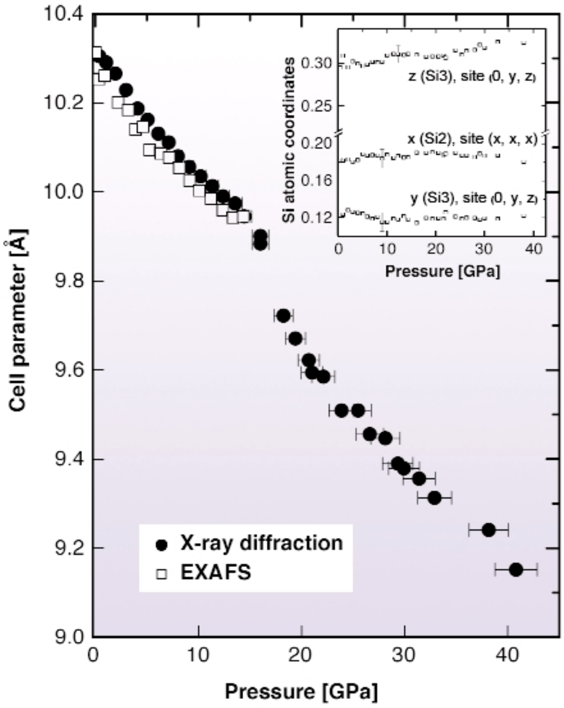

Fig. 110: Lattice parameter variation of the clathrate structure of Ba_8Si_{46} obtained by X-ray diffraction and EXAFS at the Ba K-edge assuming that the Ba atom is at the centre of the "super-atoms". Inset: observed behaviour with pressure of the silicon atomic positions, showing the homothetic evolution of the silicon cages through the isostructural volume collapse.

A further low-pressure anomaly observed in Raman experiments [2], was also visible at the Ba L-III edge, showing that the disappearance of the Ba@Si_{24} quasi-vibronic type excitations at 5-7 GPa is coupled with a change of hybridisation of the Ba atom within the larger cage. This transformation, also of isostructural nature, does not introduce any observable effect in the X-ray diffraction patterns.

The effect of barium intercalation stabilises the clathrate structure up to pressures three times higher than the ones observed for the empty silicon clathrate structures and allows tetrahedral silicon with record interatomic distances as low as 2.13 Å to be obtained. At 49 GPa, the highest pressure studied, the structure becomes irreversibly amorphous.

References

[1] A. San Miguel, P. Mélinon, D. Connétable, X. Blase, F Tournus, E Reny, S Yamanaka and J.P. Itié, *Phys Rev B* **65**, 054109 (2002).

[2] T. Kume, H. Fukuoka, T. Koda, S. Sasaki, H. Shimizu and S. Yamanaka, *Phys. Rev. Lett.* **90**, 155503 (2003).

Principal Publication and Authors

A. San Miguel (a), P. Toulemonde (a), A. Merlen (a), T. Kume (a), S. Le Floch (a), A. Aouizerat (a), G. Aquilanti (b), S. Pascarelli (b), J.P. Itié (c), S. Yamanaka (d) *Europhys. Lett.*, 69(4), (15 Feb. 2005).

(a) Laboratoire de Physique de la Matière Condensée et Nanostrucutres, University of Lyon and CNRS (France)

(b) ESRF

(c) Soleil, Saclay (France)

(d) University of Hiroshima (Japan)

X-ray Magnetic Circular Dichroism and Magnetic Scattering

Introduction by F. Wilhelm, ESRF

X-ray Magnetic Circular Dichroism (XMCD) is inherently an element specific and orbital selective experimental technique that has greatly contributed to our understanding of magnetism. This tool is now widely used to unravel the microscopic origin of magnetism in complex magnetic materials: crystals, multilayers, clusters and impurities. Recently, technological applications have stimulated the interest in new magnetic heterostructures at the nanometre scale (spin valves, magnetic tunnel junctions, etc…), which exhibit unusual magnetic properties. However, there will be no further progress in the design of such new magnetic nanostructures without a deeper understanding of the mechanisms that control their magnetic properties and govern their magneto-optical response.

It is often considered that itinerant magnetism originates mainly from the spin contribution. However, the orbital moment can be larger than 10% of the total magnetic moment (as in the case of 5*d* and 5*f* elements). XMCD experiments have shown that the orbital moment plays an important role in magnetic properties. Typically, orbital magnetism is at the origin of the magnetic anisotropy and therefore determines the easy axis magnetisation direction. The dimensionality strongly affects the orbital magnetism due to reduction of symmetry at the surfaces or interfaces. XMCD spectroscopy is one of very few experimental techniques that allow one to disentangle the spin and orbital contributions to the total magnetic moment carried by an absorbing atom. The effect of the local structure on orbital magnetism is nicely illustrated by the XMCD studies of strained superlattices under high pressure.

The effect of dimensionality on the orbital magnetic moment of transition metals is another hot topic in magnetism research. A wide variety of magnetic behaviours has been revealed in one-dimensional magnetic chains that are strikingly different from those observed in two-dimensional structures and bulk materials. Unexpectedly large orbital magnetic moments have been observed in the case of transition metal impurities in diamagnetic cubic single crystals. Such results cannot be easily understood using existing theories and certainly call for a development of more sophisticated models of magnetism in low-dimensional systems.

Another important axis for research that came out of XMCD studies is the magnetism of “non-magnetic” atoms induced via hybridisation with their magnetic neighbours. Particularly of interest are U-based multilayers in which a small induced magnetic moment on uranium is responsible for the strongly-enhanced magneto-optical response observed with Kerr rotation at room temperature.

The use of the resonant-scattering technique adds spatial sensitivity to the X-rays research in magnetism. These experiments were shown to be very efficient to unravel the magnetic structure of complex antiferromagnetic oxides. Moreover, X-ray scattering techniques can be extended to study charge and spin density waves in thin films and heterostructures.

Last but not least, continuing efforts are invested into the development of multi-element, energy-resolved detectors, which could be operated in the soft X-ray range as well as at high energies. The first experimental results obtained with this type of detector have revealed a great potential for recording high-quality XMCD spectra of magnetic nanostructures.

Simultaneous Magnetic and Structural Study of the Iron α-ε Pressure Phase Transition

The iron phase-diagram has attracted considerable interest for many years now. At the beginning, the motivation was to discover its central role in the behaviour of alloys and steel. Later its geophysical importance was underlined, because of its predominant abundance in the Earth's core. The phase diagram of iron under extreme pressure and temperature conditions is still far from being established. Under application of an external pressure, iron undergoes a transition at 13 GPa from the bcc α-phase to the hcp ε-phase structure, with the loss of its ferromagnetic long range order.

We have performed a simultaneous X-ray absorption spectroscopy (XAS) and X-ray magnetic circular dichroism (XMCD) study of the Fe bcc-hcp phase transition with pressure. In absorption spectroscopy, polarised X-rays are intrinsic structural, electronic and magnetic probes. Methods used are extended X-ray absorption fine structure (EXAFS), X-ray absorption near edge structure (XANES) and XMCD. The XAS techniques are able to clearly differentiate the signature of bcc or hcp local symmetry, while XMCD is very sensitive to changes in the magnetic moments. Thus, for each pressure point, we can obtain simultaneous information on both the magnetic and structural properties of the system, *i.e.* on the same sample and under the same thermodynamic conditions. Consequently, there is no relative pressure incertitude for each measurement. This is very important in the high-pressure domain where reproducibility of the hydrostatic conditions is difficult to obtain. As an example, **Figure 111** presents the K-edge XANES and XMCD signals of a pure Fe foil recorded at 10 GPa.

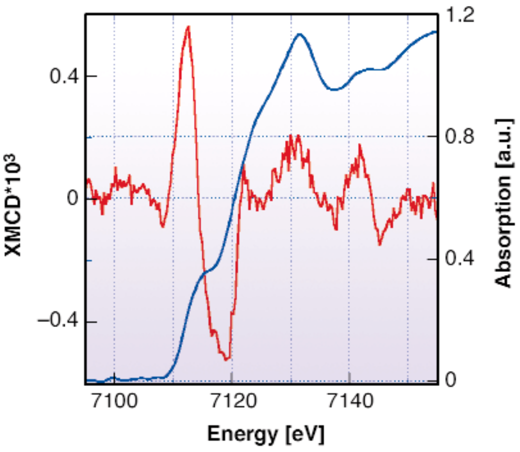

Fig. 111: K-edge XANES and XMCD signals of pure Fe foil recorded at 10 GPa.

The experiment was carried out at **ID24**, the ESRF's dispersive XAS beamline. Parallel detection of the whole spectrum is made possible by the energy-dispersive highly-focusing X-ray optics. The beamline is particularly well-suited for combined high pressure and XAS-XMCD studies at the Fe-K edge using a diamond anvil cell.

Figure 112 presents the evolution of the bcc/hcp phase fraction (full squares) and the magnetic/non-magnetic phase fraction (full circles) as a function of pressure. The onset of the structural transition occurs at about 13.8 GPa and is over at 16.2 GPa. The magnetic transition is indeed quite abrupt occurring within a pressure range of 2.2 GPa, with an onset at 13.5 GPa. Our data shows that between 13.5 and 15.7 GPa, the XMCD is suddenly reduced to zero, within the error bars, indicating the disappearance of the room temperature ferromagnetic order of iron. The abrupt drop to zero of the iron magnetic moment when the bcc to hcp phase transition occurs proves the first order nature of the pressure-induced magnetic transition. The pressure transition domain for both the structural and the magnetic phase transition is narrower with respect to previous structural and magnetic studies. It could be attributed to a lower pressure gradient within the probed region and directly correlated to the smaller sample volume probed.

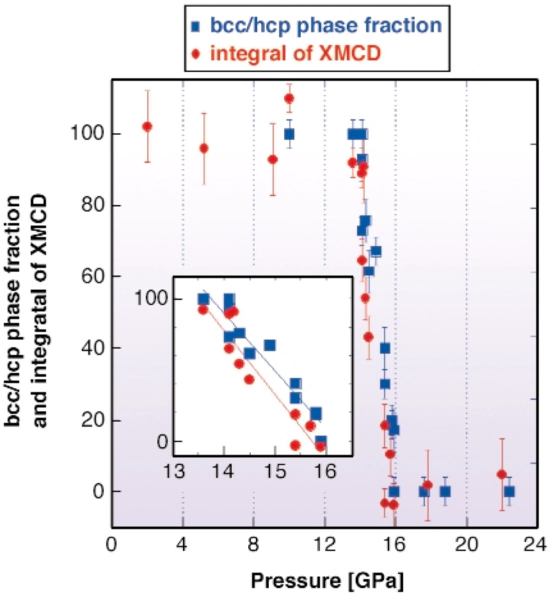

Fig. 112: Evolution of the amplitude of the XAS (full squares) and of the XMCD signals (full circles) with pressure.

A closer look at the data obtained shows that the value of the magnetic/non-magnetic phase fraction is systematically lower than that of the bcc/hcp phase fraction for each XAS/XMCD pair of measurements during the phase transition. Thanks to the combination of the two probes, there is no relative pressure incertitude between the XAS/XMCD data points. Therefore, our study suggests that the iron high spin ferromagnetic state disappears before complete transformation into hcp. This is better seen on the enlargement of the transition region in Figure 112. Our observations are in good agreement with the theoretical transition scheme given by Ekman *et al.* [2]. This could also be due to the presence of magnetically dead layers at the interface between the bcc and hcp phase.

In summary, we have measured XAS and XMCD of iron metal under pressure along the bcc to hcp phase transition. The simultaneous measurement of element specific magnetic properties using XMCD and of element specific local structural and electronic properties using XAS has an enormous potential in correlating the magnetic, electronic and structural degrees of freedom during phase transitions. For Fe at high pressure, we find that the local structure and the magnetic transition occur within 2.4 GPa and are much sharper than usually described in the literature. This proves unambiguously the first order nature of the iron bcc to hcp transition. We have also evidence of a small pressure gap between the magnetic transition and the structural one, suggesting the driving role of magnetism during the transition.

References

[1] O. Mathon, F. Baudelet, J.-P. Itié, S. Pasternak, A. Polian, S. Pascarelli, *J. Sync. Rad*., **11**, 423-427 (2004).
[2] M. Ekman, B. Sadigh, K. Einarsdotter and P. Blaha, *Phys. Rev. B* **58**, 5296 (1998).

Principal Publication and Authors

O. Mathon (a), F. Baudelet (b, c), J.-P. Itié (b), A. Polian (b), M. d'Astuto (b), J.-C. Chervin (b), S. Pascarelli (a), *Phys. Rev. Lett*., **93**, 255503 (2004).
(a) ESRF
(b) Physique des Milieux Condensés (UMR 7602), Université Pierre et Marie Curie, Paris (France)
(c) Synchrotron SOLEIL, Gif-sur-Yvette (France)

Resonant X-ray Scattering Determination of the Magnetic Structure of Li_2VOSiO_4

Two-dimensional Quantum (S = 1/2) Heisenberg Antiferromagnets (2DQHAF) have been widely studied as systems where a phase transition from the renormalised classical to the quantum disordered regime can be induced by charge doping, or by a sizeable frustration. In particular, for a square lattice with a super-exchange coupling along the diagonals of the square, J_2, about half of the one along the sides, J_1, a cross-over to a spin-liquid ground state is expected [1]. For $|J_2/J_1| < 0.35$ Néel order occurs, whereas for $|J_2/J_1| > 0.65$ a collinear order should develop, with two degenerate ground states having spins ferromagnetically aligned along the x(y)-axis and antiferromagnetically along y(x).

Theoretical models predict that in 2-dimensions the quantum fluctuations affects the value of the order parameter, which will be reduced to $m \sim 0.6\ \mu_B/V^{4+}$. A further reduction of the magnetic moment is expected for a system close to the border with the non-magnetic ground state.

While the theoretical understanding of the J_1-J_2 phase diagram has progressed considerably, an experimental verification of the theoretical predictions was still missing because suitable model compounds were not available. However, two recently-synthesised vanadates have been considered as prototypes for frustrated 2DQHAF on a square lattice, Li_2VOGeO_4 and Li_2VOSiO_4. The latter compound has been the object of a number of theoretical and experimental investigations during the past few years [2].

In Li_2VOSiO_4, see **Figure 113**, the magnetically-active network of spin 1/2 V^{4+} ions is built up by layers of VO_5 square pyramids sharing corners with SiO_4 tetrahedra. Neutron powder diffraction experiments established that the system orders antiferromagnetically below 2.8 K, with propagation vector (1/2 1/2 0). However, several points required further clarification: namely whether the magnetic structure is 2 or 3-dimensional; which of the two possible spin-arrangements is correct; and a determination of the values or at least the ratio of the values of the exchange integrals.

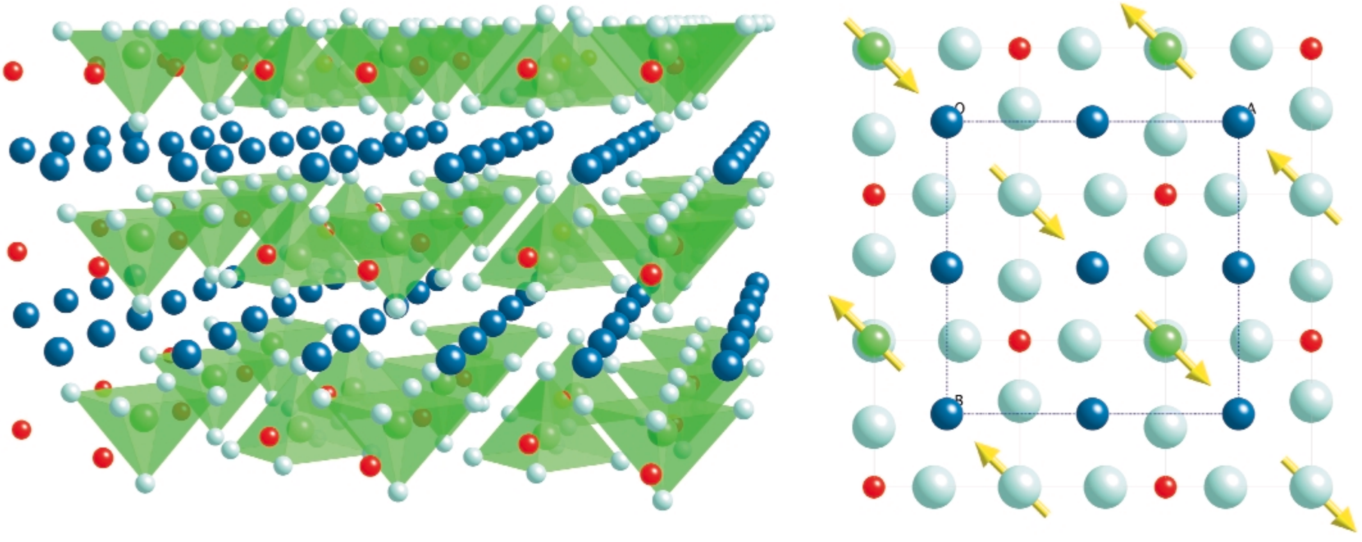

Fig. 113: Perspective view of Li_2VOSiO_4 (left) showing the layered character of the structure. Notice the VO_5 pyramids reversal. The small red circles are the Si^{4+} ions, whereas the V^{4+} ions are the larger green circles. On the right, the magnetic structure of Li_2VOSiO_4 projected along [001].

The first two of these ambiguities were solved by the results of Resonant X-ray Scattering (RXS) measurements performed at **ID20** on a 3×2×0.1 mm^3 single crystal. Determination of the exchange integrals will require much larger samples and a different experimental technique.

The results obtained have established that the ordered structure is three-dimensional with ferromagnetic coupling in the c-axis direction. The magnetic contribution to the scattering has a marked dependence on the magnetic structure and on the scattering channels (σ–σ or σ–π). It was possible to demonstrate that only the magnetic structure shown on the right in Figure 113 is compatible with the polarisation dependence of the measured magnetic reflections. The absence of a measurable magnetic scattering at high energy (5.480-5.495 keV, see **Figure 114**) is intriguing when compared with other reported Vanadium compounds. This could be related to the coordination and the valence of the Vanadium in Li_2VOSiO_4, as our calculations show that this result is not related to a different magnetic symmetry at the p states, but it is consistent with the idea that only the d states carry the magnetisation.

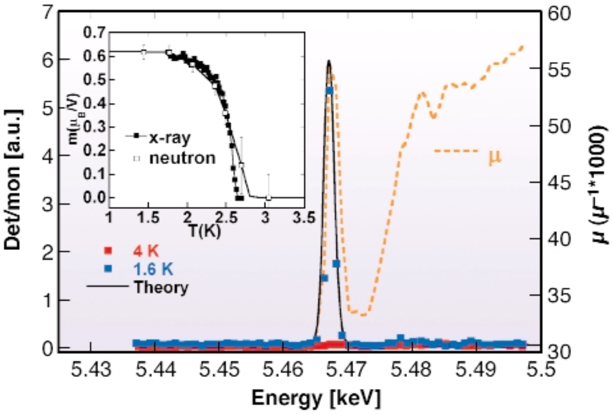

Fig. 114: Photon Energy dependence around the V K-absorption edge of the intensity of the (1/2 1/2 3) superlattice magnetic reflection collected in the σ–π channel. The inset shows the temperature dependence of the ordered magnetic moment as determined by neutron diffraction compared with the square root of the X-ray integrated intensity after normalisation at 1.7 K.

In conclusion, combining neutron powder diffraction with resonant X-ray scattering measurements on a single crystal has allowed us to establish the low temperature magnetic structure of Li_2VOSiO_4, which consists of collinear *a-b* antiferromagnetic layers stacked ferromagnetically along the *c* axis, confirming $J_2>J_1$. The neutron-measured ordered magnetic moment (0.6 μ_B/V^{4+}) is larger than previously reported and points to a system that is far from the border of the non-magnetic ground state, in good agreement with the latest theoretical predictions. In this system a mechanism to relieve the degeneracy of the two ground states is expected but, surprisingly, no structural distortion was observed close to the AF transition.

References

[1] P. Chandra *et al.*, *Phys. Rev. Lett.* **64**, 88 (1990).
[2] R. Melzi *et al.*, *Phys. Rev. Lett.* **85**, 1318 (2000).

Principal Publication and Authors

A. Bombardi (a,g), J. Rodriguez-Carvajal (b), S. Di Matteo (c), F. de Bergevin (a), L. Paolasini (a), P. Carretta (d), P. Millet (e), and R. Caciuffo (f), *Phys. Rev. Lett.* **93,** 27202 (2004).
(a) ESRF (France)
(b) LLB, CEA-Saclay (France)
(c) LNF-INFN (France)
(d) INFM (Italy)
(e) CNRS (France)
(f) Università Politecnica delle Marche (Italy)
(g) now at Diamond Light Source (UK)

Proximity Effect of Vanadium on Spin-density-wave Magnetism in Cr Films

The itinerant antiferromagnetism in Cr has attracted considerable attention during the last 40 years. Its low-temperature behaviour is associated with the existence of spin-density-waves (SDWs) and charge-density-waves (CDWs) incommensurate with the bcc lattice periodicity of Cr. Whereas the SDW behaviour in bulk Cr is now well established [1], there are a good number of gaps in our understanding of its nature in Cr thin films and heterostructures [2]. The present research addresses Cr/V layered heterostructures where the SDW state is affected by the hybridisation between very similar Fermi surfaces of chromium and vanadium. We provide direct evidence for the polarisation and propagation direction of the SDWs and CDWs in Cr films being conditioned by the V/Cr interface effects.

The investigations were done from a series of Cr(2000 Å), Cr(2000 Å)/V(14 Å), and V(14 Å)/Cr(2000 Å)/V(14 Å) layered heterostructures grown under the same conditions on MgO(001) substrates. The SDW and CDW behaviour was determined by combined X-ray and neutron scattering studies. The neutron measurements were conducted at D10 (ILL) and UNIDAS (FZ Jülich) instruments, the X-ray measurements were conducted at the **ID20** beamline. We have measured the temperature dependence of satellite peaks around the (011) and (002) Bragg reflections corresponding to the CDW positions. **Figure 115** shows a typical example with the temperature dependence of the CDW satellite peaks measured in the K direction on both sides of the (011) Cr fundamental peak in the Cr(2000 Å)/V(14 Å) heterostructure. In this case the SDW and CDW propagate in the film plane. As evident from the picture, the satellites positions move smoothly towards the (011) peak as temperature increases, while the intensity decreases continuously with temperature, which are the hallmarks for a phase

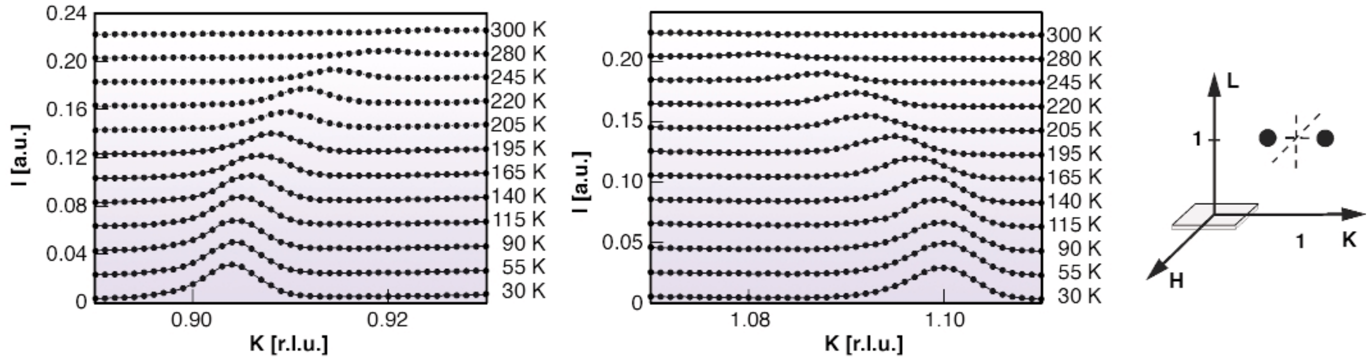

Fig. 115: Temperature dependence of CDW satellite reflections in Cr/V film along the K direction around the Cr(011) reflection taken with polarisation analysis of the scattered beam. The fundamental Cr(011) peak is removed from the figure since its intensity is many orders of magnitude higher than the intensity of the satellite reflections.

transition from the low temperature SDW to a high temperature paramagnetic phase.

The synchrotron and neutron scattering results on the SDW behaviour within the Cr/V heterostructures are summarised schematically in **Figure 116**. In thin Cr/V films, the SDW is confined and therefore the spontaneous formation of the SDW due to the Fermi surface nesting competes with hybridisation effects of adjacent vanadium layers, with interfacial structures (order and disorder), and with dimensionality effects (film thickness). The SDW propagation in the plain Cr(2000 Å) film on MgO(001) is conditioned mainly by the dimensionality effects and an in-plane epitaxial tensile stress from the substrate. The SDW and CDW propagate here in the film plane. The Cr spins are aligned in the film plane at low temperatures (longitudinal phase) and out-of-plane at higher temperatures (transverse phase). The Néel temperature for the SDWs is estimated to be about 300 K that is close to the bulk value. The addition of a neighbouring V layers initiates new mechanisms competing with the ones above. We found that the addition of one neighbouring thin V layer in the Cr/V heterostructures leads to a change in the polarisation of the transverse SDW from the out-of-plane to in-plane direction. The addition of the second V neighbouring layer changes the SDW propagation direction, such that the SDW in the V/Cr/V systems propagates out-of-plane.

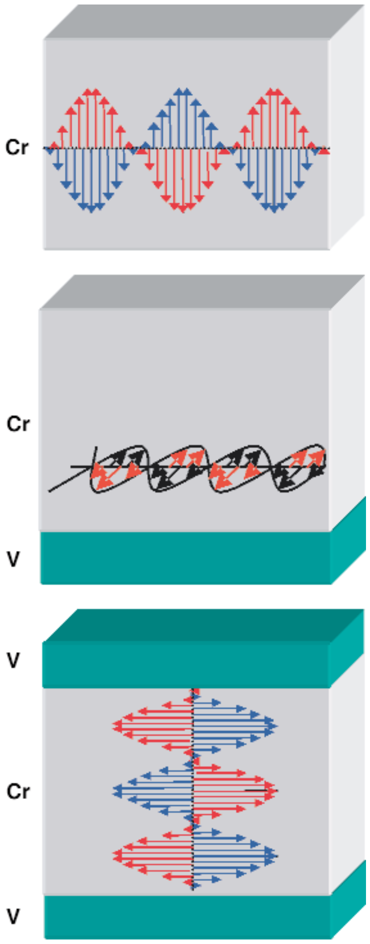

Fig. 116: Schematical pictures of the SDW behaviour in Cr, Cr/V and V/Cr/V heterostructures as determined by combined X-ray and neutron experiments.

In conclusion, we have studied the proximity effect of vanadium layers on spin density waves in Cr/V heterostructures grown on MgO(001) substrates. The Cr-V interface hybridisation produces long-range re-orientational effects in Cr/V multilayers. The vanadium proximity hybridisation determines the SDW polarisation in Cr/V systems as well as the SDW propagation direction in V/Cr/V systems. To the best of our knowledge, there is no theoretical consideration of orientational effects caused by the hybridisation of Cr with neighbouring paramagnetic layers. The strong re-orientational effects observed are unexpected and need to be explained by theory.

References

[1] E. Fawcett, *Rev. Mod. Phys.* **60**, 209 (1988).
[2] H. Zabel, *J. Phys.: Condens. Matter* **11**, 9303 (1999).

Principal Publication and Authors

E. Kravtsov (a,b), A. Nefedov (a), F. Radu (a), A. Remhof (a), H. Zabel (a), R. Brucas (c), B. Hjörvarsson (c), A. Hoser (d,e), S.B. Wilkins (f,g), *Phys. Rev. B* **70**, 054425 (2004); E. Kravtsov (a,b), A. Nefedov (a), R. Brucas (c), B. Hjörvarsson (c), A. Hoser (d,e), G. McIntyre (h), H. Zabel (a), *J. Magn. Magn. Mater.*, in press.
(a) Institut für Experimentalphysik/Festkörperphysik,

Ruhr-Universität Bochum (Germany).
(b) Institute of Metal Physics, Ekaterinburg (Russia).
(c) Department of Physics, Uppsala University (Sweden).
(d) Institut für Kristallographie, RWTH-Aachen (Germany).
(e) Institut für Festkörperforschung, Forschungszentrum Jülich (Germany).
(f) European Commission, JRC, Institute for Transuranium Elements, Karlsruhe (Germany).
(g) ESRF
(h) ILL

Direct Observation of Orbital Magnetism in Cubic Solids

The magnetic moment of the 3d transition metals consists of two contributions: the spin moment μ_S and the orbital moment μ_l. Theoretically it is often sufficient to treat the spin-orbit-coupling (SOC) as a weak perturbation. However, strictly speaking magnetism is a relativistic effect and may require a fully relativistic treatment. In principle, *l* and *s* are not good quantum numbers, whereas *j* is. An enormous amount of literature discusses the magnetic phenomena in terms of spin magnetism. However, from a certain point of view the orbital magnetism may be even more important: a finite orbital momentum *l* is an indication of a non-spherical charge distribution be it for an atom or in solids. Such a non-spherical charge distribution is the primary source for the magnetic anisotropy energy, which is an important quantity *e.g.* for the fabrication of hard or soft magnets. Nowadays the investigation of 3d transition metal clusters on surfaces has become very important in view of magnetic nanotechnology. "Giant magnetic anisotropy" has recently been reported [1]. Several groups have shown that on surfaces or in nanoclusters one observes giant orbital magnetic moments and magnetic anisotropy energies, respectively, confirming an old theory by L. Néel that the symmetry breaking at surfaces keeps the orbital momentum "alive". For 3d elements in three-dimensional bulk materials the opposite limit seems to hold: the research in the 1970's and 1980's on dilute alloys [2] focused mostly on the spin magnetism, *e.g.* the Kondo Hamiltonian ($JS\bullet\sigma$). This is in agreement with a standard exercise in solid state physics showing that the expectation value of L_z vanishes in cubic symmetry ($\langle L_z \rangle = 0$). Prototype cases in experiment and theory were *e.g.* Mn, Fe, and Co impurities in cubic Cu, Ag, and Au host materials.

The present work shows that under certain conditions orbital magnetism survives even in a cubic symmetry. X-ray magnetic circular dichroism (XMCD) at the $L_{2,3}$ edges is an excellent tool to study the ratio μ_l/μ_S. Plenty of evidence exists from hyperfine interaction measurements that the orbital magnetism may survive in cubic structures. However, only the third-generation synchrotron facilities have made it possible to measure μ_S and μ_l in a direct way. A very high sensitivity is needed because dilute alloys with ~1% impurities correspond to 1/10 monolayer of atoms on a surface. Moreover, a large magnetic field and low temperatures are required to measure dilute paramagnets. These facilities are provided by beamline **ID8. Figure 117** shows the normalised X-ray absorption spectra (XAS) of Fe and Co impurities and the corresponding XMCD spectra. The spectra were measured in an external field of 7 Tesla, at temperatures down to 4 K, with normal incidence X-rays. A complete analysis via the sum rules [3] was applied to determine the ratio μ_l/μ_S. Here we use a simplified reasoning: For spin magnetism only, theory predicts a –1:1 ratio for the integrated XMCD areas at the L_3 and the L_2 edge. If the experimental ratio differs from this (obviously for Co) a finite orbital moment survives. The experimental numbers are given in **Figure 118** (circles). The experiments find that μ_l/μ_S is almost zero for Cr, Mn, and Fe in Au, but 33% for Co/Au.

How can this be understood? Is this in conflict with the quenching of orbital momentum in cubic symmetry? Some insight is given by *ab initio* calculations (Figure 118, triangles and squares). The calculations also yield a vanishing ratio for all the 3d elements except Co. Two values for μ_l/μ_S are given: 15 % and 70 %. The lower

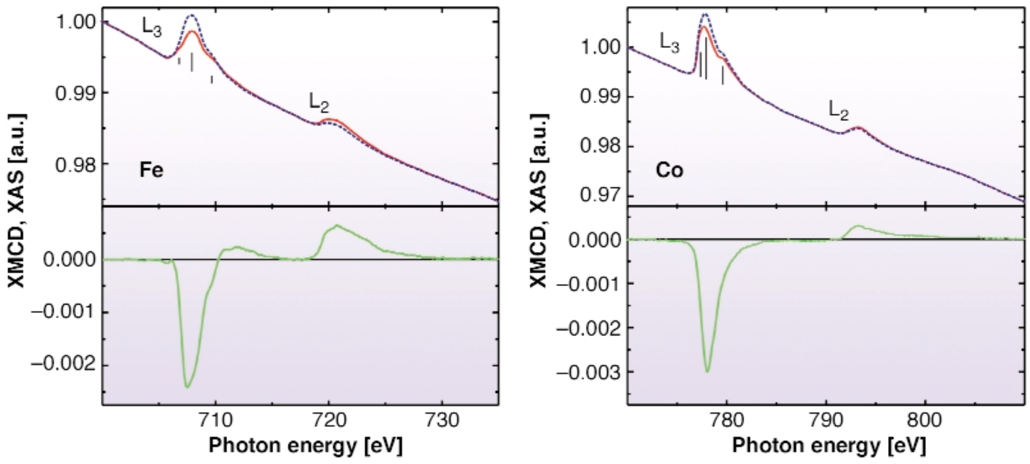

Fig. 117: XAS (upper plots) for left and right circular polarisation and XMCD spectra (lower plots) of ~1at.% Fe and Co in Au at the $L_{2,3}$ edges. Note the strongly reduced relative intensity at the L_2 edge of Co, indicating its enhanced orbital moment.

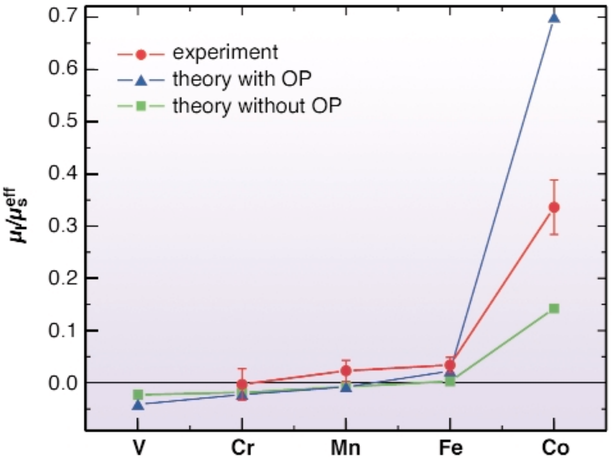

Fig. 118: Comparison of theory and experiment: Systematics of the ratio μ_l/μ_s of the 3d series as impurities in Au.

value was calculated in a scalar relativistic approach including spin-orbit-coupling only as a weak perturbation (Hund's third rule). The second larger value also takes into account orbital polarisation (OP, Hund's second rule).

These XMCD experiments on paramagnetic dilute alloys of Co/Au at ID8 are the first direct measurements of the 3d magnetic moment which show that in cubic symmetry an appreciable amount of orbital magnetism may survive. The text book arguments about the quenching of orbital moments are derived on the basis of weak SOC, distinct separation of t_{2g} and e_g states as well as no intermixing. A strong hybridisation of the 3d impurity levels with the 5d host band structure and the delicate balance of the spin-up and spin-down filling of the 3d impurity bands can indeed explain this experimental finding. Nowadays, Co atoms or clusters on Cu(001) surfaces may be used to study the Kondo-effect on surfaces *e.g.* by means of scanning-tunnelling microscopy (STM). For future work of this kind it would be interesting to also consider the surviving orbital magnetism in these many-body effects.

References

[1] P. Gambardella *et al., ESRF Highlights* p. 85 (2003).
[2] G. Rado and H. Suhl (Eds.), "*Magnetism*", vol. 5, Academic Press New York/London (1973).
[3] B. T. Thole *et al., Phys. Rev. Lett.* **68**, 1943 (1992); P. Carra *et al., Phys. Rev. Lett.* **70**, 694 (1993).

Principle Publication and Authors

W. D. Brewer (a), A. Scherz (a), C. Sorg (a), H.Wende (a), K. Baberschke (a), P. Bencok (b), S. Frota-Pessôa (c), *Phys. Rev. Lett.* **93**, 077205 (2004).
(a) Freie Universität Berlin (Germany)
(b) ESRF
(c) Universidade de São Paulo (Brazil)

Oscillatory Magnetic Behaviour in One-Dimensional Atomic Wires

Fundamental research on magnetic thin films has greatly advanced our understanding of magnetism, unveiling unknown phenomena and contributing to the rapid development of data storage devices and magnetic sensors. A prominent issue in this context is to understand how symmetry and composition effects determine the orientation and magnetisation reversal properties of nanostructured materials. Extensive work on two-dimensional (2D) magnetic layers has shown that a lowering of the symmetry compared to bulk systems

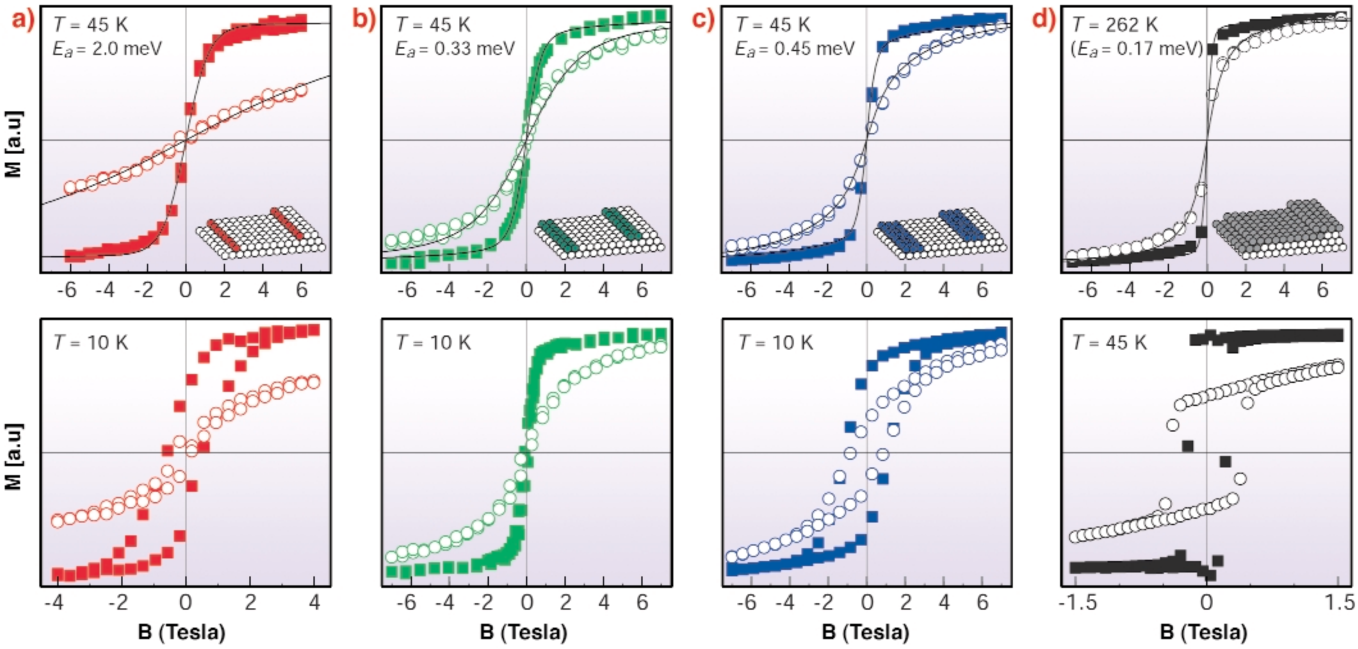

Fig. 119: Magnetisation of (a) single Co chains, (b) double chains, (c) triple chains, (d) 1.3 monolayers in the easy (filled squares) and hard direction (empty circles). The solid lines are fits to the data in the superparamagnetic regime.

results in enhanced magnetocrystalline anisotropy energy (MAE), the property that describes the tendency of the magnetisation to align along specific spatial directions in a crystal [1]. Likewise, magnetic anisotropy effects have been predicted to be particularly strong in 1D metal chains, where changes in the symmetry and atomic coordination produce strong modifications of the electronic band structure compared to 2D systems [2]. Experiments on beamline **ID08** addressed these issues for the first time in 1D metal chains of thickness controlled down to the monatomic limit, revealing a rich and unexpected magnetic behaviour.

X-ray magnetic circular dichroism (XMCD) measurements probed the magnetism of Co chains deposited along the step edges of a vicinal Pt(111) surface [3]. **Figure 119** shows the magnetisation curves for single, double, and triple atomic chains as well as for 1 Co monolayer (coverage equivalent to 8 atomic chains) recorded by monitoring the maximum of the XMCD signal at fixed photon energy (L_3 edge, 779 eV) as a function of the applied magnetic field. A fit of the magnetisation measured parallel to the easy and hard axes in the superparamagnetic regime (upper panels) reveals a very large MAE, E_a = 2 meV per Co atom, for the monatomic chains, which is one order of magnitude larger than typical values in 2D films [1]. Even more surprisingly, the MAE first decreases and then increases again in the double and triple chains, respectively, contrary to the expected monotonic decrease with increasing coordination of the Co atoms. Such strong MAE changes are mirrored by the hysteretic behaviour of the magnetisation at low temperature (lower panels) and by fluctuations of the coercive field (not shown). A previous study showed that long-range ferromagnetism in 1D systems can exist as a metastable state stabilised by strong MAE barriers [3]. Here, ferromagnetic behaviour is shown to vanish going from single to double Co chains as a consequence of the reduced MAE (Figures 119a and b, bottom panels).

XMCD measurements also allowed the tracking of the easy direction of magnetisation as a function of the Co chain thickness. **Figure 120** shows the L_3 XMCD signal measured in the plane perpendicular to the chain axis by varying the angle Φ between the surface normal and the photon beam direction. The sinusoidal behaviour indicates a predominant uniaxial character of the magnetic anisotropy for the chains and monolayer samples, with the maximum of the |cos(Φ)| function corresponding to the easy direction of magnetisation. As minimal variations of the Co coverage result in strong dimensionality changes in this system, the magnetisation turns out to be extremely sensitive to the chain transverse structure. The easy axis reverses abruptly from Φ = +46° (step up direction) for the single chains to -60° (step down) for the double chains, and reverses back towards the surface normal in the monolayer regime. This rotation of the easy axis corresponds to a sign inversion of the MAE, in addition to the magnitude oscillations discussed above. As energy considerations exclude dipolar interactions as a cause for the magnetisation rotation, such MAE oscillatory behaviour is attributed to the 1D character of the chains and related changes of the electronic configuration with increasing number of atomic rows. Electronic structure calculations for both free-standing and supported Co chains substantiate this finding [2].

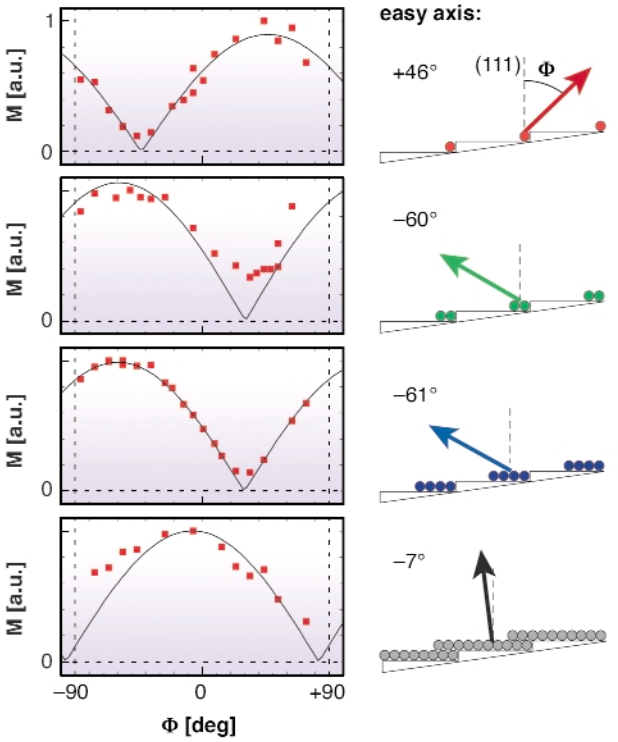

Fig. 120: Near remanence Co chain magnetisation, M, measured in the plane perpendicular to the wire axis at an angle Φ with respect to the surface normal. (a) single chains, (b) double chains, (c) 4 chains, (d) 1.3 monolayers. The data points represent the XMCD signal at the L_3 Co edge normalised by the total absorption yield. The solid lines represent a |cos(Φ)| fit as expected for uniaxial anisotropy.

In conclusion, reducing the dimensions of a 2D magnetic layer down to 1D atomic chains reveals a strikingly rich magnetic behaviour connected to the chain thickness and specific electronic configuration. In particular, the easy axis of magnetisation, the magnetic anisotropy energy, and the coercive field display strong oscillations going from monatomic chains to double and triple chains, and to a monolayer film.

References :

[1] U. Gradmann, in *Handbook of Magnetic Materials* Vol. 7., edited by K.H.J. Buschow (Elsevier, Amsterdam 1993).
[2] J. Dorantes-Dávila and G.M. Pastor, *Phys. Rev. Lett.* **81**, 208 (1998).
[3] P. Gambardella *et al.*, *Nature* **416**, 301 (2002).

Principal Publication and Authors:
P. Gambardella (a), A. Dallmeyer (b), K. Maiti (b), M.C. Malagoli (b), S. Rusponi (a), P. Ohresser (c), W. Eberhardt (b), C. Carbone(b,d), and K. Kern (a,e), *Phys. Rev. Lett*. **93**, 077203 (2004).
(a) EPF Lausanne (Switzerland)
(b) FZ Jülich (Germany)
(c) ESRF
(d) CNR-ISM, Trieste (Italy)
(e) MPI Stuttgart (Germany)

Influence of the Interface Structure on the Induced Moments in Multilayers

In recent years, much work has been done on the magnetic circular dichroism in X-ray absorption (XMCD) spectroscopy in various ferromagnetic multilayers and nanostructures driven by recent technological advances in magnetic recording and data storage. It has been shown recently that the spin and orbital magnetic moments at the interfaces could differ greatly from those observed in the bulk materials [1]. However, few studies have been dedicated to understanding the relation between the local structure at the interfaces and the induced magnetism. Using the inherent element and orbital specificity of XMCD, we have investigated the influence of interfacial structure on spin and orbital magnetic moments acquired by non-magnetic atoms.

Here we present the results of the XMCD study of induced *5d* magnetic moments of Ir in Fe/Ir multilayers. Fe/Ir multilayers have been shown to exhibit different strained structures depending on the thickness of the Fe layers [2]. For the present study we have selected two multilayers: Fe(10 Å)/Ir(6 Å) and Fe(30 Å)/Ir(6 Å). X-ray diffraction analysis [2] shows that in these high quality monocrystalline multilayers, the Fe layers grow in body centred tetragonal (BCT) and body centred cubic (BCC) structures for the thin and the thick layers, respectively. Moreover, following the Fe phase, the Ir layers were also found to be strained and they adopt either BCC or BCT structures.

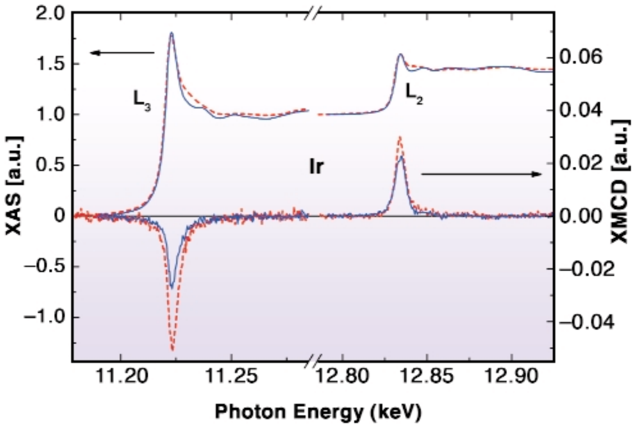

Fig. 121: Normalised XAS (top) and XMCD (bottom) spectra measured at the $L_{2,3}$ edges of Ir in Fe(10Å)/Ir (dashed line) and Fe(30Å)/Ir (full line).

The experiments have been carried out at beamline **ID12** using the total fluorescence yield detection mode. X-ray absorption and XMCD spectra at the Ir $L_{2,3}$-edges for both samples are reproduced in **Figure 121**. Since the thickness of the Ir layers is kept constant in both samples, we are confident that the variation of the XMCD spectra, displayed in Figure 121, directly reflects the effect of the Fe layer structure on the induced magnetic moment carried by the Ir atoms. The very high quality of the experimental data allowed us to quantify the observed changes by applying magneto-optical sum rules [3]. In order to determine experimentally the number of holes in the Ir *5d* shell, we have applied the procedure described in Ref. [1] using Au $L_{2,3}$ X-ray absorption spectra as the reference. The experimental values of the Ir *5d* magnetic moments (spin, orbital and total) as well as the ratio of the orbital to spin moments for the two multilayers studied are summarised in **Table 1**.

μ_{tot} μ_B/atom	μ_L/μ_S	μ_L μ_B/atom	μ_S μ_B/atom	
0.19	0.10	0.016	0.17	Fe(10 Å)/Ir(6 Å)
0.14	0.02	0.002	0.14	Fe(30 Å)/Ir(6 Å)

Table 1: Spin, orbital, their ratio and the total magnetic moment of Ir in Fe(30 Å)/Ir and Fe(10 Å)/Ir extracted from XMCD data.

We found that for both samples the Ir spin and orbital moments are parallel, as one would expect for an atom with more than a half-filled *5d* shell. The most interesting result is that the induced orbital moments of Ir change drastically with the structure of the Fe layer. The Ir *5d* orbital to spin moments ratio is bigger by more than a factor of 5 for the BCT Fe layer with respect to the BCC layer. This observation clearly indicates that the intra-atomic spin-orbit coupling is not always a dominant interaction in induced magnetism and that the interfacial structure distortions play a crucial role. The influence of various structural factors on the ratio μ_L/μ_S in polarisation of "non-magnetic" *5d* transition metals certainly requires further experimental investigation. Moreover, the local structure have to be carefully taken into account in modern *ab initio* calculations in order to elucidate a realistic mechanism responsible for induced magnetism and, therefore, for macroscopic magnetic behaviour of multilayered structures.

References

[1] F. Wilhelm *et al., Phys. Rev. Lett.* **87**, 207202 (2001).
[2] S. Andrieu *et al., Phys. Rev.* B **52**, 9938 (1995).
[3] B.T. Thole *et al., Phys. Rev. Lett.* **68**, 1943 (1992); P. Carra *et al., Phys. Rev. Lett.* **70,** 694 (1993).

Principal Publication and Authors
N. Jaouen (a), F. Wilhelm (a), A. Rogalev (a), J. Goulon (a), J.M. Tonnerre (b), S. Andrieu (c). *J. Magn. Magn. Mater.* **272-276**, Supplement 1, E1615 (2004).
(a) ESRF
(b) Laboratoire de Cristallographie, CNRS, Grenoble (France)
(c) Laboratoire de Physique des Materiaux, CNRS, Nancy (France)

A Study of UAs/Co Multilayers by X-ray Magnetic Circular Dichroism at the U-$M_{4,5}$ Edges

Much of the recent scientific interest in magnetic multilayers has been driven by their potential use in practical device applications such as magneto-optical storage media. Following the discovery of large magneto-optical Kerr effects (MOKE) in U compounds by Reim and Schoenes [1], researchers at IBM attempted to make a room temperature ferromagnet film using uranium. They started to work on amorphous USb and UAs, which they found to be ferromagnetic with a Curie temperature, $T_C \leq 140$ K. When other elements, such as Fe, Mn, Cu were mixed into the film, T_C did not increase. They then turned to the production of sputtered multilayer films of Co and UAs layers with the aim of inducing polarisation of the U through exchange coupling to the Co layers [2]. Among the limited initial studies, magneto-optical experiments showed that there was a moment on the uranium site at low temperature in all samples and even at room temperature for one multilayer. The difficulty to confirm these results unambiguously arises from the fact that the main part of the magnetic signal arises from the large Co moment, both within the multilayer and in the buffer material.

To further investigate these multilayers, X-ray magnetic circular dichroism (XMCD) measurements at the M_4 (3726 eV) and M_5 (3551 eV) edges of uranium have been performed, since such a study allows one to probe the *5f* magnetism separately. XMCD measurements were made on three of the UAs/Co samples from IBM, namely 12 × [UAs(80 Å)/Co(20 Å)], 15 × [UAs(60 Å)/Co(20 Å)] and 20 × [UAs(40 Å)/Co(20 Å)] at beamline **ID12**.

The *$5f^3$* magnetic moment deduced from the XMCD measurements, and the magnetisation value for UAs amorphous films, reported by Fumagalli *et al.* [2], of ≈ 0.7 μ_B are in good agreement. Furthermore, this result is consistent with previous studies performed on uranium monopnictides strongly suggesting a U^{3+} (*$5f^3$*) configuration. As depicted in **Figure 122**, we stress the direct relationship between the maximum polar Kerr rotation measured by Fumagalli *et al.* [2] at a temperature of 10 K and under a 3 T applied magnetic field and the *5f* magnetic moment deduced from our XMCD experiment, performed at 35 K and 4 T. We note the linear relation between the two sets of data, confirming that the MOKE results are directly related to the magnetic contribution of the uranium.

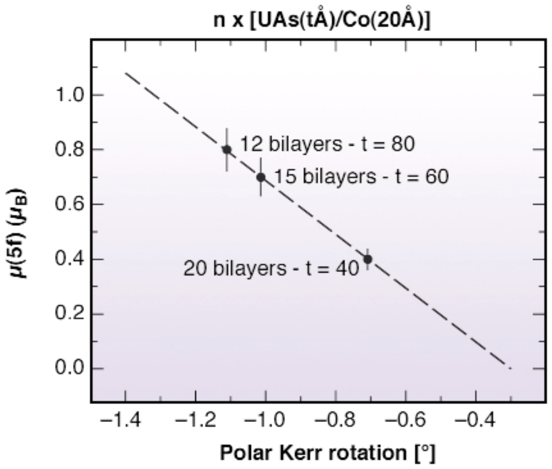

Fig. 122: The 5f magnetic moment deduced from our XMCD measurements plotted versus the maximum polar Kerr rotation [2] for the three multilayers.

The aim of our study was to see whether the uranium moment contributes to the room temperature Kerr effect. For that, we concentrated on the 12 bilayered sample which exhibits the largest uranium magnetic moment and as a consequence the largest polar Kerr rotation. The U-M_4 edge XMCD signal area has been measured as a function of temperature and field (**Figure 123**). Assuming the exchange field due to cobalt to be constant in the region of interest here, the variation of the *5f* moment has been calculated within the mean field approximation. This model oversimplifies the physics of these multilayers, but shows that the applied field alone

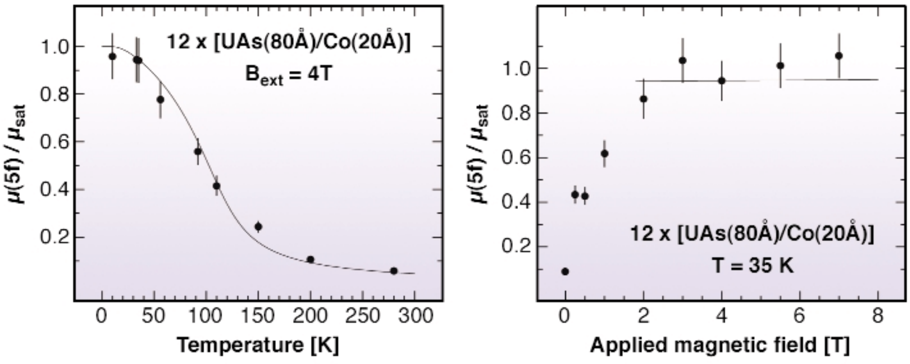

Fig. 123: Temperature dependence for a 4 T applied field (left panel) and field dependence at 35 K (right panel) of the 5f magnetic contribution. The 5f moment calculated in a mean field scheme is shown as lines (both panels).

is not sufficient for the polarisation of the uranium; the role of the cobalt is clearly demonstrated. Saturation is achieved above ≈ 2 T as shown by the field dependent measurement; *a fortiori*, 4 T applied along the direction used is enough to saturate the sample. The saturated uranium moment reaches ≈ 0.85(15) μ_B.

Finally, at room temperature we confirmed the presence of a small XMCD signal at the U-M_4 edge. This corresponds to an induced moment on the uranium of ≈ 0.05 μ_B, considerably lower than the 0.14 μ_B predicted by the IBM group [2]. Therefore, due to the strong spin-orbit coupling, even a small uranium contribution can lead to a sizeable magneto-optical effect.

References

[1] W. Reim and J. Schoenes in *Ferromagnetic materials*, K.H.J. Buschow, E.P. Wolfarth (Eds.), North Holland, Amsterdam, **5**, 133 (1990).

[2] P. Fumagalli, T.S. Plaskett, D. Weller, T.R. McGuire and R.J. Gambino, *Phys. Rev. Lett.*, **70**, 230 (1993).

Principal Publication and Authors

N. Kernavanois (a,b), D. Mannix (c,d), P. Dalmas de Réotier (b), J.-P. Sanchez (b), A. Yaouanc (b), A. Rogalev (c), G.H. Lander (e), W.G. Stirling (c,d), *Phys. Rev. B*, **69**, 054405 (2004).

(a) ILL
(b) CEA, DRFMC/SPSMS, Grenoble (France)
(c) ESRF
(d) Department of Physics, The University of Liverpool (UK)
(e) European Commission, Joint Research Centre, Institute for Transuranium Elements, Karlsruhe (Germany)

Experimental Station for Hard X-ray Magnetic Circular Dichroism on Ultra-dilute Samples

Research on magnetism has undergone a renaissance over the last few decades, following the discovery of a variety of interesting phenomena in artificially-fabricated layered magnetic structures such as the enhancement of magnetic moments in ultrathin films and at surfaces, perpendicular magnetic anisotropy and giant magnetoresistance. Some of these discoveries are of great importance for technological applications, however, the fundamental mechanisms governing the magnetic properties of these structures are not fully understood. One of the important mechanisms is the oscillatory interlayer exchange coupling of the magnetic layers *via* the ‘nonmagnetic’ ones. Surprisingly, the induced magnetism in the ‘nonmagnetic’ layer is often neglected when the magnetic properties of the whole structure are discussed. These induced magnetic moments determine the magneto-optic response, the magneto-transport properties and the magnetic anisotropy of the systems.

A new experimental station mainly dedicated to X-ray magnetic circular dichroism (XMCD) measurements on ultra-dilute magnetic samples has been recently developed at the beamline **ID12**. The key element is a 35-channel silicon drift diode (SDD) detector array [1] developed in collaboration with Eurisys-Mesures (now Canberra Eurisys). The detector shown in **Figure 124** consists of an array of 7 x 5 cylindrical Si drift-diodes with an active area of 10 mm^2 for each diode. The detector is cryogenically cooled to the optimum temperature (T ≈ 143K). The anode diameter (200 μm) can accommodate a new type of external J-FET (EuriFET) featuring a very low input capacitance (0.9 pF). This results in a very small readout noise: the FWHM energy resolution of the individual diodes measured with a ^{55}Fe source is as good as 129 eV using a standard pulse processing time of 12 μs, whereas the peak-to-background ratio is in excess of 1000. Under normal operating conditions, the peaking time can be reduced to 0.5 μs in order to maximise the counting rate (≥10^5 cps), however with some deterioration of the energy resolution. A complementary aspect of the project concerned the development of low-cost multichannel digital pulse processing electronics for energy-resolved spectroscopy (XDS boards). Each compact board, designed in the VXI c-size, can accommodate 4 channels and is fully controllable by software. XDS offers nearly the same energy resolution as a standard analog pulse processing system.

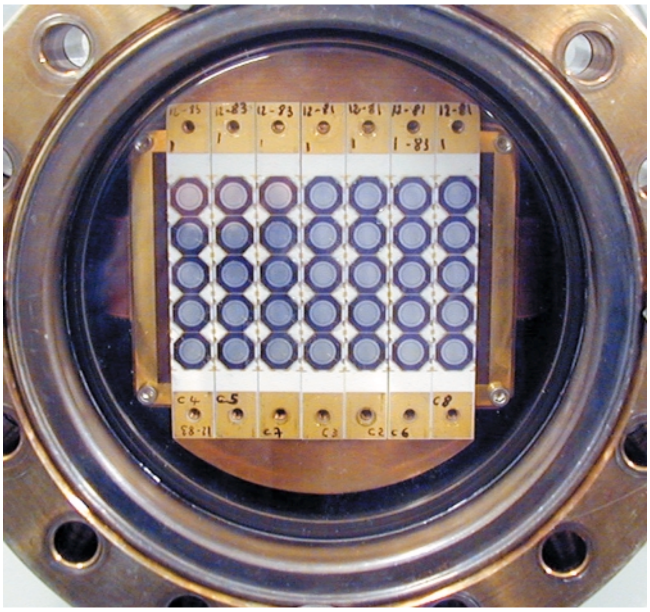

Fig. 124: The 35-element Si drift-diode array installed on ID12.

For routine XMCD measurements, a UHV compatible compact sample chamber is inserted between the poles of a 0.7 T electromagnet, while the detector is housed in a special chamber separated from the sample chamber by a gate valve. Special care has been taken to maximise the solid angle of collection of the fluorescence photons. The detector is systematically operated windowless: this allowed us to extend the operation of the detector down to the soft X-ray range where scattering is a major problem.

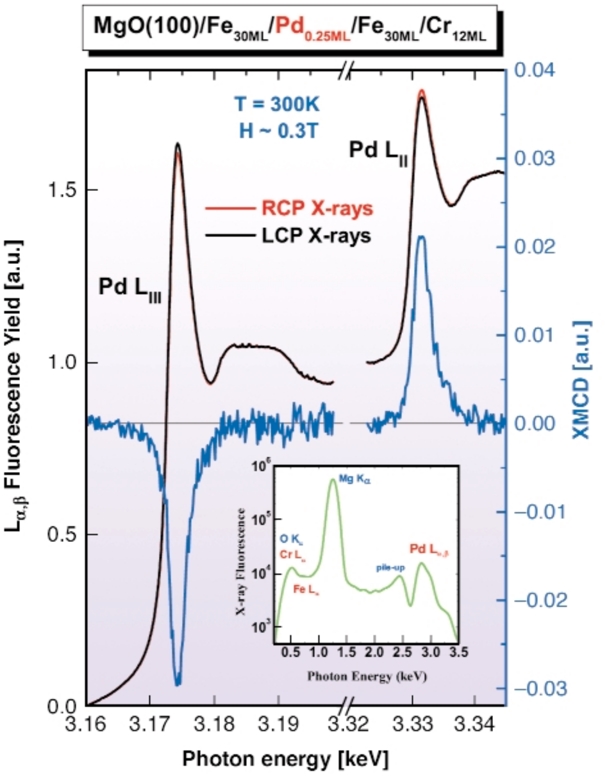

Fig. 125: XANES and XMCD spectra of $Fe_{30ML}/Pd_{0.25ML}/Fe_{30ML}$ trilayer at the Pd $L_{II,III}$-edges. Measurements were at room temperature and under applied magnetic field of 0.3T. Insert: X-ray emission spectrum of the sample with excitation at the Pd L_{II}-edge.

The XMCD spectra in **Figure 125** illustrates the excellent performances of the 35-element Si drift diode detector. It was recorded at the Pd $L_{II,III}$-absorption edges from only 0.25 atomic layers of Pd sandwiched between 30 atomic layers of Fe deposited on an MgO substrate. The emission spectrum is strongly dominated by the Mg Kα emission line (Figure 125 insert), while not resolved Cr Lα, Fe Lα and O Kα lines are of the same intensity as Pd Lα,ß lines. This shows that the SDD are working perfectly well at low photon energies down to 500 eV. Recall that the circular polarisation rates of the monochromatic beam at the Pd $L_{II,III}$-edges are only 12% and 19%, respectively: this clearly indicates that the corresponding XMCD spectra were recorded under particularly unfavourable experimental conditions. XMCD spectra were also recorded at the Pt L-edges on highly dispersed $Fe_{70}Pt_{30}$ nanoparticles deposited on a Si wafer: this indicates that the performances of the detector are also excellent in the hard X-ray range. The counting rates in both the Pd Lα and Pt Lα lines were *ca.* $2 \cdot 10^4$ cps per channel with a peaking time of 0.5 µs. Even though the X-ray beam was impinging on the sample with an angle of incidence of *ca.* 15°, the beam footprint was quite small: 300 x 30 µm^2. This is because we had to close down the slits in order to avoid saturation of the detector by the intense soft X-ray fluorescence signal from the substrates. Typical energy resolution of the emission spectra recorded with one single SDD channel (data acquisition time: 60 s; peaking time: 0.5 µs) was of the order of 132 eV for the unresolved Si Kαß, 159 eV for the Fe Kα line and 202 eV for the Pt Lα1 line. These results establish that high quality XMCD spectra can be measured on submonolayers and ultra-dilute systems in the hard X-ray range.

References

[1] J. Goulon *et al.*, *Advanced Detection Systems for X-ray Fluorescence Excitation Spectroscopy*, *J. Synch. Rad.* (2004), in press.

Authors

A. Rogalev, J. Goulon, F. Wilhelm, N. Jaouen, S. Feite, G. Goujon.
ESRF

Electronic Structure

Introduction by P. Glatzel, ESRF

The term *electron correlation* is used to describe one part of the interaction between electrons that move in the potential of nuclei. Strong electron correlations can give rise to fascinating material properties but they can also be troublesome for the theorist because the magnitudes of the interactions are difficult to calculate [1]. In fact, the underlying many body problem is impossible to solve analytically. However, understanding electron-electron interactions is the key to explaining important phenomena such as superconductivity, colossal magneto resistance and unusual phase transitions. There is thus a strong general interest in strongly correlated systems from theoreticians and, for example, from material scientists who wish to tailor the properties of materials and improve the storage capabilities of computer hard drives.

The enormous progress made over the last few decades in developing and refining theoretical models is largely driven by experiments such as those performed at the ESRF. Some of the questions that are being addressed are long-range orbital or magnetic ordering, local spin- and orbital magnetic moments, orbital hybridisation and the interplay between crystal field and electron-electron interactions. The three papers that we selected for this section are representative of the development of experimental techniques that open up new possibilities of comparing theory with experiment and allow for a detailed study of the electronic structure.

A map of the valence electron binding energy versus its momentum can be obtained by measuring the angular dependence of the valence band photoemission from a single crystal and can ultimately yield the Fermi surface. The technique is extremely surface sensitive for low incident photon energies (hν ~ 20eV) and thus low kinetic energies of the photoexcited electron. Hence the question arises whether a more bulk-sensitive probe yields different results. Claesson *et al*. took up on this question and used a photoelectron spectrometer that is capable of detecting high kinetic energies (~ 600 eV) with good energy and momentum resolution.

An element specific probe of the electronic structure is obtained in inner-shell spectroscopy. When the photon energy is tuned to an absorption edge the resulting state can decay back to the initial state or to an excited state. When the resulting X-ray is detected, with sufficient energy resolution, we refer to resonant inelastic X-ray scattering (RIXS) spectroscopy. This has proven to be a powerful technique to study correlation effects and ligand field splittings [2]. Ghiringhelli *et al.* have used RIXS at the Cu L-edge to disentangle excitations with small energy transfer, *i.e.* electron transitions that are usually only accessible using optical spectroscopies that are not element specific. Rueff *et al.* investigated the γ-α phase transition of Ce solid solutions. They treat hybridisation effects in terms of a configuration interaction approach and determine the f-orbital occupancy as a function of temperature.

Nevertheless, despite the considerable advances in experimental techniques, the nature of electron correlations and their correct theoretical treatment will continue to be subject of intense discussion for the coming years.

References

[1] P. Fulde *Electron correlations in molecules and solids* 3rd enl. ed.; Springer-Verlag: Berlin, New York, (1995).
[2] A. Kotani, S. Shin *Rev. Mod. Phys.* **73,** 203-46 (2001).

Fermi Surface of the High-temperature Superconductor $Nd_{1.85}Ce_{0.15}CuO_4$

One of the fundamental problems in contemporary physics is the understanding of high-temperature-superconductivity (HTS). Even though HTS was first discovered in 1986 and a large amount of experimental and theoretical work has been carried out since then, it is still unclear what the underlying mechanism is.

A fundamental characteristic of a material is its spectral function A(ω,k) or band structure which gives the electron momentum and corresponding energy of allowed electronic states in the material. Angle-resolved photoelectron spectroscopy (ARPES) is a direct experimental way of determining the band structure of solids and it has been extensively used in the study of high temperature superconductors during recent years. Many important results concerning the shape of the superconducting gap, phonon interactions etc. have been obtained. A crucial question in the use of ARPES is, however, the surface sensitivity of the technique. Most ARPES measurements are performed at 20-40 eV photon energy where the outermost surface layer gives the main contribution to the intensity. It has generally been believed that this was not an issue in the case of HTS compounds since these are layered materials with an electronic structure that is quasi-2-dimensional. In order to verify the validity of this assumption, we have performed bulk sensitive ARPES measurements in the soft X-ray range at beamline **ID08**.

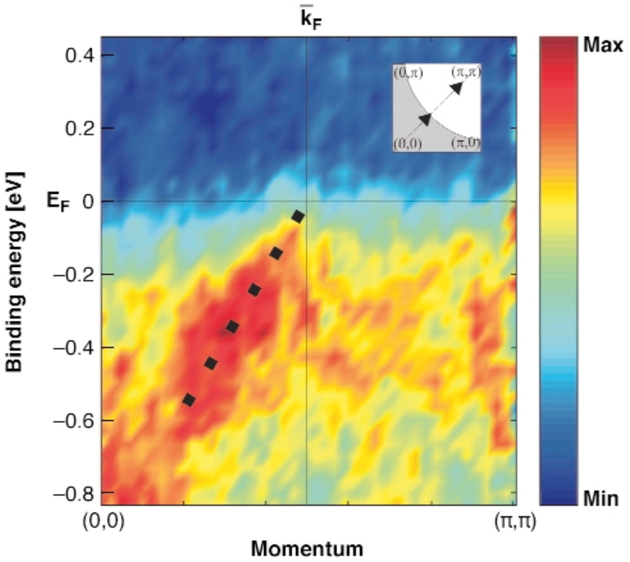

Fig. 126: Dispersion measured along a high symmetry line in $Nd_{1.85}Ce_{0.15}CuO_4$. The dotted line is a guide to the eye.

Using the latest advances in spectrometer and detector design it has been possible to measure the valence band dispersion in $Nd_{1.85}Ce_{0.15}CuO_4$ (NCCO) with 400 eV photons. An example of the observed dispersion is given in **Figure 126** where the dispersion is plotted as a colour intensity plot. The figure shows an electron state that moves towards the Fermi level as the momentum is changed from (0,0) to (π,π). Approximately halfway along the line, the state crosses the Fermi level and becomes unoccupied. This point in momentum space divides occupied states from unoccupied states and defines a point on the so called Fermi surface within which the electrons reside. The shape and volume of the Fermi surface gives information about properties such as the electron density, electron velocity and important scattering mechanisms in the material. By measuring a large number of spectra, such as those in Figure 126, one can thus determine the shape of the Fermi surface for a particular material. In the case of a simple three-dimensional metal, such as an alkali metal, the electrons are nearly free and the energy is proportional to the momentum amplitude squared (parabolic dispersion). The Fermi surface is therefore given by a sphere in momentum space. For anisotropic materials and materials where correlation effects are important, the Fermi surface will deviate strongly from a sphere and one can, roughly speaking, use the amount of deviation as a measure of correlation effects. In **Figure 127**, we show the Fermi surface of NCCO (or the Fermi line to be correct since NCCO is a two dimensional material). The Fermi surface was determined by accumulating a large number of spectra similar to the one in Figure 126. Looking at the shape of the intensity in Figure 127, one sees that it traces something that is closer to a square than a circle. Also shown is the Fermi surface as determined by earlier low energy measurements [1]. Comparing the two, one observes that the low energy measurement gives a Fermi surface that is closer to a circle. Following the general arguments given above, we conclude that the high energy data indicates the presence of stronger electron correlation in the bulk as compared to the surface. This result is surprising since any difference in the strength of electron correlations between bulk and surface is expected to be the opposite of what is observed here due to the reduced coordination at the surface. The reason for increased correlation in the bulk and the possible generalisation of the present result to other HTS compounds is still an open question.

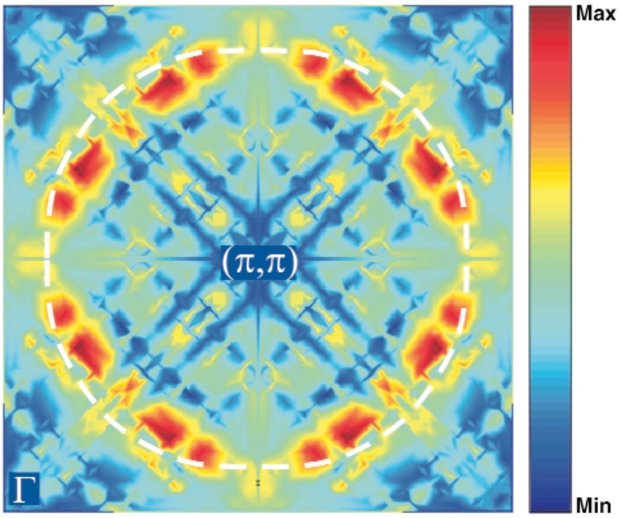

Fig. 127: The Fermi surface of $Nd_{1.85}Ce_{0.15}CuO_4$ obtained by accumulating a large number of spectra similar to the one shown in Figure 126. The white dashed line indicates earlier low-energy results [1].

References

[1] N.P. Armitage, D.H. Lu, C. Kim, A. Damascelli, K.M. Shen, F. Ronning, D.L. Feng, P. Bogdanov, Z.-X. Shen, Y. Onose, Y. Taguchi, Y. Tokura, P.K. Mang, N. Kaneko and M. Greven, *Phys. Rev. Lett.* **87**, 1472003 (2001).

Principal Publication and Authors

T. Claesson (a), M. Månsson (a), C. Dallera (b), F. Venturini (c), C. De Nadaï (c), N.B. Brookes (c), O. Tjernberg (a), *Phys. Rev. Lett.* **93**, 136402 (2004).

(a) Laboratory of Materials and Semiconductor Physics, KTH, Stockholm (Sweden)

(b) INFM-CNR and Dipartimento di Fisica, Politecnico di Milano (Italy)

(c) ESRF

Cu L_3 edge Resonant Inelastic X-ray Scattering Sheds Light on dd Excitations of Cuprates

Resonant Inelastic X-ray Scattering (RIXS) can be effectively used to study the low energy electronic and magnetic excitations in solids. Working at the $L_{2,3}$ absorption edges is ideal in 3*d* transition metals compounds, because the resonant excitation and de-excitation allow us to measure the energy of excited states unreachable by direct electric dipole transitions. Those excited states (among them the so-called *dd* excitations, which are transitions within the 3*d* states that leave unchanged the number of *d* electrons) extend from a few eV's down to the tens of millielectronvolt energy scale. As the 2*p* state binding energies of 3*d* transition metals are between 400 eV and 1000 eV, the $L_{2,3}$ absorption edges fall in the energetic range of beamline **ID08**.

To record good RIXS spectra, a high resolving power is needed both in the monochromator (before the sample) and in the spectrometer (after the sample). This is challenging as RIXS is intrinsically a very low count rate experiment, requiring a high flux in a small portion of the sample. At ID08, RIXS has been measured for more than 10 years thanks to the AXES spectrometer and to PoLIFEMo, a dedicated monochromator (both are property of INFM-CNR, designed and developed at the Politecnico di Milano). After the recent upgrade of the whole instrumentation we can now reach a combined resolving power of 2000 (recently measured at the Mn L_3 edge, 640 eV). The first use of the new remarkable performance of AXES has been the study of the *dd* excitations in the cuprates.

Cuprates are a family of Cu based oxides with layered crystalline structure. They are widely studied for their intriguing electronic and magnetic properties, leading in some cases to superconductivity at a remarkably high temperature. The Cu ions are nominally divalent in all cases: the $3d^9$ configuration is thus characterised by one hole in the 3*d* states. In all layered cuprates (and practically in CuO as well) every Cu atom is surrounded by four O atoms in a planar 90° coordination (see inset in Figure 128), whereas the out of plane coordination varies. In all cases the in-plane oxygens are the Cu nearest neighbours, forcing the 3*d* hole to have the x^2-y^2 symmetry proper of the Cu local coordination. The *dd* excitations correspond to a change of the symmetry of the Cu hole from x^2-y^2 to a different one compatible with the local crystalline symmetry, whereas the charge-transfer excitations correspond to the transfer of the Cu 3*d* hole to those states with dominant O 2*p* character. The RIXS process can be summarised as $(3d)^9 \rightarrow (2p_{3/2})^3 \rightarrow [(3d)^{9*};(3d)^{10}\underline{L}]$: the RIXS spectral distribution gives a direct image of the various excitations (we indicated the *dd* and the charge transfer excitations by the $(3d)^{9*}$ and $(3d)^{10}\underline{L}$ notation respectively).

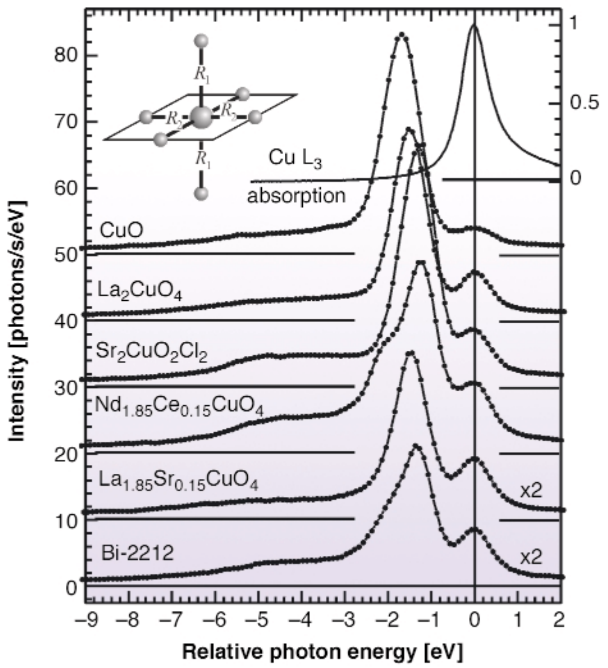

Fig. 128: The RIXS spectra measured at the Cu L_3 peak from three insulating and three superconducting cuprates. The topmost curve shows the Cu L_3 absorption peak of $La_{1.85}Sr_{0.15}CuO_4$. Inset: the local D_{4h} crystal field symmetry used in the calculations.

In **Figure 128** we compare the RIXS spectra of a variety of compounds. The peak at zero relative scattered photon energy is the elastic peak: the system returns to the ground state after the scattering. The main intensity between −1 eV and and −2.5 eV corresponds to the *dd* excitations. Between −2 eV and −7 eV we can find the charge transfer excitations. It is evident that the *dd* excitation peak has different shape and position in the various materials, as a direct consequence of the different out-of-plane coordination of the Cu ion. As a rule of thumb, a weaker electrostatic apical perturbation (for example due to a longer distance of the apical oxygen) corresponds to a higher average energy of the *dd* excitations. This trend is clearly visible in **Figure 129**, where we compare CuO, having no apical oxygens, with La_2CuO_4, having a tetragonally distorted octahedral coordination. Relatively simple calculations (atomic model, with point charge crystal field) are also shown. The calculations are in fair agreement with the experiment, providing a strong support to the general interpretation given above within a crystal field model.

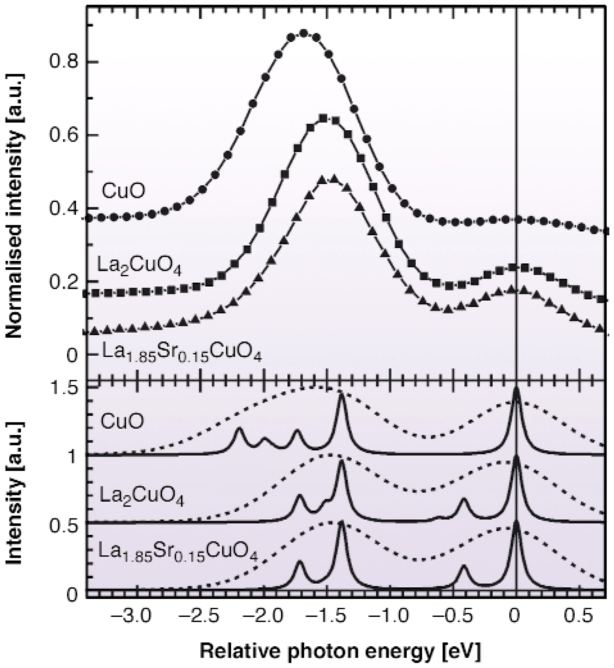

Fig. 129: Upper panel: measured RIXS spectra for CuO, La_2CuO_4, and $La_{1.85}Sr_{0.15}CuO_4$. Bottom panel: calculated RIXS spectra in D_{4h} crystal field symmetry. The spectra are given with a 0.05 eV Lorentzian broadening in the final state (solid lines) and after a 0.8 eV Gaussian broadening (dashed lines).

We have shown that high resolution and high quality RIXS at the L_3 edge of Cu is an effective tool to study the local symmetry of the electronic 3*d* population. This method can be applied to all the 3*d* transition metal compounds and to the rare earth systems.

Principal Publication and Authors

G. Ghiringhelli (a), N.B. Brookes (b), E. Annese (c), H. Berger (d), C. Dallera (a), M. Grioni (d), L. Perfetti (d), A. Tagliaferri (a), and L. Braicovich (a), *Physical Review Letters* **92**, 117406 (2004).

(a) INFM-CNR and Dipartimento di Fisica, Politecnico di Milano (Italy)

(b) ESRF

(c) INFM-CNR and Dipartimento di Fisica, Università di Modena e Reggio Emilia (Italy)

(d) Ecole Polytechnique Fédérale de Lausanne (Switzerland)

f-State Occupancy at the γ–α Phase Transition of Ce-Th and Ce-Sc Alloys

The Ce γ-α transition is one of the most intriguing phenomena in condensed matter physics. It embraces a variety of complex mechanisms, which generate anomalous behaviour both on a structural level (lattice parameter), and, more fundamentally, in the magnetic (magnetisation) and electronic properties (specific heat, etc.). There is a solid consensus even beyond the widely discussed Mott transition and the Kondo volume collapse paradigms that hybridisation between 4*f* and valence electrons plays a key role in the phase transition. In particular, the large Ce γ-α volume collapse ($\Delta V/V_0$ ~14%) is supposedly driven by a change in interactions involving *f* orbitals.

Hybridisation may be defined formally in terms of configuration interaction. Then, the ground state can be written as a linear combination of unoccupied, singly and doubly occupied *f* states. Obtaining an exact description of the cerium ground state implies a precise "counting" of the 4*f* electrons. X-ray absorption spectroscopy (XAS) and X-ray photoemission (XPS) experiments have been widely used to that purpose over the past few years. Nevertheless, both fail to provide a precise electron count for cerium: the f^2 contribution is hidden in XAS due to lifetime broadening, and surface effects in XPS lead to an artificial reinforcement of the Ce-γ character.

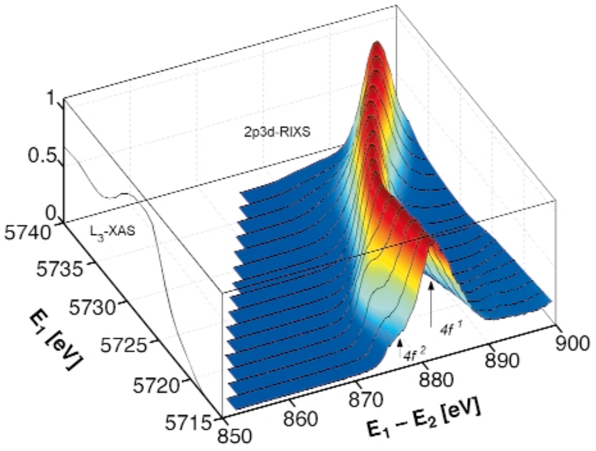

Fig. 130: *2p3d*-RIXS spectra in $Ce_{0.9}Th_{0.1}$ represented in the incident (E_1) vs transfer energy (E_1-E_2) plane.

Resonant X-ray inelastic scattering (RIXS) turns out to be a powerful alternative, thanks to the resonant enhancement and sub-lifetime resolving power. We have applied 2*p*3*d*-RIXS in Ce-Th, and Ce-Sc alloys, where the γ-α transition is driven by temperature using the doping element for chemical pressure [1]. The experiment was carried out at **ID12**, using our UHV-compatible RIXS spectrometer. The Ce-Lα emission line was measured on resonance in the vicinity of the Ce L_3-edge. **Figure 130** illustrates the 2*p*3*d*-RIXS spectra obtained in $Ce_{0.9}Th_{0.1}$ at ambient temperature. The spectra are arranged in a surface plot, laid out in the incident energy (E_1) *vs* transfer energy (E_1–E_2) plane. At low E_1, the RIXS spectra show two distinct features, attributed to the $4f^1v^{n+1}$ and $4f^2v^n$ final state configurations (*i.e.* with an extra valence electron in the valence band *v*, and in presence of a 3*d* core hole). As the incident energy increases, a clear resonance of the $4f^2$ features occurs, which permits an accurate estimate of the f^1 and f^2 spectral weights across the transition.

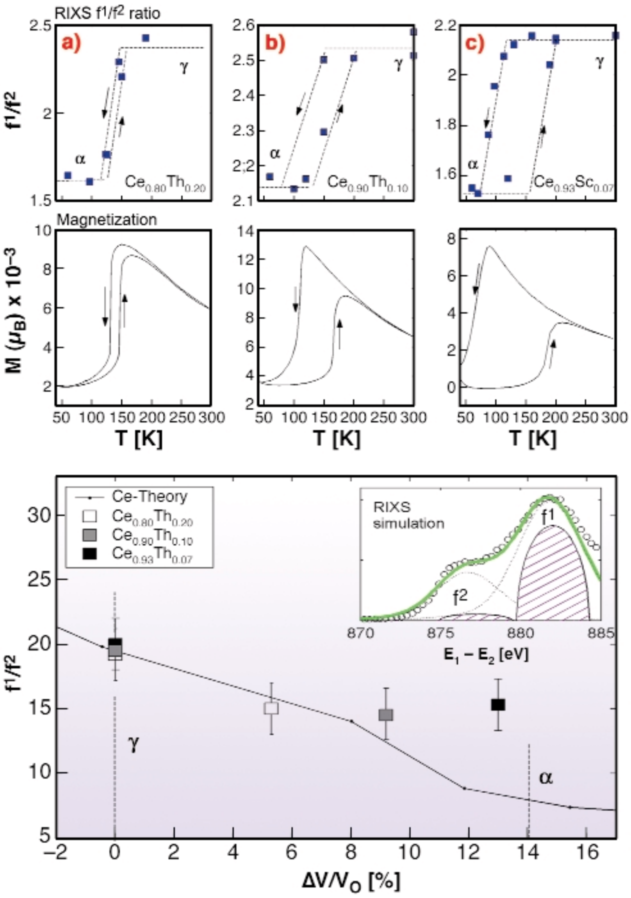

Fig. 131: f^1/f^2 ratio obtained by RIXS (upper) and bulk magnetisation measurements (middle). Corrected ratio derived from a RIXS simulation compared to *ab-initio* calculations from Ref. [2] (lower).

The temperature dependence of the f^1/f^2 intensity ratio is represented in **Figure 131** for the three alloys. All the samples show a sharp decrease at the transition temperature and hysteresis reminiscent of a first-order transition. The hysteresis loops present striking similarities with bulk magnetisation measurements plotted below. Obviously the magnetisation is a ground-state property whereas RIXS involves excited final states. Even so, the resemblance between the two sets of data is not coincidental and underlines the intimate relationship between the RIXS data and the anomalous behaviour at the transition. This assumption is confirmed when comparing the f^1/f^2 intensity ratio to first-principle calculations of the cerium ground-state properties obtained by LDA+DMFT [2]. To retrieve the correct intensity ratio, underestimated in the raw data due to tail excitation effects, we have simulated the RIXS spectra within a phenomenological approach. Both simulated and calculated results show a fair agreement when rescaled to the total volume change, especially for the Th-doped samples. The departure from the calculated value in Ce-Sc may be ascribed to interactions with Sc-3*d* electrons.

These results demonstrate that the f^2 contribution cannot be neglected in the description of the Ce ground state, and underlies the importance of the *f* electron screening. More generally, such an experiment should further establish RIXS as a major spectroscopic method to study mixed-valent systems.

References

[1] K.A. Gschneider, R.O. Elliott and R.R. McDonald, *J. Phys. Chem. Solids* **23**, 555 (1962).

[2] A.K. McMahan, K. Held, and R.T. Scalettar, *Phys. Rev. B* **67**, 075108 (2003).

Principal Publication and Authors

J.-P. Rueff (a), C. F. Hague (a), J.-M. Mariot (a), L. Journel (a), R. Delaunay (a), J.-P. Kappler (b), G. Schmerber (b), A. Derory (b), N. Jaouen (c), and G. Krill (d), *Phys. Rev. Lett.* **93**, 067402 (2004).

(a) Laboratoire de Chimie Physique - Matière et Rayonnement, CNRS - Université Paris 6 (France)

(b) Institut de Physique et Chimie des Matériaux, CNRS – Université Strasbourg (France)

(c) ESRF

(d) Laboratoire de Physique des Solides, CNRS – Université Paris Sud, Orsay (France)

Highlights 2004

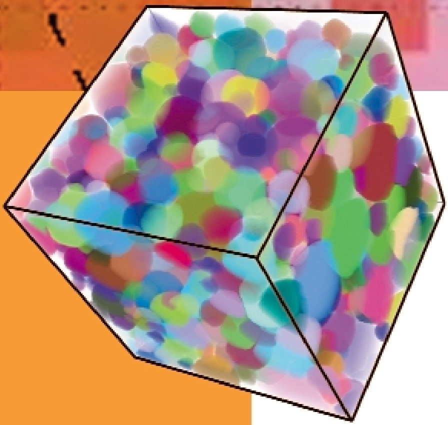

X-ray Imaging

Introduction

An increasing proportion of the experimental results obtained at the ESRF can be considered as “X-ray images”. They are maps showing the variation of a physical quantity such as absorption, diffraction, fluorescence, photoemission, within the sample. Recent years have seen an enhancement of the possibilities of imaging/microanalysis techniques and their routine application to a range of topics including physical, medical, materials science and engineering, and also some new areas like geophysical, environmental, archaeological and biological studies. An example of the extension to new topics and scientific communities is given in **Figure 132**, which shows three-dimensional renderings of fossils from two Hominoid primates from Thailand. These fossils are of high paleontological significance as they are the closest-known relatives of the modern orangutan. The oldest is aged about 12 million years and the second about 7 million years. The comparison of the 3D reconstructions of the jaws of the two fossils allows us to conclude that the two species are very similar. For the second fossil, it was possible to perform a virtual ‘extraction’ of the teeth to study their roots (courtesy P. Tafforeau, J.-J. Jaeger and Y. Chaimanee [1,2]).

The complementary microanalysis techniques already offered by the neighbouring “microscopy and microanalysis” beamlines ID21 (2-7 keV), ID22 (7-60 keV) and ID18F end station (6-28 keV) are being extended by the development of an infra-red microscopy end-station. Three examples show the present potential of these techniques: the characterisation of droplets and inclusions in “very old” ice from the Vostok lake, Antartica (page 110), the composition of 3500 million-year-old sea-water and its implications for the early stages of life (page 111), and the variations of atmospheric sulphates recorded on stalagmites (page 113).

Synchrotron radiation “wide field imaging”, which includes radiography, microtomography, and diffraction topography, is increasingly used, the requested beam time being recurrently a factor 5 above the available time. Phase contrast imaging is one of the strong contributions of modern synchrotron radiation sources: the application chosen here shows its use for real-time investigations of the directional solidification of aluminium- based alloys (page 114). Microtomography is now implemented on a series of beamlines (BM05, ID15, ID17, ID19, ID22) to cover both academic, for example the study of liquid foams (page 115), and industrial needs. One example of this last type of very applied research is for the study of the fermentation and baking of bread (page 116). This subsection devoted to the study of materials is concluded by a *in situ* investigation of the roughness evolution during the growth of a Tungsten film (page 117).

Synchrotron radiation based biomedical research is an important part of the X-ray Imaging Group’s beamline activity, and more particularly of the dedicated beamline ID17. The quantitative comparison of various phase-contrast techniques to identify the most appropriate method for a given situation is the topic of the first contribution (page 119). The parallel, and sometimes combined, development of diagnostic tools (*e.g.* using SAXS (page 120), functional imaging and radiation therapy are active research fields. For instance, spectacular survival curves have been obtained for rats bearing glioma type brain tumours (page 121). This is a highly encouraging result, which leads us to envisage its extension to clinical protocols. These programs are based on collaborations with local and European hospital teams, and the efficient use of the ESRF Biomedical Facility.

The techniques implemented at the ESRF also develop outside of the synchrotron radiation world. The common wish of the ESRF staff and of our users is to take full advantage of the specificities of third-generation synchrotron radiation facilities which are not available elsewhere. This implies continual development of the techniques, and lends particular importance to the section on advances in instrumentation.

The biomedical topics that are of fundamental or clinical relevance and for which synchrotron radiation techniques are the best tool are now well identified. The ESRF will concentrate on these topics, which will probably include clinical radiotherapy in the near future. To be able to answer the questions associated with modern science and techniques, synchrotron radiation microtomography is moving towards higher spatial and temporal resolutions. The temporal resolution (now in the 10 second range) is important for a wide range of time-evolving phenomena and should aim to reach the sub-second range. The spatial resolution, today in the 1 μm range, should be improved to the 50 nm scale (“nanoimaging” project), with the help of better focussing optics and detectors.

References

[1] Y. Chaimanee, D. Jolly, M. Benammi, P. Tafforeau, D. Duzer, I. Moussa and J.-J.Jaeger, *Nature*, **422**, 61-65 (2003).

[2] Y. Chaimanee, V. Suteethorn, P. Jintasakul, B. Marandat and J.-J. Jaeger, *Nature*, **427**, 439-441 (2004).

J. Baruchel

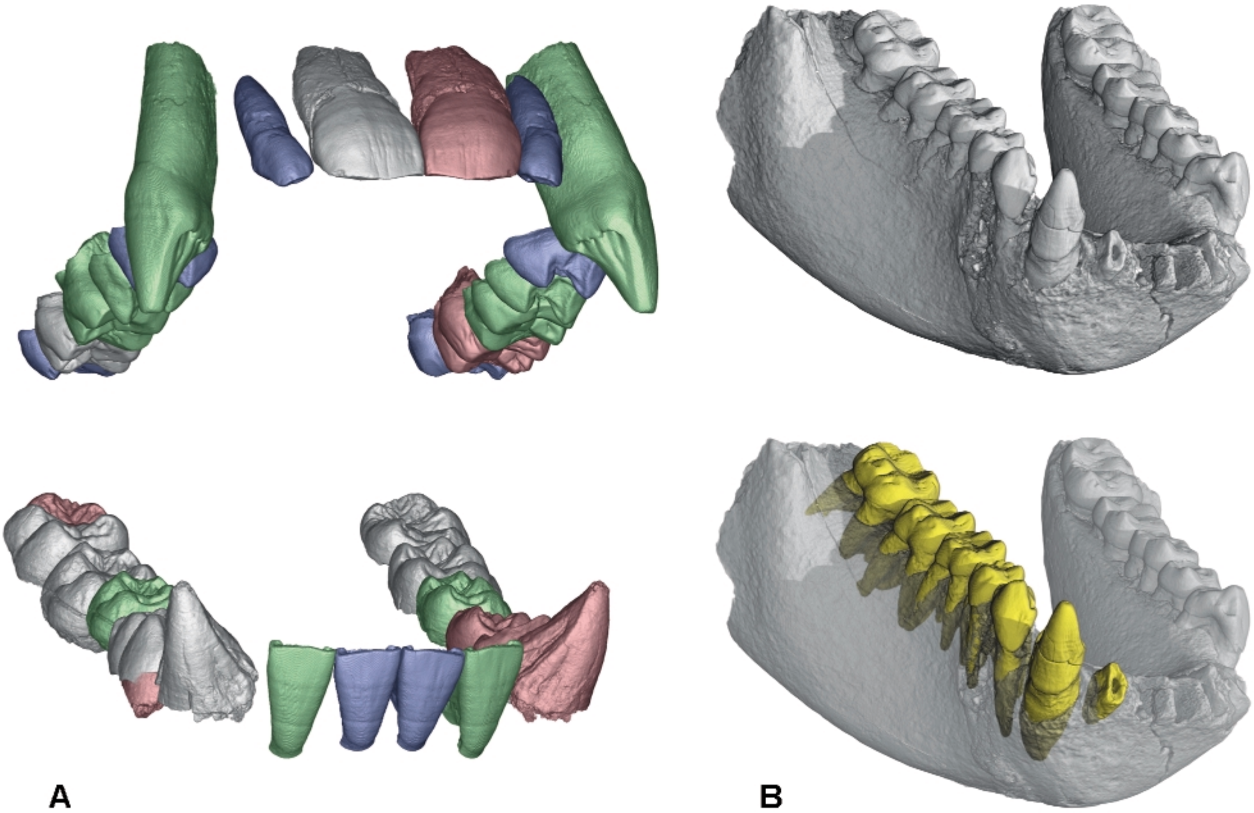

Fig. 132: 3D rendering of two fossils from Thailand, relatives of the modern orangutan. a) virtual reconstruction of the jaws of the male of *Khoratpithecus chiangmuanensis*. Grey: real teeth. Pink: symmetrical equivalents of the real teeth. Blue: teeth from female after size correction. Green: extrapolated teeth. This species dates from about 12 million years ago. b) mandible of *Khoratpithecus piriyai*. This species dates from about 7 million years ago, but is very similar to the first one. In yellow: virtual extraction of the teeth showing their roots (Imaging was at ID19 and ID17 respectively, images courtesy P. Tafforeau, J.-J. Jaeger and Y. Chaimanee).

X-ray Fluo-microscopy and Analysis

First Direct Observation of Brine Droplets and Solid Inclusions in Accreted Ice from the Sub-glacial Lake Vostok (Antarctica)

The largest sub-glacial lake (14,000 km^2) discovered by a radio-echo survey under the Antarctic ice cap is covered by 3,750 m of ice and underlies the Russian station of Vostok where a 3620 m deep ice core has been recovered. Ice coring has been stopped 130 m above the lake surface, in ice formed by the refreezing of lake water at the bottom of the glacier. Although made of large ice crystals of very high crystalline quality, accretion ice contains many visible inclusions and large amounts of soluble species (sulphate salts and NaCl) [1]. The origin of these impurities is puzzling and information on their composition and location is essential for the understanding of the lake's environment and mechanisms driving ice formation and aging process.

We present here data obtained by X-ray fluorescence at beamline **ID21**. The microprobe was set at 4.5 keV for 2D mapping of elements lighter than Ca. A specific experiment was carried out for sulphur species, tuning the excitation energy to around 2.5 keV. The shift in energy produced a clear distinction between sulphur present as sulphide (S^{II-}, 2.470 keV), sulphite (S^{IV}, 2.478 keV) and sulphate (S^{VI}, 2.482 keV) [2,3]. The cryosystem allowed the temperature of the sample holder to be kept stable and close to -140°C. The cell containing the ice sample was tightly closed by a film of "ultralene"®, making it possible to study the upper 50 µm of samples for several hours under high vacuum (2 x 10^{-5} kPa) conditions without any visual change of the ice surface. In this experiment, the plastic film was mechanically fastened to the top of the cell to avoid chlorine contamination from glue.

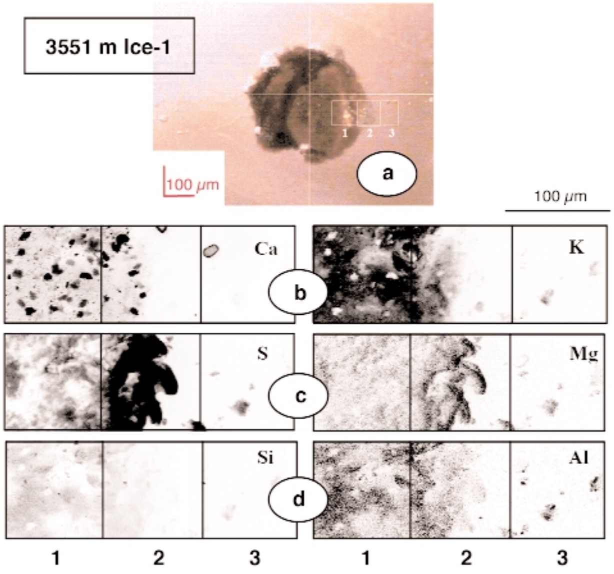

Fig. 133: Elemental maps of three contiguous areas of a very large solid inclusion (600 µm) at 3551 m. Beam energy was focused at 4.5 keV. Probe size was 1 x 1 µm^2. The highest concentration of the total area represented in elemental mapping is automatically scaled to black.

Four accretion ice samples containing visible inclusions and one grain boundary have been studied. A very large inclusion was carefully investigated (**Figure 133**).This inclusion was a very large aggregate of various particles including sulphur compounds, alumino-silicates and other silicate species, and relatively large carbonates. Several smaller dark aggregates showing rather similar composition were found inside ice crystals, while the grain boundary structure contained only very few particles per µm. One aggregate was studied for sulphur speciation, showing that reduced sulphur species were present along with sulphate salts.

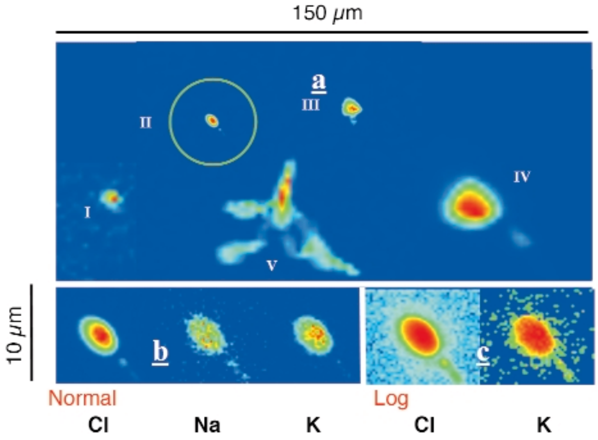

Fig. 134: Brine inclusions at 3551 m. Five colourless oblong objects were observed over an area of 200 x 200 µm^2, with apparent diameter varying from ~ 3 to ~ 15 µm. Object V exploded during the scan. Probe size ranged from 0.3 x 0.5 µm^2 (II and III) to 1 x 1 µm^2 (I, IV and V). The intensity scale extends from dark blue to red.

Chlorine was almost exclusively detected in colourless micrometer-sized structures (**Figure 134**), which are very likely to be brine micro-pockets entrapped in the ice lattice. A rough estimate of their salinity leads to a value (1.5%) significantly higher than the maximum salinity calculated for the main lake [1]. At the temperature prevailing in accreted ice (-3°C), brine should remain in a liquid state. During drilling, the outer pressure decreases from 30 to 0.1 MPa and ice cores are cooled to about -50°C. The relaxation and the freezing of water droplets can initiate ice cracks along crystallographic planes, which could explain the shape and orientation of bubble extensions clearly visible in Figure 134c. The freezing of brine droplets could also lead to concentration gradients as observed in brine bubbles (Figure 134b), solute exclusion occurring at the ice water interface during the freezing process.

This work is, to our knowledge, the first direct observation of well-preserved liquid microstructures along with other solid and complex objects in ice. Accretion ice from lake Vostok contains solid particles initially boosted by saline water in frazil slush. Single crystals that growing once the ice is accreted may keep large solid aggregates as well as haline droplets inside the ice lattice. The structure and composition of solid inclusions linked to the high salinity of brine droplets provide new arguments for the occurrence, under lake Vostok, of saline water pulses through a deeper sulphur rich sedimentary reservoir.

References

[1] M. De Angelis, J.R. Petit, J. Savarino, R. Souchez , and M.H. Thiemens, *Earth Planet. Sci. Lett.* **222**, 751-765 (2004).
[2] M. Stöhr, *NEXAFS Spectroscopy*, Berlin: Springer-Verlag (1992).
[3] J. Prietzel, J. Thieme, U. Neuhaeusler, J. Susini and I. Kogel-Knabner, *European J. Soil Sci.* **54**, 423–433 (2003).

Authors

M. de Angelis (a), M.-C. Morel-Fourcade (a), J.-M. Barnola (a), J. Susini (b) and P. Duval.
(a) LGGE/CNRS Saint Martin d'Hères (France)
(b) ESRF

Modern Composition of 3,500 Million-year-old Seawater: Implications for Life on the Primitive Earth

There are two fundamental requirements for life as we know it, liquid water and organic polymers, such as nucleic acids and proteins. At about 4.4 to 4.0 billion years (Gyr), the Earth may have been cool enough for the presence of extensive oceans for long periods. Life on Earth dates from before about 3.8 Gyr, and is likely to have gone through one or more hot-ocean environments. Only hyperthermophiles (microorganisms optimally living in water at 80–110°C) would have survived. Early hyperthermophile life probably developed near hydrothermal systems including 'black smokers' (**Figure 135a**). It would have had access to redox contrast between a more oxidised atmosphere–ocean system and the more reduced fluids emanating from mantle-derived magmas. Sulphur offers the best opportunities. With water present in the air, volcanic SO_2 would have been oxidised to sulphate. Dissolved in water, sulphate would provide oxidation power for organisms to react against reduced species in hydrothermal fluids, such as H_2S and CH_4. Considering that sulphate-reducing microbes had evolved by 3.5 Gyr ago, the poorly-fractionated Early Archaean sedimentary sulphides have been attributed to either biological sulphate reduction in a fully anoxic ocean containing little sulphate (< 200 μM to 1 mM) or to intense biological sulphate reduction at sulphate oceanic concentrations not much different from today's (28 mM). Clearly, the oxidation state and composition of the Archaean ocean and atmosphere remains essentially unconstrained.

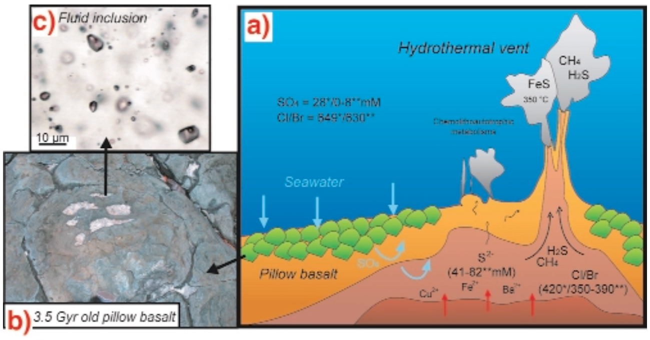

Fig. 135: (a) Hydrothermal system on the seafloor showing the main fluid pathways and elemental distribution patterns. * refers to modern day values, whereas ** corresponds to element concentration estimates in "North Pole" Archaean fluids. (b) Archaean pillow basalt. (c) Fluid inclusions in intrapillow quartz pods.

Insights into the composition of Archaean seawater and hydrothermal fluids can be obtained by direct analysis of fluid inclusions preserved in Archaean hydrothermal systems. Here, we investigated a suite of quartz pods preserved in basaltic pillow lavas (Figure 135b) that formed during oceanic hydrothermal alteration of the 3.5 Gyr North Pole formation. The pods contain myriad fluid inclusions (Figure 135c), which were analysed individually using synchrotron radiation X-ray microfluorescence (μ-SR-XRF) [1]. The main advantages of the μ-SR-XRF technique reside in its non-destructive character, high spatial resolution, multi-element analytical capability and high sensitivity. Hence, μ-SR-XRF can analyse small, diluted individual fluid inclusions, discriminate distinct inclusion populations trapped in a single crystal and provide information about complex histories of fluid circulations [2].

Calculated model composition yielded a bulk fluid salinity of four-times the present-day value reflecting a typical modern-day seawater evaporation trend in a shallow marine, closed basin environment. Individual fluid inclusion analysis using μ-SR-XRF revealed the presence of three fluid populations (**Figure 136**): a metal-depleted fluid, a Ba-rich and S-depleted fluid, and a Fe–S-rich end-member. The Cl/Br ratio of metal-depleted fluid inclusions (630) is similar to the modern seawater value (649; Figure 135a). In contrast, Ba- and Fe-rich brines have Cl/Br ratios (350 and 390) close to the bulk Earth value (420), hence arguing for a hydrothermal origin of

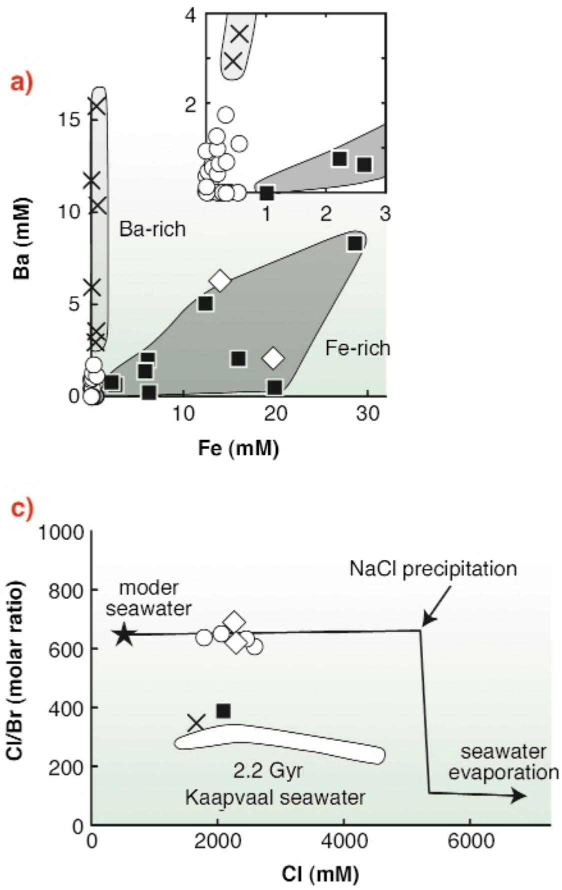

Fig. 136: Fluid inclusion composition results. (a) Fe vs. Ba concentration diagram showing the occurrence a Ba-rich fluid (crosses), a Fe-rich fluid (black squares) and a metal-depleted end-member (open circle) corresponding to "North Pole seawater". (b) Cl vs. Br concentrations for metal-depleted inclusions compared with modern seawater value (black star) and seawater Cl/Br evaporative trend (black line). (c) Cl/Br vs. Cl trend of evaporating seawater compared with present results. Also shown is the field of Kaapvaal 2.2 billion years old seawater, South Africa [3]. (d) S vs. Cl/Br plot of "North Pole seawater" and Fe-bearing inclusion fluids. Black squares = sulphur concentrations in Fe-rich fluids. Open circles = calculated sulphur detection limit and possible range of S concentrations in "North Pole seawater".

these fluids. The metal depleted fluid displays low sulphate concentration (0–8 mM compared to 28 mM in present-day ocean). Sulphur content of the Fe rich fluids ranges between 41 and 82 mM.

Fluid–rock interaction processes occurring in pillow basalts located on the seafloor are unlikely to be the cause of Cl/Br fractionation between hydrothermal fluids and the North Pole seawater end-member. Modern organic matter is strongly enriched in heavy halogens with respect to Cl. If the sedimental burial of organic matter is efficient enough to preclude return of Br to the bottom ocean water, Br can be significantly enriched in sediments and depleted in seawater. We hypothesize that high biological activities associated with vigorous sedimentation are responsible for the buffering of North Pole seawater Cl/Br value. The sulphate concentration (0 to 8 mM, Figure 135), is much lower than in present-day oceans (28 mM) and in the Black Sea anoxic bottom waters (18 mM). Under an oxygen-rich Archaean atmosphere, the relative isolation of the North Pole basin and its exposure to large detrital input, would make it a very favourable setting for the accumulation of sulphate produced by subaerial sulphide oxidation. Therefore the sulphate content of North Pole seawater may be regarded as indicative of local conditions and representing an upper limit for the rest of the Archaean ocean. This implies that the Early Archaean ocean as a whole would have been dramatically depleted in sulphate, hence arguing for a poorly oxygenated primitive atmosphere.

References

[1] J. Cauzid, P. Philippot, A. Somogyi, A. Simionovici, P. Bleuet, *Anal. Chem.*, **76**, 3988-3994 (2004).
[2] J. Foriel, P. Philippot, P. Rey, A. Somogyi, D. Banks, B. Ménez, *Earth Planet. Sci. Lett., in press* (2005).
[3] J. Gutzmer, D.A. Banks, V. Luders, J. Hoefs, N.J. Beukes, K.L. Von Bezing, *Chem. Geol.*, **201**, 37-53 (2003).

Authors

P. Philippot (a), J. Cauzid (a, b), J. Foriel (a), A. Somogyi (c), B. Ménez (a), P. Rey (d)
(a) Institut de Physique du Globe de Paris (France)
(b) ESRF
(c) Synchrotron Soleil, Gif-sur-Yvette (France)
(d) School of Geosciences, The University of Sydney (Australia)

Variations in Atmospheric Sulphate Recorded in Stalagmites

Our understanding of secular variation in sulphate aerosol concentration comes primarily from ice cores. The rise in sulphur concentration during the last 150 years detected in Greenland and Alpine ice cores reflects increasing twentieth century anthropogenic load. We need archives in mid-latitudes and at low altitudes to improve our knowledge about the role of sulphate aerosols in altering regional radiative forcing and climate. By applying synchrotron radiation micro-XRF (X-ray fluorescence) we found such an archive in calcium carbonate speleothems, mineral deposits formed in caves.

Speleothem-forming environments act as S archives because a significant fraction of atmospheric precipitation enters the karst aquifer rapidly. Rainwater and soil PCO_2 combine to form the weak carbonic acid, which dissolves the carbonate rock. Within the karstic aquifer, flowpaths are commonly short (typically 5-50 m), and when the drip waters enter the cave they release CO_2 to the cave atmosphere and precipitate calcium carbonate at the top of the growing speleothems (**Figure 137**). Seasonal variability of trace element concentration in stalagmites can result in visible annual laminae [1]. Annually laminated stalagmites are the best specimens for synchrotron radiation analyses because the chronology of scans and maps (determined by counting back in time each visible lamina from the year of removal) can be precisely reconstructed.

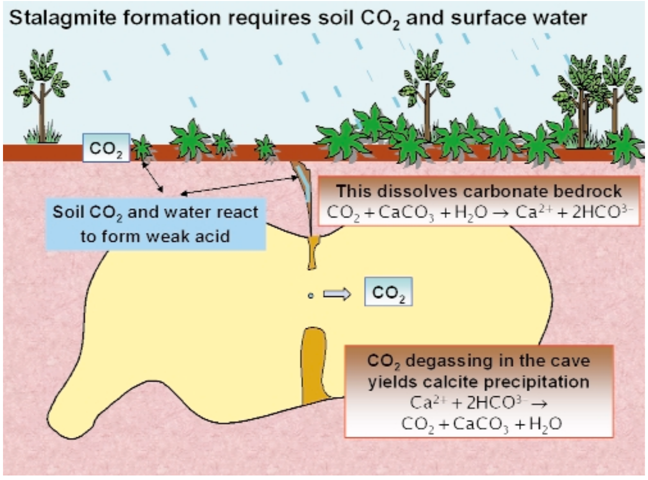

Fig. 137: Scheme illustrating how stalagmites capture atmospheric changes.

We applied X-ray micro-fluorescence coupled with X-ray absorption near edge structure spectroscopy (XANES) to detect sulphate concentration changes in the top 160 years of annually laminated stalagmite ER78 from Grotta di Ernesto, a cave located at 1167 m above sea level in north-eastern Italy. On a double polished, 200 µm-thick wafer, two parallel 7 mm-long scans (300 µm apart), dated from 1840 to 1995 AD, were analysed at **ID21**. The specimen was placed in the microscope chamber operated at a pressure of 10^{-5} mbar. A high-resolution double crystal Si 111 monochromator allowed selection of the energy relative to different coordination for sulphur, and a Fresnel zone plate generated an X-ray probe of sub-µm diameter. We reached 1 µm-diameter analytical spots, with 1 µm steps for scans and 2 x 2 µm pixels for the maps. The fluorescence signal came from a depth of 20 µm for S, but laminae are continuous enough in depth to allow most of the counts from the analysed lamina. S-oxidation state was determined by tuning the energy of the incident X-ray photons from 2.45 to 2.55 KeV, across the absorption K-edge of S, with energy resolution of 0.25eV (eV: $\Delta E/E = 10^{-4}$). The XANES spectra show clear, intense peaks at the energy of oxidised sulphur in sulphates at 2.482 keV. Sulphate distribution within the specimen was obtained through XRF mapping at high spatial resolution (probe size 0.8 x 0.8 μm^2). The excitation energy was tuned to 2.482 keV: thus the XRF maps show the pattern of sulphate concentration both in coeval stalagmite layers, and through time.

Micro-XRF scans revealed increasing sulphate since 1880 (**Figure 138**). Count rates increase by a factor of six between 1840-1870 and 1980-95, comparable to that detected in Alpine ice cores. Micro-XRF maps show that sulphate follows very weakly annual peaks of accumulation observed in soil-derived P, and it is independent from Mg, which reflects the residence time of the water in the aquifer [2]. This excludes significant bedrock and soil S sources. The most likely explanation for the observed trend is that ER78 captures twentieth century atmospheric sulphate aerosol increase related to anthropogenic emissions.

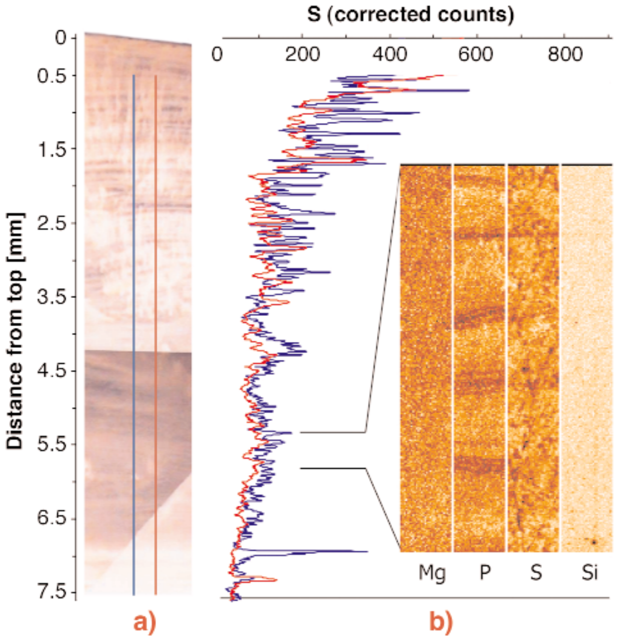

Fig. 138: The S-sulphate scans (1840 to 1995 AD). Left: stalagmite wafer and scan traces. Right: micro-XRF maps (60 x 500 µm, position along the scan is bracketed) showing element concentration (hot scale).

Sulphate rise in ER78 is not followed by the fall after 1980 that is found in ice core of the western Alps in accordance with decreased S emissions in Europe. This can be explained by partial retention of sulphate in the forest ecosystem above the cave (typically 10-15 years), but may also reflect different air mass trajectories from the ice core locations.

Synchrotron micro-XRF scans indicate that speleothems are new, valuable archives of atmospheric sulphur budgets. The post-1850 A.D. record from the Ernesto cave shows a substantial rise in sulphate, interpreted as reflecting anthropogenically-forced variation of sulphate of the atmospheric boundary layer, moderated by some ecosystem storage.

References

[1] S. Frisia, A. Borsato, N. Preto, F. McDermott, *Earth Planet. Sci. Lett.*, **216,** 411-424 (2003).
[2] I.J. Fairchild, A. Borsato, A.F. Tooth, S. Frisia, C.H. Hawkesworth, Y. Huang, F. McDermott, B. Spiro, *Chem. Geol.,* **166**, 255- 269, (2000).

Principal Publications and Authors

S. Frisia(a), A. Borsato (a), I.J.Fairchild (b), J. Susini (c), *Earth Planet. Sci. Letters*, submitted
(a) Museo Tridentino di Scienze Naturali, Trento (Italy)
(b) School of Geography, Earth and Environmental Sciences, University of Birmingham (UK)
(c) ESRF

X-ray Imaging in the Study of Materials

Application of Synchrotron X-ray Imaging to the Study of Directional Solidification of Aluminium-based Alloys

The properties of materials elaborated from the melt are largely governed by the microstructure built into the solid during processing. Materials engineering aims to devise materials and processing conditions that would give optimum properties and better reliability.

It is therefore essential to have a precise understanding of solidification pattern formation to be able to achieve new technological breakthroughs. Directional solidification has become the method of choice to study microstructure formation since the process parameters (pulling velocity V, temperature gradient G, alloy composition) are independently and accurately controlled, and the response of the interface quantitatively examined through the evolution of the solid – liquid interface morphology (smooth → cells → dendrites as growth rate increases). For metallic alloys, third-generation synchrotron X-ray sources allow *in situ* and real-time X-ray imaging with high spatial and temporal resolution. Using absorption and phase contrast radiography, we present two examples of dynamical pattern formation in thin Al-based alloys solidified from the bottom upwards in the specific Bridgman facility [1] installed at the **ID19** beamline.

Figure 139 displays the dynamical interaction between dendrite formation and buoyancy-driven convection, common in casting and welding. After the breakdown of the smooth solid – liquid interface, the corrugations progressively increase in amplitude and sidebranches begin to show up on the largest ones (Figure 139a), which indicates the inception of dendrites [2]. Fluid flow in the melt induces significant solute accumulation and a transition to a eutectic pattern on the right of Figure 139b, and localisation of dendritic growth on the left. Neighbour screening eventually results in the coupled growth of a large single dendrite, protruding into the liquid, far ahead of the eutectic at its base (Figure 139c).

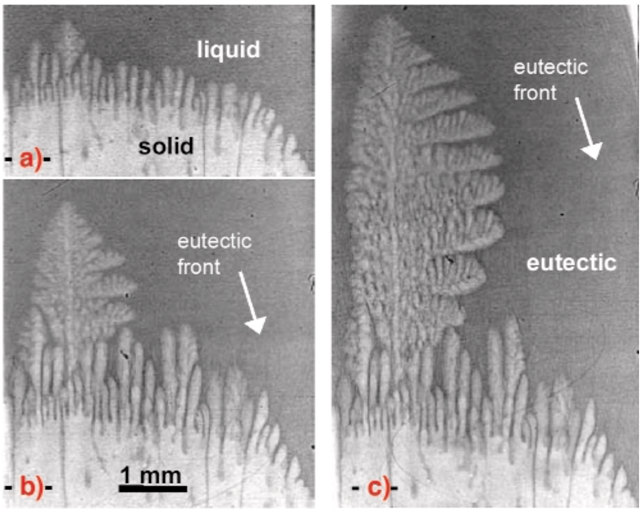

Fig. 139: Formation of the dendritic microstructure in Al-3.5 wt% Ni. V = 1 μm/s, G = 20 K/cm, thickness = 250 μm. a) 1344 sec after birth of morphological instability; b) t = 3206 sec; c) t = 4254 sec.

To the best of our knowledge, **Figure 140** provides the first direct evidence of the facetted character of the growth of icosahedral quasicrystals from an $Al_{72.4}Pd_{20.5}Mn_{7.1}$ melt. Indeed, quasicrystals still keep us wondering, particularly about how orientation order progresses over such long distance during their growth. In Figure 140a, two facet edges are visible on grain 1 and three on grain 2, and there is a narrow cusp at the level of the grain boundary. When the applied pulling rate is increased to 3.6 μm/s, the cusp evolves into a deep, wide liquid groove, and the facets exhibit salient evidence of layer-motion controlled growth (Figure 140b). Possibly due to the skeletal instability of layer motion [3], striations run parallel to the interface and notches form repeatedly on the left side of grain 2. After a while, new grains nucleate and grow facetted in the liquid just above the two initial grains, whose growth becomes blocked.

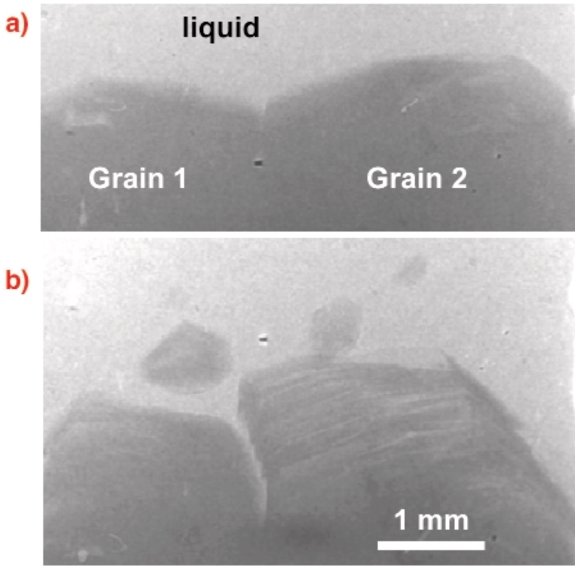

Fig. 140: Steady-state growth of AlPdMn quasicrystal grains at 0.4 μm/s (a), and evolution of the two initial grains at the beginning of their screening by new grains 750 s after increasing the pulling rate to 3.6 μm/s (b). Sample thickness = 500 μm.

In conclusion, the dynamics of pattern formation in solidification of alloys can be efficiently probed *in situ* and in real-time, and detailed information can be obtained. Firstly, it is demonstrated that, under fluid flow, the competition with eutectic microstructure results in dendrite localisation. Secondly, the first live observation of the solidification of quasicrystal grains provides sound proof of facetted growth. By filling part of the huge deficit in the knowledge of the physical mechanisms active in quasicrystal growth, reliable guidance is provided for further advancement of the theoretical modelling.

References

[1] H. Nguyen Thi *et al.*, *J. Phys. D: Appl. Phys.* **36**, A83 (2003).
[2] R.H. Mathiesen *et al.*, *Phys. Rev. Lett.* **83**, 5062 (1999).
[3] A.A. Chernov, *J. Crystal Growth* **24/25,** 11 (1974).

Principal Publication and Authors

T. Schenk (a), H. Nguyen Thi (b), J. Gastaldi (c), G. Reinhart (b), V. Cristiglio (a), N. Mangelinck-Noël (b), H. Klein (d), J. Härtwig (a), B. Grushko (e), B. Billia (b), J. Baruchel (a), *J. Crystal Growth*, *in press*.
(a) ESRF
(b) L2MP, Marseille (France)
(c) CRMCN, Marseille (France)
(d) Laboratoire Cristallographie, CNRS, Grenoble (France)
(e) IFF, Forschungszentrum Juelich (Germany)

X-ray Microtomographic Study of Liquid Foams

Fluid foams consist of gas bubbles separated by a continuous film of liquid which tends to minimise its surface energy. They are a model for various classes of materials: emulsions, magnetic garnets, and even grain boundaries in crystals [1]. The knowledge we gain from understanding foams has technological applications, ranging from food and shaving cream to fire fighting and oil recovery. Understanding the structure is an important step towards predicting a foam's mechanical properties. Moreover, the structure of fluid foams determines the structure of solid foams produced by solidification: metallic foams for the automobile industry, pumice from volcanoes, polymeric foams as filling materials and food foams.

X-ray microtomography is by far the best non-invasive method to look inside a medium which scatters visible light as much as foams do. Since X-rays pass through the foam, a raw picture is a 2D projection of the real 3D structure. The idea of tomography is to take typically 1000 pictures of the same sample at different angles. A mathematical inversion yields the 3D reconstruction of the whole foam. However, as a liquid foam can evolve, it is important to take the 1000 pictures in a short time to avoid blurring in the reconstruction. The ESRF's brightness and beamline improvements on **ID19** have enabled us to reduce the acquisition time from hours (which was fine for solid structures) to tens of minutes, then to minutes, with a resolution down to 10 or even 1 μm (**Figure 141**).

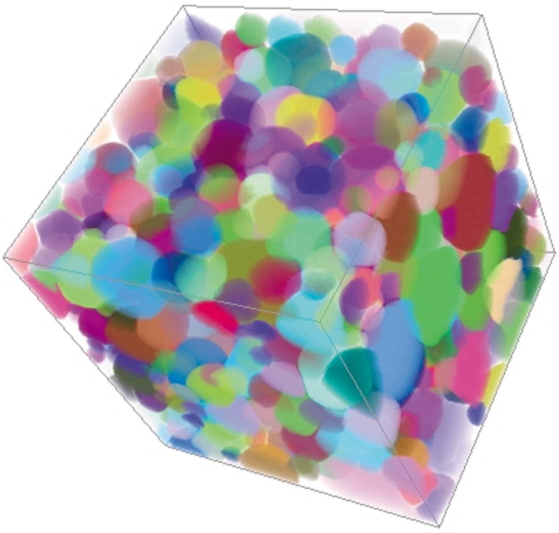

Fig. 141: Reconstructed 3D image of the 1 cm^3 liquid foam (air bubbles in soap solution): a billion of 10-μm voxels (volume image elements). The (false) colours label bubbles.

We can obtain a wealth of details. On the smallest scale, we can observe thin water films, including the accumulation of water in the borders where films meet. On the scale of bubbles, we can quantify their size, shape, and number of neighbours. Since we track thousands of bubbles individually, we can perform statistics on the scale of the whole foam, and even obtain correlations, for instance between size and number of neighbours. Finally, we can observe a phenomenon common to emulsion and grain growth in metals: since the air can slowly diffuse through water, it flows from bubbles at high pressure (actually, the smallest ones) to low pressure regions (large bubbles). Thus small bubbles shrink, and eventually disappear. The total number of bubbles decreases, and in time (few hours) the average length scale coarsens (**Figure 142**) [2]. Preliminary tests with a new Dalsa camera yielded images of an even dryer foam (that is, with more air and thinner walls) in a few tens of seconds; this opens the way to the dynamic study of evolving foams.

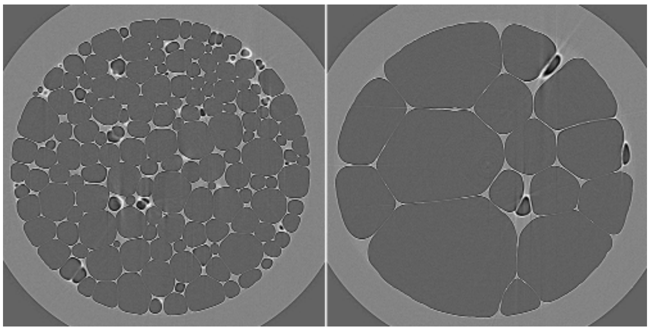

Fig. 142: 2D section of the foam after ageing 1 hour (left) and 1 day (right).

Reference

[1] D. Weaire, S. Hutzler, *Physics of Foams*, Oxford Univ. Press, 1999.

[2] Movies available at http://www-lsp.ujf-grenoble.fr/link/mousses-films.htm

Principal Publication and Authors

J. Lambert (a), I. Cantat (a), R. Delannay (a), A. Renault (a), F. Graner (b), J.A. Glazier (c), I. Veretennikov (c), P. Cloetens (d), *Colloids Surf. A: Physicochem. Eng. Aspects, in press*.

(a) GMCM, Univ. Rennes 1 (France)

(b) LSP, Univ. Grenoble 1 (France)

(c) Dept Physics, Indiana Univ. (USA)

(d) ESRF

In situ Study of the Fermentation and Baking of Bread Dough by X-ray Tomography

The consumer's appreciation of solid food foams such as bread is strongly linked to their texture. Bubble growth and coalescence phenomena during fermentation and baking govern bread texture creation, which in turn determines mechanical properties as well as sensory properties like their feeling in the mouth. Mechanisms governing the cellular structure development and setting need to be better understood, which requires a systematic and accurate mapping of microstructural characteristics. For this purpose, X-ray tomography appears to be a well-suited technology to overcome difficulties encountered with more classical imaging techniques (invasive, 2D, poor contrast, and artefacts in the sample preparation). Very recently, it has been applied to imaging the final structure of cellular food products [1,2]. The originality of the present work is to use *in situ* X-ray tomography in order to assess the bubble structure development during the fermentation and baking of bread dough.

The experiment was carried out at the **BM05** beamline using a specifically-designed "fast" tomography technique. The energy was 18 keV and the spatial resolution 15 µm. Exposure time of a single projection of 20 milliseconds allowed a scan of 400 projections over 180 degrees within 30 seconds. Product changes during this interval could reasonably be discarded in comparison with its overall evolution during total fermentation time. Scans were recorded every 5 or 10 minutes during 2 or 3 hours (depending on the yeast content), to obtain a "movie" of the whole process. Bread dough of different compositions was studied to highlight the role of the ingredients (flour, water, sucrose, oil and yeast). The fermentation step was performed for a longer time than usual to observe the coalescence mechanisms until low densities were reached. A trial of *in situ* observation of bread baking was also achieved in a small 'tomographic' oven, at a 5°C/mn heating rate.

Typical evolution of the microstructure of bread dough during the fermentation stage is displayed on **Figure 143a**. For the sake of clarity, only five 2D pictures among the overall twenty-five recorded, are shown. During the first part of the fermentation, growing spherical bubbles can clearly be identified. In the second part, bubble coalescence leads to a more heterogeneous structure with complex shape cells.

Evolutions of macroscopic (void fraction) or microscopic (cell size distribution) characteristics were calculated over the whole fermentation time. Figure 143b presents the evolution of the void fraction for four compositions. The one containing 1.5% of yeast (black points) led to a slower evolution than the three others with 3% of yeast (among them the "French baguette" recipe (red points)). The evolution of different initial bubble sizes can be fitted by the equation $R(t) = R_0e^{kt}$ where k is directly related to process and material variables (internal gas pressure, dough matrix viscosity) (Figure 143c).

Figure 144 represents images extracted from the baking experiment, at the end of which a bread crumb, Ø 8 mm base and a few mm thick was obtained. It can be shown that foam setting, here dough/crumb transition, occurs for temperature close to 70°C.

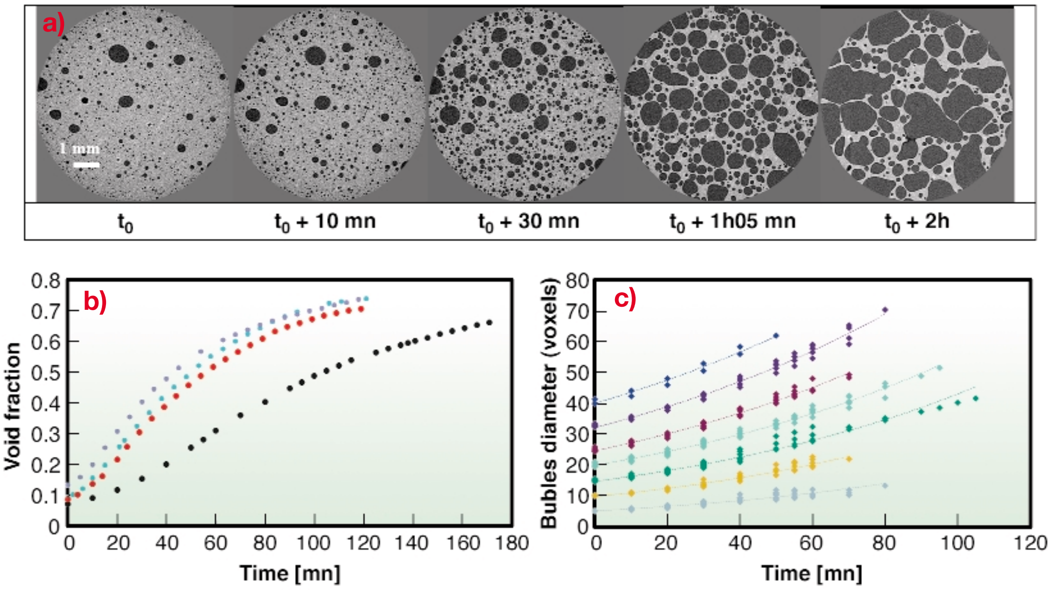

Fig. 143: Evolution during the bread dough fermentation of: a) the microstructure b) the void fraction of different formulations and c) the bubble diameter for different initial sizes.

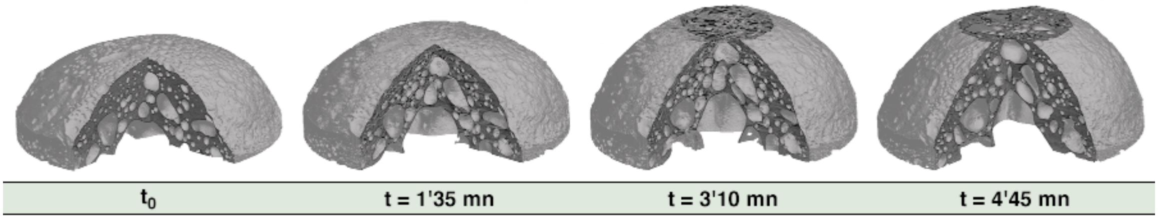

Fig. 144: Microstructure evolution during the first minutes of baking.

This work is still in progress: the complete quantitative analysis of the data will allow a better understanding of the physical mechanisms governing the growth and coalescence phenomena. It will also provide essential data for the validation of numerical models of bubbles growth during food texturing processes. In particular, dough images captured at different proofing stages leading to the same density can be numerised in order to determine the influence of microstructure by FEM simulation. Complementary sensorial characterisation is also planned for the products. Further prospects encompass a reverse engineering approach: starting from the expected sensory properties, textural properties are targeted in order to select relevant processing conditions and composition which would meet these specifications.

References

[1] P. Babin, G. Della Valle, R. Dendievel and L. Salvo, *Proceedings of the 5th International Conference Engineering and Food*, Montpellier France (2004).

[2] P.M. Falcone, A. Baiano, F. Zanini, L. Mancini, G. Tromba, F. Montanari and M.A. Del Nobile, *J. Food Science* **69,** 38 (2004).

Principal Publication and Authors

P. Babin (a,b), H. Chiron (c), J. Hoszowska (d), P. Cloetens (d), P. Pernot (d), AL. Réguerre (c), L. Salvo (a), R. Dendievel (a) and G. Della Valle (c).
(a) GPM2, INP Grenoble (France)
(b) Science Computers Consultants, St Etienne (France)
(c) URPOI, INRA Nantes (France)
(d) ESRF

Roughness Conformity during Tungsten Film Growth: An in situ Synchrotron X-ray Scattering Study

Artificial thin films and layered systems are widely used in the fields of materials science, microelectronics and optics. They are also extensively employed in reflective synchrotron X-ray optics to tailor their optical properties. When diffraction-limited performance is desired, the most important surface parameters to be optimised are the figure and finish of the optics. While the desired optical figure can be reached via specific techniques, such as diamond turning, dynamical shaping or differential coating methods, the finish demands a control of the surfacing at the atomic level. Therefore, it is essential to understand the fundamental roughening and smoothing mechanisms that occur during mirror coating process.

Studies on thin film growth are frequently performed by interruption of the process followed by *ex situ* characterisation using either X-ray scattering techniques (XRS) or local probe techniques such as AFM or STM. In contrast, with grazing incidence XRS (GIXRS) techniques, measurements can be acquired *in situ* and in real-time, thus eliminating possible artifacts of the latter methods. Moreover, GIXRS method gives the unique possibility to investigate buried interfaces and to establish the degree of vertical correlation (conformity) between the roughness of the substrate and of the external film surface. Differentiating features induced by the topography of the substrate from those generated during deposition is an important asset in the optimisation of a growth process. Hence, an instrument capable of performing time-resolved reflectometry measurements on thin films has been developed [1].

In standard XRS data analysis [2, 3], based on the DWBA formalism, the relationship between the correlation functions due to the roughness at the various film interfaces and the scattering diagram is contained in an integral equation, so that the form of the autocorrelation function at each interface as well as the cross-correlation function must be postulated. In contrast, recent results obtained at the **BM05** beamline show that, in the smooth surface limit [4], the general evolution of the roughness can be described in terms of its power spectrum density (PSD) without any model of film growth and/or correlation function (**Figure 145a**). From a direct evaluation of the PSD the roughness conformity was quantified using a replication factor defined as
$K(p,h) = PSD_{sf}(p,h) / \sqrt{PSD_f(p,h) \bullet PSD_s(p)}$.

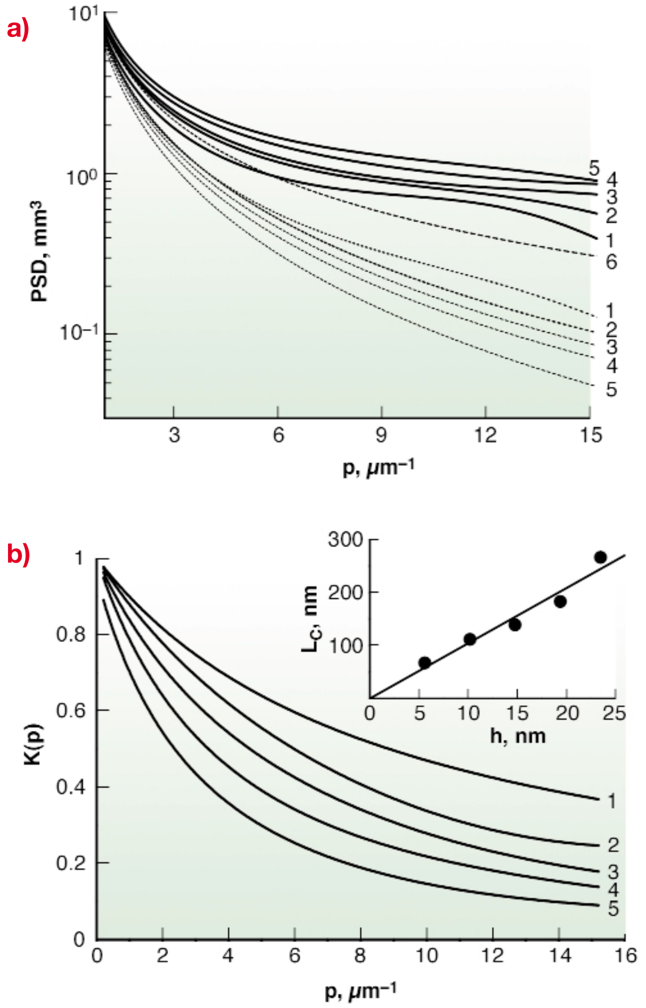

Fig. 145: (a): PSD-functions of the external film surface (solid curves) and of cross-correlation (dotted curves) extracted from the measured scattering diagrams as a function of the film thickness h (h = 5.6 nm (1), 10.2 nm (2), 14.8 nm (3), 19.4 nm (4), and 23.5 nm (5)). Curve 6 is the PSD-function of the silicon substrate. (b): Replication factor of roughness as a function of the film thickness). The inset shows the dependence of the characteristic length of roughness on the film thickness.

The evolution of *K(p)* as a function of the film thickness *h* in the case of tungsten growth by sputtering deposition is presented in Figure 145b. The results enabled a quantitative estimation of the degree of conformity arising during film deposition and the determination of a characteristic wavelength L_c defined as the spatial dimension for which the replication factor would decrease by a factor e. The inset in Figure 145b shows the evolution of L_c as a function of the film thickness. After deposition of a film of thickness h features with a lateral size greater than L_c will be correctly replicated while additional uncorrelated roughness increases at decreasing spatial scale. For the tungsten growth process presented here, the critical size of a replicated feature would increase proportionally to the film thickness and the replication would only occur for surface features with a lateral size about 10 times greater than the film thickness could be correctly replicated.

The *in situ* XRS technique and data treatment presented here are expected to bring new insights in the comprehension of a large variety of processes, including sputter growth, evaporation, ion erosion and ion beam assisted deposition.

References

[1] L. Peverini, T. Bigault, and E. Ziegler, *A real time in-situ X-ray scattering apparatus to monitor surface roughness*. in *Seventh Conference on the Physics of X-ray Multilayer Structures,* Sapporo, Japan (2004).
[2] M. Tolan, *X-ray scattering from soft-matter thin films : materials science and basic research*. Springer tracts in modern physics ; 148. Berlin ; London: Springer. viii, 197 (1999).
[3] V. Holy, U. Pietsch, and T. Baumbach, *High-resolution X-ray scattering from thin films and multilayers*. Springer tracts in modern physics ; 149. Berlin ; New York: Springer. xi, 256 (1999).
[4] I.V. Kozhevnikov, *Journal of X-ray Science and Technology* **8**, 253-275 (2000).

Principal Publication and Authors

L. Peverini (a), T. Bigault (b), I. V. Kozhevnikov (c) and E. Ziegler (a), *submitted.*
(a) ESRF
(b) ILL
(c) Institute of Crystallography, Moscow (Russia)

X-ray Imaging in Life Sciences and Medicine

Quantitative Comparison of Two Phase-contrast Techniques for Mammography

Phase-sensitive techniques extend the possibilities of X-ray imaging by exploiting both the *phase* and attenuation information [1]. They are of particular interest for medical applications as they enable objects composed of low Z materials to be explored with improved contrast and reduced dose compared to standard absorption radiography. Two X-ray phase-contrast imaging techniques were investigated at **ID19**, for a future application to mammography: the "propagation-based" (PB) and the "analyser-based" (AB) phase-contrast techniques. The first simply uses the propagation (Fresnel diffraction) of the partially coherent X-ray beam over large distances. The latter uses an analyser crystal, which is down stream of the sample and which acts as an angular filter for X-rays refracted by the sample.

In first approximation, the PB technique is sensitive to the two-dimensional Laplacian of the phase in a plane perpendicular to the incident beam whereas the AB technique is sensitive to the one dimensional gradient of the phase parallel to the plane of diffraction. Therefore, the PB technique produces contrast for objects with density or thickness variations, which are not linear such as micro-calcifications or fibrous structures. The AB technique is better adapted to rendering the low spatial frequencies in the object such as tumour mass lesions, but only in one direction.

Extraction of quantitative information was performed on both analyser- and propagation-based images. A local and statistical method has been proposed to disentangle the absorption, scattering and refraction information from AB images [2] and, for the first time with this approach, a quantitative phase map could be retrieved from the refraction component. The holographic phase retrieval method based on the distance variation was applied on PB images.

Figure 146 shows the astonishing contrast that can be observed on a phase map of a biopsy containing human breast tissues, as compared to the image obtained in simple absorption radiography.

The determination of the phase for different orientations of the sample serves as input for three-dimensional imaging to reconstruct variations of the mass density $\Delta\rho$ inside the object. Indeed, up to a proportionality factor the phase maps are identical to projections of $\Delta\rho$. **Figure 147** shows a computed tomography (CT) slice of the 13 mm diameter biopsy sample reconstructed from 1200 projections in absorption mode (a), mapping the linear attenuation coefficient in the tissues, in propagation based mode (b) and in analyser based mode (c), mapping the changes in mass density of the tissues.

Although the density map obtained with the AB technique (c) is much more noisy than that obtained with the PB technique (b), they both show a net improvement of contrast, revealing details such as the presence of collagen, that are not perceptible in the absorption CT (a).

Density CT provides clear information, and the tomography slices are qualitatively similar to a very large number of histological sections, at the same spatial resolution. This could represent an advantage for the characterisation of biopsies, enabling the bulk of the sample to be rapidly examined and avoiding the constraints and artefacts related to the sample preparation for histology. The comparison of the two

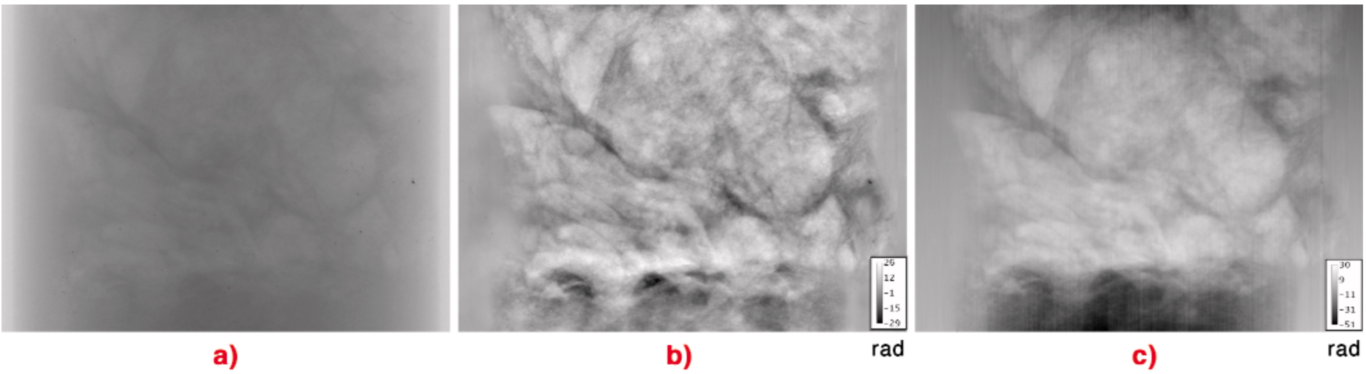

Fig. 146: Images of a 13 mm diameter biopsy sample containing human breast tissue, (a) Absorption image recorded at 0.03 m (sample-to-detector distance). (b) Phase map retrieved from 4 propagation-based images recorded at 0.03 m, 1 m, 4.3 m and 8.8 m. (c) Phase map retrieved from five analyser-based images, two acquired at the tails at ± FWHM, two acquired at the flanks at ± 1/2 FWHM and one acquired at the peak of the analyser crystal rocking curve. Energy: 25 keV, exposure time: 1 s, pixel size: 7.5 µm.

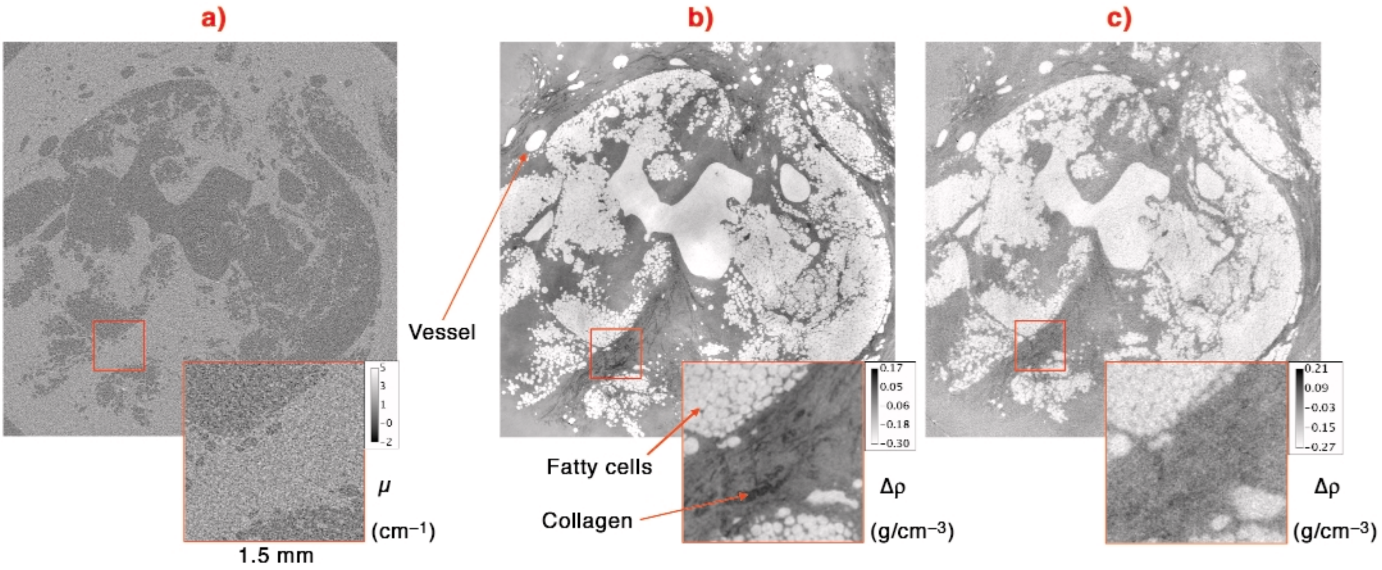

Fig. 147: Tomography slices of a 13 mm diameter biopsy sample. (a) Map of the linear attenuation coefficient in the breast tissues. (b) and (c) Maps of the variations of the mass density in the breast tissues, the colour-bar is inversed with respect to the absorption case. In the case of the CT (b), the set of projections (maps of the phase), was obtained after processing of propagation based images, and after processing of analyser based images, in the case of the CT (c). The magnified portion in (b) clearly reveals the collagen and fatty cells.

phase sensitive techniques provides furthermore valuable information for future application in mammography [3].

References

[1] R. Fitzgerarld, *Physics Today*, **53**, 7 (2000).

[2] E. Pagot, P. Cloetens, S. Fiedler, A. Bravin, P. Coan, J. Baruchel, J. Härtwig and W. Thomlinson, *Appl. Phys. Lett.* **82,** 20 (2003).

[3] E. Pagot, S. Fiedler, P. Cloetens, A. Bravin, P. Coan, J. Baruchel, K. Fezzaa and J. Härtwig, *Phys. Med and Biol.***,** (2005), *in press*.

Authors

E. Pagot (a), P. Cloetens (a), S. Fiedler (a), A. Bravin (a), P. Coan (a), K. Fezzaa (b), J. Baruchel (a), J. Keyriläyinen (c).
(a) ESRF
(b) APS
(c) Helsinki University Central Hospital, HUCH (Finland)

Human Breast Tissue Characterisation with Small-angle X-ray Scattering

Each tissue in the breast has its own small-angle scattering (SAXS) pattern, which is directly related to the molecular structure. In particular, SAXS is an excellent tool for studying the supramolecular arrangement of the collagen fibrils. Collagen is the main component of the connective tissue. It is present in the tumoural masses of the breast. Formation of collagen (fibrosis) accompanies the development of breast tumours, either benign or malignant. The supramolecular arrangement of collagen fibrils degrades upon cancer invasion, and it can be revealed by SAXS [1]. Scattering characterisation of the tissues and their pathologies is therefore possible [2].

The scattering experiments were carried out at **ID02**, the High-brilliance Beamline. The 1 mm thick samples were formalin fixed and sealed between thin foils. Mesh scans were performed across the samples, and scattering patterns were acquired point-by-point. A monochromatic (12 keV) pencil-beam of 0.2 x 0.2 mm and a 2D detector system were used: a fluoresce screen optically coupled to a FReLoN CCD, situated at 10 and 3 metres from the sample. The scattering patterns were angularly integrated to yield one-dimensional intensity curves. After the experiment, the samples were prepared for histological examination.

For every sample, the grid of measurement points was oriented and overlaid on the histology image. Adipose tissue (fat) showed low intensity, featureless scattering pattern (see **Figure 148**). Scattering from invaded fat had higher intensity and some features corresponding to the

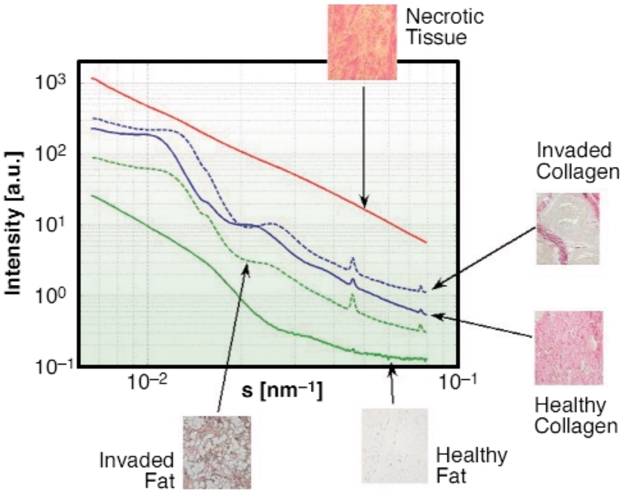

Fig. 148: Scattering patterns and histology of different breast tissues.

presence of newly formed collagen, as observed from the histology. The healthy collagen presented the characteristic collagen peaks (related to the axial period of the fibrils) and the structure and shape peaks, which correspond to the packing and diameter of the fibrils, respectively. The SAXS pattern from the invaded collagen, where cancer cells spread along the fibrils, had higher intensity between the peaks, and the fibrils had diameters and packing distances similar to those in the invaded fat, *i.e.* the fibrils were smaller in diameter and closer to each other. Furthermore, the collagen peaks were shifted to smaller angles, meaning that the axial period was longer. Finally, from the necrotic areas (*i.e.* dead tissues) scattering had a very high intensity, compared to that from other tissues, and it is rather featureless.

The differences of the scattering pattern from collagen fibrils indicate that they degrade due to cancer invasion. In invaded tissues, the fibrils appear to have smaller diameter, and they pack closer, together with the lengthening of the axial period, caused by a relaxation and reordering of the intermolecular bonds. The general intensity increase is regarded as the effect of a higher superficial area of the fibrils, compatible with a "peel-off" of the fibril's molecules due to the degradation.

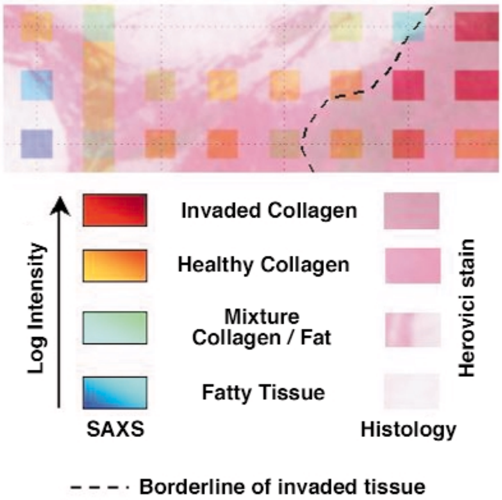

Fig. 149: Ductal Carcinoma. Correlation of the scattered intensity map and the histology.

Using the scattering signal, maps of the structural parameters of collagen can be built and then compared with the histology. Some parameters of the scattering that indicate structural changes of the tissues and the collagen were selected, and a coloured dot was assigned to every measurement point. The intensity between the peaks and the axial period of the collagen fibrils were used to plot colour maps, which give the variation of the structural parameters. **Figure 149** shows the superposition of the histology of one of the samples (a ductal carcinoma) and a map of the scattered intensity. The histology was stained in such way that collagen appear pink, fat white and cancer cells brownish. The intensity colour code was selected to be red for the higher intensity and blue for the lower. It is very clear from the Figure 149 that the scattering intensity correlates one-to-one with the histology. For instance the blue dots (low scattering intensity) correspond to the fatty tissue (white in the histology). The median intensity dots correspond to the areas of healthy collagen, whereas the dots of higher intensity are found to be in those areas that are invaded by cancer cells.

The scattering signal not only carries information about the composition of the sample, but also about the pathology of the tissues. In other words, it can help to determine whether cancer cells have invaded the tissue. Therefore, this method has the potential of being developed as a diagnostic tool.

References

[1] M. Fernández, J. Keyriläinen, R. Serimaa, M. Torkkeli, M-L. Karjalainen-Lindsberg, M. Tenhunen, W. Thomlinson, V. Urban and P. Suortti. *Phys. Med. Biol.*, **47**, 577-592 (2002).

[2] M. Fernández, J. Keyriläinen, M.-L. Karjalainen-Lindsberg, M. Leidenius, K. von Smitten, S. Fiedler and P. Suortti. *Spectroscopy*, **18**, 167-176 (2004).

Principal Publication and Authors

M. Fernández (a,b), J. Keyriläinen (b,c), M-L Karjalainen-Lindsberg (c), M. Leidenius(c), K. von Smitten (c), T. Weiss (a), S. Fiedler (d), A. Bravin (a) and P. Suortti (a,b).
(a) ESRF
(b) University of Helsinki (Finland)
(c) Helsinki University Central Hospital (Finland)
(d) EMBL-Hamburg (Germany)

Synchrotron Photoactivation of Platinum Against Brain Tumours

Despite significant advances in cancer therapy, treatment of high-grade gliomas is still palliative. To date, the median survival for patients with glioblastoma is less than one year. Brain tumour treatment generally includes surgery, radiotherapy and chemotherapy. Although radiotherapy enhances tumour local control, the radiosensitivity of the healthy tissues does not permit the use of a sufficiently high X-ray dose to treat such radioresistant tumours. Furthermore, adjuvant chemotherapy has predominantly failed to improve patient survival mainly because of the difficulty for these drugs to penetrate through the blood-brain barrier.

Among recent therapeutic techniques, photoactivation therapy (PAT) consists in selectively introducing a high-Z atom into the DNA of tumour cell and irradiating with

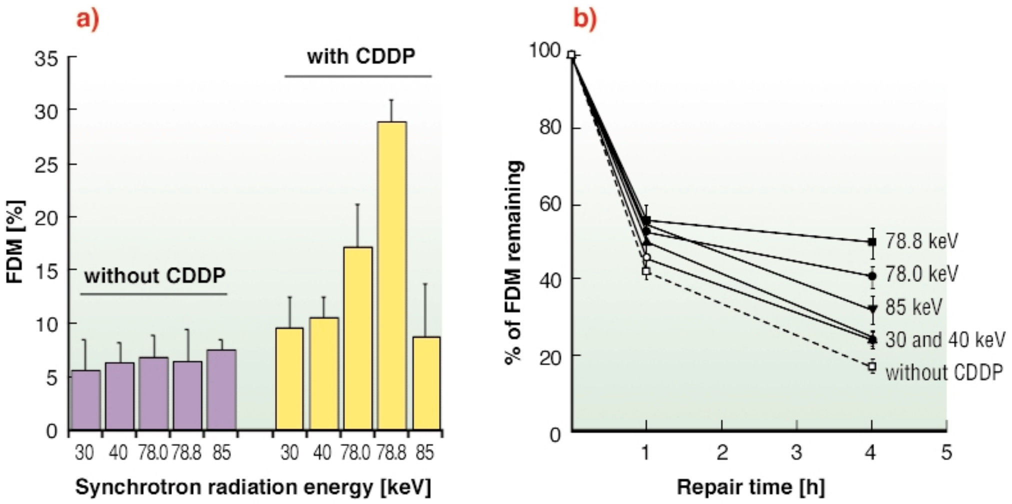

Fig. 150: (a) Yields of DSB induced (expressed in fraction of DNA fragments migrating out of the gel (FDM)) after treatment of F98 cells irradiated (30 Gy) at different energies in presence of cisplatin. (b) DSB repair data as a function of post-irradiation time.

X-rays of suitable energy for an enhanced photoelectric effect on this atom. Thus, the local toxicity is increased. A monochromatic radiation beam would potentially optimise this physical effect. Therefore, synchrotron radiation appears to be the optimal tool for irradiation: its high fluence (10^5 times brighter than conventional X-ray sources) allows the beam to be tuned to a convenient wavelength while keeping a sufficient flux to allow radiotherapy applications. PAT experiments have been recently performed at beamline **ID17**. These experiments on F98 rat glioma demonstrated that synchrotron irradiation of a widely-used chemotherapy drug called cisplatin at the platinum absorption K-edge results in an increased toxicity most likely due to an enhanced photoelectric effect on the platinum atoms [1].

In vitro experiments were performed on F98 cells treated with cisplatin and irradiated at 30, 40, 78, 78.8 or 85 keV. The induction of DNA double strand breaks (DSB) and their subsequent repair were studied in function of the energy of the beam (**Figure 150**). Cells without cisplatin lead to the same DSB rate whatever the radiation energy tested (Figure 150a). However, when combined with cisplatin, cells irradiated at 78.8 keV (just above the platinum K-edge) showed two and three times more DSB than at 30, 40, 85 and 78 keV, respectively. Furthermore, 4 hours after treatment, the DSB rate was found to be higher at 78.8 keV (Figure 150b). Therefore we demonstrated that cisplatin treatment of F98 cells and irradiation at 78.8 keV, results in a greater amount of more slowly repaired DNA double strand breaks. These conclusions were consistent with those obtained previously in SQ20B human cell line with the same treatment [2].

In vivo experiments were thereafter performed on rats inoculated with F98 glioma cells. On day 13 after stereotactic tumour inoculation, 3 μg of cisplatin were injected intra-cerebrally at the tumour site. Rats were irradiated on day 14, with 78.0 and 78.8 keV photons. Median Survival Time (MeST) of untreated rats was 26 days (**Figure 151**). When cisplatin or synchrotron radiation alone was applied, the MeST was found to be 37 and 48 days, respectively. When both treatments were combined, a very large increase in life span was obtained (MeST = 206.5 days) compared to the controls. One year after treatment, 6 out of the 18 rats treated with CDDP *and* radiation, were still alive. Furthermore, histological studies performed on these surviving rats did not show any trace of residual tumour suggesting its irreversible regression. This outstanding life span increase (694 %) is the largest obtained to date with the F98 glioma model. Previously, Barth *et al.* reported an relative increase in life span of 188% using Boron Neutron Capture Therapy [3].

To conclude, our data demonstrated the efficiency of an innovative anticancer treatment involving both cisplatin and synchrotron radiation. *In vivo* experiments showed that the combination of cisplatin with synchrotron radiation resulted in the longest reported survival for this radioresistant glioma model. Furthermore, our most recent experiments demonstrate that a synchrotron radiation source is more efficient than a conventional X-ray source used at a hospital for treatment involving cisplatin. This innovative therapeutic method opens new perspectives for brain tumour treatment.

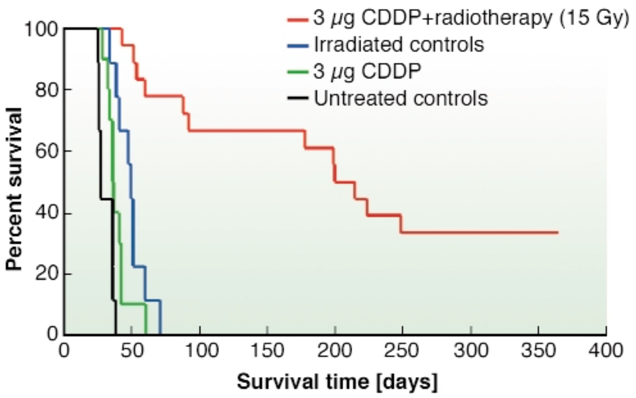

Fig. 151: Kaplan-Meier survival curves of rats bearing F98 glioma and subjected to the indicated treatments.

References

[1] M. C. Biston, A. Joubert, J. F. Adam, H. Elleaume, S. Bohic, A. M. Charvet, F. Estève, N. Foray, J. Balosso, *Cancer Res*, **64**, 2317-2323 (2004).

[2] S. Corde, J. Balosso, H. Elleaume, M. Renier, A. Joubert, M. C. Biston, J. F. Adam, A. M. Charvet, T. Brochard, J.F. Le-Bas, F. Estève, N. Foray, *Cancer Res*, **63**, 3221-3227 (2003).

[3] R.F. Barth, W.Yang, J.H. Rotaru, M.L. Moeschberger, C.P. Boesel, A.H. Soloway, D.D. Joel, M.M. Nawrocky, K. Ono, J.H. Goodman, *Int J Radiat Oncol Biol Phys*, **47**, 209-218 (2000).

Author

M.C. Biston on behalf of the INSERM U647 RSRM and ID17 Team Members.

INSERM-RSRM CHU/ESRF, Grenoble (France)

Advances in Instrumentation

Calibration of a Hard X-ray Telescope

Focusing optics for the hard X-ray band above 10 keV are now poised to open a new window on the high-energy universe. Hard X-ray observations will provide a vehicle for discovering collapsed stars and black holes on all scales, for testing theories of where the elements are born, and for exploring the most extreme environments in the universe. We have developed thermally-formed glass substrates, depth graded W/Si multi-layer coatings for enhanced hard X-ray reflectivity and a unique mounting technique to build high performance, lightweight telescopes with the large effective area necessary to bring high-energy astrophysics into this new era. The large collecting area is achieved by tightly nesting shells of grazing-incidence mirrors in a conical approximation to a Wolter I geometry. Each shell is made of five quintant segments thermally formed into the appropriate conical shape. The raw glass material is flat panel display glass of thickness 0.3 mm (Schott glass D263 and AF45). Each glass segment is coated with optimised depth graded W/Si multilayer coatings capable of reflecting in the energy band up to the W-K absorption edge of 69.5 keV [1]. The novel mounting technique involves constraining the mirrors to successive layers of precisely machined graphite spacers [2]. Our approach is being demonstrated through the High Energy Focusing Telescope (HEFT) balloon program which is a collaboration between California Institute of Technology, Columbia University, Lawrence Livermore National Laboratory and the Danish Space Research Institute (DSRI). We have completed three telescope modules. Each of these contains 72 nested shells totalling several thousand individual mirror segments.

The hard X-ray calibration of the first flight telescope was performed at beamline **BM05**. We used a double bounce Si(111) monochromator with higher order suppression capable of operating in the energy range up to 70 keV. The beam was collimated to 1 arcsec. The optic was mounted in a ring, which allowed precise rotation around the optical axis. This in combination with a simultaneous translation of the optic and the detector allowed the illumination of the entire telescope aperture and thus generating a composite image. A CCD was used as the imaging detector. **Figure 152** shows a photograph of the optic as it sits in the rotation mechanism.

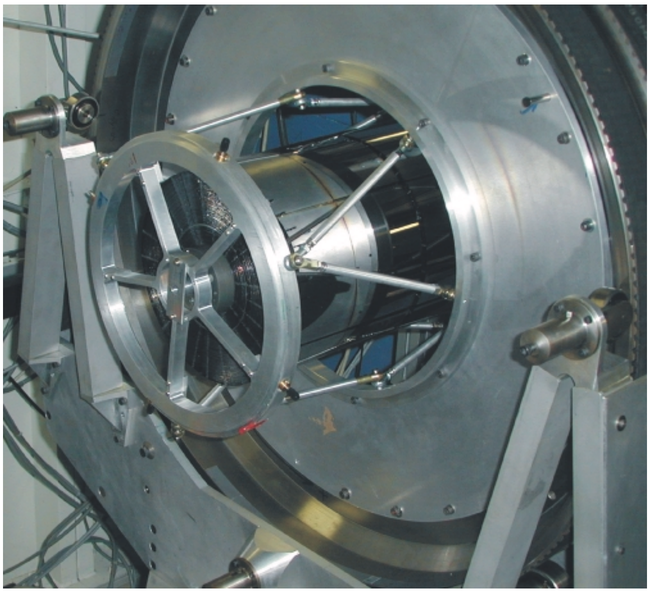

Fig. 152: The hard X-ray telescope in the rotation mechanism.

The purpose of the measurements was to measure the imaging performance specifically the Half Power Diameter (HPD) which is the angular range within which half of the photons are focused for an on-axis source and the absolute throughput versus energy. Imaging measurements was performed at four selected hard X-ray energies, 18, 40, 50 and 68 keV and we measured the absolute throughput of selected shells at their specific on-axis graze angle versus energy from 8 to 70 keV. We found that the imaging performance varied slightly with energy with an average HPD of 1.3 arcmin. This variation was, however, not due to any additional scatter at high energies but rather resulted from the different weighting of the imaging performance from the mirror shells. The high energy throughput is mainly facilitated by the small radius mirrors and lower energy throughput facilitated from outer radius shells and the slight variation of the imaging performance with energy was completely explained by the difference in mirror shell figure versus radius. **Figure 153** shows the

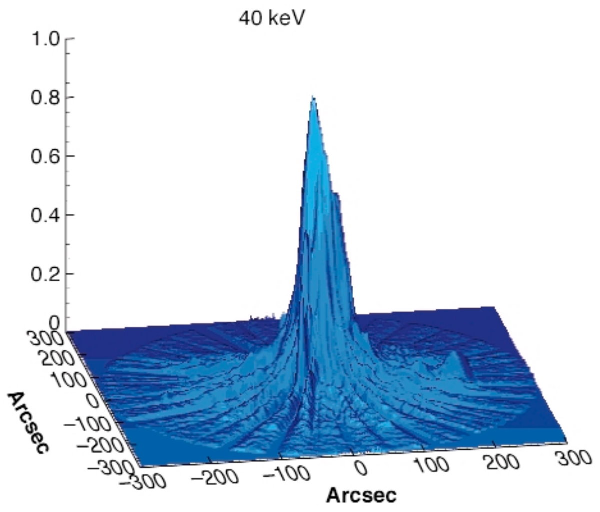

Fig. 153: On-axis image measured at 40 keV. The HPD is 1.3 arcmin.

composite image at 40 keV. The measurements of the absolute throughput from selected shells quantitatively verified our model for the multilayer reflectivity and obscuration effects in the entire energy range from 8 to 70 keV. **Figure 154** shows reflectivity data versus energy for selected shells in the telescope along with model calculations including known obscuration effects and theoretical reflectivities.

References

[1] C.P. Jensen, C.M.H. Chen, F.E. Christensen, K.K. Madsen, E. Ziegler; *SPIE*, **4851**, 724-733 (2002).
[2] J.E. Koglin, F.E. Christensen, J. Chonko, W.W. Craig, T.R. Decker, F.A. Harrison, C.P. Jensen, M. Sileo, D.L. Windt, H. Yu; *SPIE*, **4851**, 607-618 (2002).

Principal Publication and Authors

J.E. Koglin (b), C.M.H. Chen (c), J. Chonko (b), F.E. Christensen (a), W.W. Craig (d), T.R. Decker (d), K.S. Gunderson (d), C.J. Hailey (b), F.A. Harrison (c), C.P. Jensen (a), K.K. Madsen (a), M. Stern (b), D.L. Windt (b), H. Yu (b), E. Ziegler (e); *SPIE*, **5168**, 100-111 (2003).
(a) Danish Space Research Institute (Denmark)
(b) Columbia University, New York (USA)
(c) California Institute of Technology (USA)
(d) Lawrence Livermore National Laboratory (USA)
(e) ESRF

Refocussing of a Submicrometre Beam from an X-ray Waveguide

Among the various X-ray optics for synchrotron radiation producing micrometre and sub-micrometre beams with high intensity, the X-ray waveguide (WG) provides the smallest hard X-ray beam (few tens of nanometres) with a gain of up to 100 [1].

Resonances take place at given angles in planar WGs constituted by a three layer structure where the middle guiding layer, has the highest refractive index. The X-ray beam which is produced at the WG end has a spatial distribution with Full Width at Half Maximum (FWHM) equal to one half the guiding layer thickness d, and an angular distribution with FWHM ϕ simply given by: $\phi \approx \lambda/d$, where λ is the X-ray wavelength. Two important features characterise the WG with respect to other optical elements: i) the beam dimension is independent on the X-ray source, but only depends on the thickness of the

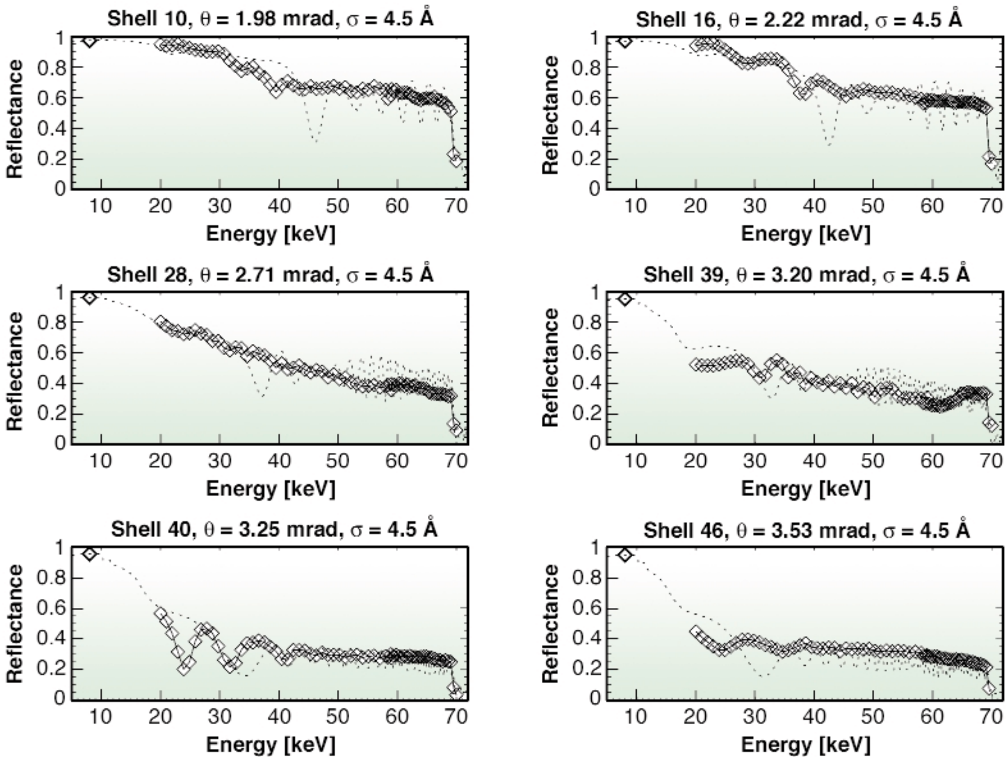

Fig. 154: Measured reflectivity versus energy from selected shells. The dotted line is the theoretical reflectivity. The measured data show a smoother variation as expected from mirrors with figure error on order 1 arcmin. In all cases an interfacial roughness of 4.5 Å in the multilayer stack is consistent with the data.

guiding layer; ii) the beam produced by the WG is essentially coherent because it is the result of an interference effect. A drawback of this optics is that, due to the divergence at the exit, a nanometre-sized spot on sample can only be obtained at a very short distance from the WG exit. Another limitation is that in planar WGs the beam is compressed only in one direction. A WG compressing the beam in two directions has been fabricated and tested [2], but its efficiency is quite low. If, however, the guided beam could be efficiently re-focussed at some distance from the WG end, both drawbacks could be overcome. In this way, the large working distance between the device and the sub-micrometre focus would leave free space for the sample environment (vacuum chamber, furnace, cryostat, magnets, high-pressure device, etc). Also, an improved signal/noise ratio could be achieved. Moreover, the beam from a planar WG could be focussed at the exit of a second WG perpendicular to the first one, thus realising a cross-coupled geometry for efficient compression in two directions. We have demonstrated the feasibility of such an approach with an experiment carried out at **BM05**.

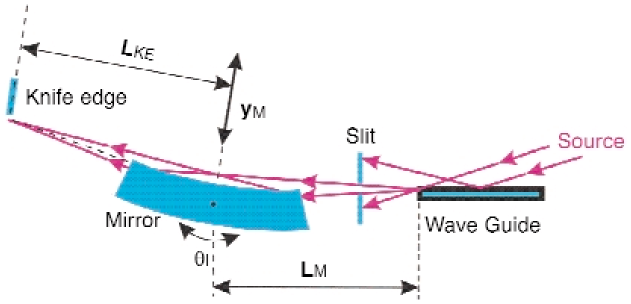

Fig. 155: Schematic view of the experimental setup.

Figure 155 shows a schematic view of the experimental arrangement. A planar WG constituted by a three-layer stack: C (20 nm) / Cr (130 nm) / C (3 nm), was adjusted in its first resonance mode TE0 under illumination by a monochromatic beam ($\lambda \approx 0.1$ nm). Suitable slits allowed passage of the guided beam but cut the direct and the reflected beams. A 170 mm long Pt-coated Si mirror, located at a distance LM = 450 mm from the WG exit, was adjusted in order to refocus the guided beam at a distance $L_{KE} = L_M$ (see Figure 155). An elliptical shape was given to the mirror with a dynamical bender, developed by the ESRF optics group. The deviation from the stigmatic ellipse in term of slope errors, measured with a Long Trace Profiler (LTP), was of the order of 2 μrad RMS. Knife-edge scans were performed optimising the mirror-knife edge distance L_{KE} for different incidence angles θ_I and mirror positions Y_M transversal to the incident beam direction.

Figure 156 shows five beam profiles obtained at different L_{KE} values (closed points) for the θ_I and Y_M couple which gave the minimum spot size. The best scan in Figure 156 has a FWHM of 0.85 μm. Ray-tracing simulation (solid line in Figure 156) of the experiment was carried out. A good agreement with experiment has been obtained assuming a perfect alignment but a small slope error of 2 μrad. (*i.e.* the value found by LTP). Note the double peak present in both the theoretical and experimental curves for smaller distances L_{KE}. No good agreement could be obtained considering only mirror misalignment without slope error. Better results are expected with improved experimental conditions.

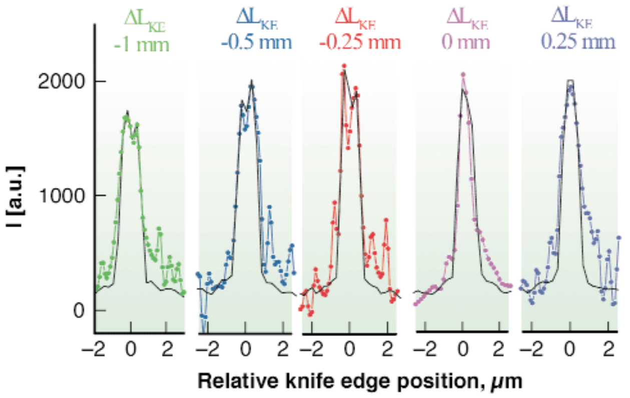

Fig. 156: Beam intensity profiles. Closed points: experimental result. Solid line: ray-tracing simulation. ΔL_{KE} is the variation with respect to the focal distance L_F.

The experiment shows the possibility of submicrometre beam refocussing at large distance from the end of the optical device (about 365 mm in this case). This could not have been realised on a standard length beamline with other optical elements based on source demagnification, such as mirrors. The arrangement proposed has the potential to allow experiments with nanometre spatial resolution even with bulky equipment and with improved signal/noise ratio. The combination of two WGs' in cross-coupled geometry for efficient beam compression in two directions is also foreseen.

References

[1] W. Jark, A. Cedola, S. Di Fonzo, M. Fiordelisi and S. Lagomarsino, N.V. Kovalenko and V.A. Chernov, *Appl. Phys. Lett.* **78**, 1192-1194 (2001).
[2] F. Pfeiffer, C. David, M. Burghammer, C. Riekel, T. Salditt, *Science* **297**, 230-234 (2002).

Principal Publication and Authors

S. Lagomarsino (a), I. Bukreeva (a), V. Mocella (b), A. Surpi (a), T. Bigault (c) and A. Cedola (a), *Nuclear Instruments and Methods* A, *submitted*.
(a) Istituto di Fotonica e Nanotecnologie (IFN) - CNR - Roma (Italy)
(b) Istituto per la Microelettronica e Microsistemi (IMM) – CNR - Sezione di Napoli (Italy)
(c) ESRF

ESRF

Highlights 2004

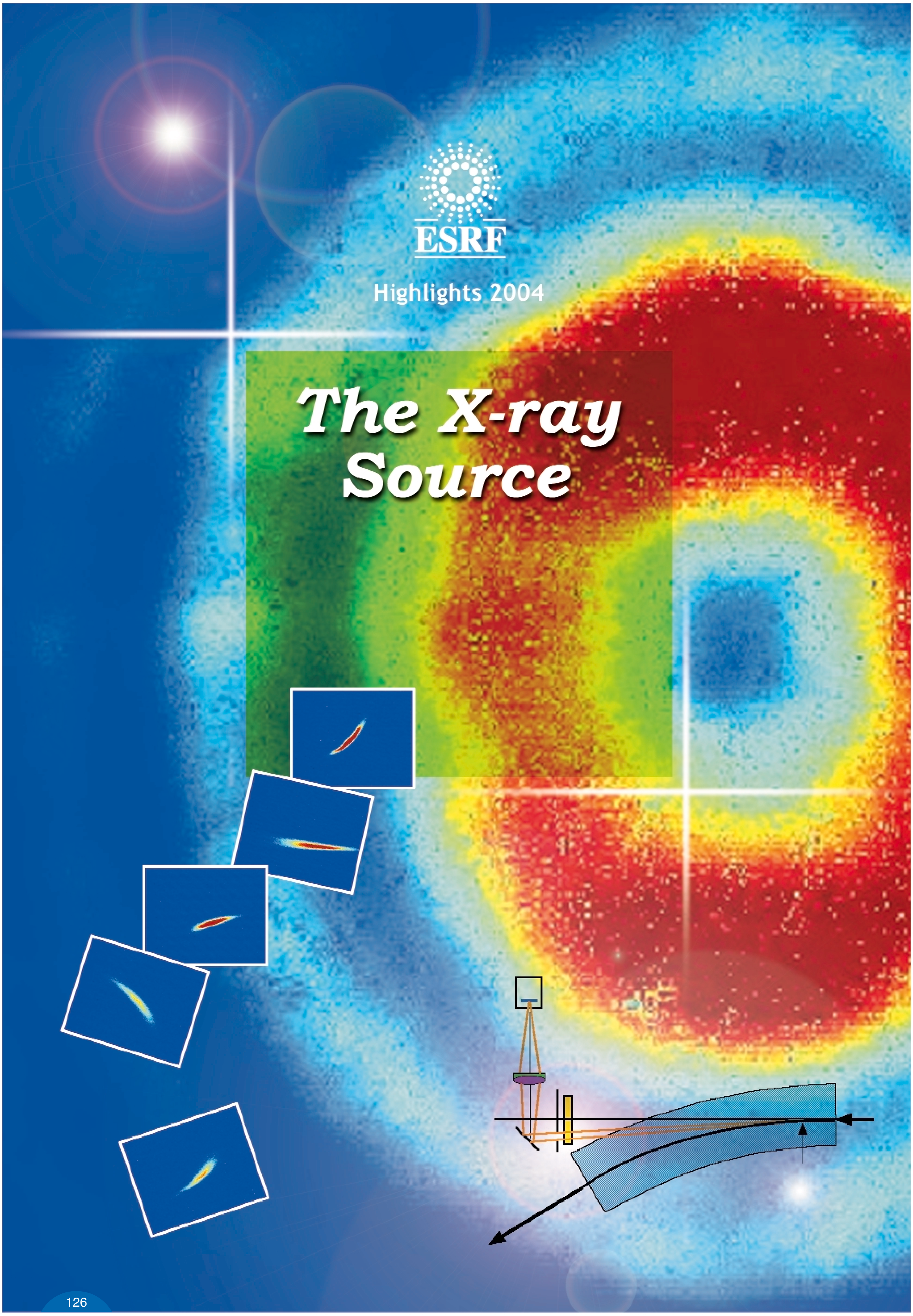

The X-ray Source

Introduction

Throughout 2004, the Machine Division continued its efforts to improve performance whilst carrying out a number of developments, which are described hereunder.

Machine Parameters

Table 2 presents a summary of the characteristics of the storage ring's electron beam:

Energy	[GeV]	6.03
Maximum Current	[mA]	200
Horizontal emittance	[nm]	4
Vertical emittance (*minimum achieved)	[nm]	0.03
Revolution frequency	[kHz]	355
Number of bunches		1 to 992
Time between bunches	[ns]	2816 to 2.82

Table 2: Main global parameters of the electron beam.

Table 3 gives the main optics functions, electron beam sizes and divergences at the various source points. For insertion device source points, the beta functions, dispersion, sizes and divergences are computed in the middle of the straight section. Two representative source points of bending magnet radiation have been selected, corresponding to an observation angle of 3 mrad (9 mrad) from the exit, which corresponds to a different magnetic field. Electron beam profiles are Gaussian and the size and divergence are presented in terms of rms quantities. The associated full width half maximum sizes and divergences are 2.35 times larger. Horizontal electron beam sizes and divergences are given for the uniform filling modes and apply to almost all filling patterns except for the single bunch, for which a slightly larger size and divergence is attained due to the increased energy spread of the electron beam. Vertical electron beam sizes and divergences apply to the Uniform, 2 x 1/3 and Hybrid filling modes only. To increase the lifetime of the stored beam, the vertical beam sizes and divergences are increased typically by 50% in the 16 and 4 bunch filling patterns.

The lifetime, bunch length and energy spread depend, to a large extent, on the filling pattern. These are given in **Table 4** for a few representative patterns. Note that in both the 16 bunch and 4 bunch filling patterns, the energy spread and bunch length decay with the current (the value indicated in the table corresponds to the maximum current). The bunch lengths are given for the usual RF accelerating voltage of 8 MV.

		Even ID Section (ID2,ID6…)	**Odd ID Section (ID1,ID3 …)**	**Bending Magnet 3 mrad**	**Bending Magnet 9 mrad**
Field	[T]	Depends on ID	Depends on ID	0.4	0.85
Horiz. Beta Functions	[m]	35.2	0.5	1.41	0.99
Horiz. Dispersion	[m]	0.137	0.037	0.061	0.045
Horiz. rms e- beam size	[µm]	402	59	100	77
Horiz rms e- divergence	[µrad]	10.7	90	116	111
Vert. Beta Functions	[m]	2.52	2.73	34.9	34.9
Vert. rms e- beam size	[µm]	7.9	8.3	29.5	29.5
Vert. rms e- divergence	[µrad]	3.2	3	0.85	0.85

Table 3: Beta functions, dispersion, rms beam sizes and divergences for the various source points of the ESRF.

Filling pattern		Uniform	Hybrid	16-b	4-b
Number of bunches		992	24x8+1	16	4
Maximum current	[mA]	200	200	90	40
Lifetime	[h]	80	30	11	6
Rms energy spread	[%]	0.11	0.11	0.12	0.16
Rms bunch length	[ps]	20	25	48	55

Table 4: Current, lifetime, bunch length and energy spread in various representative filling modes.

RUN NUMBER	TOTAL 2003	2004-01	2004-02	2004-03	2004-04	2004-05	TOTAL 2004
Start		23/01/04	26/03/04	04/06/04	27/08/04	22/10/04	
End		17/03/04	25/05/04	04/08/04	13/10/04	20/12/04	
Total number of shifts	**837**	162	180	183	141	177	**843**
Number of USM shifts	**680**	129	145.125	150	110.1	146.7	**681**
Beam available for users (h)	**5275**	1009.9	1111.4	1168.9	856.4	1148.6	**5275.2**
Availability	**97.95%**	**98.2%**	**96.7%**	**98%**	**98.1%**	**98.8%**	**97.95%**
Dead time for failures	**2.05%**	1.8%	3.3%	2.0%	1.9%	1.2%	**2.05%**
Dead time for refills	**1%**	0.3%	0.9%	0.6%	0.9%	0.9%	**0.75%**
Average intensity (mA)	**135**	183	135	150	138	147	**150.6**
Number of failures	**138**	21	33	25	15	17	**111**
Mean time between failures (h)	**39.4**	49.1	35.2	48	58.7	69	**49.1**
Mean duration of a failure (h)	**0.8**	0.9	1.2	1	1.1	0.8	**1.01**

Table 5: number of shifts, failures, average current, MTBF and availability along the year 2004.

Summary of Machine Operation

In 2004, 681 shifts (5448 hours) of beam were scheduled, out of which 5295 hours of beam were effectively delivered (including 41 hours of refills). This represents a beam availability of 97.95 %. Dead time due to failures accounts for the remaining 2.05 %. It should be recalled that since February 2003, and throughout 2004, the current in the ring has been topped-up with “Front Ends open” in all filling modes. As a result, the refill time is considered as ‘working USM time’ and is included in the availability figures of the accelerator. The availability figure for 2004 is well in line with that of 2003, itself already a record. All runs but one were especially good with more than 98% availability! Run 2 was spoilt by several storms and electrical drops coming from the electricity supplier, which were not compensated for because the High Quality Power Supply (HQPS) was out of service at that time.

The mean time between failures reached the satisfactory score of 49.1 hours, which is well above the 2003 score. As in 2003, all failures occurring during a refill are taken into account. This was not the case in 2002 and provides an explanation for the ‘artificial’ drop of the MTBF between 2002 (58 hours) and 2004. See Table 4 for detailed statistics.

Of great importance for the beamlines, many long periods of delivery took place without a single failure. There were 22 periods greater than 3 days of uninterrupted beam The absolute record of beam delivery without a single failure occurred during run 2004-05 when the beam was delivered for 12 days with no interruption (**Figure 157**).

In view of the aging of some components, and in spite of intensive preventive maintenance, it appears difficult to further improve the availability beyond the present figure and our goal is to maintain it at this level.

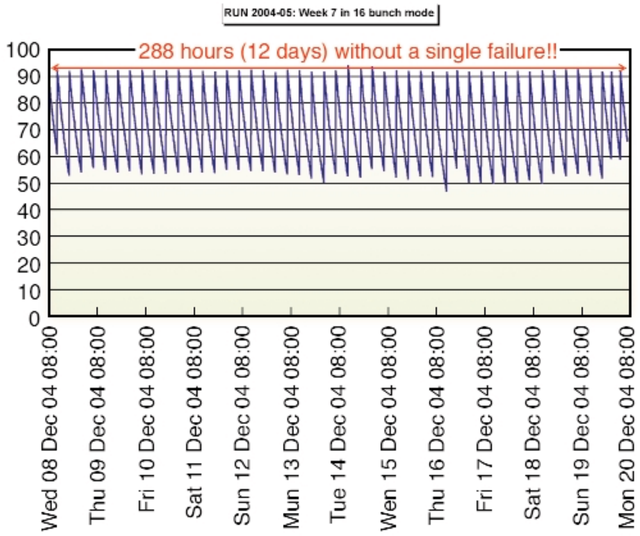

Fig. 157: current decay over 12 consecutive days of 16 bunch filling mode.

Filling Patterns

The multibunch filling pattern, which represents 67% of the total user time, is mostly delivered in uniform mode with a lifetime of ~80 hours at 200 mA. Despite a slightly lower lifetime, the 2*1/3 fill is also used for experiments needing a non-uniform time structure. The remaining 33% is shared between the 16 bunch, the 4 bunch and the hybrid filling patterns (**Figure 158** and **Figure 159**).

In 2004, the 4-bunch mode (4*10 mA) replaced the single bunch mode (15 mA). This new mode was proposed following the difficulties experienced in 2002-2003 with the latter. Whereas it has been possible in the past to deliver an intensity of 20 mA, this is no longer possible, a situation linked to the increasing number of low gap chambers installed in the ID straight sections. The maximum current is now limited by horizontal beam instabilities and incoherent tune shift, which saturate the injection process. With four equidistant bunches of 10 mA each, the beam parameters are now more stable

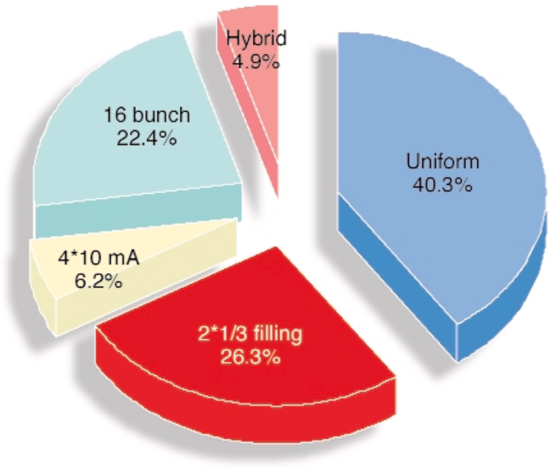

Fig. 158: Distribution of the 2004 user time in the various filling modes.

during the decay. Such a time structure also allows a higher average current than the single bunch and is therefore more attractive for all users.

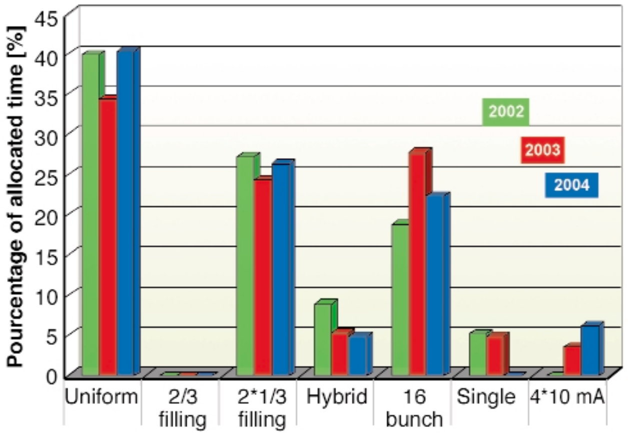

Fig. 159: Evolution of filling patterns over the last 3 years.

The hybrid mode was delivered with a new filling pattern developed in 2003. It consists of 24 groups of 8 bunches of current close to 1 mA and a single bunch of 4 mA corresponding to a total current of 200 mA (see **Figure 160**). A purity higher than 10^9 between the filled and the unfilled bucket has been routinely achieved.

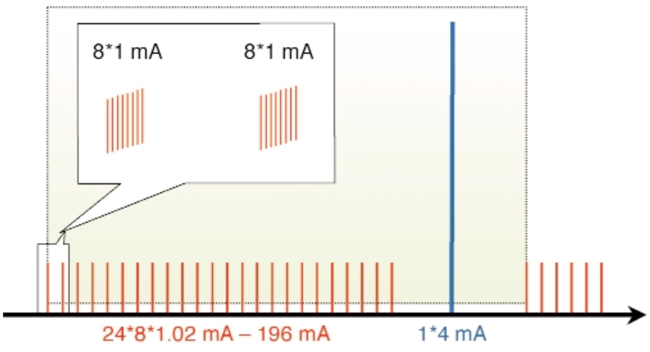

Fig. 160: Hybrid mode filling patterns.

Insertion Devices and Beamline Front Ends

Insertion devices, as well as beamline front-ends, are continuously being modified to satisfy the evolution and refurbishment needs of the beamlines. In 2004, the first prototype revolver undulator was installed on ID18 and successfully commissioned, and a second one has been installed on ID10. Such a revolver structure allows the beamline users to switch from one undulator period to another in matter of seconds. A number of conventional undulator segments were refurbished to make full use of the new 10 mm high aluminium vessels which are gradually replacing the stainless steel 15 mm and 10 mm chambers. The beamline front-ends are being refurbished at a rate of 4 beamlines per year, making use of every shutdown. The “high power” design allows the operation of a 5 m long undulator at a minimum gap of 11 mm with a stored current of 200 mA, or alternatively a 4 m long in-vacuum undulator at a minimum gap of 6 mm.

NEG Coating Facility

Over the past few years, as the magnetic gap of the undulators was reduced from 20 to 10 mm, excessive Bremsstrahlung has been observed downstream from the beamlines. This Bremsstrahlung is created by the collision of the electron beam with the residual gas inside the ID vacuum chambers and becomes a serious problem for small aperture chambers where the small conductance results in high pressure. The Bremsstrahlung is scattered off-axis by the optical component in the beamline (monochromator, mirror,…) and can be detected in the air outside the lead hutch. Even though more shielding can be added to the beamline hutches, for a number of beamlines this is not desirable or practical.

During the early times, some freshly-installed 10 mm external chambers showed a high level of Bremsstrahlung and a very slow conditioning with time to the point that the ID chambers had to be removed and replaced with wider aperture chambers to allow safe operation of the beamline. To cope with this situation, two solutions were found: one consisting in using in-vacuum undulators with a large pumping capacity, the other in designing the ID chambers with an antechamber. However, the presence of such an antechamber restricts the space available for the magnets of the associated insertion device and therefore, given the large number of existing undulator magnet arrays, it was deemed inappropriate for the ESRF to adopt such a solution.

A third solution was explored and developed following collaboration with CERN. It consists of depositing a thin layer of a Non Evaporable Getter (NEG) material on the surface of the chamber. The NEG material is an alloy of titanium, zirconium and vanadium deposited by magnetron sputtering. The vacuum in a NEG coated chamber benefits from two effects: a reduced desorption yield as well as direct pumping by the NEG material.

From 1999 to 2003, a number of chambers made from either stainless steel or aluminium were coated at CERN and gave satisfying results. In 2003, a NEG coating facility was commissioned at the ESRF with the ability to coat 5 m long, 8 mm aperture chambers. This facility was operated throughout 2004 and 6 ID chambers made of aluminium (5 m long, 8 mm aperture) were coated. Five of these were installed on the ID6 beamline for vacuum pre-conditioning and Bremsstrahlung measurement vs. integrated dose. When qualified, the chamber is moved to its final beamline destination during the following shutdown. The low desorption of the NEG, its pumping effect as well as the memory of the conditioning made on ID6 are such that, under normal conditions, the beamline receiving such a new chamber restarts user operation immediately after the shutdown with no delays to the user program. As of January 2005, 17 ID vessels installed in the ring are NEG coated.

The initial coating thickness, which was close to 1 micron, has been reduced recently to 0.5 micron. Measurements show that the smaller thickness does not change the pumping and desorption capacity significantly but such chambers could be coated more rapidly with a lower risk of insufficient adhesion of the NEG layer to the chamber walls. Indeed, out of the 6 chambers processed in 2004, 5 perform as expected vacuum-wise while one has shown adhesion problems with NEG strips detaching from the wall. This adhesion problem, which is specific to aluminium chambers (not observed on stainless steel), is believed to be linked to an insufficient surface preparation before the coating is applied and is presently being looked into.

A short sample chamber was successfully coated in 2004 with a magnetic field generated by a permanent magnet array rather than a solenoid. The interest of this procedure is the ability to coat chambers of complex shape than cannot be embedded into a cylindrical solenoid.

Global Position Feedback

The closed orbit stabilisation of the ring is performed using a slow and a fast system. The slow system, which includes more than 200 beam position monitors, operates in both the horizontal and vertical plane and corrects the closed orbit every 30 seconds. The slow system is efficient for correcting the orbit drift during current decay. The fast orbit correction system operates in the .1Hz to 150Hz frequency range and corrects beam motion induced by quadrupole and girder vibrations. Beam vibrations at frequencies higher than 150 Hz are typically lower and therefore of less importance to the beamlines. Until 2004, the fast orbit correction was performed on the storage ring by means of a global feedback loop system which damps the vertical orbit distortion all over the storage ring, and by four local feedback systems damping the horizontal orbit distortion only in the ID8, ID14, ID21 and ID24 straight sections.

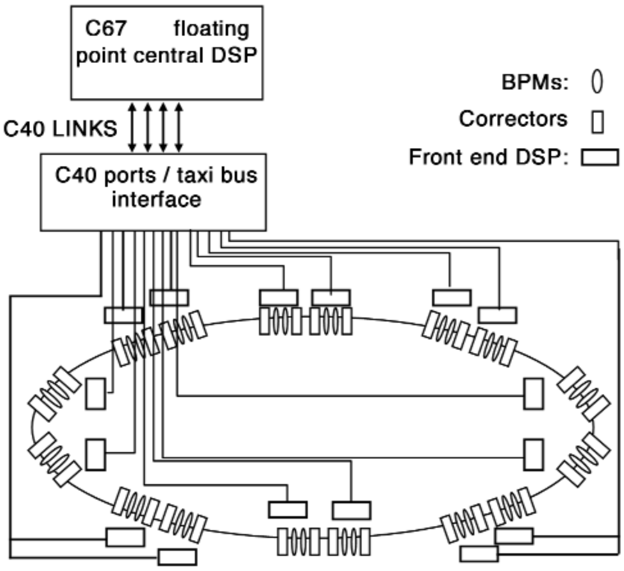

Fig. 161: layout of the upgraded global feedback system in the storage ring.

In the early days of operation, the global vertical feedback showed a significantly improved vertical stability of the beam. In 2000, damping pads were fixed to all the quadrupole girders and resulted in a significant damping and reduction of the residual beam oscillations. As a result, the improved stability induced by the vertical global feedback system became marginal. The limitation in the correction come from the noise in the beam position monitor reading and it appears that the only way of further improving the vertical beam stability consists in increasing the number of beam position monitors in the feedback loop. With respect to horizontal stability, the situation has become unsatisfactory with the impossibility to add any new beamlines without generating horizontal position instability. This is due to the imperfect closure at high frequency of the local bumps. Instabilities are generated when more than four local feedback systems are operated at the same time. As a consequence the gain, and therefore the performance, of the feedback loops had to be reduced as more local feedbacks were implemented from one (in

	ß value at the BPM location	Rms motion without feedback	Rms motion with feedback	Rms motion / rms size
Horizontal	36 m	5 to 12 µm	1.2 to 2.2 µm	0.3 to 0.6 %
Vertical	5.6 m	1.5 to 2.5 µm	.8 to 1.2 µm	7 to 10 %

Table 6: Stabilisation of the residual beam motion obtained with the newly developed global feedback measured in the frequency range 0.1 to 200 Hz. The range of rms motion shown in the table corresponds to measurements made on several beam position monitors. The steerers, the BPMs and the source of noise are not uniformly located along the ring circumference, which explains the difference or residual rms motion from one beam position monitor to the next.

1999) to four (in 2001). The obvious way to improve the stability in all beamlines is to transform the 4 local feedback loops into a single global horizontal feedback loop allowing stabilisation in all beamlines simultaneously. Such an upgraded two-plane global feedback with twice more beam position monitors as compared to the first system was put into operation in 2004. It includes 32 beam position monitors and 24 steerer magnets. The layout is shown in **Figure 161**.

The measured beam stability with and without feedback is summarised in **Table 6**. The beam position monitors used in the global feedback are located on both extremities of the Insertion Device chambers. It can be clearly seen from Table 6 that the absolute stability achieved is higher in the vertical plane than in the horizontal plane. However, the relative stability (residual motion scaled to the electron beam size) is higher in the horizontal plane.

Dipole Light Monitors in TL-1 and TL-2

The visible part of the synchrotron radiation produced in each of the bending magnets of the linac-to-booster (TL-1) and linac-to-storage ring (TL-2) transfer lines is now extracted to obtain images of the electron beam profile in the corresponding bending magnet. In contrast to the fluorescent screen monitors in use since 1991, this provides a non-destructive, high resolution and high sensitivity beam monitoring during the booster and storage ring injections. The light collection and imaging system are shown in **Figure 162** and **Figure 163** for the TL-1 and TL-2 bending magnets.

The bending magnets of TL-1 (180MeV, 0.387T) produce sufficient visible light to obtain a low-noise image for a circulating electron current as low as 200 µA. For the bending magnets of TL-2 (6GeV, 0.9T), the current limit drops to 50 µA. Compared to the screen monitors in use since 1992, the imaging is not only more sensitive to low current but it is non destructive and provides a much improved spatial resolution. Images obtained on each 5 bending magnets of TL-2 are shown in **Figure 164**.

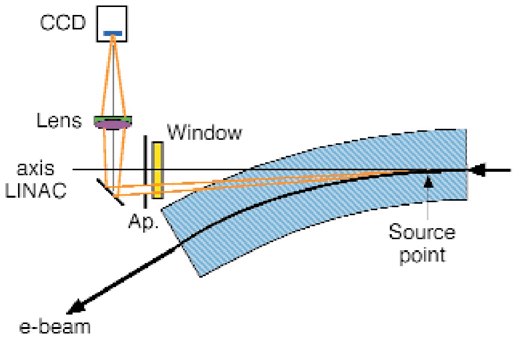

Fig. 162: Top-view of the light collection and imaging system for the TL-1 dipoles.

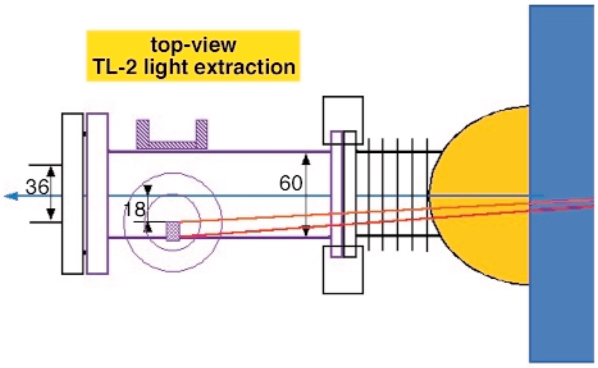

Fig. 163: Top-view of the light collection and imaging system for the TL-2 dipoles.

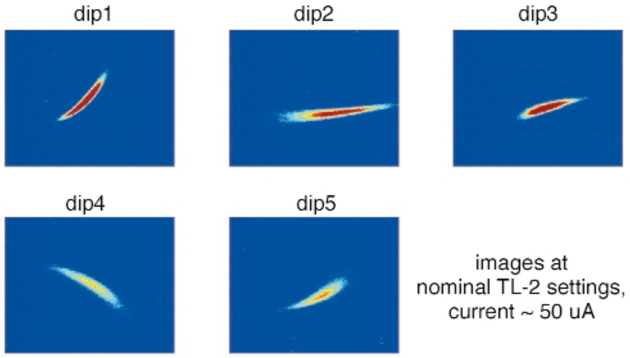

Fig. 164: Images of the electron beam recorded in each 5 bending magnets of the TL-2 transfer line during injection into the storage ring.

Infrared Beamport

An Infrared beamport was constructed in a dedicated laboratory on ID21 during 2004. It is intended to be used for infrared microscopy and makes use of the high brightness of the so-called edge radiation produced when electrons enter a bending magnet. Whereas the ESRF would compete unfavourably with lower energy facilities to collect a high flux of infrared radiation, the need of high brightness for microscopy makes the edge radiation from the ESRF quite competitive.

A delicate engineering issue in designing this beamport is the collection of infrared by a mirror exposed to very high power bending magnet radiation. The water-cooling of such a mirror is a source of mechanical noise on the mirror and therefore on the reflected light which, from experience at other infrared beamlines in the world, must be minimized. As a result, it was decided to suppress the water-cooling of the mirror. This was made possible by opening a slot in the mirror and letting the hard X-ray pass through. The much wider vertical divergence of the infrared radiation is collected on both sides above and below the slot. This is illustrated in **Figure 165**. To allow for a slow drift of the closed orbit of the electron beam in the bending magnet and avoid overheating of the mirror, the vertical position of the mirror is remotely controlled and permanently driven in a closed loop by monitoring the temperature on two thermocouples located on both sides of a 2.5 mm aperture inside which the hard X-ray propagates (see Figure 165).

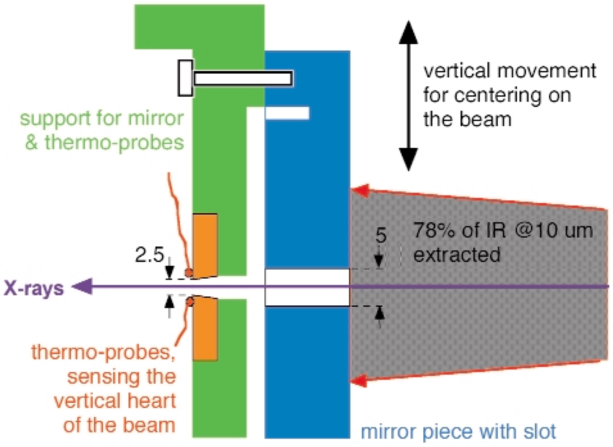

Fig. 165: The vertically motorised slotted mirror M1 designed for collecting infrared radiation and avoiding thermal deformation. The hard radiation propagates through the slot while most of the infrared is reflected.

Figure 166 presents the beamport layout including 7 mirrors. Another specificity of this infrared line is the use of a 37 mm diameter 0.8 mm thick CVD window located as upstream as possible. This window, which defines (and limits) the angular collection of the infrared radiation, is leak tight. It has been tested to both overpressure and accidental venting in the line; it isolates the ring vacuum from the beamline vacuum while staying transparent to the infrared. The whole line is operated in a low UHV type pressure which allows the use of ion pumps and facilitates the design of the vacuum protection.

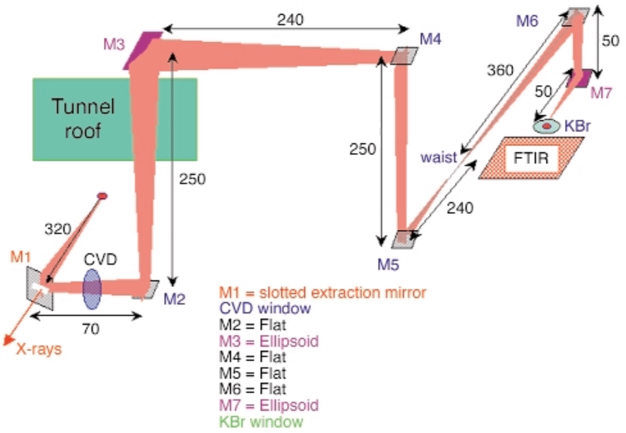

Fig. 166: Optics scheme of the extraction & transfer-line.

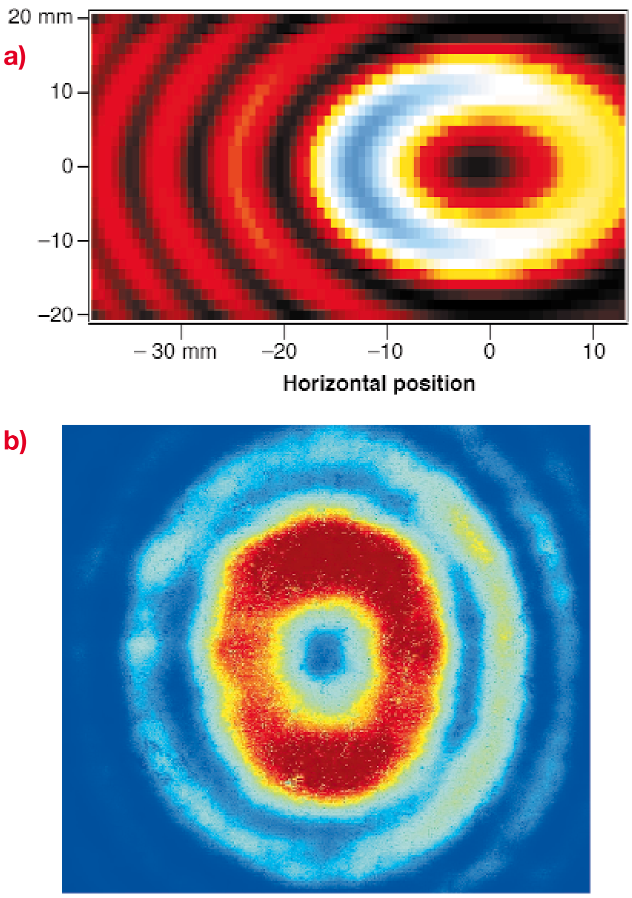

Fig. 167: Visible light pattern observed in the visible around 500 nm at the place of the M3 mirror. (a) Measurement; (b) Prediction from the SRW software.

The extracted light was recorded in the visible using a CCD camera located in front of M3, *i.e.* at the farthest distance possible from the source before any refocusing is applied. The image recorded in the visible part of the spectrum behind an interferential filter is shown in **Figure 167a** in good agreement with expectation from the SRW software [1] shown in Figure 167b. Both images show a ring-like structure that is produced by the interference of the fringe fields radiated by the electrons in the upstream and downstream bending magnets. Note that to perform such a measurements the slotted mirror M1 was lowered to a position where the whole of the visible light is collected, and to prevent any thermal deformation of M1 the ring current was limited to 1 mA.

A blackening on both the M1 surface and a quartz window (that was temporarily installed for a few months at the location of the CVD window location) was observed. Remedies are being sought with the possible use of Au or Ni coatings on M1, and/or by improving vacuum quality at this location.

Progress in the Modelling of the Impedance of the ESRF Storage Ring

The interaction of an electron beam with a vacuum chamber with varying and/or small cross section results in a variation of the tune with current (also called detuning) which is particularly significant for the ESRF ring when compared to other synchrotron sources. The interaction of the beam with such chambers can also generate a so-called transverse head-tail instability [2]. The main source of perturbation is the RF-fingers located below the dilatation bellows, the small slit between the flanges connecting adjacent chambers and the low aperture ID chambers and associated tapers connecting them to the larger cross-section of the quadrupole chambers.

The effect can be explained in terms of a wake field. It is an electromagnetic field generated behind a (so-called exciting) particle travelling close to the speed of light in a vacuum chamber. The wake field is a function of the distance s to the particle. The Fourier transformation of the wake field expressed as a function of s is the so-called coupling impedance. It only depends on the shape and electrical properties of the material constituting the vacuum chamber. It is often simply called the impedance of the chamber.

The wake and its associated coupling impedance can be longitudinal, in which case it perturbs the longitudinal oscillations and possibly increases the bunch length and the energy spread. In the following, we shall only deal with the transverse component of the wakefields in the horizontal and vertical planes.

In the past few years, a lot of effort has been put into computing the transverse wake field and its associated coupling impedance produced by the electron beam in each piece of vacuum chamber of the ring. This has been done using the GdfidL computer code [3] and has involved heavy parallel-type computing. The wake field due to the resistivity of the vacuum chamber wall was also taken into account in the analytical calculation.

In this study, it was realised that a significant part of the transverse wake fields are of quadrupolar type [4]. Therefore, a narrow flat chamber with a taper, which is known to generate an important vertical wake, also generates a horizontal wake of opposite polarity. The same is true for resistive wall generated wake fields in a constant cross-section chamber.

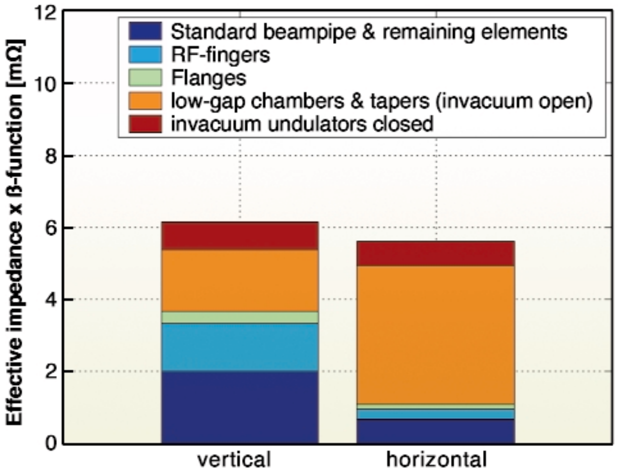

Fig. 168: Various contributions to the total effective horizontal and vertical coupling impedance (averaged of the power spectrum of a 5 mm bunch) of the ESRF ring weighted by the beta function as predicted from GdfidL computation.

The tune and the growth/damping of horizontal (vertical) oscillations are perturbed proportionally to the horizontal (vertical) impedance multiplied by the beta function at the place of the chamber inducing the perturbation. Low gap ID chambers are at locations with a low vertical beta function (2.5 to 5 m), while their impedance contribution is very likely the dominant, their overall contributions to the detuning or the instability threshold is reduced. On the other hand, in the horizontal plane, every even-numbered straight section has a large horizontal beta (37 m) function strongly enhancing the contribution to the detuning. This is confirmed experimentally by the observation that, as more and more narrow aperture ID vessels have been installed over the years, the current threshold of vertical instability has not changed very much while the horizontal instability current threshold has been significantly reduced. The horizontal chromaticity of the machine optics had to be increased in order to keep such current threshold constant. This is also clearly visible in **Figure 168**, which shows contributions to the effective impedance (impedance averaged over the power spectrum of the electron bunch) times the beta function. The orange and the brown contributions are generated by all the insertion device vacuum chambers and the in-vacuum undulators. While the predicted contribution in the horizontal plane matches the one expected from the measured detuning, only half of the observed vertical coupling impedance can yet be accounted for in the calculations made with GdfidL. It is suspected that the missing impedance contributions can be attributed to small elements in the achromat which have not yet been taken into account and/or to geometry simplifications applied to accelerate the simulations.

Modernisation of the Machine Control System

The ESRF accelerators are currently running a distributed control system called TACO, which was designed at the ESRF in the early 90s. It is used to run the accelerators and beamlines. TACO is based on the concept of distributed objects written in the C language and has a client/server architecture. The control hardware was based on VME computers with a real-time operating system called OS9, as well as UNIX computers running HP-UX. TACO has been upgraded over the years to keep up with the emerging needs. At the end of 1999, the machine control system included 92 VME crates and 25 Unix servers controlling more than 8000 pieces of equipment. During the same period of time, the computing world evolved dramatically. The CPU power and disk size were multiplied by more than 100. This triggered a decision in 2000 to launch an ambitious refurbishment program of the accelerator control system. The re-design of our control software has been carried out with the goal of being as independent as possible from the hardware platform and operating systems and maintaining compatibility with the TACO system. The new system called TANGO [5] makes use of international standards such as CORBA and modern object-oriented patterns and languages (Java, C++). The development is in line with open-source strategy and TANGO is available for free download from the Web [6]. In the mean time, several other laboratories have expressed the interest in using TANGO and an international collaboration has been formally established with SOLEIL and ELETTRA.

Simultaneously to the implementation of the TANGO control system, a process to modernise the hardware was set under way. As OS9 was frozen with no support available and no access to the source code; it was essential to replace it. Moreover the 10 year old VME CPUs all required an upgrade. Whenever economically possible, parts of the control system were moved from VME to PC technology. The PC hardware makes use of PCI and Compact PCI acquisition cards, and operates preferably under Linux but sometimes under Windows when Windows-based software solutions are provided by the card vendor. Whenever the control of certain pieces of equipment could not be easily migrated to PC technology, VMEs were kept but refurbished. In such cases, the obsolete 680x0 CPU type processors operating under OS9 were replaced by recent Intel type processors operating under Linux. The TACO type servers operating in the VMEs where correspondingly recompiled. Now, after many years of strict standardisation limited to one single hardware platform (VME), given the pressure from the market the control system has been opened up to several platforms. Fortunately, the TANGO system is designed to deal with this sort of hardware heterogeneity.

While the core of TANGO was developed in 2000-2001 and prototyping took place in 2002 together with the porting to Linux, it was only in 2003 that the full-scale migration process was really launched. Priority was given to the ring vacuum system, beamline front-end, radiation measurement, and personal safety system which could be easily migrated to industrial PCs running Linux. In 2004, the image acquisition system in the transfer lines, booster and ring was moved to windows based PCs, while the whole RF system control of the booster and ring was ported to Linux keeping the same VME hardware. Work is progressing with the insertion devices and beamline front-ends as well as beam diagnostic systems. Out of the 92 VME creates operated under OS9 in 2002, only 22 remain in December 2004. Full migration is scheduled for 2005. This large scale and somewhat frightening migration was made in a fully transparent manner to the ESRF user program and is now well under way. It has been made possible thanks to the modularity of the system as well as the excellent coordination between the staff responsible for the equipment and the staff of the computing service.

References

[1] SRW was developed at ESRF by O. Chubar and P. Elleaume. It is available for download from http://www.esrf.fr/machine/groups/insertion_devices/Codes/software.html

[2] J.L. Revol, R. Nagaoka, P. Kernel, L. Tosi, E. Karantzoulis, EPAC 2000 Vienna

[3] W. Bruns, "The GdfidL Electromagnetic Field Solver", www.gdfidl.de

[4] T.F.Günzel, Coherent and incoherent tune shifts deduced from the modelling of the impedance of the ESRF-ring, EPAC 2004, Lucerne

[5] Icaleps 2001 The ESRF TANGO control system status by J.M. Chaize *et al.*; Icaleps 2003 TANGO a CORBA Based Control System by A. Goetz *et al.* (MP705).

[6] Homepage: http://www.esrf.fr/tango; Sourceforge: http://sourceforge.net/projects/tango-cs/

ESRF

Highlights 2004

Facts and Figures

Member and Associate Countries

(as of January 2005)

Members' share in contribution to the annual budget:

27.5%	France
25.5%	Germany
15%	Italy
14%	United Kingdom
4%	Spain
4%	Switzerland
6%	Benesync (Belgium, The Netherlands)
4%	Nordsync (Denmark, Finland, Norway, Sweden)

Additional contributions
(percentages refer to Members' total contribution):

1%	Portugal
1%	Israel
1%	Austria
0.6%	Poland
0.44%	Czech Republic
0.2%	Hungary

The Beamlines

Details of the thirty-one public ESRF beamlines are given in **Table 7**. Three of these beamlines possess two end-stations, so there are thirty four end-stations in total, which can be run independently. An additional sixteen beamline branches, situated on bending magnets, are devoted to Collaborating Research Groups (CRG). Eleven of the CRG beamlines are now in operation (including GRAAL), and one (SpLine) is being commissioned. **Figure 169** shows the location of the beamlines in the experimental hall; a list of the CRG beamlines is presented in **Table 8**.

The Partnership for Structural Biology (PSB) initiated the construction of a new beamline complex at ID23. The first (multi-wavelength) branch has been operational since June 2004, the second (single wavelength microfocus) branch is currently being commissioned.

The High Pressure beamline has been moved from ID30 to a new location, ID27, that was previously used for an industrial beamline. The refurbished High Pressure beamline will be operational in February 2005.

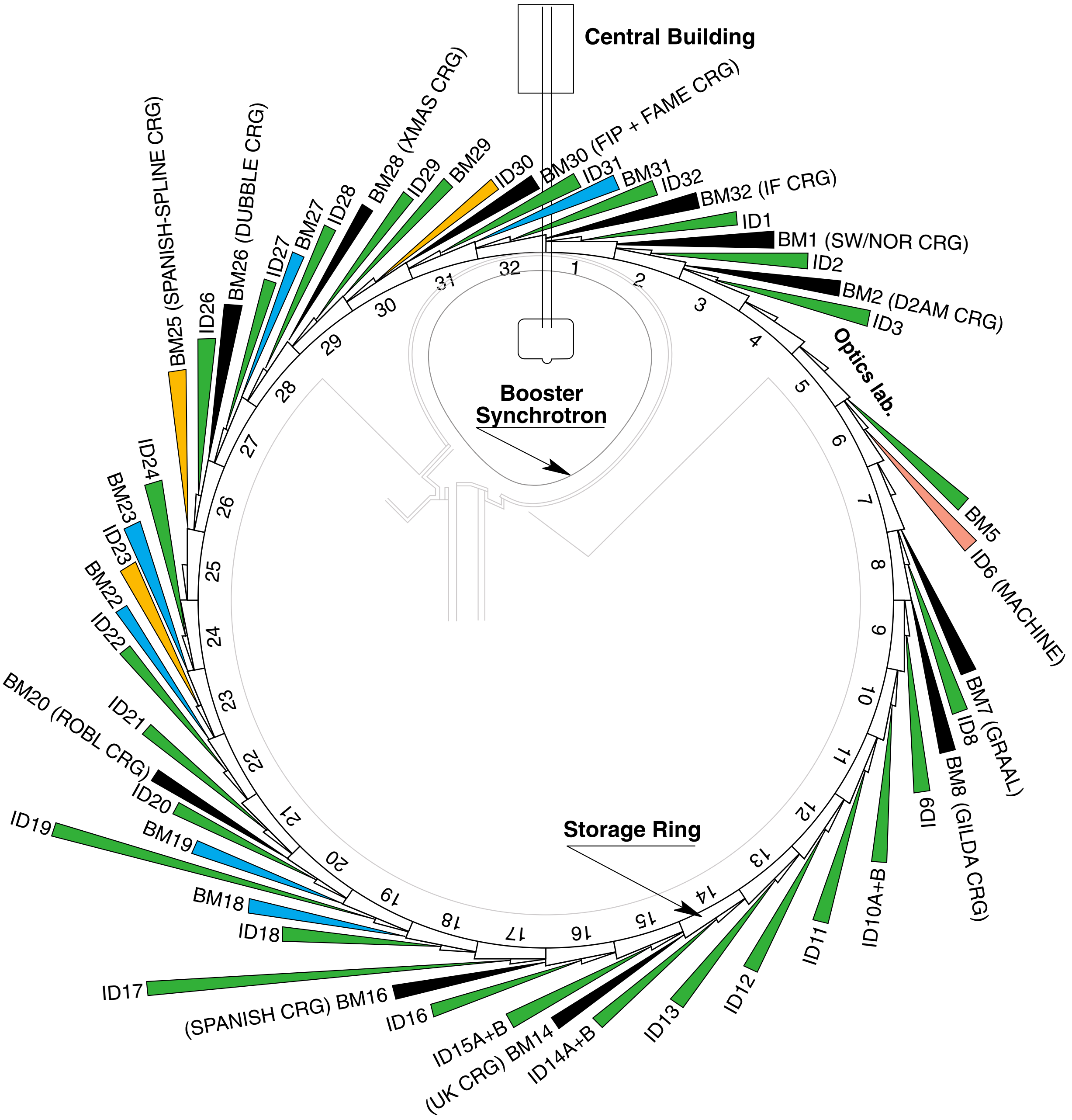

🟩	Public beamlines (operational)	30
	Number of independent end-stations	32
🟧	Insertion device ports for the machine	1
⬛	CRG beamlines (operational)	11
🟦	Free bending magnet ports	6
🟨	Under construction	3

Fig. 169: Experimental hall with the operational and scheduled beamlines (public and CRG beamlines).

SOURCE POSITION	NUMBER OF INDEPENDENT END-STATIONS	BEAMLINE NAME	STATUS
ID1	1	Anomalous scattering	Operational since 07/97
ID2	1	High brilliance	Operational since 09/94
ID3	1	Surface diffraction	Operational since 09/94
ID8	1	Dragon	Operational since 02/00
ID9	1	White beam	Operational since 09/94
ID10A	1	Troika I + III	Operational since 09/94
ID10B	1	Troika II	Operational since 04/98
ID11	1	Materials science	Operational since 09/94
ID12	1	Circular polarisation	Operational since 01/95
ID13	1	Microfocus	Operational since 09/94
ID14A	2	Protein crystallography EH 1	Operational since 07/99
		Protein crystallography EH 2	Operational since 12/97
ID14B	2	Protein crystallography EH 3	Operational since 12/98
		Protein crystallography EH 4	Operational since 07/99
ID15A	1	High energy diffraction	Operational since 09/94
ID15B	1	High energy inelastic scattering	Operational since 09/94
ID16	1	Inelastic scattering I	Operational since 09/95
ID17	1	Medical	Operational since 05/97
ID18	1	Nuclear scattering	Operational since 01/96
ID19	1	Topography	Operational since 06/96
ID20	1	Magnetic scattering	Operational since 05/96
ID21	1	X-ray microscopy	Operational since 12/97
ID22	1	Microfluorescence	Operational since 12/97
ID23	2	Macromolecular crystallography MAD	Operational since 06/04
		Macromolecular crystallography microfocus	Operational in 09/05
ID24	1	Dispersive EXAFS	Operational since 02/96
ID26	1	X-ray absorption on ultra-dilute samples	Operational since 11/97
ID27	1	High pressure	Operational since 02/05
ID28	1	Inelastic scattering II	Operational since 12/98
ID29	1	Multiwavelength anomalous diffraction	Operational since 01/00
ID30	1	High pressure	Operation stopped 07/04
ID31	1	Powder diffraction	Operational since 05/96
ID32	1	SEXAFS	Operational since 11/95
BM5	1	Optics - Open Bending Magnet	Operational since 09/95
BM29	1	X-ray absorption spectroscopy	Operational since 12/95

Table 7: List of the ESRF public beamlines in operation and under construction.

SOURCE POSITION	NUMBER OF INDEPENDENT END-STATIONS	BEAMLINE NAME	FIELD OF RESEARCH	STATUS
BM1	2	Swiss-Norwegian BL	X-ray absorption & diffraction	Operational since 01/95
BM2	1	D2AM (French)	Materials science	Operational since 09/94
BM7	1	GRAAL (Italian / French)	Gamma ray spectroscopy	Operational since 06/95
BM8	1	Gilda (Italian)	X-ray absorption & diffraction	Operational since 09/94
BM14	1	UK CRG	Macromolecular crystallography (MAD)	Operational since 01/01
BM16	1	SPANISH CRG	Structural biology (MAD, SAX)	Operational in 2003
BM20	1	ROBL (German)	Radiochemistry & ion beam physics	Operational since 09/98
BM25	2	SPLINE (Spanish)	X-ray absorption & diffraction	Construction phase
BM26	2	DUBBLE (Dutch/Belgian)	Small-angle scattering & interface diffraction Protein crystallography + EXAFS	Operational since 12/98 Operational since 06/01
BM28	1	XMAS (British)	Magnetic scattering	Operational since 04/98
BM30	2	FIP (French) FAME (French)	Protein crystallography EXAFS	Operational since 02/99 Operational since 08/02
BM32	1	IF (French)	Interfaces	Operational since 09/94

Table 8: List of the Collaborating Research Group beamlines in operation and under construction.

User Operation

The year 2004 saw the 10th anniversary of the opening of beamlines at ESRF for User Operation, on 1st September 1994. The full complement of 30 public beamlines, together with 11 additional beamlines (including GRAAL) operated by Collaborating Research Groups (CRGs) were open for user experiments. **Figure 170** shows the increase in the number of applications for beam time since 1998, and confirms that although the main beamline construction effort was complete by 1999, the number of proposals for beam time continues to rise.

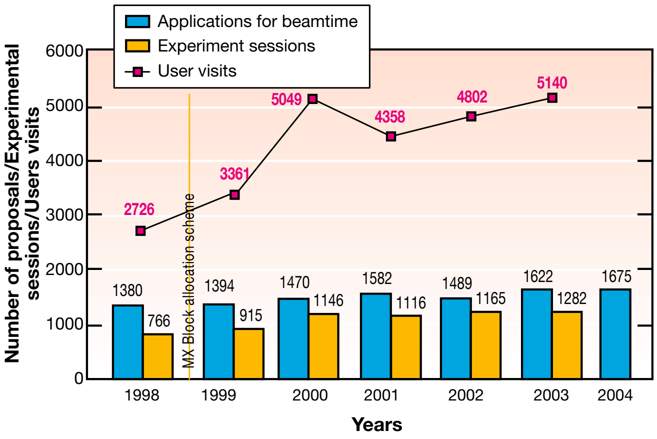

Fig. 170: Numbers of applications for beam time, experimental sessions, and user visits, 1998 to 2004. N.B. Final numbers of experiments and user visits for 2004 were not available at the time of going to press.

Proposals for experiments are selected and beam time allocations are made through peer review. Review Committees of specialists for the most part from European countries and Israel, have been set up in the following scientific areas:

- chemistry
- hard condensed matter: electronic and magnetic properties
- hard condensed matter: structures
- materials engineering and environmental matters
- macromolecular crystallography
- medicine
- methods and instrumentation
- soft condensed matter
- surfaces and interfaces

The Review Committees met twice during the year, some six weeks after the deadlines for submission of proposals (1 March and 1 September). They reviewed a total of 1675 applications for beam time, and selected 786 (47 %), which were then scheduled for experiments.

Features of this period have been:

- increasing numbers of projects concerned more with applied than basic research in materials science, engineering, environmental and cultural heritage matters. As shown in **Figure 171**, experiments in these areas accounted for 13 % of the total number of experiments carried out in the first half of 2004, an increase from 10% in 2002.
- the continued successful operation of the Block Allocation Group (BAG) scheme for macromolecular crystallography users. This scheme, designed to encourage groups of users to block together their multiple requests for beam time, and the scheduling of their experiments, encompassed 44 groups from Europe and Israel in 2004.

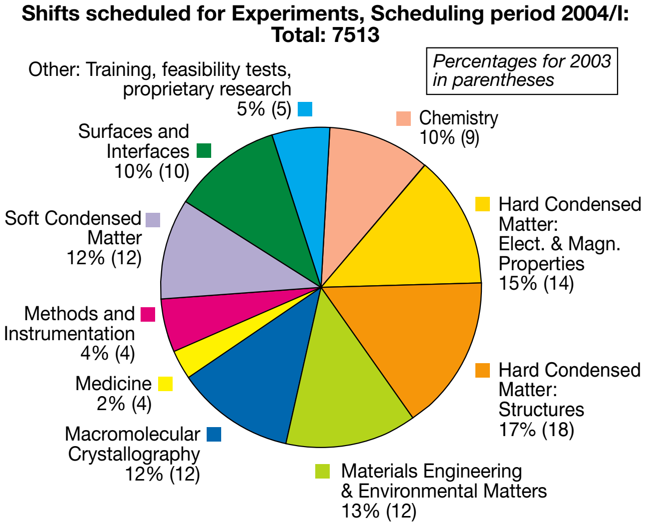

Fig. 171: Shifts scheduled for experiments, March to August 2004, by scientific area.

Requests for beam time, which is scheduled in shifts of 8 hours, totalled 26 251 shifts or 210 008 hours in 2004, of which 12 425 shifts or 99 400 hours (47.3%) were allocated. The distribution of shifts requested and allocated, by scientific area, is shown in **Table 9**.

Scientific field	Total shifts requested	Total shifts allocated
Chemistry	3 203	1 309
Hard condensed matter:		
• Electronic and magnetic prop.	4 108	1 839
• Structures	4 956	1 914
Materials engineering & environmental matters	3 269	1 593
Macromolecular crystallography	2 943	1 974
Medicine	879	423
Methods & instrumentation	868	414
Soft condensed matter	3 643	1 432
Surfaces & interfaces	2 382	1 527
Totals	**26 251**	**12 425**

Table 9: Number of shifts of beam time requested and allocated for user experiments, year 2004.

The first half of 2004 saw 2711 visits by scientists to the ESRF under the user programme, to carry out 665 experiments. Figure 170 shows the rapid rise in the number of user visits since 1998, the higher numbers in recent years reflecting in part the multiple visits made by macromolecular crystallography BAG teams. The peak in 2000 is due to a somewhat longer scheduling period, and correspondingly higher overall number of experimental sessions, and visits by users.

Overall, the number of users in each experimental team averaged 4 persons, and they stayed for some 4 days. Users responding to questionnaires indicate that they particularly appreciate the assistance they receive from scientists and support staff on beamlines, and smooth administrative arrangements, in addition to the quality both of the beam and of the experimental stations. Facilities on site, such as preparation laboratories, a canteen and the Guesthouse, also make an important contribution to the quality of user support.

Industrial Use

The ESRF was originally conceived for academic use and thus mainly for non-proprietary research. Industry was entitled to access the ESRF beamlines under similar conditions to those of academic users, through the peer-review system, free of charge, however with the obligation to publish results.

With the excellent performances obtained on the different beamlines, industry started to show greater interest in the ESRF and in particular for proprietary research, where the user is the owner of the data collected, confidentiality is ensured, publication of results is not required, rapid access is possible but … access to beam time has to be paid for.

Relations with industry for proprietary research are managed by the Industrial and Commercial Unit (ICU), in close collaboration with the Experiments Division. The ICU, created in 2002, reports to the Director General and is responsible for all initiatives related to the sale of beamtime and associated services, technology transfer, patents, licence agreements and special collaborations, in particular contracts within the framework programmes of the European Union.

To encourage industry to use ESRF beamlines, the ICU intends to create an industry-optimised environment, considering that industry has specific needs. The ICU has carried out market surveys to understand the industrial needs and the value of the service for industry.

However, the ESRF is not a commercial company and the industrial use for proprietary research should be fully compatible with academic research, which is the main mission of the ESRF. For this reason, only a maximum of 10% of the total scheduled beam time can be dedicated to proprietary research. Therefore, our offer is based on the quality and efficiency of the services provided to industry. The industrial users are assisted before, during and, if required, after the experiment by the scientific staff of the relevant beamline and by the technical staff from both the beamline and the Technical Beamline Support Group of the Experiments Division. Services related to the use of beam time can be provided with or without scientific assistance and a full service is possible on demand. In this case the customer sends the samples to be measured by courier to the ESRF, our scientists analyse them and send the results back using a secured system. This option permits customers to avoid spending time, especially nights, at the synchrotron. It is used in particular by the macromolecular crystallography beamlines providing the MXpress^{TM} service. All the ESRF staff involved in relations with industry have been trained to respect confidentiality, which is the basis for a mutual confidence and a fruitful collaboration.

If the industrial users carry out the experiment themselves, they can be accommodated on the ESRF site and make use of both the Guesthouse and the restaurant which are open 7 days a week, during normal service periods.

As a result of this organisation, the growth of beamtime sales for proprietary research strongly increased last year, as indeed it has over the last few years. In 2004 the turnover generated was about 300% higher than in 2001 and industrial activity is taking an increasing role in overall research activities. Even if there is no obligation to publish the results of proprietary research, part of these results are nevertheless published.

The use of the macromolecular crystallography beamlines represents more than 2/3 of the global industrial activity for proprietary research. In 2005 there will be four MX beamlines and a total of seven MX stations operating at the ESRF, including the two stations of the newly-created beamline ID23, built in the framework of the Partnership for Structural Biology (PSB). In order that the data collection becomes fully automated, all the stations will be equipped with sample changers, jointly developed by the ESRF and the EMBL, and automatic sample centring systems. This will enable the users to process many more crystals in the same period of time and in a reliable manner. The PSB combines the skills and resources of four world-leading institutes: the ESRF, the EMBL, the ILL and the IBS. This centre of excellence for structural biology, unique in Europe, will certainly be a strong tool to develop relations with industry.

A similar growth has been obtained in other groups of beamlines using different techniques, like imaging (ID19 – microtomography for characterisation, control and process development), diffraction (ID15, ID31), small-angle scattering (ID2 and ID13) or spectroscopy (ID24 for catalysis studies). Most of these beamlines are now equipped (ID2, ID19, ID31, etc) or are being equipped with robots which lead to an increasing capacity to respond to demand from both academic and industrial users.

The majority of our industrial users come from European countries. There are also some from North-America and Japan.

M. Rodriguez Castellano
Head of Industrial and Commercial Unit

Administration and Finance

Revised expenditure and income budget for 2003

Expenditure

		kEuro
Machine		
Personnel		4 730.5
Recurrent		2 324.6
Operating costs	*1 833.4*	
Other recurrent costs	*491.2*	
Capital		4 280
Machine developments	*4 280*	
Beamlines, instruments, experiments and in-house research		
Personnel		21 295.2
Recurrent		6 404.4
Operating costs	*3 657.9*	
Other Recurrent costs	*2 746.5*	
Capital		7 631.4
Beamline developments	*3 898.8*	
Beamline refurbishment	*3 732.6*	
Technical and administrative supports		
Personnel		15 156.6
Recurrent		9 066.7
Capital		2 538.7
Unexpended committed funds		
Funds carried forward to 2004		13.0
Total		**73 441.1**

Income

	kEuro
2003 Members' contributions	64 871.8
Funds carried forward from 2002	18.0
Other income	
Scientific Associates	3 124.4
Sale of beamtime	1 733.3
Other sales	443.3
Compensatory funds	1 281.0
Scientific collaboration and Special projects	671.3
Other	1 298.0
Total	**73 441.1**

Revised expenditure and income budget for 2004

Expenditure

		kEuro
Machine		
Personnel		4 680
Recurrent		2 425
Operating costs	*2 090*	
Other recurrent costs	*335*	
Capital		3 415
Machine developments	*4 415*	
Beamlines, instruments, experiments and in-house research		
Personnel		21 880
Recurrent		6 505
Operating costs	*3 540*	
Other Recurrent costs	*3 965*	
Capital		7 060
Beamline developments	*3 855*	
Beamline refurbishment	*3 225*	
Technical and administrative supports		
Personnel		15 120
Recurrent		9 110
Capital		3 017
Industrial and commercial activity		
Personnel		435
Recurrent		195
Personnel costs provision		1 710
Total		**75 552**

Income

	kEuro
2004 Members' contributions	65 358
Funds carried forward from 2003	13
Other income	
Scientific Associates	3 422
Sale of beamtime	2 040
Other sales	989
Compensatory funds	1 159
Scientific collaboration and Special projects	1 245
Other	1 326
Total	**75 552**

Expenditure 2003 by nature of expenditure

	kEuro
PERSONNEL	
ESRF staff	39 525.7
External temporary staff	80.6
Other personnel costs	1 576.2
RECURRENT	
Consumables	6 467.3
Services	9 167.9
Other recurrent costs	2 160.4
CAPITAL	
Buildings, infrastructure	1 116.6
Lab. and Workshops	270.4
Machine incl. ID's and Fes	4 279.9
Beamlines, Experiments	7 631.4
Computing Infrastructure	1 020.7
Other Capital costs	131.0
Unexpended committed funds	
Funds carried forward to 2004	13.0
Total	**73 441.1**

Revised budget for 2004 by nature of expenditure

	kEuro
PERSONNEL	
ESRF staff	40 335
External temporary staff	80
Other personnel costs	1 700
RECURRENT	
Consumables	6 050
Services	9 915
Other recurrent costs	2 270
CAPITAL	
Buildings, infrastructure	1 195
Lab. and Workshops	425
Machine incl. ID's and Fes	3 415
Beamlines, Experiments	7 060
Computing Infrastructure	992
Other Capital costs	405
Personnel costs provision	1 710
Total	**75 552**

2004 manpower

(posts filled on 31/12/2004)

	Scientists, Engineers, Senior Administrators	Technicians and Administrative Staff	PhD students	Total
Staff on regular positions				
Machine	25	39	3	67
Beamlines, instruments and experiments*	196	64.4	25.5	285.9
General technical services	52.6	64.6		117.1
Directorate, administration and central services	27.5	51.7		79.2
Sub-total	*301.0*	*219.7*	*28.5*	*549.2*
Other positions				
Short term contracts	8.6	13.5	22	
Scientific collaborators	5		5	
Staff under "contrats de qualification" (apprentices)		11	11	
European Union grants	5.8	3	8.8	
Total	**320.4**	**247.1**	**28.5**	**596.0**
Absences of staff (equivalent full time posts)				26.7
Total with absences				*569.3*
External funded research fellows				*30.5*

** Including scientific staff on time limited contract.*

Financial resources in 2002, 2003, 2004 and 2005, by major programme

(current prices in MEuro for the respective years)

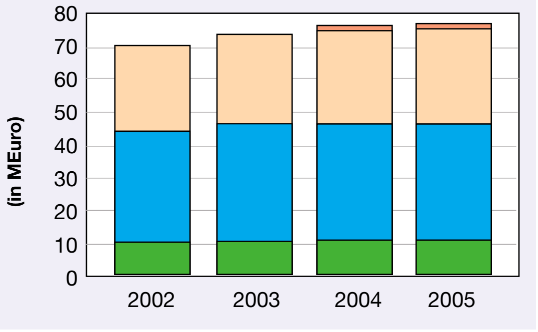

Financial resources in 2002, 2003, 2004 and 2005, by nature of expenditure

(current prices in MEuro for the respective years)

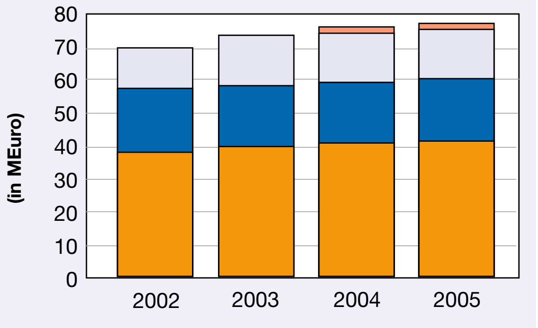

Organisation Chart of the ESRF
(as of January 2005)

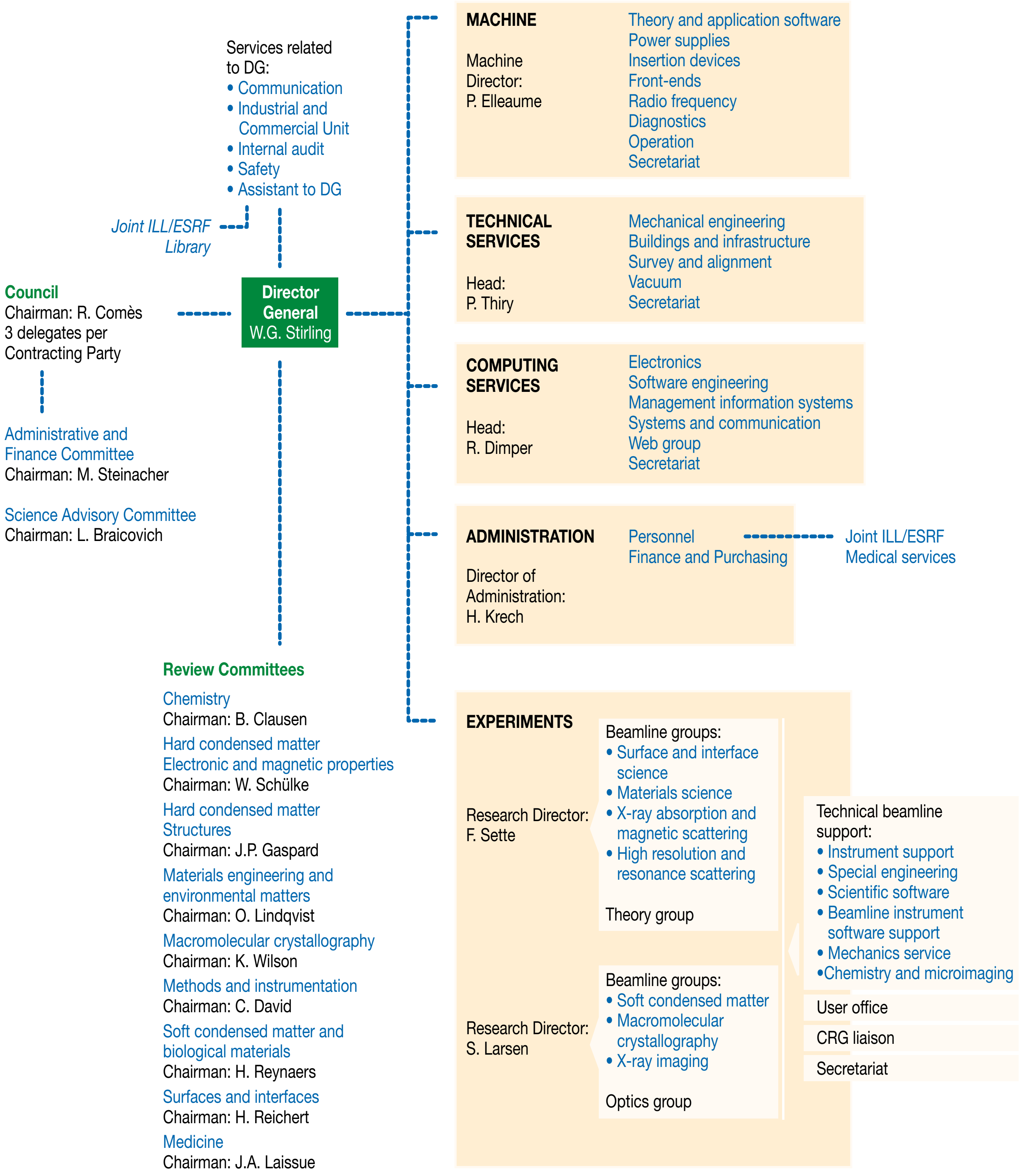

Services related to DG:
- Communication
- Industrial and Commercial Unit
- Internal audit
- Safety
- Assistant to DG

Joint ILL/ESRF Library

Council
Chairman: R. Comès
3 delegates per Contracting Party

Director General
W.G. Stirling

Administrative and Finance Committee
Chairman: M. Steinacher

Science Advisory Committee
Chairman: L. Braicovich

Review Committees

Chemistry
Chairman: B. Clausen

Hard condensed matter
Electronic and magnetic properties
Chairman: W. Schülke

Hard condensed matter
Structures
Chairman: J.P. Gaspard

Materials engineering and environmental matters
Chairman: O. Lindqvist

Macromolecular crystallography
Chairman: K. Wilson

Methods and instrumentation
Chairman: C. David

Soft condensed matter and biological materials
Chairman: H. Reynaers

Surfaces and interfaces
Chairman: H. Reichert

Medicine
Chairman: J.A. Laissue

MACHINE

Machine Director:
P. Elleaume

Theory and application software
Power supplies
Insertion devices
Front-ends
Radio frequency
Diagnostics
Operation
Secretariat

TECHNICAL SERVICES

Head:
P. Thiry

Mechanical engineering
Buildings and infrastructure
Survey and alignment
Vacuum
Secretariat

COMPUTING SERVICES

Head:
R. Dimper

Electronics
Software engineering
Management information systems
Systems and communication
Web group
Secretariat

ADMINISTRATION

Director of Administration:
H. Krech

Personnel
Finance and Purchasing

Joint ILL/ESRF Medical services

EXPERIMENTS

Research Director:
F. Sette

Beamline groups:
- Surface and interface science
- Materials science
- X-ray absorption and magnetic scattering
- High resolution and resonance scattering

Theory group

Research Director:
S. Larsen

Beamline groups:
- Soft condensed matter
- Macromolecular crystallography
- X-ray imaging

Optics group

Technical beamline support:
- Instrument support
- Special engineering
- Scientific software
- Beamline instrument software support
- Mechanics service
- Chemistry and microimaging

User office

CRG liaison

Secretariat

We gratefully acknowledge the help of:
C. Argoud, R. Barrett, J. Baruchel, N. Brookes, T. Bouvet,
D. Cornuejols, P. Elleaume, A. Freund, A. Kaprolat, Å. Kvick,
S. Larsen, G. Leonard, R. Mason, T. Metzger,
C. Riekel, M. Rodriguez Castellano, R. Rüffer, F. Sette,
W.G. Stirling, S. McSweeney, K. Witte, J. Zegenhagen,
and all the users and staff that have contributed
to this edition of the Highlights.
Thank you.

Editor
G. Admans
Layout
Pixel Project
Printing
Imprimerie du Pont de Claix

Communication Unit
ESRF
BP220 • 38043 Grenoble • France
Tel. (33) 4 76 88 20 25 • Fax. (33) 4 76 88 24 18
http://www.esrf.fr